

AN ABSTRACT OF THE THESIS OF

Gary E. McCown for the degree of Doctor of Philosophy in Physics  
presented on May 3<sup>rd</sup>, 1990.

Title: Submonolayer Adsorption on a Metal Surface, Investigated  
with Rydberg Atoms as Electric-Field-Sensitive Probes

## Redacted for Privacy

Abstract approved: \_\_\_\_\_

Carl A. Kocher

Electric fields due to adsorbates on a metal surface are studied experimentally with Rydberg atoms as probes. A beam of lithium Rydberg atoms, produced by an oven in a high-vacuum system, passes within  $3\mu\text{m}$  of the surface of a metal mesh having  $6\mu\text{m}$  square openings. Rydberg states with principal quantum numbers in the range  $20 \lesssim n \lesssim 80$  are produced by electron impact. Detected changes in the Rydberg atom flux through the mesh allow adsorption to be studied. The adsorption information obtained includes sticking probability, electric dipole moment, and desorption energy.

Methods are presented for the calculation of surface electric fields produced by adsorbed atoms or molecules, which are modeled as individual dipoles. Coverages of  $10^{-2}$  monolayer can produce electric field magnitudes  $E \gtrsim 120 \text{ V/cm}$  at distances  $\lesssim 3\mu\text{m}$  from the surface. Fields of this magnitude can ionize Rydberg atoms present in the atomic beam, reducing the flux through the mesh. A relationship is derived connecting the adsorbate dipole-moment

density on a metal surface to the electric field produced by adsorbates.

Desorption energies were measured at surface temperatures near 300 K for  $\text{H}_2\text{O}$  ( $1.05 \pm 0.05$  eV), CO ( $0.70 \pm 0.05$  eV), and  $\text{O}_2$  ( $0.86 \pm 0.06$  eV) on a polycrystalline Ni surface and for  $\text{H}_2\text{O}$  ( $0.85 \pm 0.05$  eV) and  $\text{SO}_2$  ( $0.93 \pm 0.06$  eV) on a polycrystalline Au surface. The product of the sticking probability and dipole moment,  $\mu s$ , was measured at surface temperatures near 300 K for CO, NO,  $\text{O}_2$ ,  $\text{H}_2\text{O}$ , and  $\text{SO}_2$  on the Ni surface and for  $\text{H}_2\text{O}$  and  $\text{SO}_2$  on the Au surface. The orientations of the dipole moments for CO, NO, and  $\text{O}_2$  were inferred from the experimental data and the dipole moment for  $\text{SO}_2$  ( $0.086 \pm 0.004 e a_0$ ) on Ni was measured. The measured desorption energies are comparable, within approximately 30%, to values reported in the literature for adsorbates on specific crystal faces. Other measured quantities are compared to values reported in the literature.

The limitations of the technique are discussed.

Submonolayer Adsorption on a Metal Surface,  
Investigated with Rydberg Atoms as Electric-Field-Sensitive Probes

by

Gary Edward McCown

A THESIS

submitted to

Oregon State University

in partial fulfillment of  
the requirements for the  
degree of

Doctor of Philosophy

Completed May 3<sup>rd</sup>, 1990

Commencement June 10<sup>th</sup>, 1990

APPROVED:

Redacted for Privacy

---

Associate Professor of Physics in charge of major

Redacted for Privacy

---

Chairman of Department of Physics

Redacted for Privacy

---

Dean of Graduate School

Date thesis presented May 3<sup>rd</sup>, 1990

Typed by the author, Gary E. McCown

## ACKNOWLEDGEMENTS

In the course of completing a Ph.D., there are many individuals who support and contribute to the work. The individuals who have made truly significant contributions to this Ph.D. work are mentioned below. I will, no doubt, miss someone. However, I hope forgiveness will be forthcoming.

At the top of this list is, as for any graduate student, the thesis adviser (major professor). Prof. Carl A. Kocher has been mine. In my estimation I could not have had a better individual for major prof. His continual support and encouragement have been inspiring during the long duration required for an experimental thesis. He is an excellent teacher both in the class and in the lab. His expertise in the lab has been greatly appreciated. There are many other positive attributes to mention in way of thanking him for his help, but I will stop after saying that his compassion and kindness to me have been greatly helpful and greatly appreciated.

The Chairman of the Physics Department, Prof. Ken Krane, has been very supportive during the time I have been at O.S.U. This support has kept me here. Thanks are due him.

My mother and father have been a help and an encouragement to me during the struggle to finish. I wish that my dad had lived to see this day, but I am thankful for the things that he and mom taught me. I am grateful to God for these great parents.

Oops! I have run over onto another page!!

There are others to thank. Chuck Taylor began the work that this thesis is built on and he helped educate me in the workings of the lab equipment.

Prof. Hetherington has been helpful in his consultations. He has much insight about surfaces and such.

Rod Eisenberg has been a true friend.

The daily coffee provided by Espresso Roma has been a necessity.

Thanks to all my great friends, Craig, Clark, Carl, Steve, Robin, Lisa, Erin, Scott...

## TABLE OF CONTENTS

|  |    |
|--|----|
| CHAPTER 1: INTRODUCTION  |    |
| 1.1 Statement of the Problem   | 1  |
| 1.2 Related Experiments  | 2  |
| 1.3 Properties of Rydberg Atoms  | 2  |
| 1.4 Interaction between Rydberg Atoms and Surfaces                           | 4  |
| 1.5 Description of the Method  | 5  |
| CHAPTER 2: THEORETICAL FOUNDATIONS   | 9  |
| 2.1 Gas-Surface Interactions   | 9  |
| 2.1.1 Physisorption  | 10 |
| 2.1.2 Chemisorption  | 10 |
| 2.1.3 Surface Diffusion  | 12 |
| 2.1.4 Desorption   | 13 |
| 2.2 Electric Field Calculations  | 14 |
| 2.2.1 A Uniformly Covered Closed Surface                                     | 15 |
| 2.2.2 A Cylindrical Conducting Mesh Filament                                 | 15 |
| 2.2.3 A Nonconducting Dipole Strip   | 19 |
| 2.2.4 Inside a Mesh Opening  | 23 |
| 2.3 The Electric Field in a Mesh Opening,<br>Including Distant Mesh Elements | 25 |
| CHAPTER 3: EXPERIMENTAL APPARATUS  | 35 |
| 3.1 Description of the Experimental Apparatus                                | 35 |
| 3.2 Data Acquisition   | 44 |
| 3.3 Particle Currents in the Vacuum Chamber                                  | 49 |
| 3.3.1 Composition of the Residual Gas  | 49 |
| 3.3.2 Lithium Particle Current at the Mesh                                   | 50 |
| 3.3.3 Adsorbate Particle Current at the Mesh                                 | 51 |

TABLE OF CONTENTS CONTINUED

|            |   |    |
|------------|---|----|
| CHAPTER 4: | TIME-DEPENDENT MODEL FOR ADSORBATE COVERAGE                               | 53 |
| 4.1        | Langmuir-Type Model   | 53 |
| 4.1.1      | Adsorption on the Detector Side   | 55 |
| 4.1.2      | Adsorption on the Source Side   | 56 |
| 4.2        | Model for Adsorption-Desorption Equilibrium                               | 57 |
| 4.3        | Application of the Model and Comparison to Experiment                     | 58 |
| CHAPTER 5: | TECHNIQUES FOR DATA ANALYSIS  | 66 |
| 5.1        | Relation Linking Adsorbate Dipole-Moment Density to the Mesh Transmission | 66 |
| 5.2        | Dipole-Moment Density with and without Introduced Adsorbate               | 74 |
| 5.2.1      | Comparison of Densities with and without Introduced Adsorbate             | 76 |
| 5.2.2      | Changes Occurring When $s_a c_a \gg s_w c_w$                              | 79 |
| 5.2.3      | Transmission Changes after Equilibrium is Reached                         | 80 |
| CHAPTER 6: | EXPERIMENTAL PROCEDURES AND OBSERVATIONS                                  | 81 |
| 6.1        | Procedures  | 81 |
| 6.1.1      | Treatment of the Mesh   | 84 |
| 6.1.2      | Mesh Temperature Control and Heating                                      | 85 |
| 6.2        | Observations  | 87 |
| 6.2.1      | Au Mesh   | 87 |
| 6.2.2      | Ni Mesh   | 91 |
| 6.3        | Externally Introduced Adsorbate Gasses                                    | 93 |
| 6.3.1      | CO Adsorption on Ni   | 94 |
| 6.3.1.1    | CO Gated  | 94 |
| 6.3.1.2    | CO Introduced Continuously  | 96 |

TABLE OF CONTENTS CONTINUED

|              |   |     |
|--------------|---|-----|
| 6.3.2        | O <sub>2</sub> Adsorption on Ni           | 98  |
| 6.3.2.1      | O <sub>2</sub> Gated                      | 98  |
| 6.3.2.2      | O <sub>2</sub> Introduced Continuously    | 104 |
| 6.3.3        | H <sub>2</sub> O Adsorption on Au         | 106 |
| 6.3.4        | H <sub>2</sub> O Adsorption on Ni         | 110 |
| 6.3.5        | H <sub>2</sub> O Desorption from Ni       | 112 |
| 6.3.6        | SO <sub>2</sub> Adsorption on Au          | 112 |
| 6.3.7        | SO <sub>2</sub> Adsorption on Ni          | 115 |
| 6.3.8        | NO Adsorption on Ni                       | 117 |
| CHAPTER 7:   | ANALYSIS OF EXPERIMENTAL OBSERVATIONS     | 120 |
| 7.1          | CO Adsorption on Ni                       | 121 |
| 7.2          | O <sub>2</sub> Adsorption on Ni           | 129 |
| 7.3          | H <sub>2</sub> O Adsorption on Au         | 138 |
| 7.4          | H <sub>2</sub> O Adsorption on Ni         | 140 |
| 7.5          | SO <sub>2</sub> Adsorption on Au          | 146 |
| 7.6          | SO <sub>2</sub> Adsorption on Ni          | 146 |
| 7.7          | NO Adsorption on Ni                       | 156 |
| CHAPTER 8:   | SUMMARY                                   | 158 |
| 8.1          | Review of the Results                     | 158 |
| 8.2          | Difficulties of the Technique             | 161 |
| 8.3          | Limits of this Work                       | 165 |
| 8.4          | Suggestions for Future Work               | 166 |
| BIBLIOGRAPHY |   | 170 |
| APPENDIX A:  | CALCULATION OF TEMPERATURE DIFFUSION TIME | 174 |
| APPENDIX B:  | SELECTED NOTATIONS                        | 175 |
| APPENDIX C:  | ELECTRIC FIELDS DUE TO A THICK MESH       | 177 |

## LIST OF FIGURES

| Figure |   |    |
|--------|---|----|
| 1-1    | Apparatus Schematic Diagram   | 6  |
| 2-1    | Geometry of a Dipole Layer on a Conducting Cylinder   | 16 |
| 2-2    | Electric Field Lines (solid lines) and Equipotentials<br>(broken lines) Produced by a Nonuniform Dipole Layer on<br>an Infinitely Long Cylinder | 20 |
| 2-3    | Electric Field Lines (solid lines) and Equipotentials<br>(broken lines) Produced by a Uniform Dipole Layer on<br>an Infinitely Long Strip       | 22 |
| 2-4    | Electric Field Contours Inside a Mesh Opening,<br>Showing Electric Field Magnitude  | 26 |
| 2-5    | A Quarter Mesh Opening, Showing Electric Field<br>Contours Scaled to the Field at the Center  | 27 |
| 2-6    | Mesh Frame  | 29 |
| 2-7    | Geometry of a Square Dipole Patch   | 31 |
| 2-8    | Geometry of the Mesh for Peripheral Openings  | 33 |
| 3-1    | Schematic of the Experimental Apparatus   | 36 |
| 3-2    | Diagram of the Mesh Mount   | 39 |
| 3-3    | Electron Micrographs of the Mesh Samples<br>(a) Side toward Source      (b) Side toward Detector  | 40 |
| 3-4    | Diagram of Apparatus for Adsorbate Gas Introduction   | 42 |
| 3-5    | Typical Measured Mesh Transmission  | 45 |
| 3-6    | Dipole-Moment Density Converted from Transmission   | 48 |
| 4-1    | Transmission with H <sub>2</sub> O Varied<br>(a) $\tau_w = 105$ s      (b) $\tau_w = 65$ s  | 60 |

LIST OF FIGURES CONTINUED

|      |   |     |
|------|---|-----|
| 4-2  | Model Transmission Calculations with H <sub>2</sub> O Varied                      |     |
|      | (a) $\tau_w = 120$ s      (b) $\tau_w = 75$ s                                     | 61  |
| 4-3  | Transmission with Li Varied   |     |
|      | (a) $\tau_{LI} = 100$ s      (b) $\tau_{LI} = 290$ s      (c) $\tau_{LI} = 540$ s | 64  |
| 4-4  | Model Transmission Calculations with Li Varied                                    |     |
|      | (a) $\tau_{LI} = 100$ s      (b) $\tau_{LI} = 200$ s      (c) $\tau_{LI} = 540$ s | 65  |
| 5-1  | Effective Open Area vs Electric Field at Center                                   | 68  |
| 5-2  | Rydberg Atom Survival Probability vs Electric Field                               | 69  |
| 5-3  | Differential Area dA within a Mesh Opening  | 71  |
| 5-4  | Mesh Transmission vs Dipole-Moment Density  | 73  |
| 5-5  | Typical Experimental Data   |     |
|      | (a) $ \langle N\mu \rangle $ vs t      (b) $\langle N\mu \rangle$ vs t            | 75  |
| 6-1a | Au Mesh Transmission Prior to Heating   | 82  |
| 6-1b | Ni Mesh Transmission Prior to Heating   | 83  |
| 6-2  | Typical Transmission Sequence for Au Mesh   | 88  |
| 6-3  | Typical Transmission Sequence for Ni Mesh   | 92  |
| 6-4  | CO on Ni with CO Gated  |     |
|      | $c_1=0.077/s$ $c_2=0.143/s$ $c_3=0.152/s$ $c_4=c_5=0.017/s$                       | 95  |
| 6-5  | CO on Ni  |     |
|      | (*) Constant CO: $c=0.018/s$  |     |
|      | (.) No Introduced Adsorbate   | 97  |
| 6-6a | Ni with No Introduced Adsorbate Gas   | 99  |
| 6-6b | O <sub>2</sub> on Ni with O <sub>2</sub> Gated                                    |     |
|      | $c_1=0.19/s$ $c_2=0.25/s$ $c_3=0.28/s$ $c_4=0.35/s$ $c_5=0.12/s$                  | 100 |
| 6-7a | Ni with No Introduced Adsorbate Gas   | 102 |

LIST OF FIGURES CONTINUED

|      |  |     |
|------|--|-----|
| 6-7b | O <sub>2</sub> on Ni with O <sub>2</sub> Gated<br>c <sub>1</sub> =0.15/s c <sub>2</sub> =0.33/s c <sub>3</sub> =0.15/s                               | 103 |
| 6-8  | O <sub>2</sub> on Ni with T <sub>S</sub> ≅ 350 K<br>(* ) Constant O <sub>2</sub> : c=0.072/s<br>(·) No Introduced Adsorbate                          | 105 |
| 6-9a | Au with No Introduced Adsorbate Gas  | 107 |
| 6-9b | H <sub>2</sub> O on Au with H <sub>2</sub> O Gated<br>c <sub>1</sub> =0.127/s c <sub>2</sub> =0.207/s c <sub>3</sub> =0.149/s                        | 108 |
| 6-10 | H <sub>2</sub> O on Ni<br>(+) Constant H <sub>2</sub> O: c=0.21/s<br>(·) No Introduced Adsorbate   | 111 |
| 6-11 | H <sub>2</sub> O Desorption from Ni  | 113 |
| 6-12 | SO <sub>2</sub> on Au with SO <sub>2</sub> Gated<br>(+) SO <sub>2</sub> : c <sub>1</sub> = 0.23/s, c <sub>2</sub> = 0<br>(·) No Introduced Adsorbate | 114 |
| 6-13 | SO <sub>2</sub> on Ni<br>(·) SO <sub>2</sub> : c=0 (X) SO <sub>2</sub> : c=0.059/s<br>(O) SO <sub>2</sub> : c=0.044/s                                | 116 |
| 6-14 | NO on Ni<br>(·) No Introduced Adsorbate (O) NO: c=0.06/s   | 118 |
| 7-1  | Dipole-Moment Density: Ni Substrate: CO Gated  | 124 |
| 7-2a | Dipole-Moment Density: Ni Substrate:<br>No Introduced Adsorbate  | 125 |
| 7-2b | Dipole-Moment Density: Ni Substrate: Constant CO   | 126 |
| 7-2c | Dipole-Moment Density Difference: CO on Ni Substrate   | 128 |
| 7-3a | Dipole-Moment Density: Ni Substrate: O <sub>2</sub> Gated  | 131 |

LIST OF FIGURES CONTINUED

|       |   |     |
|-------|---|-----|
| 7-3b  | Dipole-Moment Density: Ni Substrate: O <sub>2</sub> Gated<br>(400 s Through 1600 s Shown) | 132 |
| 7-4a  | Dipole-Moment Density: Ni Substrate:<br>No Introduced Adsorbate                           | 134 |
| 7-4b  | Dipole-Moment Density: Ni Substrate: O <sub>2</sub> Gated                                 | 135 |
| 7-5   | a) Dipole-Moment Density: Ni Substrate:<br>No Introduced Adsorbate                        |     |
|       | b) Dipole-Moment Density: Ni Substrate: Constant O <sub>2</sub>                           | 136 |
| 7-5c  | Dipole Moment Density Difference: O <sub>2</sub> on Ni Substrate                          | 137 |
| 7-6   | Dipole-Moment Density: Au Substrate: H <sub>2</sub> O Gated                               | 139 |
| 7-7a  | Dipole-Moment Density: Ni Substrate:<br>No Introduced Adsorbate                           | 142 |
| 7-7b  | Dipole-Moment Density: Ni Substrate: Constant H <sub>2</sub> O                            | 143 |
| 7-7c  | Dipole-Moment Density Difference: H <sub>2</sub> O on Ni Substrate                        | 144 |
| 7-8   | Dipole-Moment Density: Ni Substrate: H <sub>2</sub> O Desorption                          | 145 |
| 7-9a  | Dipole-Moment Density: Au Substrate:<br>No Introduced Adsorbate                           | 147 |
| 7-9b  | Dipole-Moment Density: Au Substrate: SO <sub>2</sub> Gated                                | 148 |
| 7-9c  | Dipole-Moment Density Difference: SO <sub>2</sub> on Au Substrate                         | 149 |
| 7-10a | Dipole-Moment Density Difference: SO <sub>2</sub> on Ni Substrate                         | 150 |
| 7-10b | Dipole-Moment Density Difference: SO <sub>2</sub> on Ni Substrate                         | 152 |
| 7-10c | Dipole-Moment Density: Ni Substrate:<br>No Introduced Adsorbate                           | 153 |
| 7-10d | Dipole-Moment Density: Ni Substrate: Constant SO <sub>2</sub>                             | 154 |
| 7-10e | Dipole-Moment Density: Ni Substrate: Constant SO <sub>2</sub>                             | 155 |
| 7-11  | Dipole-Moment Density Difference: NO on Ni Substrate                                      | 157 |

LIST OF FIGURES CONTINUED

|     |   |     |
|-----|---|-----|
| 8-1 | Comparison of T vs $\langle N\mu \rangle$ for Two Calculations of E | 163 |
| 8-2 | New Apparatus Design  | 169 |
| C-1 | Geometry of the Thick Mesh  | 179 |

## LIST OF TABLES

|         |  |    |
|---------|--|----|
| TABLE 1 | Incidence Times and Particle Currents for H <sub>2</sub> O on<br>Au and Ni | 50 |
| TABLE 2 | Incidence Times and Particle Currents for Li on<br>Au and Ni               | 51 |
| TABLE 3 | Incidence Times and Pressures for Adsorbate Gases                          | 52 |

SUBMONOLAYER ADSORPTION ON A METAL SURFACE,  
INVESTIGATED WITH RYDBERG ATOMS AS ELECTRIC-FIELD SENSITIVE PROBES

CHAPTER 1: INTRODUCTION

1.1 Statement of the Problem

Traditional methods for surface investigations include the deflection of charged particles from a surface, the interaction of photons with the surface, and the bombardment of the surface by neutral atoms such as helium. The present work will show that a beam of neutral atoms may be used to investigate adsorption onto and desorption from a metallic surface. These atoms do not make physical contact with the surface, but act as a probe of surface electric fields due to adsorbed particles. A discussion of the usefulness of Rydberg atoms in the investigation of properties of atoms or molecules adsorbed on metal surfaces will be made.

This work will show experimentally that Rydberg atoms, as probes of surface electric fields, may be used to determine sticking probabilities, adsorbate orientations, desorption energies and dipole moments. A theory describing the interaction between Rydberg atoms and the electric field produced by surface

adsorbates will be presented. An original theoretical model and method of analysis will be developed to explain and interpret the observations. Experimental procedures and results will be shown to substantiate premises and conclusions. Values for physical properties of adsorbates will be obtained from the data presented. Finally, necessary assumptions and limitations will be discussed in the context of this and future work.

### 1.2 Related Experiments

C.R. Taylor and C.A. Kocher have shown experimentally that Rydberg atoms may be used as probes of surface electric fields produced by adsorbed layers.<sup>1,2</sup> This work is an advancement of their seminal experiments. It will be shown in this work that particles adsorbed on the surface of a metal generate electric fields that extend from the surface of the metal. These fields may be large enough to ionize Rydberg atoms passing near the surface. Therefore, the survival probability for Rydberg atoms passing near a metal surface is dependent upon the concentration, species, dipole moment, orientation and binding energy of the adsorbate(s) on the surface.

### 1.3 Properties of Rydberg Atoms

Edelstein and Gallagher describe the Rydberg state as an atom in a state of sufficiently high principal quantum number  $n$  that the outermost electron is far from the ionic core and other

electrons.<sup>3</sup> Therefore, the atom appears hydrogenic, so that the electron has many of the properties of an electron in a hydrogen atom. The outer electron in these states is primarily influenced by the positively charged ionic core and is very weakly bound to it. To first order, penetration of the ionic core by the electron can be ignored. Hydrogenic theory may, with close accuracy, be applied to these states.

Several physical properties of Rydberg atoms are relevant. The average electron orbit radius is  $r_n = n^2 a_0$ , where  $a_0 = \hbar^2 / m e^2 \cong 5.3 \times 10^{-9}$  cm is the Bohr radius. The radius increases rapidly with  $n$ . For a quantum state  $n = 35$  the radius is  $r_n \cong 6 \times 10^{-6}$  cm. The electron binding energy is  $W_B = e^2 / 2n^2 a_0$ . For  $n = 35$  the electron binding energy is  $W_B \cong 11$  meV, whereas the binding energy for an electron in the ground state of hydrogen is 13.6 eV. The radiative lifetime for a state with high  $n$  and low orbital angular momentum quantum number  $\ell$  varies as  $n^3$ , and as  $n^5$  for states with  $\ell = \ell_{\max} = n - 1$ . For Li most of the states with  $n \geq 20$  survive for more than  $10^{-3}$  s.<sup>4</sup> Additionally, the decay proceeds primarily by dipole radiation:  $|\delta n| = |\delta \ell| = 1$ . Therefore, one long lived state decays to another long-lived state:  $|n, \ell\rangle$  decays to  $|n - 1, \ell - 1\rangle$ .

The electric field threshold for ionization of Rydberg states may be derived semi-classically and is  $E_n = E_0 / n^4$  where  $E_0$  is  $6.4 \times 10^8$  V/cm. This relationship between  $E_n$  and  $n$  has been

verified experimentally.<sup>5</sup> The electric field required to ionize an atom with  $n = 35$  is  $E_n \cong 425$  V/cm. The rate for electric field ionization as reported by Jeys et al.<sup>6</sup> when the electric field exceeded  $E_n$  was greater than  $10^9$  s<sup>-1</sup>. Thus state  $n = 35$  will be ionized when it has been exposed to an electric field  $E \geq E_n$  for  $10^{-9}$  s. The time of flight for a Rydberg atom is dependent upon the beam velocity given by  $\bar{v} = (8 k T / \pi m)^{1/2}$  where  $m$  is the atomic mass,  $T$  is the oven temperature and  $k$  is Boltzmann's constant. The time of flight also depends on the distance between oven and detector. For this experiment a typical value of the Rydberg atom velocity is  $\bar{v} = 2 \times 10^5$  cm/s, and the oven-to-detector distance is  $L_{OD} = 60$  cm. These conditions imply a time of flight for a typical Rydberg atom of  $t = L_{OD} / \bar{v} = 3 \times 10^{-4}$  s. The time for an atom to travel through the mesh may be determined by taking the width of the mesh,  $2 \times 10^{-4}$  cm, and dividing it by the typical Rydberg atom velocity,  $2 \times 10^5$  cm/s. This yields a typical transit time of  $10^{-9}$  s for a Rydberg-Atom passing through the mesh.

#### 1.4 Interaction between Rydberg Atoms and Surfaces

Many experiments have used beams of ground-state atoms to study solid surfaces. For example, neutral ground-state He atoms have been deflected from surfaces to investigate atom-surface interactions and surface structure. Shih et al. passed a well collimated thermal beam of atoms within  $0.1 \mu\text{m}$  of a metallic

cylinder to investigate the interaction force between surface and atom.<sup>7</sup> The deflection of the beam was small. A maximum deflection of approximately 5 milliradians was observed.

Surface ionization is the tunneling of the electron into the surface and the stripping away of the electron from the atomic core. This occurs when the force of attraction due to the image charge in the surface is greater than the force of attraction due to the atomic core. Fabre, Gross, Raimond, and Haroche used state-selected Na Rydberg atoms passing through a mesh to investigate the ionization of these atoms due to their interaction with the surface.<sup>8</sup> Fabre et al. found that the Na atoms were surface ionized when they passed within a distance of approximately  $4n^2a_0$  from the surface: the outer electron was stripped from the ion core and absorbed into the mesh surface. Surface ionization places a limit on the minimum distance between a Rydberg atom and the surface for which it will not be ionized.

### 1.5 Description of the Method

The experiment consists physically of a beam generation region, an atom-mesh interaction region, and a detection region. Figure 1-1 shows a schematic diagram of the apparatus. Li atoms are excited to Rydberg states in the beam generation region, and these atoms collide with or pass through the mesh in the atom-mesh interaction region. The detection region contains a detector that allows the flux of highly excited atoms to be

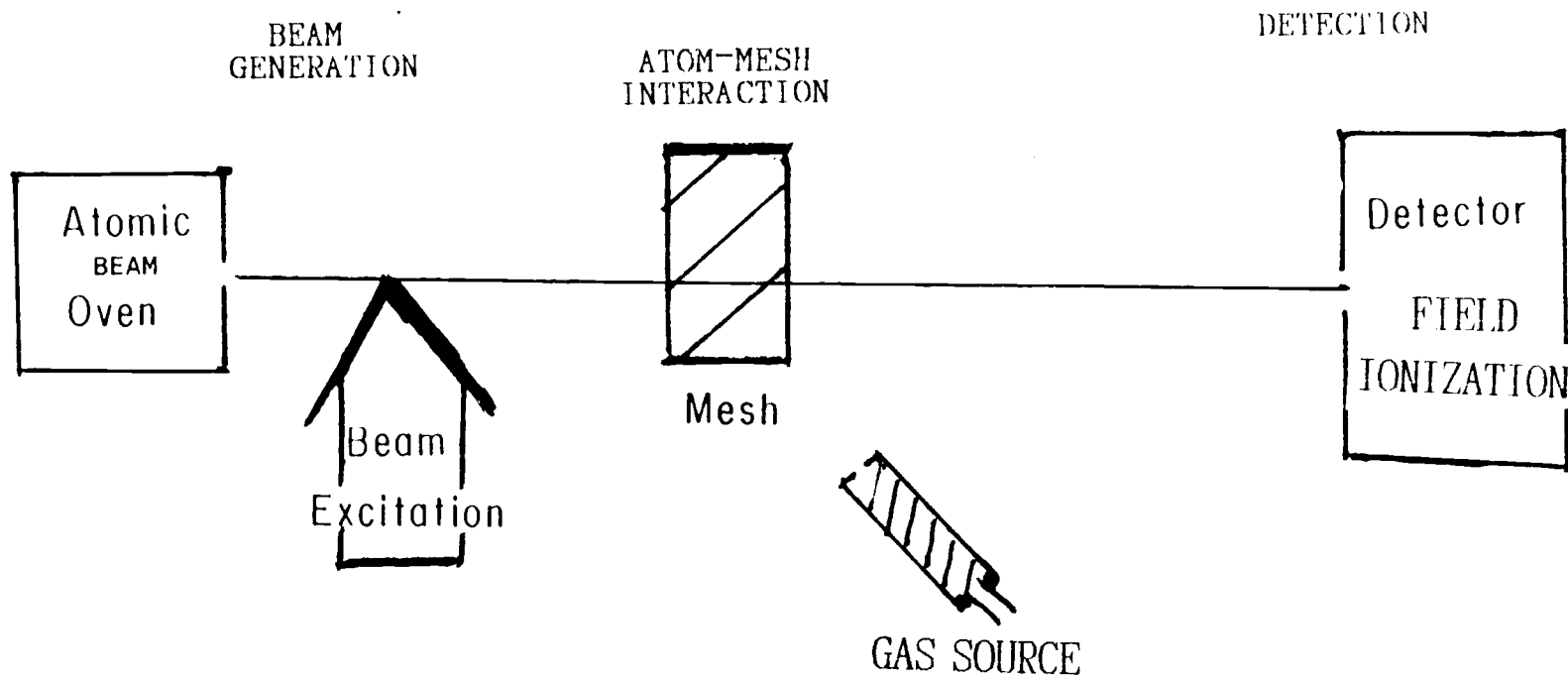


Fig. 1-1 Apparatus Schematic Diagram

determined.

The interaction region contains the mesh sample and gas introduction system. The mesh is a thin sheet of metal that has  $6 \mu\text{m}$  square openings. These openings constitute 25% of the surface area of the mesh. The mesh may be removed or inserted into the atomic beam as desired. A mesh is used so that all highly excited Li atoms, with quantum number  $n$  between 20 and 80, pass within  $3 \mu\text{m}$  of the metal surface. Adsorption onto the metal surface may occur. The adsorbates may be from the background gas in the vacuum system or from the gases introduced externally through the gas introduction system. These adsorbates may produce an electric field near the metal surface, extending several microns outward. The gas source system allows various species of gases to be introduced onto the metal surface.

Li atoms with quantum numbers  $n$  between about 20 and 80 are ionized by electric fields produced by adsorbates on the mesh surface. In Sec. 2.2.3 it will be calculated that electric fields  $E \gtrsim 300 \text{ V/cm}$  are produced by adsorbate coverages on the mesh surface of less than one monolayer. An electric field of this magnitude will ionize quantum states with  $n \gtrsim 40$ .

Field ionization occurs when the force on the electron due to an external electric field exceeds the attractive force due to the ionic core. The electron is removed from the atomic core, and the atom is lost from the beam. Therefore, when the electric field due to the adsorbates on the metal surface exceeds the

ionization threshold for a given n-state, those Rydberg atoms experiencing that field are lost from the beam.

Adsorption onto the mesh surface may produce a decrease in the number of Rydberg atoms in the beam. Therefore, the flux of Rydberg atoms that survive the passage through the mesh is compared to the flux without the mesh in the beam. Rydberg atoms are detected by field ionization followed by detection of the resulting ions in a Channeltron Electron Multiplier in the detection region.

The transmission  $T$  is defined as a ratio of counting rates:  $T = \frac{\text{flux detected with mesh}}{\text{flux detected without mesh}}$ . At each point the electric field is dependent upon the dipole moment and coverage of the adsorbate. The relationships between adsorbate coverage and electric field, and between transmission and electric field will be calculated in Chapters 2 and 4. Therefore, the measured transmission vs time may be converted to dipole-moment density vs time. Analysis of the time dependence of the dipole-moment density allows the determination of properties of adsorption and desorption. These measured properties include dipole moment, desorption energy and sticking probability. The advantages of this technique include sensitivity to adsorbate layers,  $\lesssim 10^{-4}$  monolayers (when  $\mu \cong ea_0$ ), method to measure absolute value of dipole moment  $\mu$ , and new method to accomplish desorption studies. Additionally, this technique provides another method of surface analysis.

## CHAPTER 2: THEORETICAL FOUNDATIONS

## 2.1 Gas-Surface Interactions

The interaction between a solid surface and a molecule is complex, and the large variety of processes which may occur on the surface makes a complete theory difficult. The processes that will be considered explicitly in this work are adsorption, desorption and surface diffusion.<sup>9</sup>

A typical interaction scenario for an atom or molecule impinging on a surface may include adsorption at a single site, hopping to other surface sites, and then desorbing from the surface. Because adsorption is a complex process, several variations of the typical scenario may occur. Since adparticles may also simply strike the surface and bounce back into the gas a new parameter  $s$ , the sticking probability, is defined to be the probability that a molecule will adsorb to the surface upon impact. The adsorbate may remain at the same site where it initially adsorbed, or it may diffuse any number of lattice sites along the surface, hopping from site to site. Surface diffusion is a random walk process along the surface, in the limit of low coverage. If the adsorbate receives enough thermal energy in a "kick" from the surface, it will desorb back into the gas. Following sections will briefly discuss aspects of physisorption, chemisorption and surface diffusion.

### 2.1.1 Physisorption

The adsorbate may bind weakly to the surface by means of the attraction between the adsorbate and its image in the surface. Physisorption may be thought of as a Van der Waals attraction. In physisorption no charges are exchanged or shared between adsorbate and surface, and no chemical bonding occurs. The amount of energy required to remove physisorbed particles from the surface is generally small: less than 0.25 eV.<sup>9</sup> For this type of adsorption the particle surface separation is typically large, in the range from 3 to 5 Å.<sup>10</sup> Examples of physisorption on metals are gas atoms, e.g. He, adsorbing on Ag, and neutral molecules, e.g. H<sub>2</sub>, adsorbing on Cu.<sup>11</sup>

### 2.1.2 Chemisorption

Chemisorption is the more important of the two types of adsorption because it is more common. More attention is paid to chemisorption in the literature, both experimentally and theoretically. Chemisorption is the chemical bonding of an atom or molecule (adsorbate) to a surface. The surface atom or atoms may form ionic, covalent or metallic bonds with the adsorbate. Corresponding desorption energies  $E_d$  (the energy required to remove the adsorbate) are typically greater than 0.5 eV.<sup>12</sup> Chemisorbates which have been studied extensively include alkali metals, H<sub>2</sub>, N<sub>2</sub>, CO, and NO; these substances adsorb readily on many metals.

Chemisorption involves charge transfer to or from the adsorbate. The sign and magnitude of this transfer can be determined from a knowledge of the dipole moment  $\mu$  of the molecule on the surface. The dipole moment of a molecule on a surface and the same molecule in a gas may vary greatly.

Adsorption on a metallic surface has been shown to change the work function of the surface. The change in workfunction  $\delta\phi$  is proportional to the adsorbate coverage  $\theta$  and the dipole-moment  $\mu$  on the surface:  $\delta\phi = -4\pi N\mu$ . This relation will be discussed further in Sec. 2.2.4. The coverage,  $\theta = N/N_s$ , is the number of adsorbate molecules per unit area  $N$  on the surface divided by the number surface sites per unit area  $N_s$ .<sup>13,14,15</sup>

For the chemisorption of Na on Ni(111) Gerlach and Rhodin report a maximum work function change of 3 eV, a decrease.<sup>13</sup> J. P. Muscat and D. M. News report that the workfunction of Ni increases by as much as 0.5 eV when H or O are adsorbed at coverages less than one monolayer.<sup>12</sup> J.E. Muller and J. Harris determine the dipole moment  $\mu$  for  $H_2O$  on Al with cluster calculations which yield values for  $\mu$  ranging from  $0.02 e a_0$  to  $0.16 e a_0$ .<sup>16</sup>

R. L. Gerlach and T. N. Rhodin<sup>13</sup> measured the workfunction change on a Ni face due to the adsorption of alkali metals, Na referred to above, and for Cs, and K as a function of coverage. They found that the workfunction (and therefore the dipole moment) decreased nonlinearly as adsorbates accumulated on the

surface. The functional dependence of  $\delta\phi$  and  $\mu$  on coverage is not generally linear<sup>17,18</sup> but instead, for  $\mu$  specifically, has a Lorentzian-like character  $\mu(\theta) \approx \mu_0/(1+\beta\theta^2)$  where  $\beta$  is a constant that is determined experimentally and depends upon the specific adsorbate-metal interaction. Similar behavior was described semi-empirically by Topping in 1927.<sup>17</sup> Dipoles on a surface produce a workfunction which gives rise to an electric field near the surface.

### 2.1.3 Surface Diffusion

When the adsorbate remains on the surface, it may hop from one surface site to another. If the adsorbate receives enough energy from surface atoms, due to thermal fluctuations, to surmount the potential barrier between adjacent sites it will hop to an adjacent site. The hopping probability is proportional to  $\exp(-E_{\text{diff}}/kT_s)$ .  $T_s$  is the temperature of the surface. The activation energy  $E_{\text{diff}}$  is the energy required to overcome the potential barrier between adjacent surface sites. Diffusion rates, reported as an area per second, can be expressed as  $D = D_0 \exp(-E_{\text{diff}}/kT_s)$  with  $D_0 = \nu l_s^2/4$ , if 4 represents the number of nearest neighbors per surface site,  $\nu$  is an oscillation frequency of order  $10^{13} \text{ s}^{-1}$ , and  $l_s$  of order  $3 \text{ \AA}$  is the distance to an adjacent surface site.<sup>19</sup>

The time required for an adsorbate to diffuse a given distance on the surface is of interest in this experiment.

Diffusion time may be found with simple statistical mechanics for a random walk,  $\langle \Delta r \rangle^2 = 4Dt$ .<sup>19</sup> Zhu and co-workers<sup>20</sup> used second-harmonic generation to measure the diffusion of CO on Ni(111). They found the diffusion energy to be  $E_{\text{diff}} = 0.3$  eV and the pre-exponential factor  $D_0 = 1.2 \times 10^{-5}$  cm<sup>2</sup>/s. These values imply  $D = 2.1 \times 10^{-10}$  cm<sup>2</sup>/s at 300 K. The time required for CO to diffuse around a mesh strand may be calculated as  $t = \langle \Delta r \rangle^2 / 4D$ . For a diffusion distance  $\Delta r = 6$   $\mu\text{m}$ , the time to diffuse from one side of the mesh to the other is of order  $t \cong 400$  s. Mesh dimensions are given in Sec. 3.1.

Diffusion into the bulk may for some situations be an important effect. However, in this experiment the molecules are assumed to not diffuse into the bulk.

#### 2.1.4 Desorption

Thermal desorption is perhaps the most straightforward process that may occur on a surface. Thermal fluctuations of the surface give the adsorbate a kick that may liberate it from the surface. The probability of desorption per unit time may be written as follows:  $\Gamma = \Gamma_0 e^{-E_d/kT_s}$ , where  $\Gamma_0$  is an oscillation rate,  $E_d$  is the desorption energy,  $k$  is Boltzmann's constant and  $T_s$  is the temperature of the surface.<sup>21</sup> An average stay time  $\tau$  is represented by  $\tau = 1/\Gamma = \tau_0 e^{E_d/kT_s}$ , where  $\tau_0$  is the time for one oscillation of the adsorbate on the surface, typically  $10^{-13}$  s.<sup>9</sup> The desorption energy  $E_d$  is the energy required to

desorb a molecule from a surface. The number of molecules remaining,  $N(t)$ , on a surface after a time  $t$  can be shown to be exponentially dependent on  $t$  and the desorption rate  $\Gamma$ , having the form  $N(t) = N_0 e^{-\Gamma t}$ .<sup>22</sup>

Adamson<sup>23</sup> and others<sup>24</sup> list desorption energies  $E_d$  for several systems:

|              |                 |
|--------------|-----------------|
| $H_2$ on Ni: | $E_d = 1.29$ eV |
| $O_2$ on W:  | $E_d = 8.41$ eV |
| O on Ni:     | $E_d = 8.10$ eV |

These values exemplify the wide range of desorption energies that are possible.

## 2.2 Electric Fields Calculations

The electrostatic potential due to a dipole layer may be calculated (in cgs units) with electrostatic theory:<sup>25</sup>

$$V(\vec{r}) = \int_S N(\vec{r}') \mu \, d\Omega(\vec{r}, \vec{r}') \quad , \quad (2-1)$$

where  $\mu$  is the electric dipole moment for each dipole,  $N(\vec{r})$  is the adsorbate surface dipole number density, and  $d\Omega(\vec{r}, \vec{r}')$  is the solid angle element subtended at  $\vec{r}$  by a surface element at  $\vec{r}'$ .

Electric field can be calculated for regions near an adsorbate covered surface, which can be modeled as a layer of dipoles. In the remaining sections of this chapter, several different geometries are investigated in an effort to model the mesh surface.

### 2.2.1 A Uniformly Covered Closed Surface

For a uniformly covered closed surface the dipole-moment density is a constant,  $N(r') = \text{constant}$ . The integral in Eq. (2-1) for this situation yields  $V = -4\pi N\mu$  for points inside the closed surface and zero for points outside. Therefore, the electrostatic potential is constant outside the surface and the electric field must be zero. Consequently a uniformly covered mesh filament produces no external electric field.

### 2.2.2 A Cylindrical Conducting Mesh Filament

In this section the filaments which constitute the mesh in this experiment are modeled as cylinders that accumulate dipoles nonuniformly on one side, adsorbing dipoles in a cosine distribution. The following calculation, with Eq. (2-1), determines the electrostatic potential and electric field due to a nonuniform layer of dipoles on a single cylindrical conductor.

The electrostatic potential due to an infinitely long grounded cylinder of radius  $\underline{a}$ , covered by a nonuniform dipole layer of surface charge density  $\sigma = \sigma_0 \cos \psi$  surrounding one side ( $-\pi/2 < \psi < \pi/2$ ), may be calculated from the potential due to a line of charge outside a conducting infinitely long cylinder of radius  $\underline{a}$ . Coordinates and geometry are shown in Fig. 2-1. The electrostatic potential, found by the method of images for a

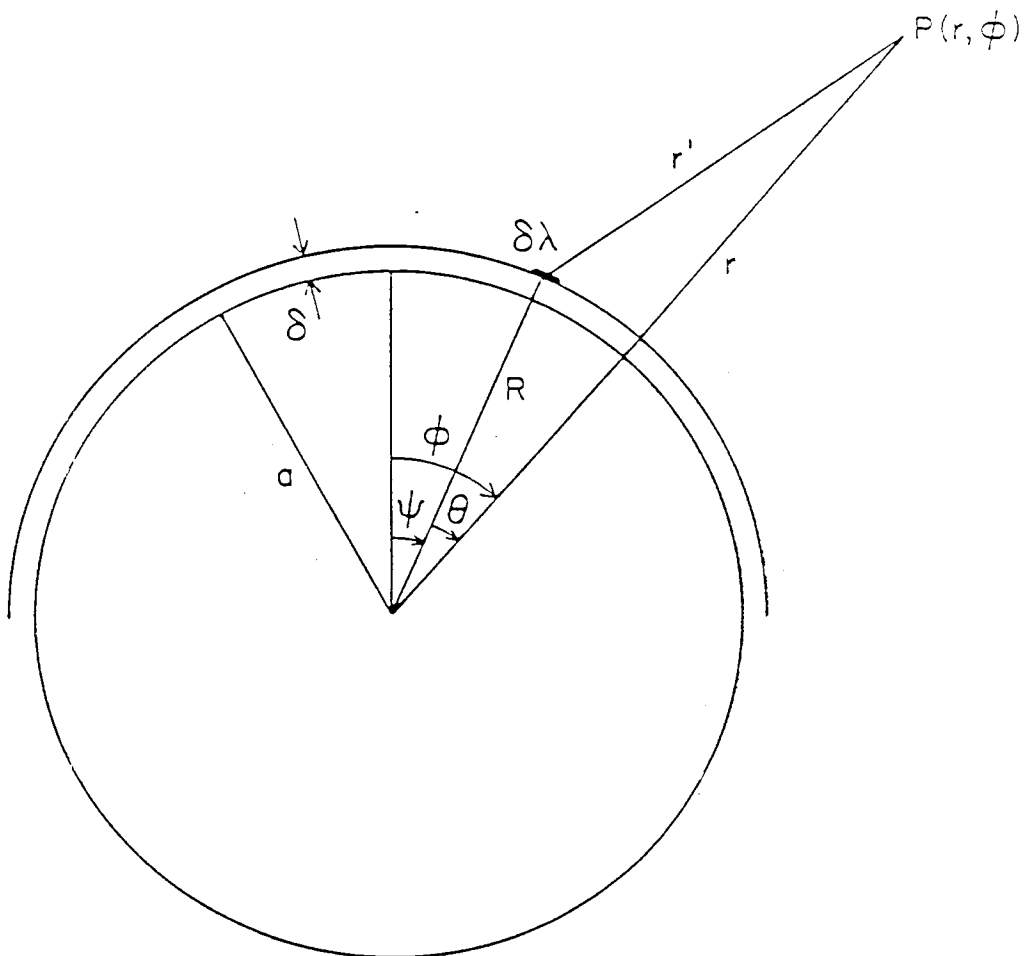


Fig. 2-1 Geometry of a Dipole Layer on a Conducting Cylinder

line of charge outside a conducting cylinder, is

$$\delta V(r, \psi, z) = \delta \lambda \ln \left[ \frac{a^2 r^2 + a^2 R^2 - 2a^2 rR \cos \psi}{r^2 R^2 + a^4 - 2a^2 rR \cos \psi} \right], \quad (2-2)$$

where  $R$  is the distance from the cylinder axis to the line charge of density  $\delta \lambda$ ,  $r$  is the distance from  $\delta \lambda$  to the observation point, and  $a$  is the radius of the cylinder. The line charge density is

$$\delta \lambda = \sigma R \delta \psi = \sigma_0 R \cos \psi \delta \psi.$$

The potential due to a distribution of line charges outside a conducting cylinder is then found by integrating Eq. (2-2) with respect to  $\psi$ :

$$V(r, \phi, z) = \sigma_0 R \int_{-\frac{\pi}{2}}^{\frac{\pi}{2}} \ln \left[ \frac{a^2 r^2 + a^2 R^2 - 2a^2 rR \cos(\phi - \psi)}{r^2 R^2 + a^4 - 2a^2 rR \cos(\phi - \psi)} \right] \cos \psi \, d\psi, \quad (2-3)$$

where  $\phi$  is the azimuthal angle of the observation point. Equation (2-3) expression satisfies the grounded-cylinder boundary condition  $V(a, \phi, z) = 0$  for all  $\phi$  and  $z$ .

If we define  $\delta = R - a$  to be the distance between the line charge and the surface, then the case for a dipole on the surface of a metallic cylinder may be determined by taking  $\delta \ll a$  and  $\delta \ll r - a$ . Then  $R \approx a$ ,  $\delta \ll R$  and  $\delta \ll a$ . Equation (2-3) becomes

$$V(r, \phi, z) \approx -\sigma_0 a \int_{-\frac{\pi}{2}}^{\frac{\pi}{2}} \ln \left[ \frac{r^2 + a^2 + 2a\delta - 2ar \cos(\phi - \psi)}{r^2 + a^2 + 2r^2 \delta/a - 2ar \cos(\phi - \psi)} \right] \cos \psi \, d\psi. \quad (2-4)$$

Expansion of the integrand in the limit of small  $\delta$  gives

$$V(r, \phi, z) = -2\sigma_o a \left( a\delta - \frac{r^2 \delta}{a} \right) \int_{-\frac{\pi}{2}}^{\frac{\pi}{2}} \frac{\cos \psi \, d\psi}{r^2 + a^2 - 2ar \cos(\phi - \psi)}. \quad (2-5)$$

Now let  $\beta = \phi - \psi$ . Then  $\cos \psi = \cos \phi \cos \beta + \sin \phi \sin \beta$  and  $d\psi = -d\beta$ , so that

$$V(r, \phi, z) = 2\sigma_o \delta (r^2 - a^2) \left\{ \int_{\phi - \frac{\pi}{2}}^{\phi + \frac{\pi}{2}} \frac{\cos \phi \cos \beta \, d\beta}{r^2 + a^2 - 2ar \cos \beta} + \int_{\phi - \frac{\pi}{2}}^{\phi + \frac{\pi}{2}} \frac{\sin \phi \sin \beta \, d\beta}{r^2 + a^2 - 2ar \cos \beta} \right\}. \quad (2-6)$$

The integrals may be evaluated by recognizing that

$$\int \frac{\cos \beta \, d\beta}{A + B \cos \beta} = \frac{\beta}{B} - \frac{2A}{B\sqrt{A^2 - B^2}} \tan^{-1} \left( \sqrt{\frac{A-B}{A+B}} \tan \frac{\beta}{2} \right) \quad (2-7)$$

$$\text{and} \quad \int \frac{\sin \beta \, d\beta}{A + B \cos \beta} = -\frac{1}{B} \ln (A + B \cos \beta). \quad (2-8)$$

Therefore,

$$V(r, \phi, z) = 2\sigma_o \delta (r^2 - a^2) \left[ \frac{\sin \phi}{2ar} \ln (r^2 + a^2 - 2ar \cos \beta) - \frac{\cos \phi}{2ar} + \frac{(r^2 + a^2) \cos \phi}{ar (r^2 - a^2)} \tan^{-1} \left( \frac{r+a}{r-a} \tan \frac{\beta}{2} \right) \right] \Bigg|_{\phi - \frac{\pi}{2}}^{\phi + \frac{\pi}{2}}. \quad (2-9)$$

The following identity allows simplification of the final term:

$$\tan^{-1} x - \tan^{-1} y = \tan^{-1} \left( \frac{x - y}{1 + xy} \right) + \pi H \left( \frac{\pi}{2} - |\phi| \right), \quad (2-10)$$

The principal value of the arctangent is to be taken. The

Heaviside unit-step function  $H(\frac{\pi}{2} - |\phi|)$  maintains the continuity of the potential. In the limit  $\delta \ll a$ , the dipole-moment density is given by  $N_0 \mu \cos \psi = 2\sigma_0 \delta \cos \psi$ , so that  $\sigma_0 \delta \cong N_0 \mu / 2$ . The final result is

$$V(r, \phi, z) = \frac{N_0 \mu}{2ar} \left\{ (r^2 - a^2) \left[ \sin \phi \ln \left( \frac{r^2 + a^2 + 2ar \sin \phi}{r^2 + a^2 - 2ar \sin \phi} \right) - \pi \cos \phi \right] - 2(r^2 + a^2) \cos \phi \left[ \tan^{-1} \left( \frac{r^2 - a^2}{2ar \cos \phi} \right) - \pi H\left(\frac{\pi}{2} - |\phi|\right) \right] \right\}. \quad (2-11)$$

Equation (2-11) is the basis for the potential and field plots shown in Fig. 2-2, which shows equipotential lines and lines of constant electric field produced by dipoles on the cylinder. Point P is the position where  $E = 200$  V/cm when  $N_0 \mu = ea_0 \times 10^{13} / \text{cm}^2$ . An electric field of this magnitude is capable of ionizing Rydberg atoms with  $n \gtrsim 40$ . The dipole-moment density  $N_0 \mu$  at  $\psi = 0$ , which produces an electric field of magnitude 200 V/cm, covers approximately 1% of the surface for  $\mu \cong ea_0$ : the coverage is approximately 0.01 monolayers.

### 2.2.3 A Nonconducting Dipole Strip

Cylindrical filaments present an analytical problem when they are constructed into a complete mesh. However, a complete mesh surface may be constructed from flat sections containing dipoles. Therefore, in a first effort to model the mesh surface,

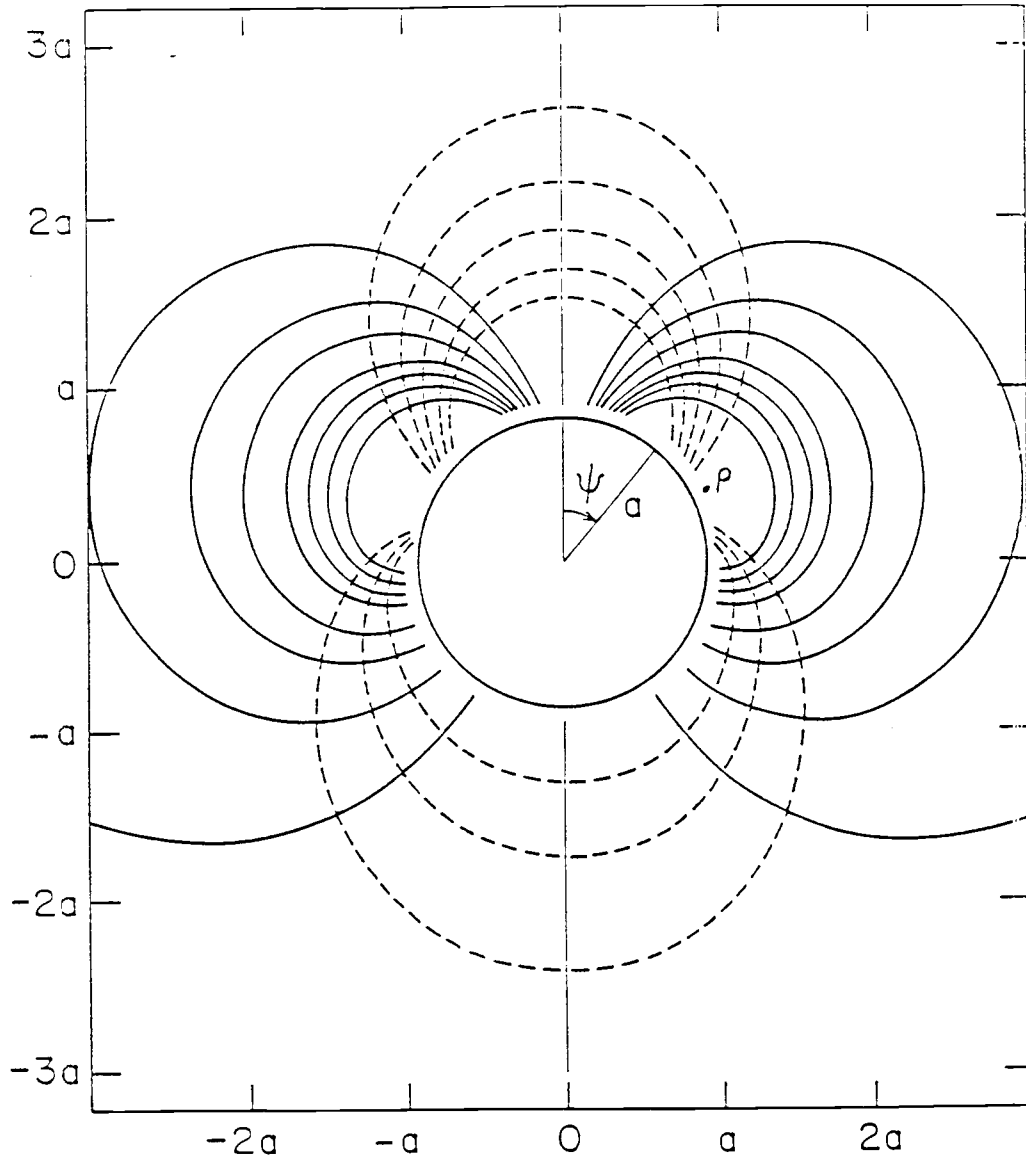


Fig. 2-2 Electric Field Lines (solid lines) and Equipotentials (broken lines) Produced by a Nonuniform Dipole Layer on an Infinitely Long Cylinder

the electric field due to an infinitely long nonconducting flat strip is calculated. The electric field magnitudes due to the infinite strip at equally distant points are similar to those of the cylindrical filament. Dipoles on the strip are uniformly distributed, and the strip is nonconducting. Figure 2-3 shows the geometry of the dipole strip.

The electrostatic potential for a single infinitely long dipole strip is found by first considering the potential due to a uniform dipole layer on a semi-infinite plane (xy-plane with  $x < 0$ ). This dipole-moment distribution is  $N(r') = N\mu(d/dz)\delta(z)$  for a semi-infinite plane,  $x < 0$  and  $z = 0$ . Equation (2-1) for this distribution yields the potential  $V = -2N\mu\phi$ . The angle  $\phi$  is measured clockwise from the negative x-axis.

The electric potential is obtained for a uniform dipole layer on an infinitely long strip between  $x = -b$  and  $x = 0$  in the xy-plane:

$$V = 2N\mu \left[ \tan^{-1} \left( \frac{x+b}{z} \right) - \tan^{-1} \left( \frac{x}{z} \right) \right]. \quad (2-12)$$

For a dipole the electric field components are found from  $\vec{E} = -\vec{\nabla}V$ :

$$E_x = 2N\mu z \left( \frac{-1}{(x+b)^2 + z^2} + \frac{1}{x^2 + z^2} \right), \quad (2-13)$$

$$E_y = 0 \quad (2-14)$$



$$\text{and, } E_z = 2N\mu \left( \frac{(x+b)}{(x+b)^2 + z^2} - \frac{x}{x^2 + z^2} \right). \quad (2-15)$$

The magnitude of the electric field is maximum at  $z = 0$ , in the plane of the dipole strip:

$$E_{\text{max}} = \frac{2N\mu b}{x(x+b)}. \quad (2-16)$$

A typical excited atom in the beam of Fig. 1-1 has  $n = 35$  and is ionized by a field  $E \approx 400$  V/cm. A field of this magnitude is generated by the mesh in this experiment at  $x = b/10$  if  $N\mu = 1.9 \times 10^{13} \text{ ea}_0/\text{cm}^2$ . This value of  $N\mu$  corresponds to a coverage  $\theta \approx 0.01$  ML for a Ni substrate.

Figure 2-3 shows the potential and field lines for the dipole strip, with P being the position where  $E = 200$  V/cm when  $N\mu = \text{ea}_0 \times 10^{13}/\text{cm}^2$ . A comparison of the positions of the point P in Figs. 2-2 and 2-3 shows that when  $b \approx \underline{a}$ , the fields at corresponding distances from the surface are of comparable magnitude and direction for similar adsorbate coverages. The simple plane-strip calculations shown in Fig. 2-3 provide a reasonable means of determining the local electric field due to an adsorbed layer on one strand of the mesh substrate used in this experiment.

#### 2.2.4 Inside a Mesh Opening

An appropriate approximation of the electric field inside a mesh opening may be made by assuming that the mesh consists of an

infinite dipole layer with a square hole at the center. Distant holes in the mesh are ignored in this discussion, but will be considered in Sec. 2.3.

Consider a square of dipoles bounded by  $0 < x < b$  and  $0 < y < b$ . The potential for an infinite plane of dipoles with a square hole at the center may be found as a superposition of the potential for an infinite plane of dipoles and the negative of the potential for a square of dipoles. The potential for an infinite plane of dipoles is  $V = 2\pi N\mu \operatorname{sgn}(z)$ . Thus,  $V = -2\pi N\mu$  is the potential below the plane of the dipoles ( $z < 0$ ), and  $V = 2\pi N\mu$  is the potential above the dipoles ( $z > 0$ ). Therefore the change in potential when crossing the plane is  $\delta V = -4\pi N\mu$ , and the workfunction for the surface is  $\delta\phi = -4\pi N\mu$ .  $\delta\phi$  is potential difference an electron must overcome in crossing the surface dipole layer.

The electrostatic potential for a square containing a uniform layer of adsorbed dipoles is calculated with Eq. (2-1), where  $N(r') = -N\mu(d/dz')\delta(z')$ , yielding a contribution to the potential containing four arctangent terms that replace the two arctangent terms in Eq. (2-12). Superposition of the potentials for the square of dipoles and the infinite plane of dipoles is

$$V = 2\pi N\mu \operatorname{sgn}(z) - N\mu \left\{ \tan^{-1} \left( \frac{xy}{z\sqrt{x^2+y^2+z^2}} \right) - \tan^{-1} \left( \frac{x(y-b)}{z\sqrt{x^2+(y-b)^2+z^2}} \right) - \tan^{-1} \left( \frac{(x-b)y}{z\sqrt{(x-b)^2+y^2+z^2}} \right) + \tan^{-1} \left( \frac{(x-b)(y-b)}{z\sqrt{(x-b)^2+(y-b)^2+z^2}} \right) \right\}. \quad (2-17)$$

Equation (2-17) may be differentiated to find the electric field inside the mesh opening. Within the open area, in the  $z = 0$  plane, the field is

$$E_z = -N\mu \left\{ \frac{\sqrt{x^2+y^2}}{x y} - \frac{\sqrt{x^2+(y-b)^2}}{x (y-b)} - \frac{\sqrt{(x-b)^2+y^2}}{(x-b) y} + \frac{\sqrt{(x-b)^2+(y-b)^2}}{(x-b)(y-b)} \right\}. \quad (2-18)$$

Figure 2-4 shows this function plotted with contours of constant electric field magnitude  $|E_z|$ . The peripheral openings in Fig. 2-4 were treated as if they were covered with dipoles, in Sec. 2.3 these openings are considered without dipoles. In the  $z = 0$  plane, the field is singular everywhere except within the hole. At the center of the opening ( $x = y = b/2$ ) the field magnitude is given by

$$E_c = 8\sqrt{2} N\mu/b. \quad (2-19)$$

Equation (2-18) will be used to determine the relative open area contained inside a given electric field contour. Figure 2-5 shows a quarter of a mesh opening with the electric field contours as a function of position scaled to the field magnitude at the center  $E_c$  from Eq. (2-19).

### 2.3 The Electric Field in a Mesh Opening,

#### Including Distant Mesh Elements

The electric field at the center of an opening may be calculated more accurately than in the previous section. Eq. (2-1) is used with the appropriate dipole-moment density to

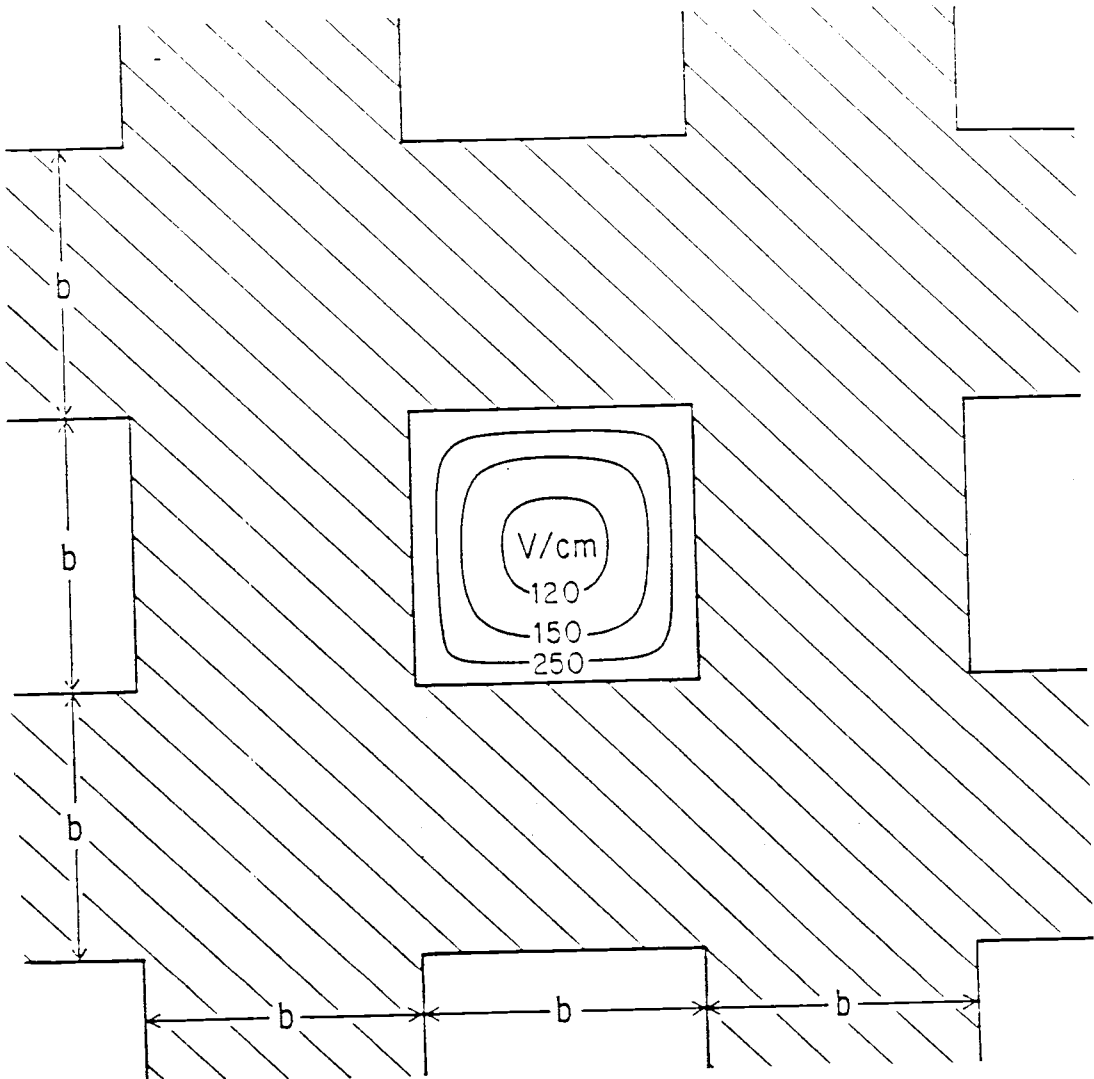


Fig. 2-4 Electric Field Contours Inside a Mesh Opening,  
Showing Electric Field Magnitude

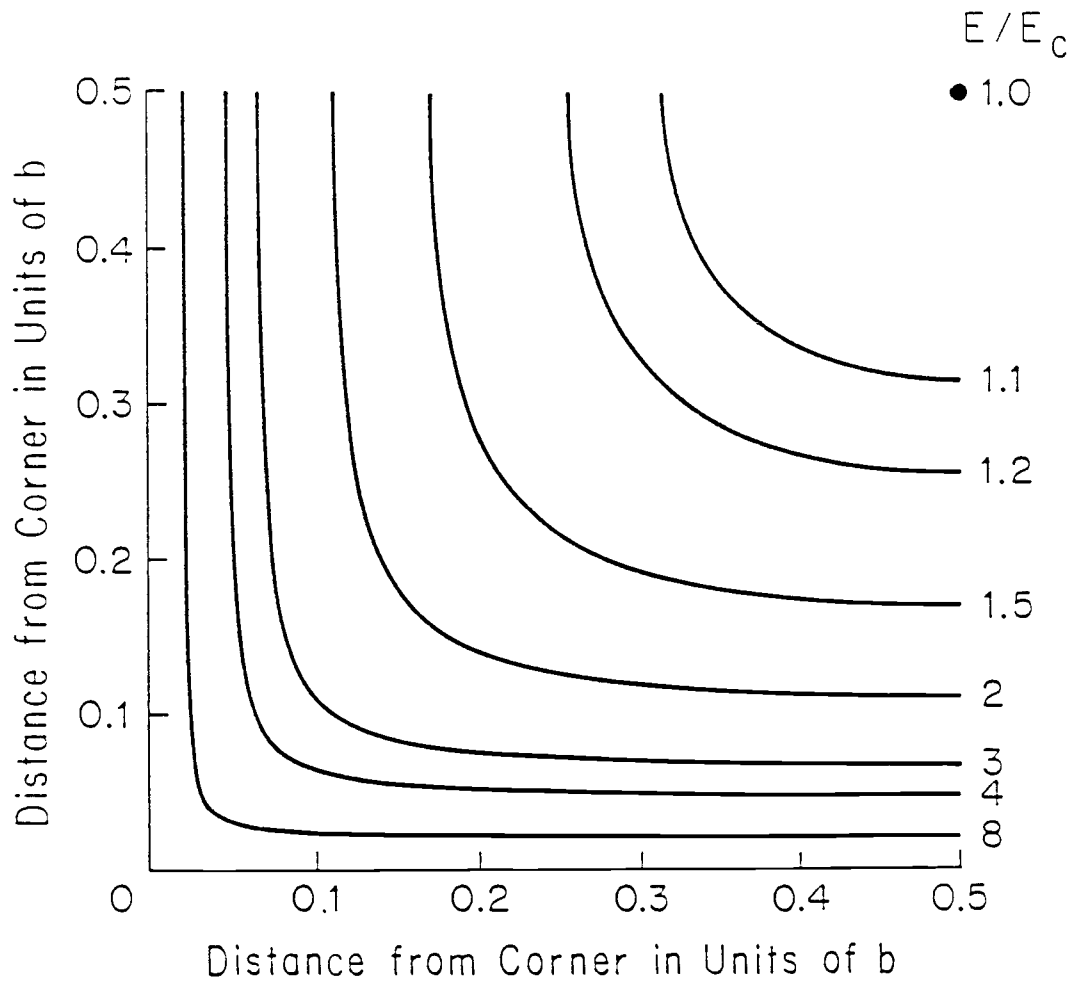


Fig. 2-5 A Quarter Mesh Opening, Showing Electric Field  
Contours Scaled to the Field at the Center

determine the electric field at the center of the mesh opening due to a frame of dipole moments surrounding the opening. The entire mesh can be considered as a system of successive frames, so dipoles at distant mesh openings are excluded.

Figure 2-6 shows the geometry of the first frame. The first frame has dimensions  $-b$  to  $2b$  in the  $x$ -direction and  $-b$  to  $2b$  in the  $y$ -direction. With these boundaries and Eq. (2-1) the field due to the first frame may be calculated. For brevity, the electric field only at the center of the main opening will be found. The sum of the contributions to  $E_c$ , the electric field in the  $z$ -direction at the center of the mesh opening ( $x = b/2$ ,  $y = b/2$ ), from each frame gives the electric field for the entire mesh covered with dipoles accounting for distant mesh openings.

Therefore, the electric field at the center of the mesh opening in the  $z$ -direction may be found as follows.

$$V(x, y, z) = N\mu \int \frac{\frac{d}{dz'} \delta(z')}{[(x-x')^2 + (y-y')^2 + (z-z')^2]^{1/2}} dx' dy' dz' \quad (2-20)$$

is the potential due to a layer of dipole moments in the plane of the dipoles. Equation (2-20) may be simplified and integrated over the variable  $z$  from  $-\infty$  to  $+\infty$ , yielding

$$V(x, y, z) = N\mu z \int \frac{1}{[(x-x')^2 + (y-y')^2 + z^2]^{3/2}} dx' dy' \quad (2-21)$$

The electric field in the  $z$ -direction is found by differentiating

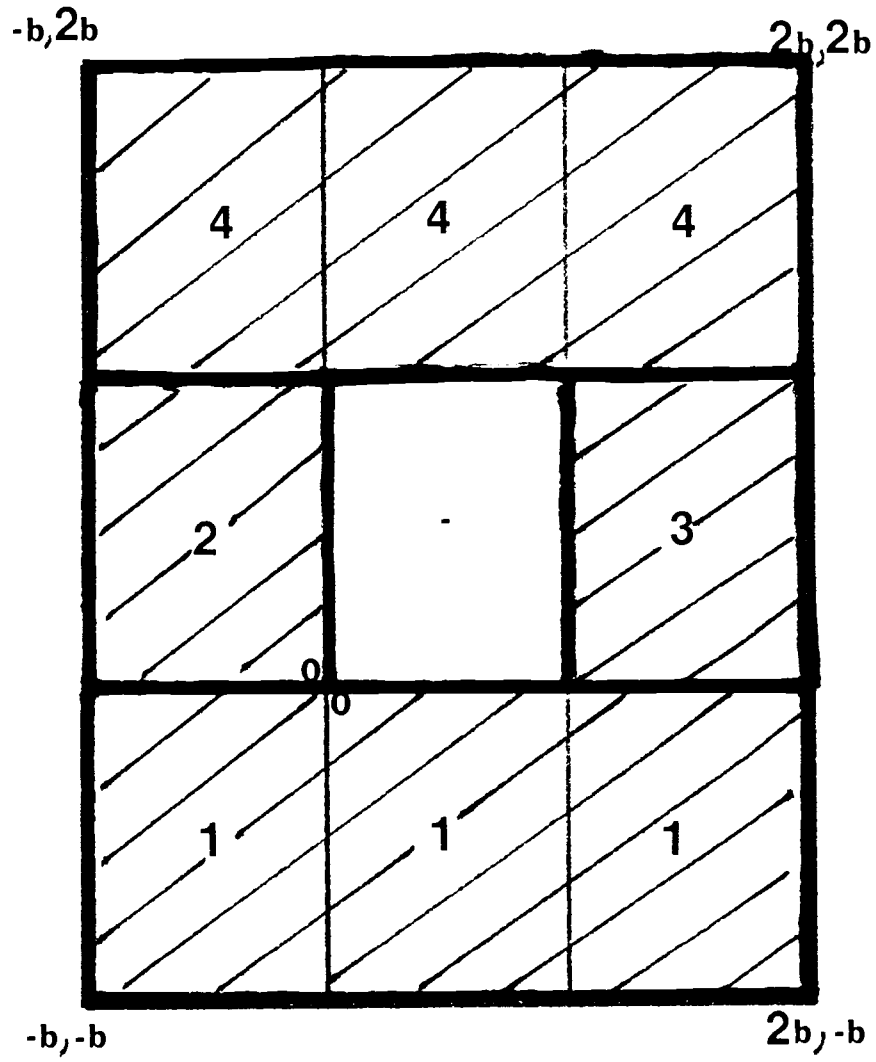


Fig. 2-6 Mesh Frame

Eq. (2-21) with respect to the variable  $z$ . This yields

$$E_z = \frac{\partial V(x,y,z)}{\partial z} = -N\mu \iint \frac{1}{[(x-x')^2 + (y-y')^2]^{3/2}} dx' dy', \quad (2-22)$$

Equation (2-22) gives the field in the  $z = 0$  plane for a square of dipoles. The geometry for a general square is shown in Fig. 2-7 with boundaries as shown. Inserting the limits of integration yields for region 1 shown in Fig. 2-6

$$E_1 = -N\mu \int_{-b}^{2b} \int_{-b}^0 \frac{1}{[(x-x')^2 + (y-y')^2]^{3/2}} dy' dx' \quad (2-23)$$

Similarly the results are for region 2,

$$E_2 = -N\mu \int_{-b}^0 \int_0^b \frac{1}{[(x-x')^2 + (y-y')^2]^{3/2}} dy' dx' \quad (2-24)$$

for region 3,

$$E_3 = -N\mu \int_b^{2b} \int_0^b \frac{1}{[(x-x')^2 + (y-y')^2]^{3/2}} dy' dx' \quad (2-25)$$

and for region 4,

$$E_4 = -N\mu \int_{-b}^{2b} \int_b^{2b} \frac{1}{[(x-x')^2 + (y-y')^2]^{3/2}} dy' dx' \quad (2-26)$$

Summing the results of Eqs. (2-23) through (2-26) yields the electric field in the mesh opening due to the dipoles on the mesh in the frame shown in Fig. 2-6.

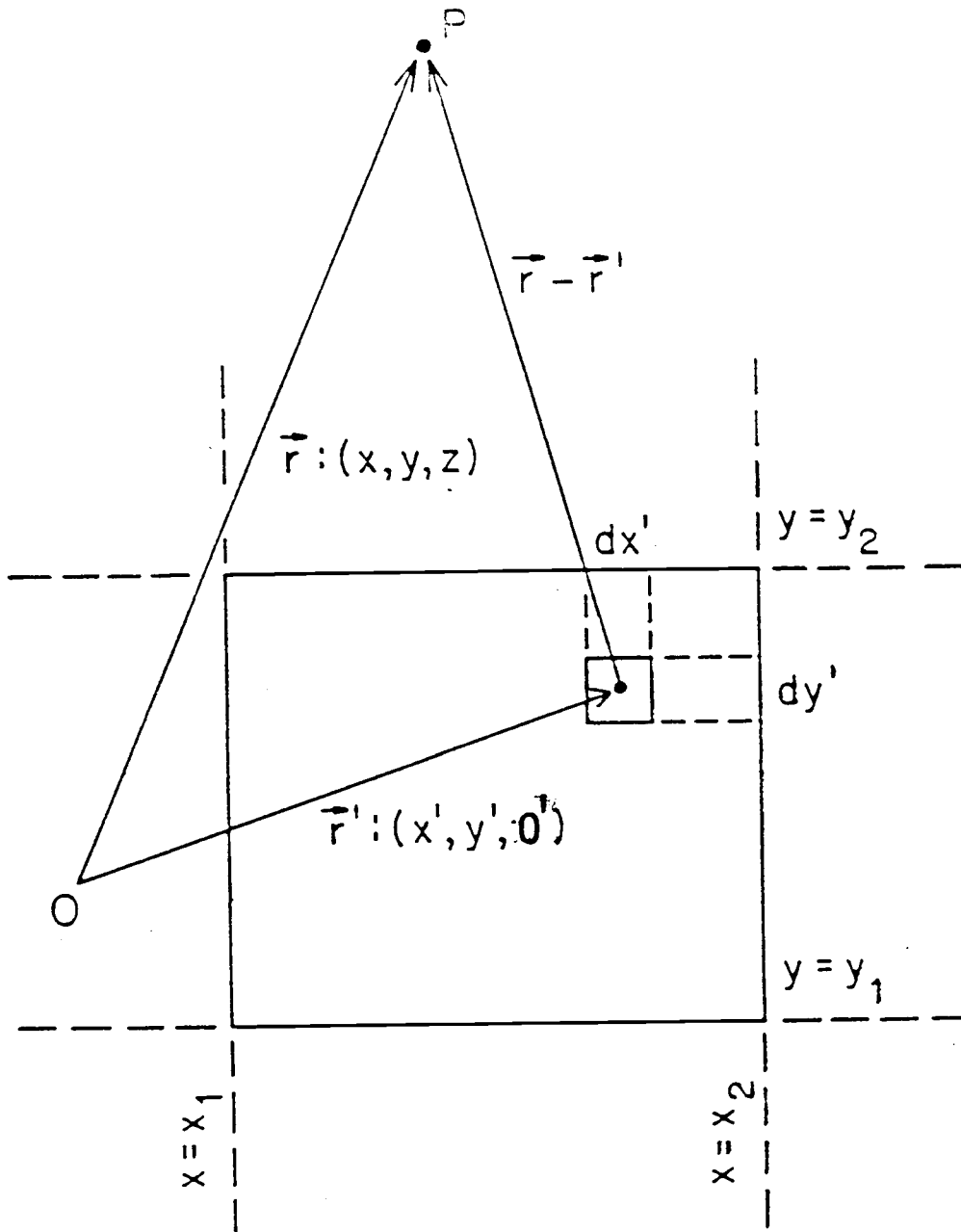


Fig. 2-7 Geometry of a Square Dipole Patch

$$\begin{aligned}
E_z = N\mu \left\{ \frac{((y-2b)^2 + (x+b)^2)^{1/2}}{(y-2b)(x+b)} - \frac{((y+b)^2 + (x+b)^2)^{1/2}}{(y+b)(x+b)} + \frac{(x^2 + y^2)^{1/2}}{xy} \right. \\
- \frac{(y^2 + (x-b)^2)^{1/2}}{y(x-b)} + \frac{((y-b)^2 + (x-b)^2)^{1/2}}{(y-b)(x-b)} - \frac{((y-b)^2 + x^2)^{1/2}}{x(y-b)} \\
\left. + \frac{((y+b)^2 + (x-2b)^2)^{1/2}}{(y+b)(x-2b)} - \frac{((y-2b)^2 + (x-2b)^2)^{1/2}}{(y-2b)(x-2b)} \right\}. \quad (2-27)
\end{aligned}$$

For a comparison of this result with other methods the electric field is calculated at the center of the opening:  $x = b/2$ ,  $y = b/2$ . For these values of  $x$  and  $y$  the field at the center due to the first frame is  $E_{c_1} = -\frac{8\sqrt{2} N\mu}{b} \left(1 - \frac{1}{3}\right)$ . Figure 2-8 shows the mesh divided into additional frames. The contribution due to all the odd-numbered frames, which contain no openings, may be found quickly by simply changing the limits of integration. This procedure yields for the odd-numbered frames the infinite series

$$E_{c_{\text{odd}}} = -\frac{8\sqrt{2} N\mu}{b} \left(1 - \frac{1}{3} + \frac{1}{5} - \frac{1}{7} + \frac{1}{9} - \frac{1}{11} + \dots\right) = -\frac{8\sqrt{2} N\mu}{b} \frac{\pi}{4}$$

The contributions from the even-numbered frames are calculated by a different procedure, because they contain mesh openings without dipoles. For these even-numbered frames the electric field may be calculated with Eq. (2-22). This calculation yields the electric field for an individual square of dipoles. The contribution for all squares must be added together. For frame 2 there are eight individual patches, for frame 4 there are sixteen patches, and for frame 6 there are thirty-two. The contributions for frames 2, 4, and 6 are:

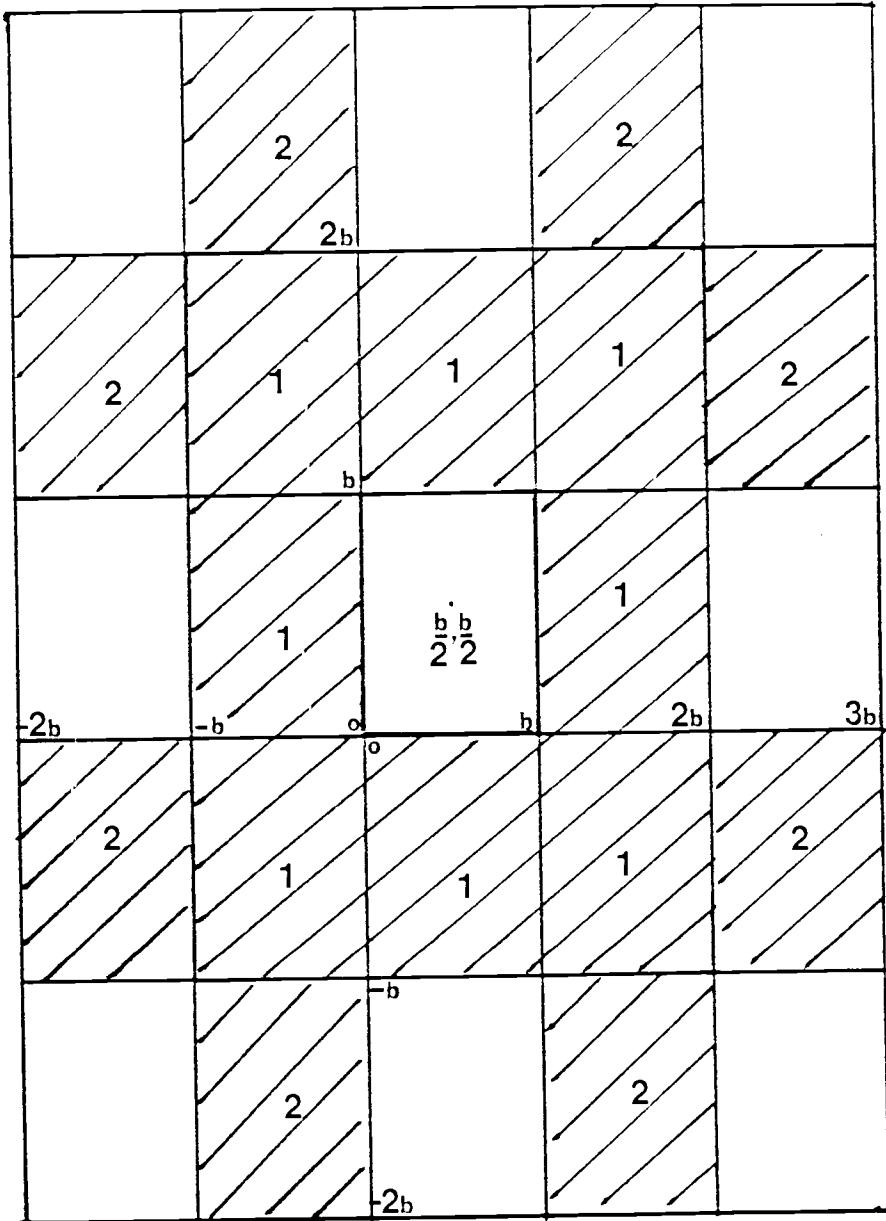


Fig. 2-8 Geometry of the Mesh for Peripheral Openings

$$E_{C_2} = -\frac{8\sqrt{2}N\mu}{b}(.07) , E_{C_4} = -\frac{8\sqrt{2}N\mu}{b} (.01) , E_{C_6} = -\frac{8\sqrt{2}N\mu}{b} (.008).$$

Finally, the electric field at the center of the central mesh opening accounting for distant mesh openings is approximately

$$E_{Z_C} \cong -\frac{8\sqrt{2}N\mu}{b} (0.88) . \quad (2-28)$$

As a result of the truncation of the series for even-numbered frames the value obtained in Eq. (2-28) underestimates the correct value. If the additional even-frame terms were included, Eq. (2-28) would be in close agreement with Eq. (2-19), where the mesh was approximated as a square hole in an infinite sheet of dipoles. Therefore, the contributions to the electric field from openings in peripheral frames is small. The difference between Eq. (2-19) and Eq. (2-28) is smaller than the uncertainties in the experimental measurements. The calculations made in Sec. 5-1 use Eq. (2-19).

## CHAPTER 3: EXPERIMENTAL APPARATUS

## 3.1 Description of the Apparatus

The experimental apparatus consists of a multi-chambered high-vacuum system. Figure 3-1 shows the major components of this apparatus. These major components are mounted within a source chamber, a target chamber and a detector chamber.

The source chamber contains the atomic beam oven, electron excitation region and electric field plates. The atomic beam oven is constructed from molybdenum and holds between 0.3 and 0.8 grams of Li. Holes are drilled in the molybdenum block to hold tantalum coils that serve as heating elements. Electric current is passed through the tantalum elements, allowing normal oven temperatures between 670 K and 800 K. A beam of ground-state Li atoms emerges from a 3-mm-diameter opening in the oven. The area of the oven opening is  $A_o = 7.1 \times 10^{-4} \text{ cm}^2$ . Chromel-alumel thermocouples, in the oven well and oven channel, are used to monitor the oven temperature. Typical average atomic velocities are found from kinetic theory<sup>27</sup> for particles in a beam:  $\bar{v} = (8 k T_o / m_{\text{Li}} \pi)^{1/2}$ . A typical oven temperature  $T_o = 700 \text{ K}$  corresponds to an average velocity  $\bar{v} = 2 \times 10^5 \text{ cm/s}$ . Since the total beam path is 60 cm, a typical time of flight, from oven to detector, is 0.3 ms.

The electron excitation region contains a porous-tungsten dispenser cathode located a few centimeters

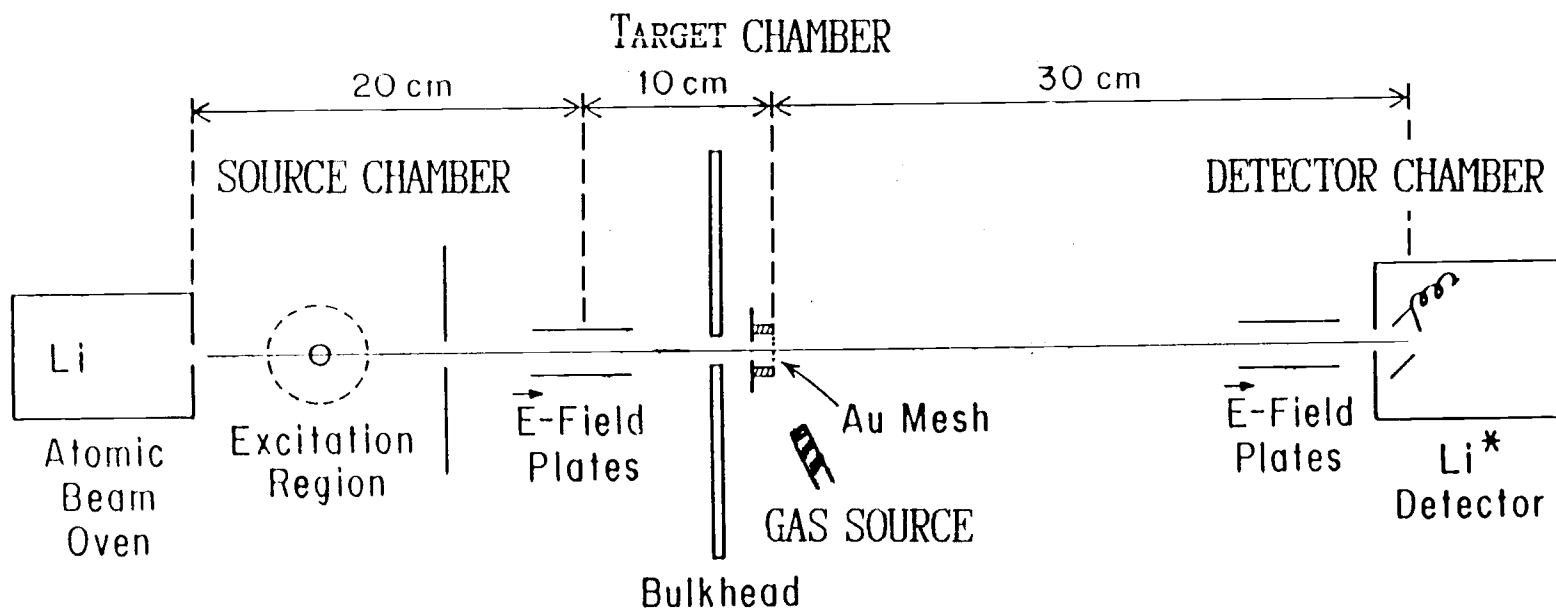


Fig. 3-1 Schematic of the Experimental Apparatus

downstream from the oven. The cathode emits electrons, which are accelerated across a 100 V potential difference to the anode. The electrons move from the cathode to the anode perpendicular to the direction of flow of the Li atoms, and the electrons do not interfere with the detection of the Rydberg atoms downstream. Electrons collide inelastically with the ground-state Li atoms and excite some of the atoms to Rydberg states or to ionization. Ionized Li atoms are removed from the beam by two sets of electric-field plates.

The first set of electric field plates is located 20 cm downstream from the oven. These plates are 0.8 cm apart and during normal experimental operation are held at a potential difference of 10 V, so that  $E \cong 12$  V/cm, which imposes an upper limit on the quantum number  $n$  for Rydberg states in the atomic beam. The maximum quantum state  $n$  is  $n_{\max} \cong 85$ . These plates can also be used to determine the  $n$ -state distribution of the Li Rydberg beam and the survival probability  $P(E)$  for Rydberg atoms in the beam. Generally,  $n$  is between 20 and 80.

During normal operation the source chamber is typically pumped to  $5 \times 10^{-8}$  Torr with a Varian VHS-6 diffusion pump. Source and target chambers are separated by a bulkhead with a 3 mm-wide atomic beam collimating slit. The bulkhead is approximately 30 cm downstream from the oven. The slit allows passage and beam collimation of both the ground-state Li atoms and the Rydberg atoms.

The target chamber contains the mesh mount, mesh, mesh thermocouples, external gas source and  $\text{LN}_2$  cold finger. The mesh mount is a rectangular piece of stainless steel with two 1.4-cm by 2.5-cm openings cut to allow Li atoms to pass through. The mesh mount is attached to a stainless steel rod that passes from the outside through a Wilson seal into the vacuum system. A Wilson seal allows the mesh mount, and meshes, to be inserted into or removed from the atomic beam. Each mesh is attached to the mount at the top and bottom by clamps. Clamps which sandwich the mesh are 0.1 cm thick copper sheets. Copper sheets are then attached to insulating posts which are bolted to the mount with brass screws. Figure 3-2 shows the mesh mount and the locations of the thermocouples TC1, TC2, and TC3.

Each thermocouple is a chromel-alumel junction that produces a voltage difference of approximately 1 mV for every 25 degree change in temperature. A thermocouple is located at the bottom of each mesh and one is affixed to the mount itself. The necessary electrical connections are fed through a vacuum flange to allow continuous temperature monitoring.

The targets are nickel or gold meshes made by the Buckbee Mears Co., type MG-47, specified to have 2000 filaments per inch. Electron micrographs were taken by the author with the guidance of W. Warnes, Asst. Prof. of Mechanical Engineering at Oregon State University. Figures 3-3a and 3-3b show the source side and the detector side of used Au meshes. Notice should be taken

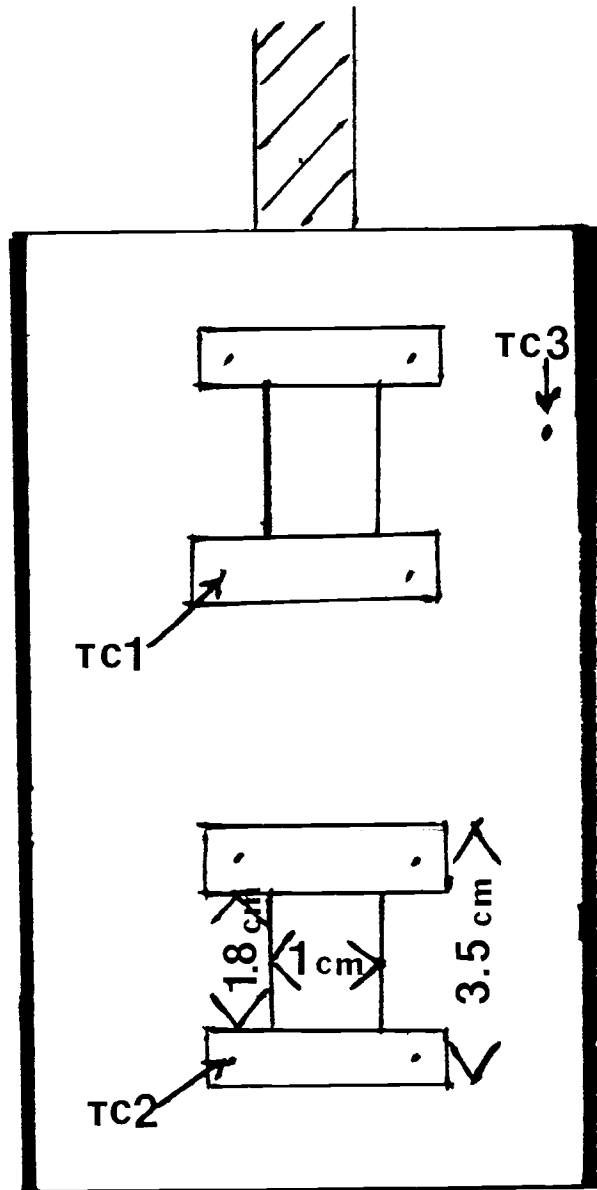


Fig. 3-2 Diagram of the Mesh Mount

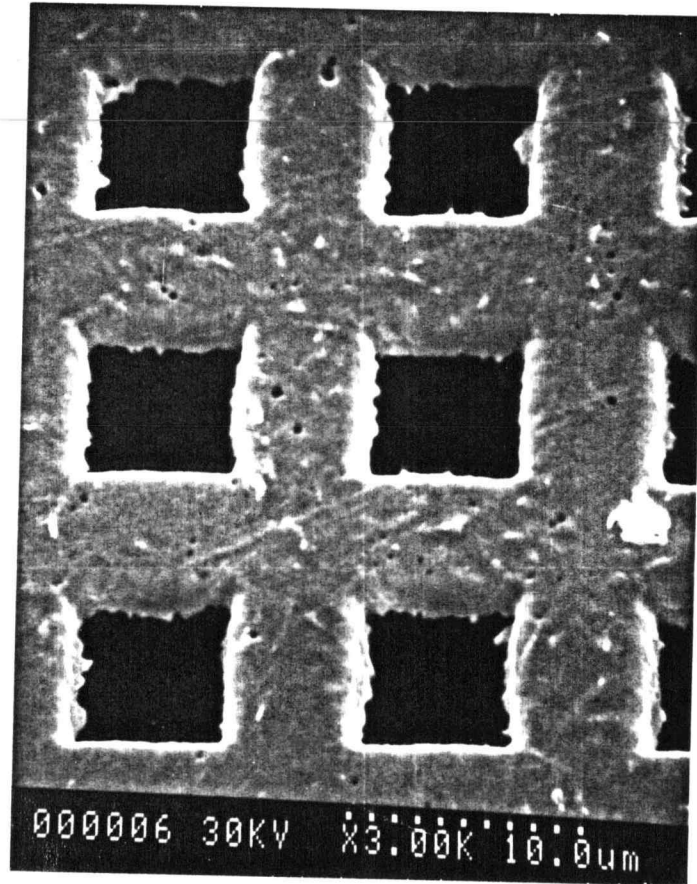
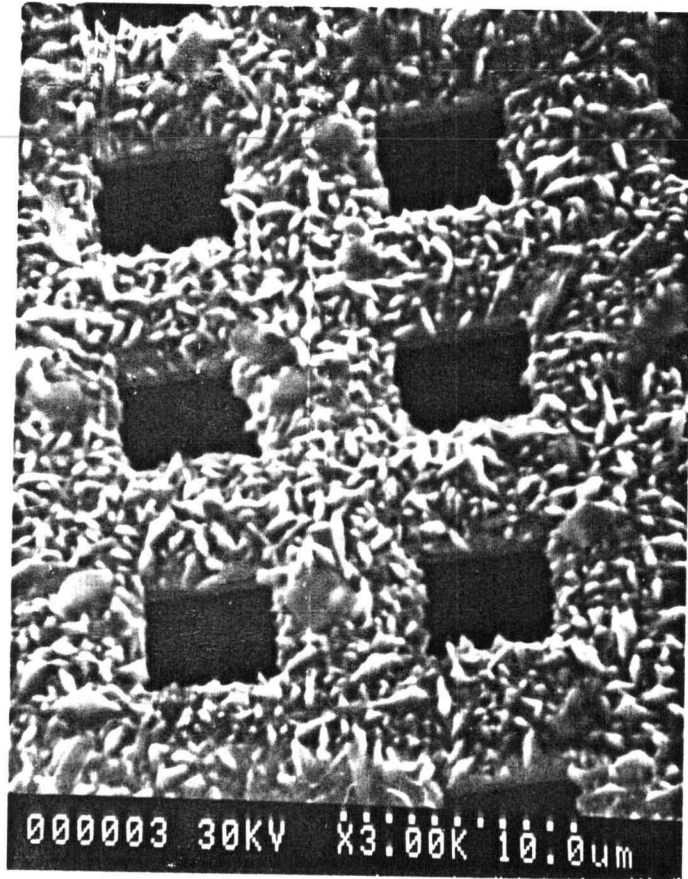


Fig. 3-3 Electron Micrographs of the Mesh Samples  
(a) Side toward Source (b) Side toward Detector

that the detector side seems smooth at a magnification of 3000 and is the side onto which the "adsorbate" gas was introduced. These micrographs show that each filament is 6.5 microns in diameter and the filaments are spaced 13 microns from center to center. The mesh dimensions imply that the mesh is only 75% solid and yields an optical transmission of 25%. The area of a surface site  $A_s$  depends upon the mesh material. For the Au(100) face-centered cubic structure (FCC)  $A_s = 8.33 \times 10^{-16} \text{ cm}^2$ , and for the Ni(100) FCC structure  $A_s = 6.20 \times 10^{-16} \text{ cm}^2$ . The (100) face of the FCC structure is the most densely populated face. Other faces have a slightly larger single surface site area: however, in general, this does not vary by more than a factor of 2.

The external gas source is constructed from 1/4-inch i.d. stainless steel tubing terminated into a fitting with a 0.29-mm-diameter opening, which allows an adsorbate to enter the vacuum system. The gas source is positioned below and 5 cm away from the mesh on the detector side. A capacitance manometer is connected to the source to monitor the gas pressure in the tubing. A Granville-Phillips bleeder valve closely controls the flow of gas into the system from external compressed gas cylinders. Figure 3-4 shows the physical setup of the gas introduction system.

The coldfinger consists of a  $\text{LN}_2$  reservoir external to the vacuum system. The reservoir is connected through a vacuum

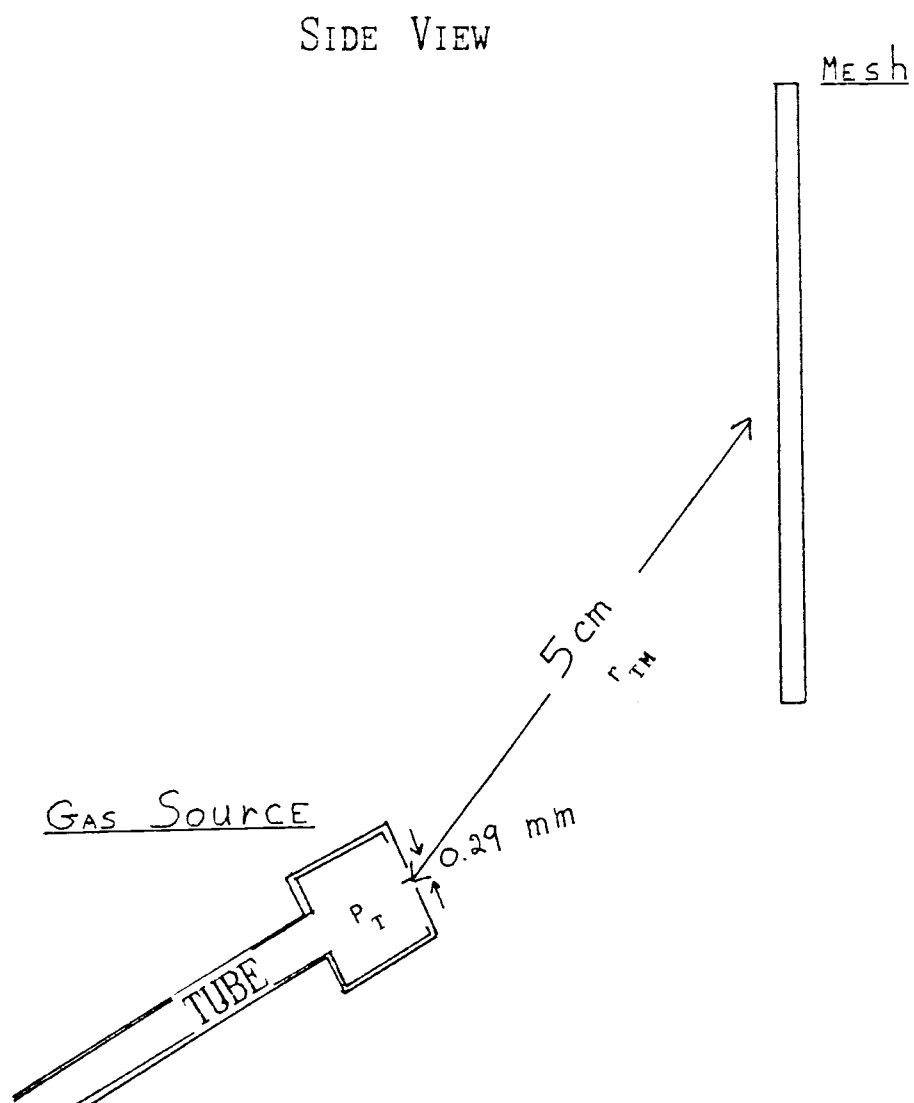


Fig. 3-4 Diagram of Apparatus for Adsorbate Gas Introduction

flange to the mesh mount by a copper thermal conduit. The temperature reduction is about 30 degrees. Poor cooling is due to the transfer of heat through the electrical connections made to each mesh sample; the mesh samples are not thermally well isolated.

Copper heating wires are attached at the top and bottom of each mesh to allow resistive heating for cleaning and temperature control. The heating wires are attached through a flange to a power supply which can supply up to 10 amps of current.

The detection chamber contains a Channeltron electron multiplier and a second set of electric field plates. Typical chamber pressure is  $1 \times 10^{-7}$  Torr. The Channeltron is housed in a metal box 30 cm downstream from the mesh. When a Rydberg atom enters the detector, it is exposed initially to an electric field produced by the second set of electric field plates, which removes ions and electrons from the beam. The Rydberg atom then is exposed to an electric field at the front of the Channeltron, which ionizes it so that detection may occur. At the Channeltron front end the electric potential is -1000 V. The rear of the Channeltron is held at +2000 V. The Rydberg atom is field-ionized, causing a cascade of electrons within the Channeltron. The output pulse is amplified and fed into the data acquisition system.

Electric field plates are mounted in front of the entrance to the Channeltron housing. These are maintained at a field

magnitude of 12 V/cm for typical operation to remove ions produced by Rydberg atom collisions with the residual background gas during transit between mesh and Channeltron.

### 3.2 Data Acquisition

Channeltron pulses are amplified by an HP 5554A pre-amplifier and fed into an Ortec 406A single channel analyzer. This electrical signal is sent to a 16-bit counter interfaced and to a DEC PDP-11 computer programmed as a multichannel analyzer. A multichannel analyzer holds data in banks of 70 to 200 memory locations (channels). Each channel contains the number of counts recorded per time interval, typically 20 sec per channel. The computer may also be used to control electric field plate voltages for determination of Rydberg atom survival probability, discussed in Sec. 5.1. Data are stored on floppy disks for analysis at a later time.

A typical bank of data, containing fluxes of Rydberg atoms vs time, is shown in Fig. 3-5. Experimental conditions for this data were an incidence time  $\tau_w = 60$  sec for  $H_2O$  and an incidence time  $\tau_{Li} = 250$  sec for Li. Incidence time  $\tau$  is defined as the average time interval between collisions of an adsorbate gas on a single surface site.  $\tau$  is also the reciprocal of the particle current  $c$  (number of particles per unit time striking a surface site). For a unit sticking probability ( $s = 1$ ), the

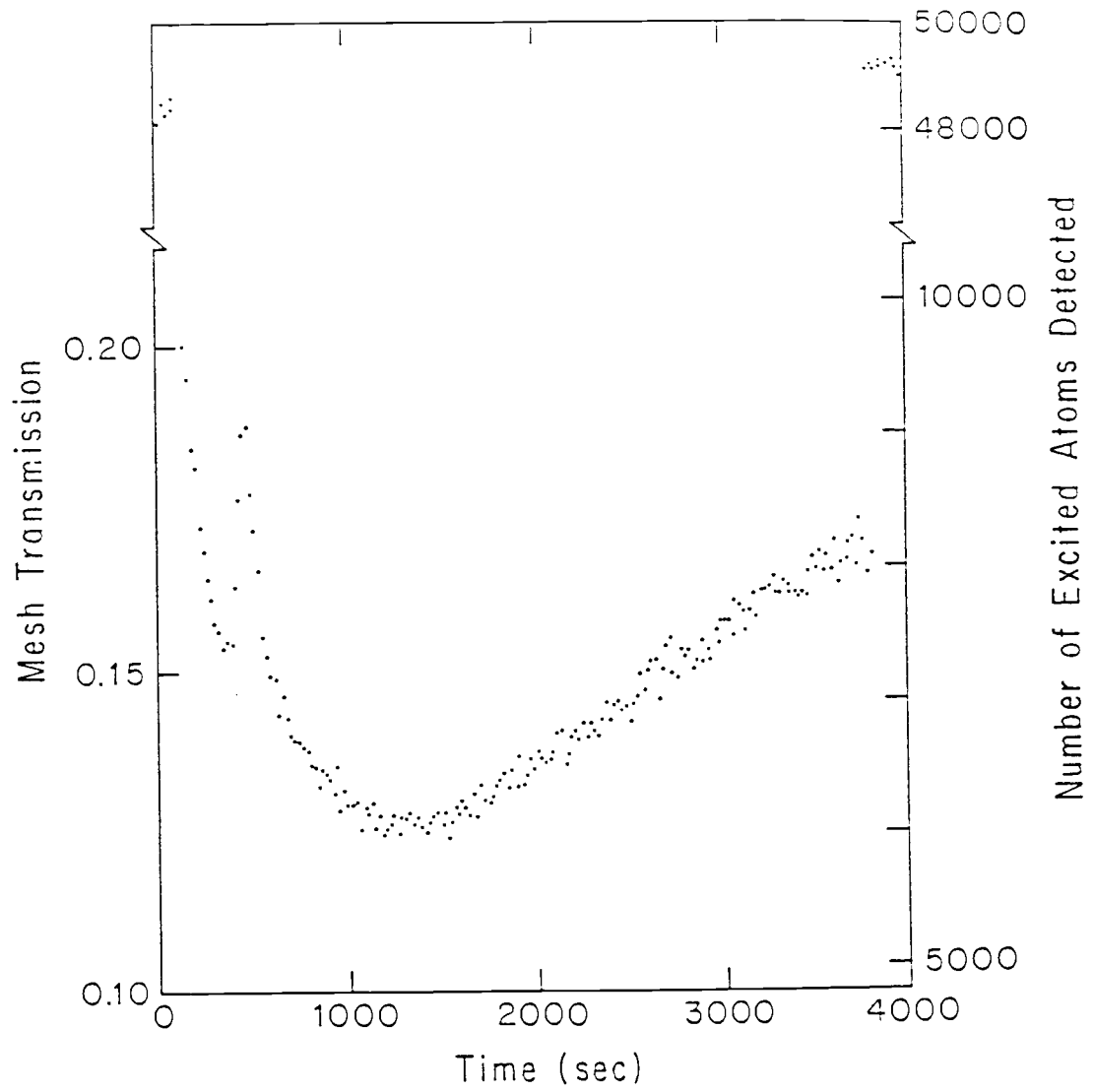


Fig. 3-5 Typical Measured Mesh Transmission

incidence time represents the amount of time to form one monolayer of adsorbate on the surface. However, in general when  $s < 1$ , the monolayer time is  $\tau/s$ . Procedures followed for experimental sequences are described in greater detail in Sec. 6.1. The initial 4 or 5 channels, used for normalization, are taken without the mesh in the atomic beam. Initial channels are compared to the final few channels to check for beam stability. The mesh is cleaned by resistive heating and then is inserted into the atomic beam. When the mesh is inserted into the beam, the cleaning is terminated and the transmission sequence is initiated.

Transmission, initially at  $T \approx 0.20$ , falls to a preliminary minimum  $T \approx 0.15$ , which occurs 240 sec after initiation of the transmission event. The transmission then rises sharply to a cusp, with  $T \approx 0.19$  after 340 sec. A second minimum, with  $T \approx 0.12$ , occurs after 1200 sec. Finally, toward the end of the 4000 sec data bank, the transmission increases slowly, approaching  $T \approx 0.18$ .

In Chapter 4 a model is presented which shows that since the mesh has two sides, a source side and a detector side, the transmission sequence may be reproduced by allowing adsorption on both sides. Adsorption of Li on the source side probably causes the sticking probability and the rate of adsorption of  $H_2O$  on this side to be initially higher than on the detector side. Therefore, the initial decrease in transmission, seen in

Fig. 3-5, is interpreted to be due primarily to the adsorption of  $H_2O$  on the detector side.

A possible explanation for the changes in transmission vs time is as follows. The increase to a maximum may be due to the adsorption of  $H_2O$  on the detector side. The rate of adsorption of  $H_2O$  on the source side decreases and the faster rate of adsorption of  $H_2O$  on the detector side produces an increase in transmission. The cusp occurs when the dipole-moment density  $\langle N\mu \rangle$  on the detector side equals that on the source side.  $\langle N\mu \rangle$  represents the density of dipoles averaged over many surface sites, because the electric field that Rydberg atoms experience is produced by many dipoles. Therefore, the net electric field due to adsorbates on both sides is essentially zero. A relative maximum occurs in the transmission at this time. After the cusp the sign of the net dipole-moment density has changed and adsorption continues to occur on the detector side. The source side has become saturated and the concentration of adsorbates on it approaches a constant value. The final increase in transmission is attributed to the decrease in the dipole moment  $\mu$  as function of coverage. Section 4-3 will examine this behavior more carefully.

In Chapter 5 a conversion between transmission and dipole-moment density will be derived. Figures 3-6a and 3-6b show the transmission data of Fig. 3-5 converted into dipole-moment density. The relation developed in Chapter 5 is

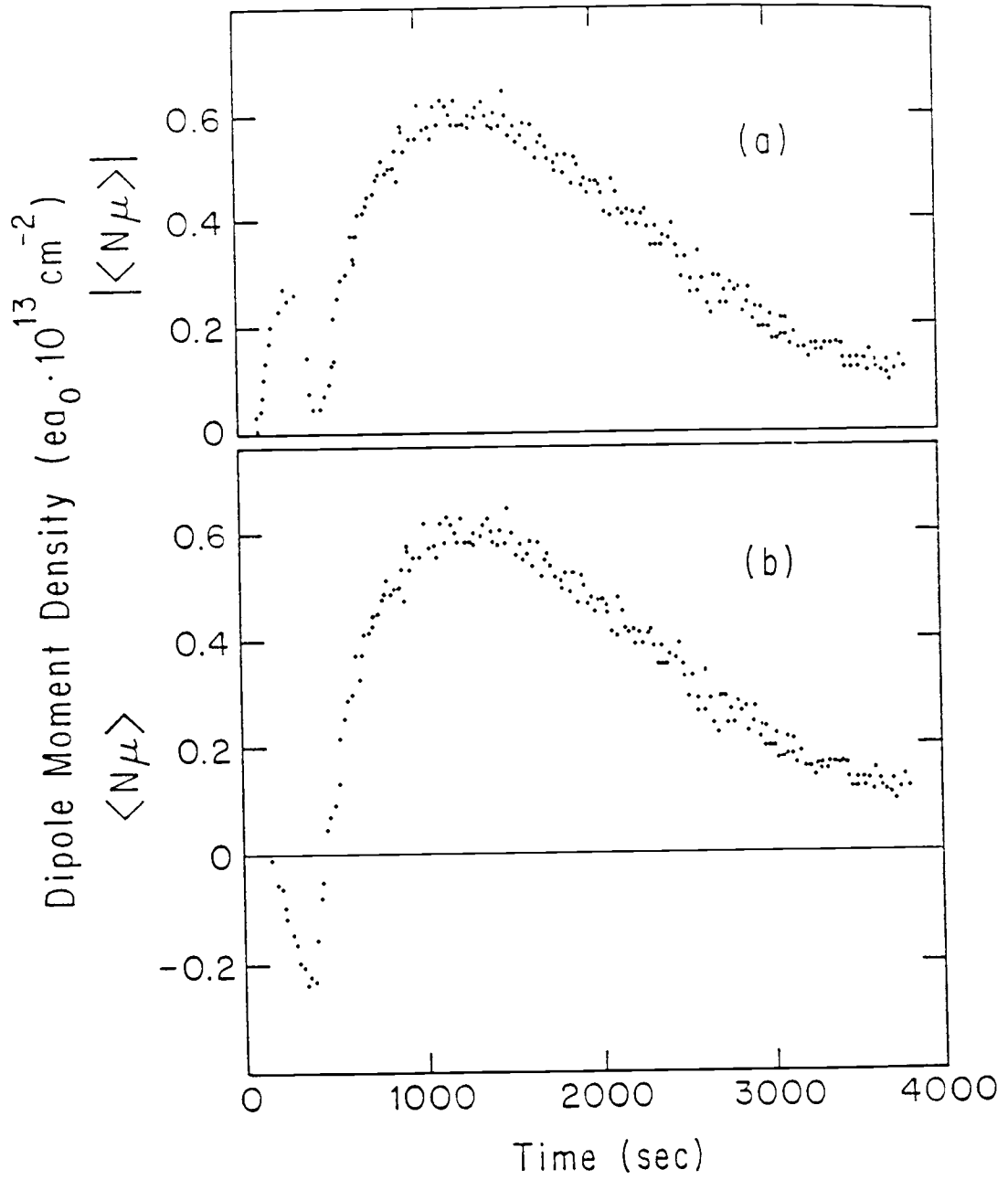


Fig. 3-6 Dipole-Moment Density Converted from Transmission

used to convert the data in Fig. 3-5 into the plots presented in Figs. 3-6a and 3-6b. Figure 3-6a shows the absolute value of the net dipole-moment density, where Fig. 3-6b shows the magnitude and direction of the net dipole-moment density. In Fig. 3-6b the cusp present in Figs. 3-5 and 3-6a is seen to occur where the dipole-moment density changes sign.

### 3.3 Particle Currents in the Vacuum Chamber

#### 3.3.1 Composition of the Residual Gas

A Varian mass spectrometer, Model: 974-0036, was used to determine the relative composition of the residual gas. The mass spectrometer showed that the residual gas was composed predominantly (more than 90%) of  $N_2$  and  $H_2O$ . The  $H_2O$  partial pressure was reduced by baking the detector chamber at  $80^\circ C$  for about 10 h. The baking reduced the  $H_2O$  partial pressure by a factor of 3 to 5. The role of  $N_2$  on adsorption may be ignored, since it does not readily stick to metal surfaces at 300 K.<sup>28</sup> However, the role of  $H_2O$  was seen to be significant in Sec. 3.2.

The particle current may be determined by using elementary kinetic gas theory<sup>29</sup>

$$c = \frac{P A_s}{4 k T} \left( \frac{8 k T}{\pi m} \right)^{1/2}, \quad (3-1)$$

where  $P$  and  $T$  are the residual-gas pressure and absolute temperature,  $m$  is the adsorbate mass,  $k$  is the Boltzmann constant, and  $A_s$  is the area of a surface site for the adsorbed

gas.

After the detector chamber has been baked, the total pressure is approximately  $1 \times 10^{-7}$  Torr with the  $H_2O$  partial pressure typically  $\lesssim 3 \times 10^{-8}$  Torr. In Table 1 the calculated values for particle current and incidence time for  $H_2O$  are shown for  $T = 300$  K and for various values of  $P_{H_2O}$  on Au and Ni substrates.

Table 1: Incidence Times and Particle Currents for  $H_2O$  on Au and Ni

| $P_{H_2O}$ (Torr)  | Au(100)    |                      | Ni(100)    |                      |
|--------------------|------------|----------------------|------------|----------------------|
|                    | $\tau$ (s) | $c$ ( $s^{-1}$ )     | $\tau$ (s) | $c$ ( $s^{-1}$ )     |
| $2 \times 10^{-8}$ | 123        | $8.2 \times 10^{-3}$ | 163        | $6.2 \times 10^{-3}$ |
| $3 \times 10^{-8}$ | 82         | $1.2 \times 10^{-2}$ | 108        | $9.2 \times 10^{-3}$ |
| $5 \times 10^{-8}$ | 49         | $2.0 \times 10^{-2}$ | 65         | $1.5 \times 10^{-2}$ |
| $1 \times 10^{-7}$ | 25         | $4.0 \times 10^{-2}$ | 33         | $3.0 \times 10^{-2}$ |

### 3.3.2 Lithium Particle Current at the Mesh

The Li particle current and incidence time on the mesh may also be calculated with kinetic theory. However, the expression becomes slightly more complicated than Eq. (3-1) since the Li is

$$c_{Li} = \frac{A_o P_{Li}}{4 k T_o} \left( \frac{8 k T_o}{\pi m_{Li}} \right)^{1/2} \frac{A_s}{\pi r_{om}^2}, \quad (3-2)$$

where  $A_o$  the area of the oven opening,  $T_o$  is the oven temperature,

$r_{om}$  is the oven-to-mesh distance,  $m_{Li}$  is the mass of Li<sup>7</sup>,  $A_s$  is the area of a single surface site, and  $k$  is Boltzmanns constant. Finally,  $P_{Li}$  is the vapor pressure of Li inside the oven, which may be calculated with the following equation

$$P_{Li} = 1\text{MPa} \exp \{ 13.07 - 18880/T - 0.494 \ln T \}^{30}$$

Table 2 gives incidence time and particle currents:

Table 2: Incidence Time and Particle Currents for Li on Au and Ni

| $T_o$ (K) | <u>Au(100)</u> |                      | <u>Ni(100)</u> |                      |
|-----------|----------------|----------------------|----------------|----------------------|
|           | $\tau_L$ (s)   | $c_L$ ( $s^{-1}$ )   | $\tau_L$ (s)   | $c_L$ ( $s^{-1}$ )   |
| 670       | 1610           | $6.2 \times 10^{-4}$ | 2150           | $4.7 \times 10^{-4}$ |
| 700       | 502            | $2.0 \times 10^{-3}$ | 673            | $1.5 \times 10^{-3}$ |
| 800       | 19             | $5.3 \times 10^{-2}$ | 26             | $3.8 \times 10^{-2}$ |

### 3.3.3 Adsorbate Particle Current at the Mesh

The incidence time and the particle current for the introduced adsorbate on the mesh may be calculated with Eq. (3-2) with appropriate changes in the subscripts. Particle current is

$$c_a = \frac{P_T A_T}{4 k T_a} \left( \frac{8 k T_a}{\pi m_a} \right)^{1/2} \frac{A_s}{\pi r_{Tm}^2}, \quad (3-3)$$

where  $P_T$  is the introduced adsorbate pressure inside the gas introduction tube (measured with the capacitance manometer),  $A_T$  is the area of the tube opening (equal to  $2.8 \times 10^{-3} \text{ cm}^2$ ),  $T_a$  is the temperature of the introduced adsorbate,  $m_a$  is the mass of

the gas molecule, and  $r_{\text{TM}}$  is the tube-to-mesh distance.

The incidence time  $\tau_a = 1/c_a$  for a tube pressure  $P_T = 10$  mTorr, see Fig. 3-4, is shown in Table 3 for several introduced adsorbates. The final column in the table is the adsorbate-gas pressure  $P_a$  at the surface calculated with the following relation:

$$P_a = \frac{4 k T_a c_a}{A_s} \left( \frac{8 k T_a}{\pi m_a} \right)^{-1/2} . \quad (3-4)$$

Table 3: Incidence Times and Pressures for Adsorbate Gases

| Gas              | Atomic Mass | Au(100)    |                         | Ni(100)    |                         |
|------------------|-------------|------------|-------------------------|------------|-------------------------|
|                  |             | $\tau$ (s) | $P_a$ ( $10^{-7}$ Torr) | $\tau$ (s) | $P_a$ ( $10^{-7}$ Torr) |
| CO               | 26          | 8.4        | 2.4                     | 11.2       | 1.8                     |
| CO <sub>2</sub>  | 44          | 10.5       | 1.9                     | 14.0       | 1.4                     |
| SO <sub>2</sub>  | 64          | 12.7       | 1.6                     | 17.0       | 1.2                     |
| H <sub>2</sub>   | 2           | 2.2        | 9.1                     | 2.9        | 6.7                     |
| NO               | 30          | 8.7        | 2.3                     | 12.0       | 1.7                     |
| H <sub>2</sub> O | 18          | 6.7        | 3.0                     | 9.0        | 2.2                     |
| O <sub>2</sub>   | 16          | 5.2        | 3.9                     | 6.9        | 2.9                     |

The time-dependent coverage of a metal surface depends on the surface gas particle current,  $c$ . The previous calculations of  $c$  will be used in calculations described in Chapter 4 for the dipole-moment density  $\langle N\mu \rangle$  and adsorption rates on a surface. The calculations in Chapter 4 will be used in Chapters 6 and 7.

## CHAPTER 4: TIME-DEPENDENT MODELS FOR ADSORBATE COVERAGE

## 4.1 Langmuir-Type Model

The adsorption of gases on a metal surface may be modeled with a Langmuir-type approach, which primarily ignores adatom-adatom interactions on the surface.<sup>31</sup> Desorption of adatoms from the surface is not explicitly considered in this model. This limit is valid at sufficiently high desorption energies, which will be shown to be appropriate for most of the experiments described in Chapters 6 and 7. The net dipole-moment density is found when time-dependent simultaneous equations are solved for the relative coverage of each adsorbate on the surface, and then the contributions from the adsorbates are added together.

The contribution for each adsorbate is the coverage multiplied by the appropriate coverage-dependent dipole moment. The sum of the partial coverages (i.e., the total coverage of the surface) is unity at all times. The net dipole-moment density is

$$\langle N\mu \rangle = \sum_i \mu_i \theta_i / A_s, \quad (4-1)$$

where  $\mu_i$  is the dipole moment of a specific adsorbate,  $\theta_i$  is the relative coverage of the adsorbate, and  $A_s$  is the area of a surface site, which is adsorbate-surface dependent.

For these experiments the adsorbates are Li and H<sub>2</sub>O from the background gas and an externally introduced adsorbate. Although

H<sub>2</sub>O may be introduced into the vacuum system as an adsorbate gas, always present are significant amounts of H<sub>2</sub>O and Li that may adsorb on the metal surface. The mesh consists of a source side and a detector side, and H<sub>2</sub>O and the introduced gas accumulate on the detector side. Li and H<sub>2</sub>O accumulate on the source side. When an H<sub>2</sub>O molecule arrives at a surface site already occupied by a Li atom, or vice versa, the atom and molecule combine to form an overlayer that is essentially permanent. "Permanent" in this context means that mesh heating does not remove this layer. The permanent layer is formed after the mesh has been exposed to both the H<sub>2</sub>O and Li and the mesh has been heated at 700°C to 800°C for a total time of approximately 5 to 10 h.

H<sub>2</sub>O and the introduced gas accumulate on the detector side. Therefore, the dipole-moment density depends as follows on the respective coverages and moments of H<sub>2</sub>O and the introduced adsorbate.

$$\langle N\mu \rangle = \frac{1}{A_S} \left( \mu_w \theta_{wd} + \mu_a \theta_a - \mu_L \theta_L - \mu_p \theta_p - \mu_w \theta_{ws} \right) : \quad (4-2)$$

The subscripts are defined below.

|    |                                   |   |                 |
|----|-----------------------------------|---|-----------------|
| w  | H <sub>2</sub> O                  | L | lithium         |
| wd | H <sub>2</sub> O on detector side | p | permanent layer |
| ws | H <sub>2</sub> O on source side.  |   |                 |

The sign convention is that dipoles pointing outward (negative at the surface) on the detector side are oriented in a positive

direction, and conversely, those pointing outward on the source side are oriented in a negative direction. The direction is defined to be the same as the direction of flow for the Rydberg atoms in the beam.

The adsorption rates depend upon the particle currents  $c$  and the sticking probabilities  $s$ .

#### 4.1.1 Adsorption on the Detector Side

On the detector side, the mesh begins as a clean polycrystalline Au surface. The time dependences are as follows:

$$\text{For Au: } \dot{\theta}_{\text{Au}} = -\theta_{\text{Au}} \left( s_{\text{wd}} c_w + s_a c_a \right) \quad (4-3)$$

$$\text{For H}_2\text{O: } \dot{\theta}_{\text{wd}} = s_{\text{wd}} c_w \theta_{\text{Au}}, \quad (4-4)$$

For the adsorbate:

$$\dot{\theta}_a = s_a c_a \theta_{\text{Au}}. \quad (4-5)$$

The solution is straightforward in the case of no introduced adsorbate. The initial conditions are  $\theta_{\text{Au}} = 1$  and  $\theta_{\text{wd}} = 0$ , and the solution for the coverage of  $\text{H}_2\text{O}$  becomes

$$\theta_{\text{wd}} = 1 - e^{-s_{\text{wd}} c_w t}. \quad (4-6)$$

The solutions for the case  $c_a \neq 0$  are

$$\theta_{\text{wd}} = \frac{s_{\text{wd}} c_w}{s_{\text{wd}} c_w + s_a c_a} \left( 1 - e^{-(s_{\text{wd}} c_w + s_a c_a)t} \right) \quad (4-7)$$

$$\text{and } \theta_a = \frac{s_a c_a}{s_{\text{wd}} c_w + s_a c_a} \left( 1 - e^{-(s_{\text{wd}} c_w + s_a c_a)t} \right). \quad (4-8)$$

#### 4.1.2 Adsorption on the Source Side

In the model the source side of the mesh begins with a permanent layer, because all experiments in Chapters 6 and 7 are run after the permanent layer has formed. The formation time for the permanent layer is of order the monolayer time for Li and H<sub>2</sub>O. The monolayer time is  $\tau_L = 1/s_L c_L$  for Li and  $\tau_{ws} = 1/s_{ws} c_{ws}$  for H<sub>2</sub>O. The initial conditions are  $\theta_p = 1$ ,  $\theta_L = 0$ , and  $\theta_{ws} = 0$ . The differential equations for this case are

for Li:

$$\dot{\theta}_L = s_{L L} c_{L P} \theta_P - s_{L W} c_{L L} \theta_L, \quad (4-9)$$

for H<sub>2</sub>O:

$$\dot{\theta}_{ws} = s_{wp} c_{wp} \theta_p - s_{L L} c_{L ws} \theta_{ws}, \quad \text{and} \quad (4-10)$$

for the permanent layer:

$$\dot{\theta}_p = -s_{L L} c_{L p} \theta_p - s_{wp} c_{wp} \theta_p + s_{L L} c_{L ws} \theta_{ws} + s_{L W} c_{W L} \theta_L. \quad (4-11)$$

Equations (4-9) through (4-11) may be solved with the initial conditions  $\theta_p = 1$ ,  $\theta_{ws} = 0$ , and  $\theta_L = 0$  and the condition that  $\theta_p + \theta_{ws} + \theta_L = 1$ . The solutions are presented below.

For Li:

$$\theta_L = \frac{\beta P - \omega_{21}}{\alpha - \beta} e^{-\alpha t} + \frac{\omega_{21} - \alpha P}{\alpha - \beta} e^{-\beta t} + P; \quad (4-12)$$

for H<sub>2</sub>O on the source side:

$$\theta_{ws} = 1 - \left( \frac{\beta P - \omega_{21}}{\alpha - \beta} e^{-\alpha t} \right) \left( 1 + \frac{\omega_2 - \alpha}{\omega_{21}} \right) - \left( 1 + \frac{\omega_2}{\omega_{21}} \right) P - \left( \frac{\omega_{21} - \alpha P}{\alpha - \beta} e^{-\beta t} \right) \left( 1 + \frac{\omega_2 - \beta}{\omega_{21}} \right); \quad (4-13)$$

for the permanent layer :

$$\theta_p = \frac{1}{\omega_{21}} \left[ (\omega_2 - \alpha) \left( \frac{\beta P - \omega_{21}}{\alpha - \beta} e^{-\alpha t} \right) + \omega_2 P \right. \\ \left. + (\omega_2 - P) \left( \frac{\omega_{21} - \alpha P}{\alpha - \beta} e^{-\beta t} \right) \right] ; \quad (4-14)$$

where

$$\alpha = \frac{1}{2}(\omega_1 + \omega_2 + \omega_3) \pm \left[ (\omega_1 + \omega_2 + \omega_3)^2 - 4(\omega_2\omega_{31} + \omega_2\omega_3 + \omega_{21}\omega_3) \right]^{1/2}, \text{ and}$$

$$P = \frac{\omega_{21}\omega_3}{\omega_{31}\omega_2 + \omega_{21}\omega_3 + \omega_2\omega_3}, \text{ in which}$$

$$\omega_1 = s_{ws} c_w + s_{Ll} c_l \omega_2 = s_{ws} c_w \omega_3 = s_{Ll} c_l,$$

$$\omega_{21} = s_{Ll} c_l, \text{ and } \omega_{31} = s_{ws} c_w.$$

#### 4.2 Model for Adsorption-Desorption Equilibrium

In this model desorption is considered explicitly for a single adsorbate in the limit of  $c_a \gg c_{Li}$  and  $c_a \gg c_w$ . The effect of all other adsorbates may be neglected when equilibrium between adsorption and desorption for a single adsorbate occurs rapidly. "Rapidly" means that the change in coverage for other adsorbates can be ignored. The rate of change of coverage for the adsorbate when equilibrium is rapidly approached is

$$\dot{\theta}_a = s_a c_a - \Gamma \theta_a. \quad (4-15)$$

The adsorbate coverage is given by  $\theta_a = N_a / N_s$  where  $N_a$  is the number of adsorbates on the surface and  $N_s$  is the total number of surface sites available for adsorption. Equation (4-15) is correct in the limit that the coverage  $\theta_a$  is small compared to unity. If this is not the case then Eq. (4-15)

becomes  $\dot{\theta}_a = s_a c_a (1 - \theta_a) - \Gamma \theta_a$ . The first term on the right hand side of Eq. (4-15) describes the adsorption, and the second term describes desorption as discussed in Sec. 2.1.3:  $\Gamma = \Gamma_o e^{-E_d/kT}$  where  $\Gamma_o \approx 10^{13} \text{ s}^{-1}$ .<sup>9</sup> Equation (4-15) has the following solution, valid for  $\theta_a \ll 1$ ,

$$\theta_a = \frac{s_a c_a}{\Gamma} (1 - e^{-\Gamma t}) \quad (4-16)$$

For the case when  $\Gamma t \gg 1$  the exponential may be ignored, and the dipole-moment density due to the adsorbate becomes

$$\langle N\mu \rangle = \frac{\mu_a s_a c_a}{A_s \Gamma} \quad (4-17)$$

Equilibrium is reached rapidly, in comparison to a typical channel duration of 20 sec, when the desorption rate is large, i.e.,  $\Gamma t \gg 1$ . This condition is satisfied when the desorption energy is small (relative to  $kT$ ) or when the surface temperature is sufficiently large. This analysis is appropriate when a sufficiently rapid change in transmission occurs as an adsorbate is introduced onto the mesh surface. These results are used in Sec. 7.1, for example, in the determination of the desorption energy.

#### 4.3 Application of the Model and Comparison to Experiment

Model results are compared to experimental results. More complete descriptions of the experiments will be made in Chapters 6 and 7. A preliminary description of the transmission sequence was given in Sec. 3.2. For the data presented in this section

the adsorbate particle currents have been varied.

The model described in Sec. 4.1 may be used to qualitatively and semi-quantitatively interpret and understand the experimental data. Parameters of the model are the sticking probabilities  $s$ , the particle current  $c$ , the adsorbate dipole moments  $\mu$ , and the dependence of  $\mu$  upon coverage. The dipole moment decreases with coverage because of dipole-dipole interactions of the adsorbates on the surface. Coverage dependence of the dipole moment may be described in a manner similar to that of the Topping model,  $\mu(\theta) = \mu_0 / (1 + \beta\theta^2)$ ,<sup>17</sup> where  $\mu_0$  is the zero-coverage limit of the dipole-moment and  $\beta$  is a parameter that depends on the adsorbate and the substrate.

Variation of oven temperature, Li particle current, and background  $H_2O$  particle current is seen to affect the timing of the qualitative features of the mesh transmission.

Figures 4-1a and 4-1b show the transmission vs time for two experiments in which the particle current of  $H_2O$  on the Au mesh is varied. First, when the  $H_2O$  partial pressure in the system increases by a factor of 1.6, the incidence time for  $H_2O$  decreases from  $\tau_w = 105$  s in Fig. 4-1a to  $\tau_w = 65$  s in Fig. 4-1b. An increase in  $H_2O$  particle current reduces the time duration of the initial dip and rise to the cusp from 320 s to 200 s and also deepens the second dip. Therefore, at a sufficiently large  $H_2O$  particle current the initial dip may disappear altogether.

The model can qualitatively reproduce the data presented in

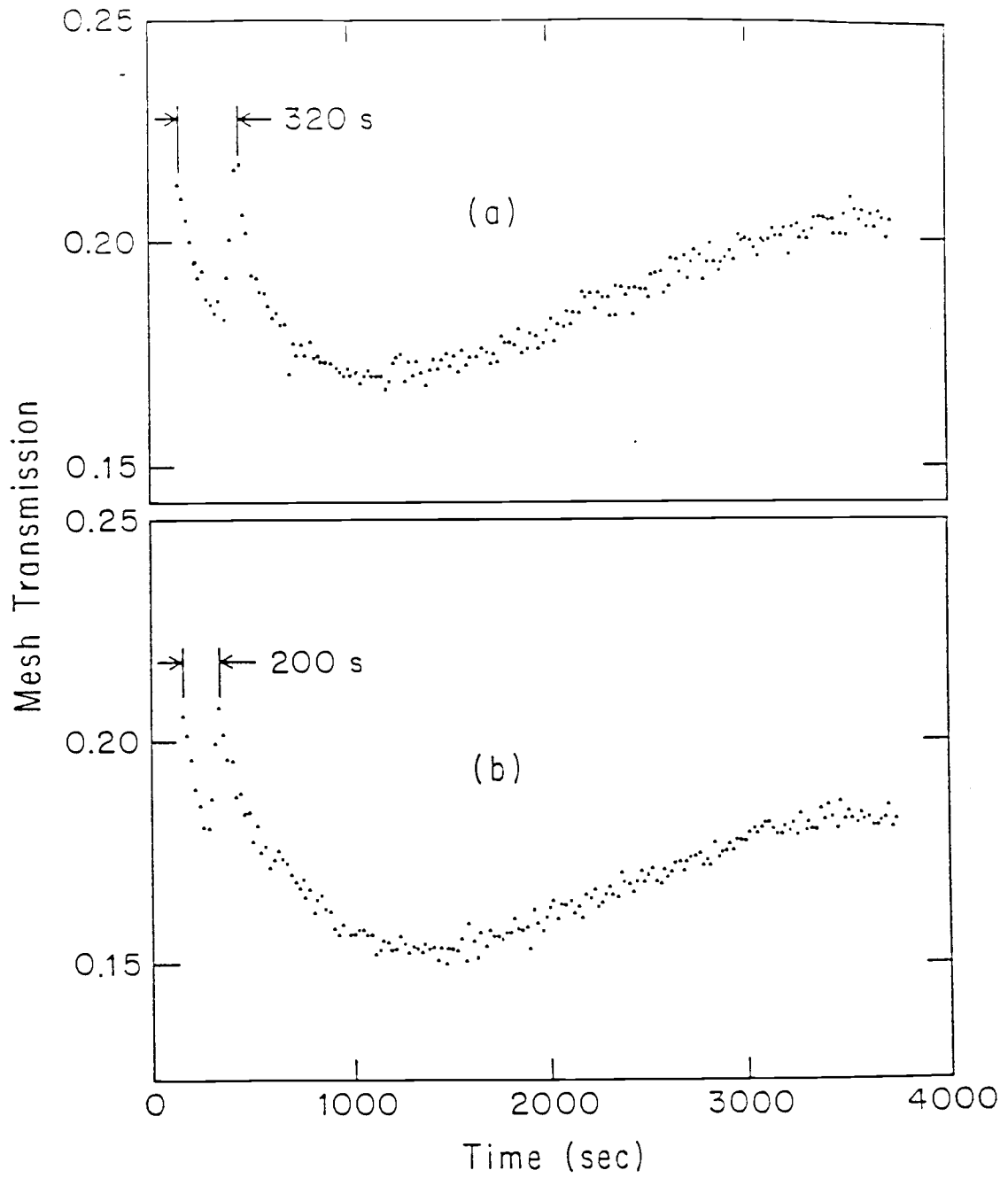


Fig. 4-1 Transmission with  $H_2O$  Varied  
(a)  $\tau_w = 105$  s (b)  $\tau_w = 65$  s

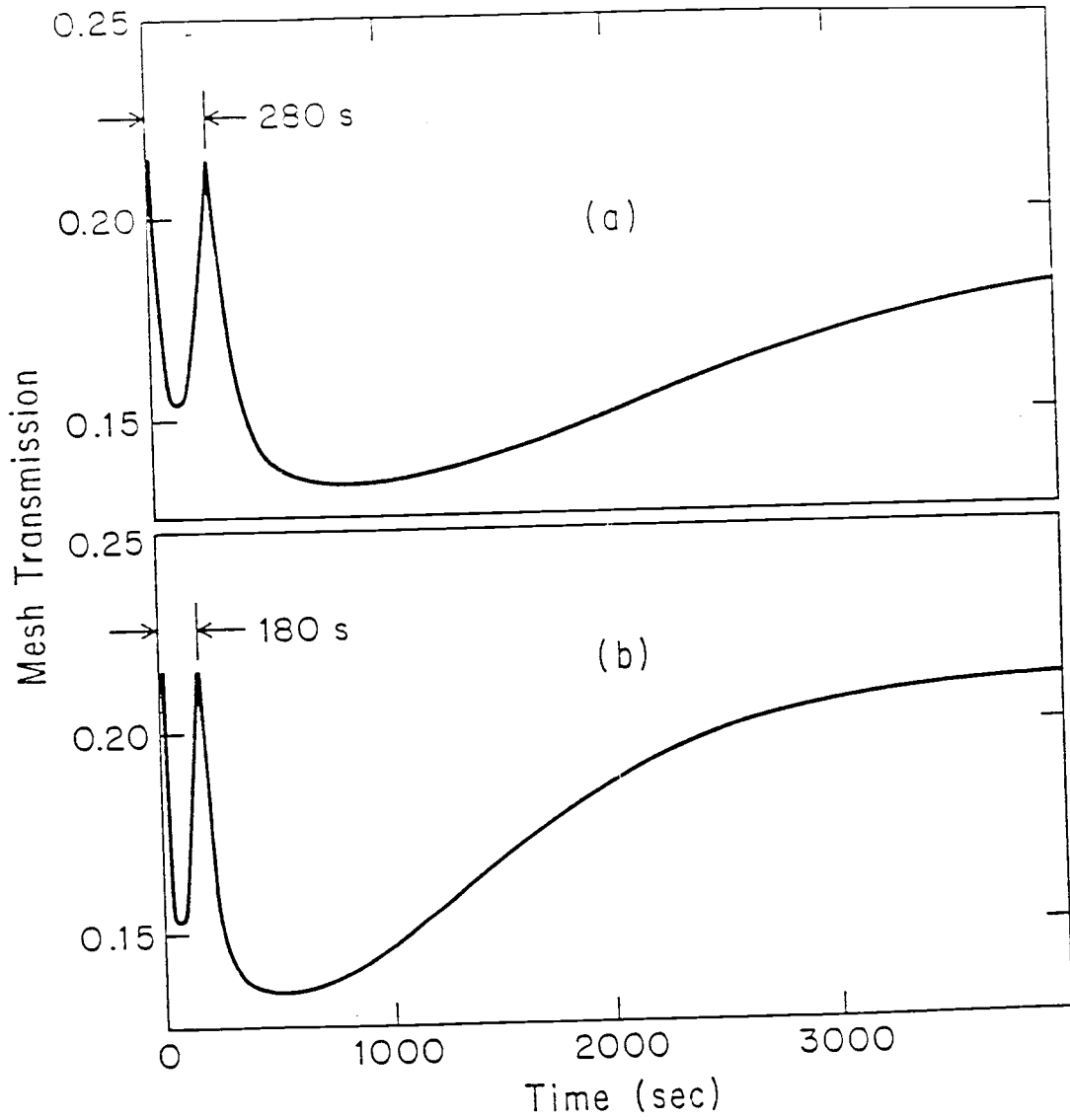


Fig. 4-2 Model Transmission Calculations with  $H_2O$  Varied

(a)  $\tau_w = 120$  s

(b)  $\tau_w = 75$  s

Figs. 4-1a and 4-1b. Figures 4-2 a and 4-2b show the transmission vs time generated with the model. For  $H_2O$  the parameters used for these calculations are a dipole-moment of  $\mu_0 \cong 0.1 ea_0$  and sticking probabilities  $s \cong 0.1$  for  $H_2O$  on the source side and  $s = 0.1$  for  $H_2O$  on the detector side. Values of  $\mu_0$  and  $s$  correspond to values found by Bajpai et al.<sup>32</sup> The best fit to the data is obtained when  $\beta = 4$ . For Li  $\mu_0$  is taken to be  $0.04 ea_0$ ,  $\beta$  is taken to be 2, and  $s$  for both sides is taken to be 1. The values for  $\mu_0$  and  $\beta$  correspond to the work presented by Gerlach et al.<sup>13</sup> Under both the experimental conditions for Fig. 4-1 and the model conditions in Fig. 4-2 the Li incidence time is  $\tau_{Li} = 250$  s.

The value of  $\mu_0$  chosen for  $H_2O$  corresponds to values calculated by J.E. Muller and J. Harris.<sup>16</sup> The value of  $\mu_0$  chosen for Li is in line with values found by R.L. Gerlach and T.N. Rhodin for alkali metals adsorbed to a Ni substrate.<sup>13</sup> The sticking probability for Li is taken to be unity since it is known that alkali metals have a high sticking affinity. The particle currents  $c$  are chosen to correspond to experimental conditions. The other parameters are chosen to cause the model to reproduce the experimental data.

The particle current  $c$  for Fig. 4-2a was chosen to give an incidence time of  $\tau_w = 120$  sec. Model calculations yield a cusp after 280 sec. The particle current  $c$  for Fig. 4-2b was chosen to give an incidence time of  $\tau_w = 75$  sec, which yields a cusp after

180 sec. Figures 4-2 and 4-1 are seen to be qualitative similar in the timing of the initial dip and rise.

Li atom particle current from the oven may be varied producing a change in the transmission vs time. This difference is due to a long term change in the Li coverage on the surface. Figures 4-3a, 4-3b, and 4-3c show experimental data for three Li particle currents. The particle current for Fig. 4-3a gives an incidence time  $\tau_{Li} = 100$  sec,  $\tau_{Li} = 290$  sec for Fig. 4-3b, and  $\tau_{Li} = 540$  sec for Fig. 4-3c. The initial dip and cusp are not significantly affected by the variation of Li particle current. However, the second dip and rise are greatly changed. In the case of the smallest particle current there is essentially no final rise. The magnitude of the long-term net dipole-moment density increases as the Li particle current decreases.

The model for this case also provides qualitative agreement with the data. Figures 4-4a, 4-4b, and 4-4c show T vs t. The same parameters are used in the model as for H<sub>2</sub>O particle current variation with the exception of  $\tau_w$ , which is 75 sec.  $\tau_{Li}$  is varied from 100 sec for Fig. 4-4a to 200 sec for Fig. 4-4b and to 540 sec for Fig. 4-4c. Figure 4-4 should be compared to Fig. 4-3, revealing the similarities between the experiment and the model calculations. Other experimental results have been observed and can be reproduced with this model by variation of the parameters. Specifically,  $\mu$ , s, and c may be changed to reproduce all the experimental results seen in Chapters 6 and 7.

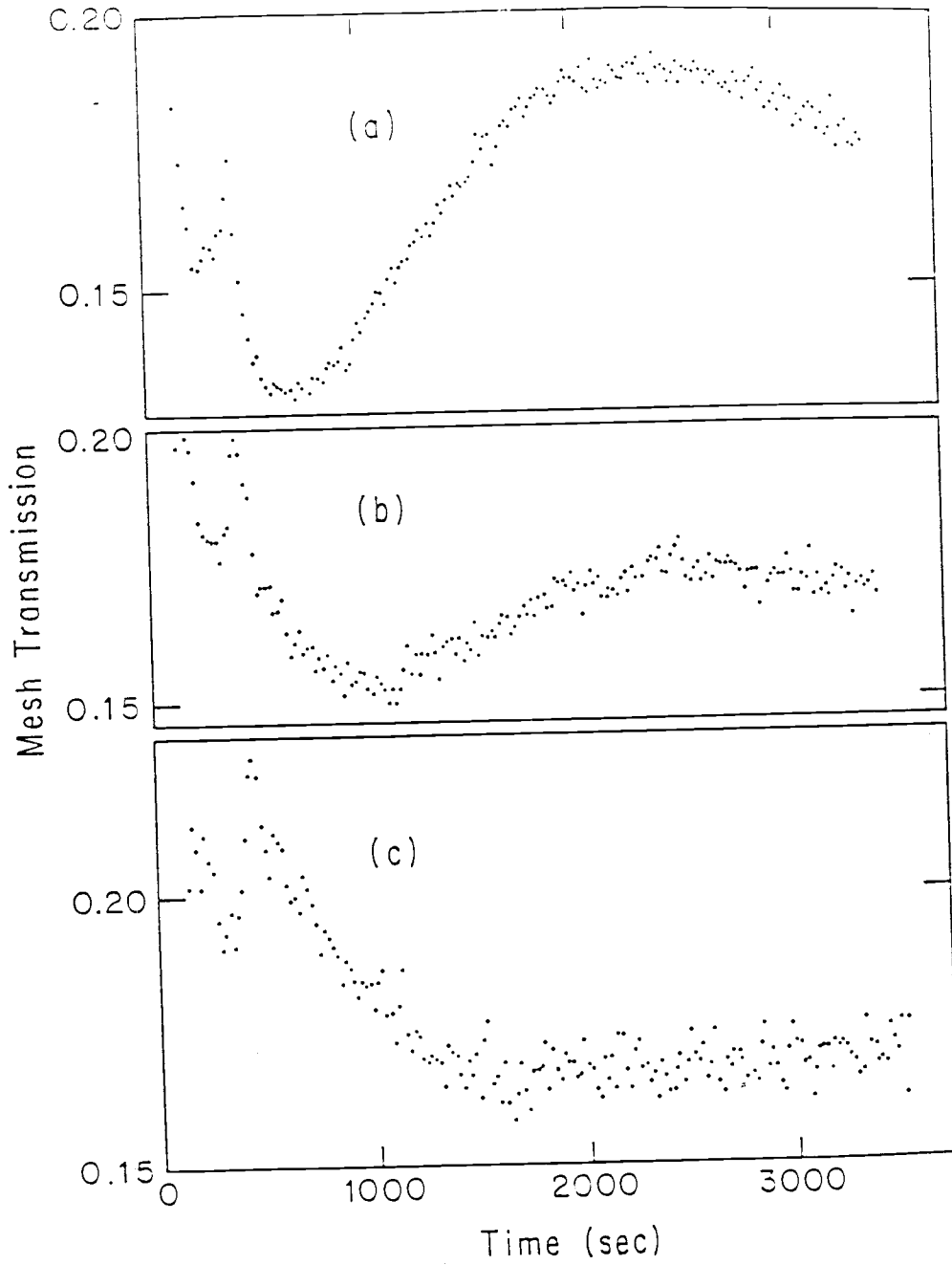


Fig. 4-3 Transmission with Li Varied  
 (a)  $\tau_{Li} = 100$  s (b)  $\tau_{Li} = 290$  s (c)  $\tau_{Li} = 540$  s

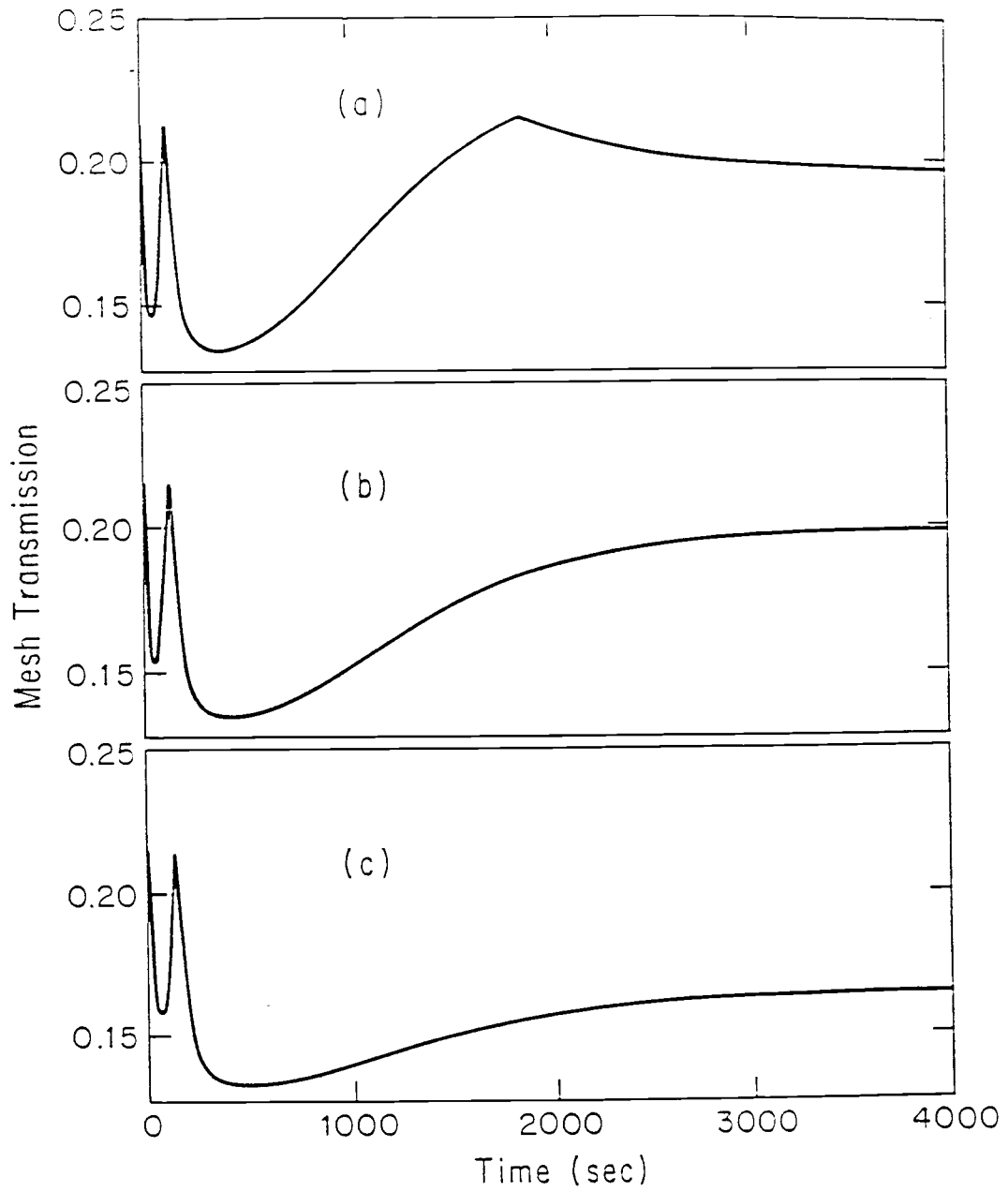


Fig. 4-4 Model Transmission Calculations with Li Varied  
(a)  $\tau_{Li} = 100$  s (b)  $\tau_{Li} = 200$  s (c)  $\tau_{Li} = 540$  s

## CHAPTER 5: TECHNIQUES FOR DATA ANALYSIS

The interpretation of data -- in this experiment the time dependence of the Rydberg atom transmission through the mesh -- is an important aspect of this work. Since the analysis is somewhat complex, an entire chapter will be devoted to techniques used to extract meaningful information from the data, including dipole moments, sticking probabilities, and desorption energies.

### 5.1 Relation Linking Adsorbate Dipole-Moment Density to the Mesh Transmission

Rydberg atoms are ionized by the electric fields produced by adsorbates on the mesh surface. The nonuniform adsorption of particles onto the mesh produces an electric field extending from the surface, as discussed in Secs. 2.2 and 2.3. Changes in the electric fields produce changes in the transmission of Rydberg atoms through the mesh. In Sec. 1.5 the mesh transmission  $T$  was defined as the rate of detection of Rydberg atoms with the mesh in the beam, divided by the rate without the mesh in the beam. In this chapter a method will be developed to relate the mesh transmission to the adsorbate dipole-moment density. This procedure must make use of the field-ionization properties of the Rydberg atoms and the magnitudes of the electric fields near the mesh surface.

In Chapter 2 the external electric field near the surface of

the mesh was calculated as a function of dipole-moment density. Equation (2-18) shows that the maximum electric field occurs in the plane of the dipole moments, the  $z = 0$  plane for an infinitely thin mesh. If the magnitude of electric field is greater than the ionization threshold, Rydberg atoms will be lost from the beam. Equation (2-18) can be used to determine the area enclosed by a contour at electric field magnitude  $|E|$ .

The effective open area represents the region through which a Rydberg atom may pass and survive the electric field present. Consequently, the effective open area is zero when the ionization threshold for a particular  $n$ -state is less than  $E_c$ , the field at the center of the hole. Figure 5-1 shows the effective area  $A$ , in units of  $b^2$ , versus the electric field  $E$  in units of  $E_c$ . Figure 5-1 was obtained by calculating the area inside an electric field contour generated from Eq. (2-18).

Figure 5-2 shows the survival probability  $P(E)$  for Rydberg atoms in the atomic beam as a function of electric field  $E$ .  $P(E)$  is experimentally obtained by varying the electric field between one of the sets of electric field plates, described in Chapter 3. As the electric field is stepped from zero to 2000 V/cm, the Rydberg-atom rate is recorded.  $P(E)$  is the ratio of the counting rate for atoms surviving for a particular  $E$  to the rate when  $E = 0$ . For an electric field of  $E = 0$  the survival probability is defined to be  $P(E) = 1$ . As  $E$  increases,  $P(E)$

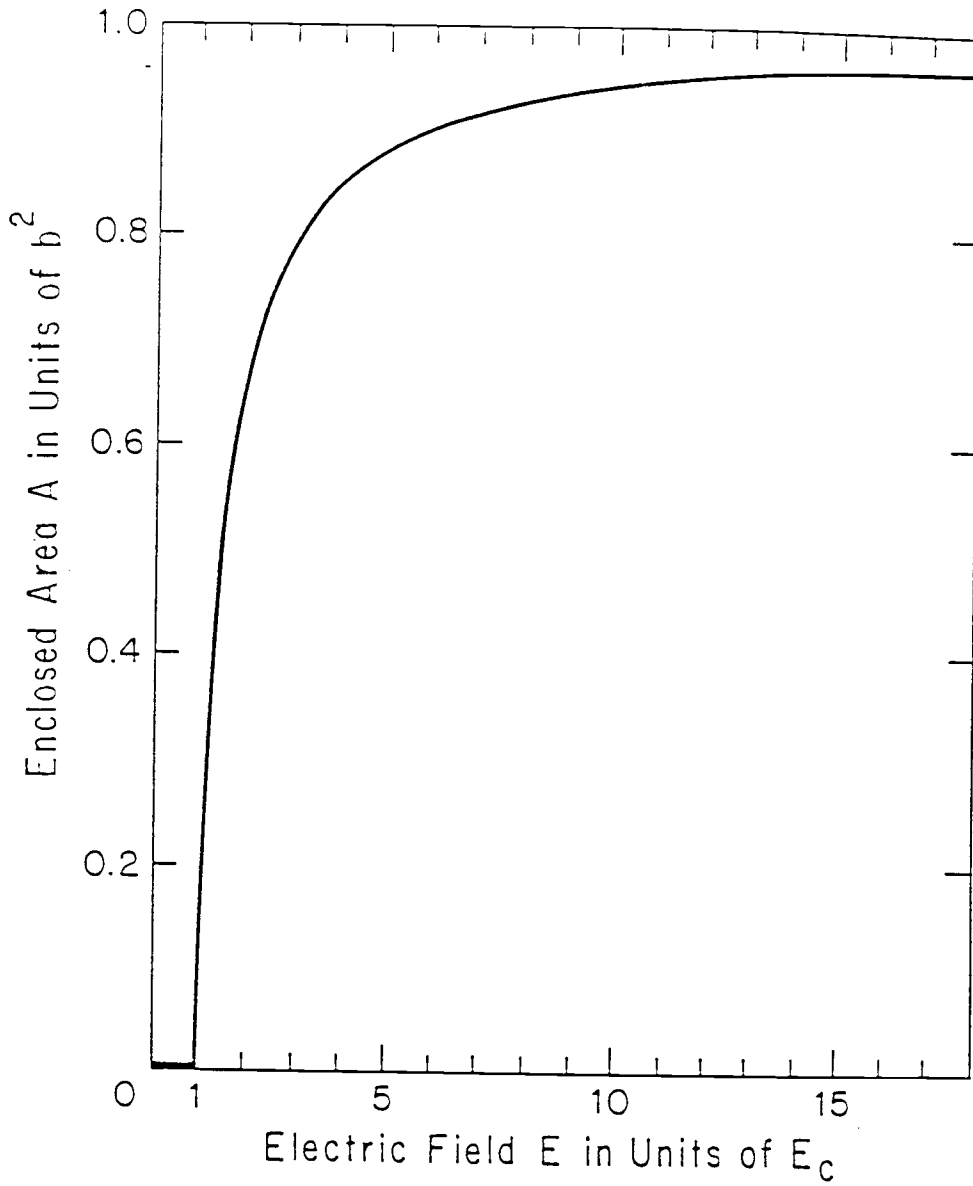


Fig. 5-1 Effective Open Area vs Electric Field at Center

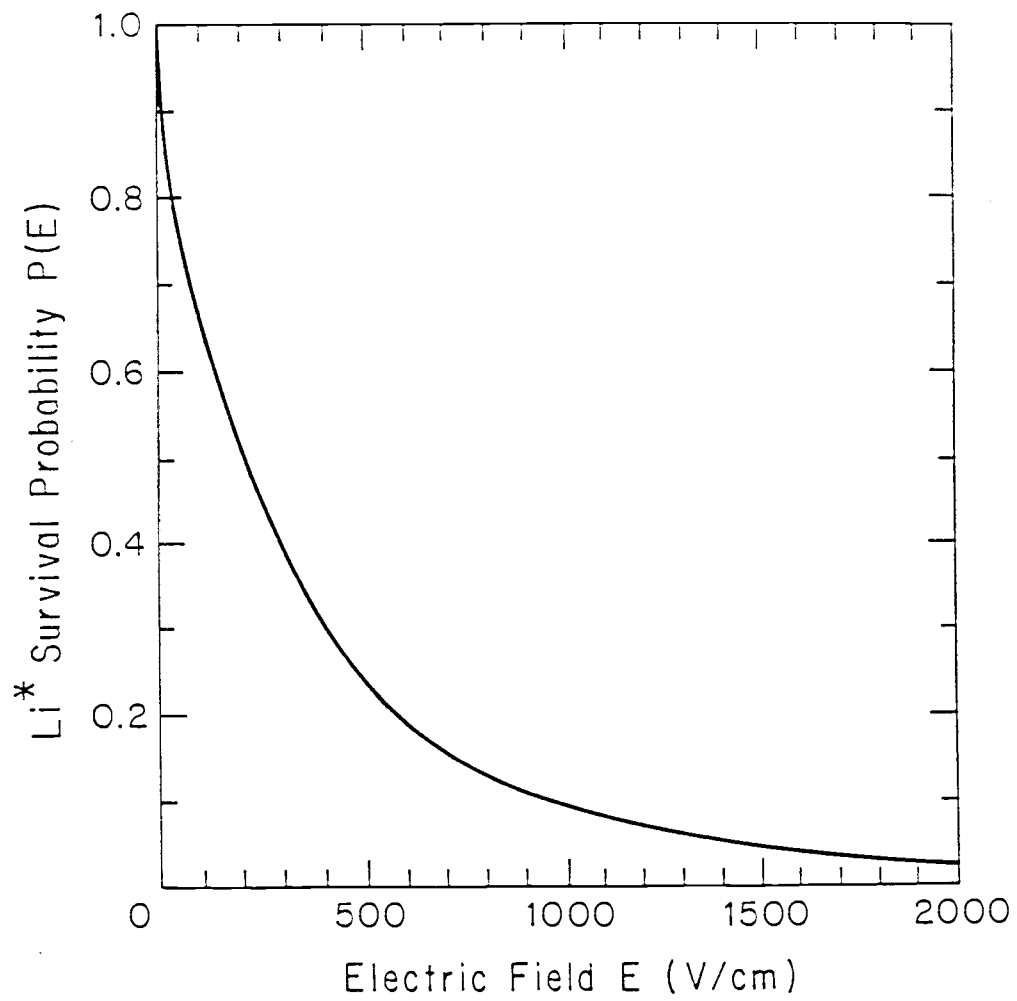


Fig. 5-2 Rydberg Atom Survival Probability vs Electric Field

decreases monotonically. The experimental measurement of  $P(E)$  is made by applying an electric field along the beam path for a time  $t \approx 10^{-5}$  sec to an excited state. However, the field applied to an excited state by the mesh occurs only for  $t \approx 10^{-9}$  sec. The difference in time between the two events is negligible because the ionization rate increases extremely rapidly with field strength.<sup>33</sup>

The area within a mesh opening can be divided into small regions of area  $dA$ , each bounded by two electric field contours,  $E_j$  and  $E_k$ . Figure 5-3 shows a mesh opening and a region of area  $dA$ . Contribution to the mesh transmission through this area element is then  $dT = P(E) dA / 4b^2$ . The denominator is introduced because the mesh unit cell has an area  $(2b)^2$ , where  $b$  is the mesh filament width. Dimensions of the mesh were determined in Chapter 3: see also Fig. 3-3.

The total transmission through the mesh may be determined by integrating over all the differential area elements  $dA$  between adjacent electric field contours. Therefore,  $T$  may be written

$$T = \frac{1}{4b^2} \int_{E_c}^{E_i} P(E) dA \quad \text{or} \quad (5-1)$$

$$T = \frac{1}{4} \int_1^{\epsilon_i} P(\epsilon E_c) \left[ \frac{d(A/b^2)}{d\epsilon} \right] d\epsilon, \quad (5-2)$$

where  $\epsilon = E/E_c$  and  $\epsilon_i = E_i/E_c$ .

$E_i$  represents the value of  $E$  at which surface ionization occurs. The atom experiences this electric field at the minimum

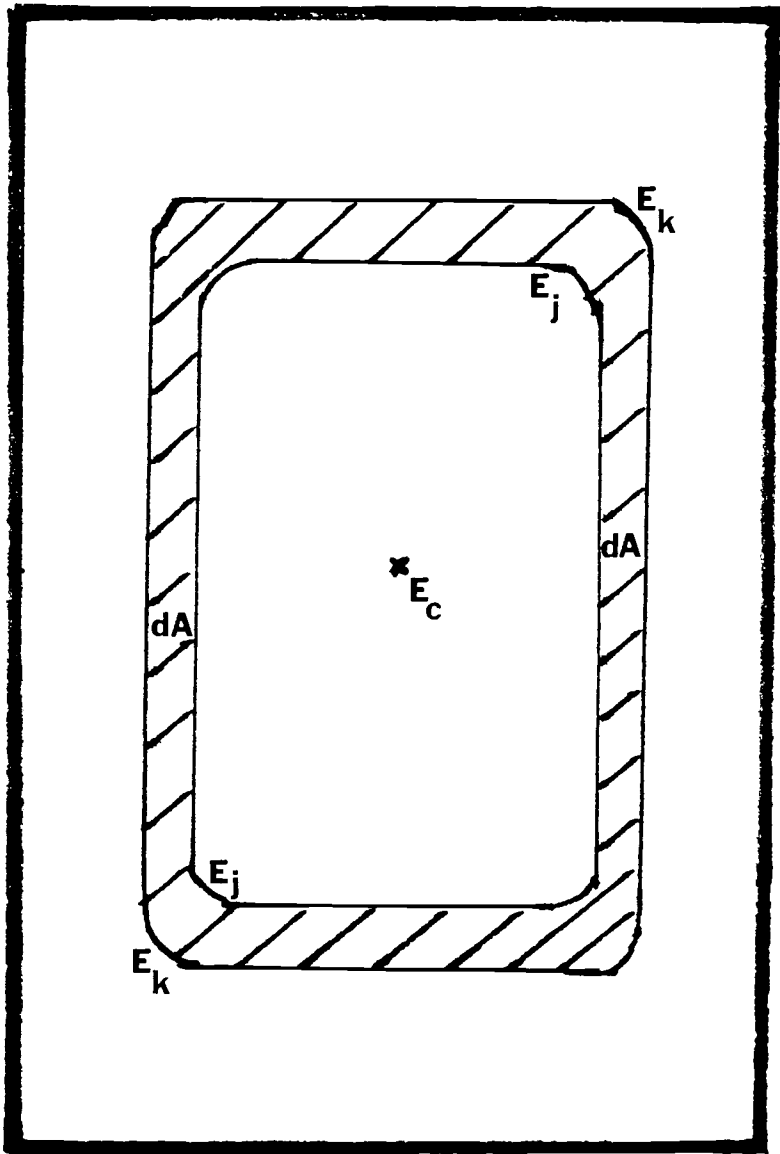


Fig. 5-3 Differential Area  $dA$  within a Mesh Opening

mesh-surface to atom distance at which the atom may survive. Surface ionization limits the maximum effective open area to a value  $A_{\max} = (b - \delta)^2$ , which is less than the geometric open area  $b^2$ . The transmission of the mesh must be less than 0.25. A characteristic orbit radius  $\delta$  is given by Fabre et al. as  $\delta \approx 4n^2 a_0$ .<sup>8</sup> The maximum transmission, for a typical  $n$ , with surface-ionization included becomes  $T_{\max} = 0.25 - \delta/b$ . A typical state has  $n = 35$ , so  $\delta \approx 3 \times 10^{-5}$  cm and  $\delta/b \approx 0.05$ , giving  $T_{\max} \approx 0.20$ , which is in good agreement with values experimentally measured.

The quantity  $\frac{d(A/b^2)}{d\varepsilon}$ , which appears in the integral in Eq. (5-2), is the normalized slope of the plot of the effective open area  $A$  vs  $\varepsilon$ , given in Fig. 5-1. The remaining factor in the integrand,  $P(\varepsilon E_c)$  is the normalized survival probability, the fraction of Rydberg atoms not field-ionized when the beam passes through a mesh opening.

Figure 5-4 shows  $T$  vs  $|\langle N\mu \rangle|$ , which is the result of the numerical integration of Eq. (5-2). The electric field magnitude  $|E|$  is related to  $|\langle N\mu \rangle|$  through field calculations for dipole moments on a plane with a square hole, as in Eq. (2-18). Integration is performed for values of the electric field from  $E_c$  to  $E_i$ . This procedure provides a value of  $T$  for each value of  $|\langle N\mu \rangle|$ . The method described here does not give specific information about the orientation of the adsorbates, only information about the concentration of dipole moments on the

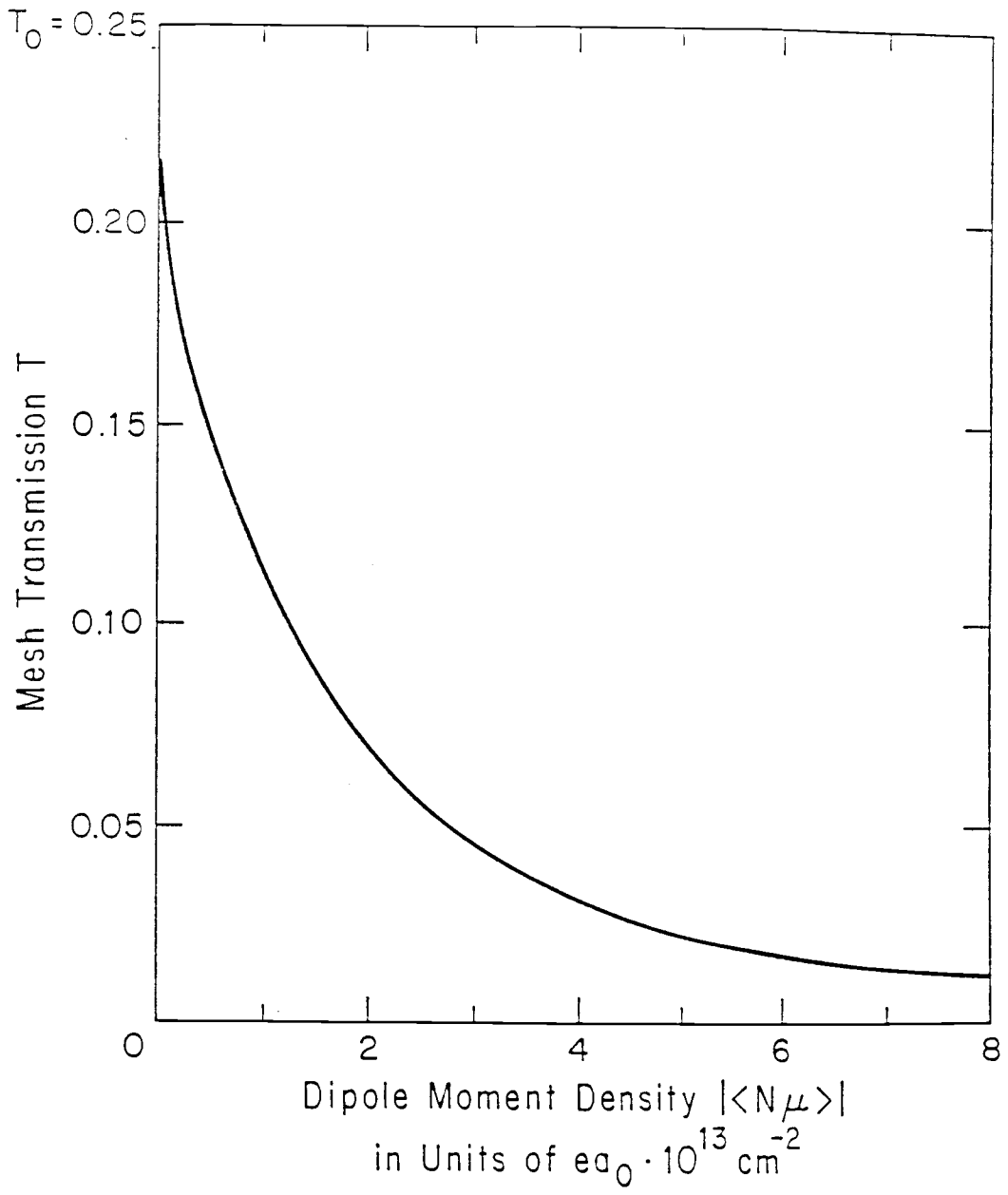


Fig. 5-4 Mesh Transmission vs Dipole-Moment Density

surface. Specific knowledge of the field-ionization process, n-state distribution in the beam, or the state dependence of detector response is not required.

The experimental calibration presented in Fig. 5-4 is used in Chapter 7 to interpret experimental data. The transmission data obtained from the experiment will be transformed via the derived relationship presented in Fig. 5-4.

The relationship between T and  $\langle N\mu \rangle$  derived here is used to transform the transmission into the dipole-moment density. Figures 5-5a and 5-5b show the dipole-moment density vs time derived from the transmission vs time data of Fig. 3-5. Figure 5-5a shows the absolute value of the dipole-moment density, and Fig. 5-5b shows the dipole-moment density, suggesting that the sign of  $\langle N\mu \rangle$  changes at the cusp.

## 5.2 Dipole-Moment Density with and without Introduced Adsorbate

Experiments were conducted with no introduced adsorbate. These experiments measured the dipole-moment density  $\langle N\mu \rangle_{\text{noGas}}$  without introduced adsorbate. This quantity is modeled as follows:

$$\langle N\mu \rangle_{\text{noGas}} = \frac{1}{A_s} \left[ \mu_w \theta_{wd} - \mu_L \theta_L - \mu_p \theta_p - \mu_w \theta_{ws} \right]. \quad (5-3)$$

Experiments were also conducted with an adsorbate introduced. Again the dipole-moment density  $\langle N\mu \rangle_a$  was measured vs time.

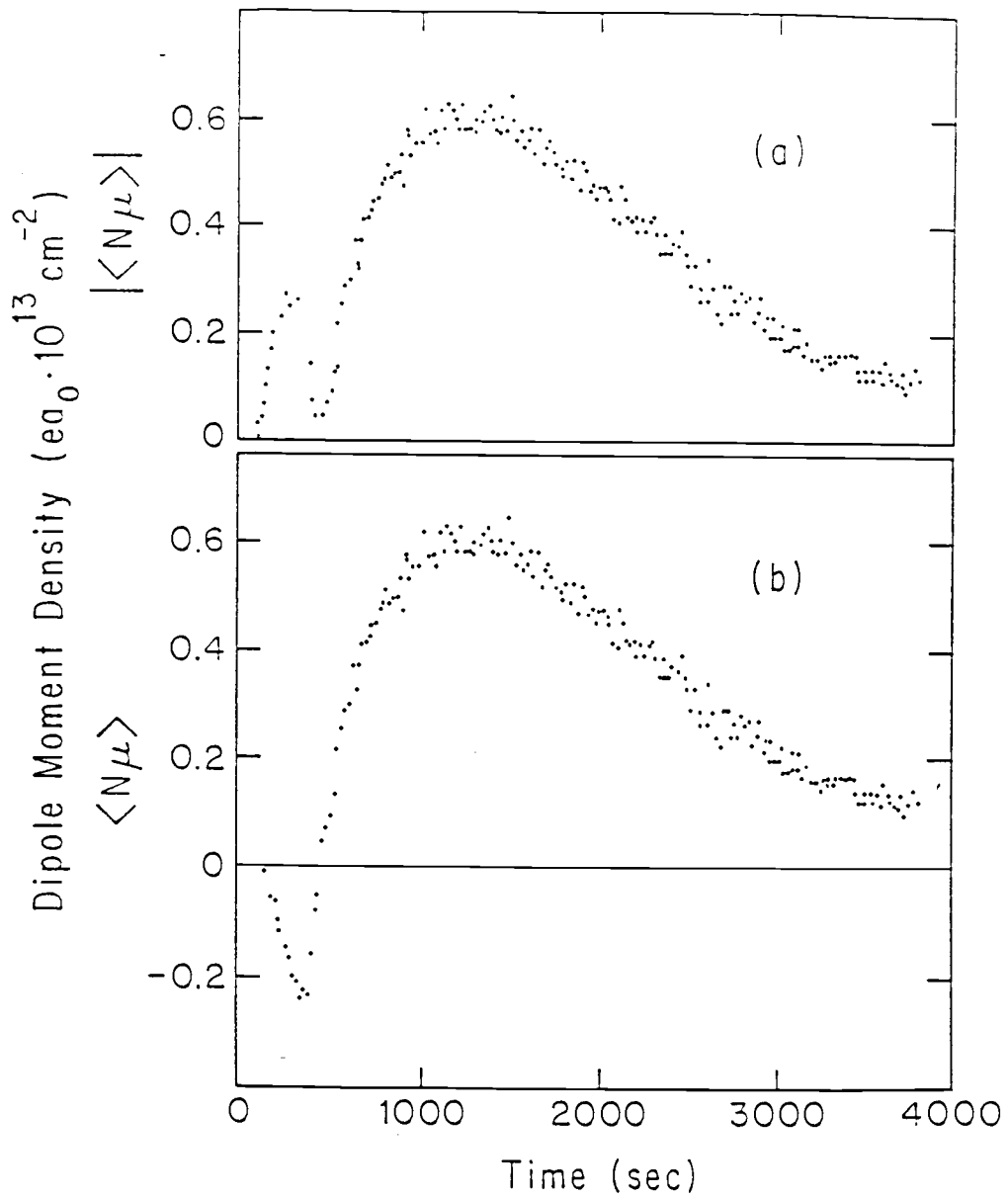


Fig. 5-5 Typical Experimental Data  
 (a)  $|\langle N\mu \rangle|$  vs  $t$       (b)  $\langle N\mu \rangle$  vs  $t$

$$\langle N\mu \rangle_a = - \frac{1}{A_s} \left[ \mu_w \theta_{wd} + \mu_a \theta_a - \mu_L \theta_L - \mu_p \theta_p - \mu_w \theta_{ws} \right]. \quad (5-4)$$

Equations (5-3) and (5-4) may be subtracted, revealing the effect on the dipole-moment density of the introduced adsorbate. The coverages on the source side of the mesh are unaffected by the introduction of the adsorbate, which is introduced onto the detector side. However, the H<sub>2</sub>O coverage on the detector side may be greatly altered with respect to the case with no introduced adsorbate.

### 5.2.1 Comparison of Densities with and without Introduced Adsorbate

The difference between the dipole-moment densities for the two situations is found from Eqs. (5-3) and (5-4):

$$\Delta |\langle N\mu \rangle| = |\langle N\mu \rangle|_{\text{noGas}} - |\langle N\mu \rangle|_a = - \frac{1}{A_s} \left[ \mu_w \theta_{wd, \text{noGas}} - \mu_w \theta_{wd} - \mu_a \theta_a \right] \quad (5-5)$$

The coverage of water on the detector side with no introduced adsorbate present is found as before from Eq. (4-6) and the model of Sec. 4.1. The coverage of water and adsorbate are found from the following time dependent equations. All the coverages must add to unity on the detector side.

$$\dot{\theta}_{Au} = - \theta_{Au} (s_w c_w + s_a c_a) \quad (5-6)$$

$$\dot{\theta}_a = s_a c_a \theta_{Au} \quad (5-7)$$

$$\dot{\theta}_w = s_w c_w \theta_{Au} \quad (5-8)$$

These equations are solved simultaneously to determine  $\theta_a$  and  $\theta_w$ .

$\Delta\langle N\mu \rangle$  is given by

$$\Delta\langle N\mu \rangle = \frac{\mu_w}{A_s} (1 - e^{-s_w c t}) - \frac{\mu_w}{A_s} \left( \frac{s_w c}{s_w c + s_a c} \right) (1 - e^{-(s_w c + s_a c)t}) - \frac{\mu_a}{A_s} \left( \frac{s_a c}{s_w c + s_a c} \right) (1 - e^{-(s_w c + s_a c)t}) \quad (5-9)$$

There are several situations that may exist depending upon the choice of introduced adsorbate, particle current, and sticking probability. These will now be considered and used in Chapter 7.

If the particle current of the residual gas ( $H_2O$ ) is large compared to the introduced adsorbate particle current, then  $s_w c \gg s_a c$ . For this case, Eq. (5-9) simplifies to

$$\Delta\langle N\mu \rangle = - \frac{\mu_a}{A_s} \left( \frac{s_a c}{s_w c} \right) (1 - e^{-s_w c t}). \quad (5-10)$$

A further simplification results if the additional constraint that the exposure time  $t$  is much less than  $s_w c$ , so that  $s_w c t \ll 1$ . Then

$$\Delta\langle N\mu \rangle \cong - \frac{\mu_a s_w c t}{2A_s}. \quad (5-11)$$

However, if Eq. (5-9) is simplified with the additional constraint that  $s_w c t \gg 1$ , then the dipole-moment density difference becomes

$$\Delta\langle N\mu \rangle \cong - \frac{\mu_a s_w c}{A_s s_w c}. \quad (5-12)$$

Therefore, for long times the difference  $\Delta\langle N\mu \rangle$  is simply a

constant.

If the residual gas particle current is small compared to the introduced adsorbate particle current, then  $s_w c_w \ll s_a c_a$ . If the exposure time satisfies  $t \gg 1/s_a c_a$  then Eq. (5-9) becomes

$$\Delta\langle N\mu \rangle = -\frac{\mu_w}{A_s}(1 - e^{-(s_w c_w)t}) - \frac{\mu_w s_w c_w}{A s_a c_a} - \frac{\mu_a}{A_s}. \quad (5-13)$$

If  $t \gg 1/s_w c_w$  and  $t \gg 1/s_a c_a$ , then Eq. (5-13) becomes

$$\Delta\langle N\mu \rangle \cong \frac{\mu_w - \mu_a}{A_s}. \quad (5-14)$$

However, if the constraints  $t \ll 1/s_w c_w$  and  $t \ll 1/s_a c_a$  are applicable then Eq. (5-9) becomes

$$\Delta\langle N\mu \rangle \cong -\frac{\mu_a s_a c_a t}{2A_s}. \quad (5-15)$$

If the condition  $(s_a c_a + s_w c_w)t \gg 1$  is met then Eq. (5-9) is

$$\Delta\langle N\mu \rangle = \frac{\mu_w}{A_s}(1 - e^{-s_w c_w t}) - \frac{\mu_w}{A_s} \left( \frac{s_w c_w}{s_w c_w + s_a c_a} \right) - \frac{\mu_a}{A_s} \left( \frac{s_a c_a}{s_w c_w + s_a c_a} \right). \quad (5-16)$$

If the condition  $(s_a c_a + s_w c_w)t \ll 1$  applies, then Eq. (5-9) is

$$\Delta\langle N\mu \rangle = \frac{\mu_w}{A_s} - \frac{\mu_w s_w c_w}{A_s} - \frac{\mu_a s_a c_a}{A_s}. \quad (5-17)$$

If water vapor is the introduced adsorbate, then an interesting simplification occurs in which the subscript a is chosen to be  $w_a$ . In this case  $\Delta\langle N\mu \rangle$  in Eq. (5-9) may be written

$$\Delta\langle N\mu \rangle = \frac{\mu_w}{A_s} \left( e^{-s_w c_w t} - e^{-s_w(c_w + c_{w_a})t} \right), \quad (5-18)$$

where  $c_{w_a}$  is the particle current due to the introduced adsorbate  $H_2O$ . The experimentally measured transmission is converted to a

dipole-moment density via the calibration shown in Fig. 5-4.

### 5.2.2 Changes Occurring When $s_a c_a \gg s_w c_w$

The case where  $s_a c_a$  is much greater than  $s_w c_w$  may be analyzed by assuming that the change  $\Delta\langle N\mu \rangle$  is due only to the introduced adsorbate and that the transmission would without the introduced adsorbate remain constant for the time period of interest. For these assumptions the differential equation governing the introduced adsorbate coverage is

$$\dot{\theta}_a = s_a c_a (K - \theta_a) \quad , \quad (5-19)$$

where  $K$  is the relative coverage of metal surface sites and previously adsorbed particles ( $K \leq 1$ ). Also the value of  $K$  can account for the case when the maximum coverage of introduced adsorbate on a surface is less than unity. Interesting examples of  $s_a c_a \gg s_w c_w$  occur for CO on Ni and  $O_2$  on Ni. For CO on Ni the maximum coverage is  $\theta \cong 0.5$ <sup>34</sup> and for  $O_2$  on Ni is  $\theta \cong 0.3$ .<sup>35</sup>

The solution of Eq. (5-19) for  $\theta_a$  is

$$\theta_a(t) = K (1 - e^{-s_a c_a t}) \quad . \quad (5-20)$$

Therefore,  $\Delta\langle N\mu \rangle$  may be written

$$\Delta\langle N\mu \rangle = \frac{\mu_a}{A_s} (1 - e^{-s_a c_a t}) \quad . \quad (5-21)$$

And if  $s_a c_a t \gg 1$ , then Eq.(5-21) becomes

$$\Delta\langle N\mu \rangle = \frac{\mu_a}{A_s} \quad . \quad (5-22)$$

Sections 5.2.1 and 5.2.2 have ignored desorption, which in

general should not be neglected. However, when the desorption energy is greater than 0.80 eV, the residence time for a molecule ( the inverse of the desorption rate ) is of order 1000 s or greater. This time is long compared to the duration of any experiment reported in Chapters 6 and 7. Desorption energies of molecules used are all greater than or equal to 0.80 eV, except for  $O_2$  on Ni. For the case of  $O_2$  on Ni the duration of the experiment requiring results from Secs. 5.2.1 and 5.2.2 was kept short compared to the residence time,  $1/\Gamma$ .

### 5.2.3 Transmission Changes after Equilibrium is Reached

If the adsorption of the introduced adsorbate occurs quickly (i.e., if  $1/s_a c_a$ , the monolayer time, is short compared to the time for data to be accumulated in a few channels) and  $1/s_a c_a$  is much shorter than the monolayer time for  $H_2O$  on the mesh, then the introduced adsorbate may be considered to have reached equilibrium, with  $\theta_a = \text{constant}$ . Coverage of adsorbate gases may then predicted with Eq. (4-17) and the model of Sec. 4.2. The change in the dipole-moment density  $\Delta|<N\mu>|$  becomes

$$\Delta|<N\mu>| = \frac{\mu_a s_a c_a}{A_s \Gamma} \quad (5-23)$$

The results in Secs. 5.2.1, 5.2.2 and 5.2.3 are used in Chapter 7 in the calculation of desorption energies, sticking probabilities and dipole moments.

## CHAPTER 6: EXPERIMENTAL PROCEDURES AND OBSERVATIONS

## 6.1 Procedures

Preparation of the mesh surface contributes significantly to the results obtained from this work. The mesh sample, either Ni or Au, is taken from a sheet supplied by the Buckbee Mears Co. The dimensions are nominally 2000 lines/inch. The dimensions were measured with a SEM (Scanning Electron Microscope) to be a strand width of  $6.5 \mu\text{m}$  and a strand separation of  $6.5 \mu\text{m}$ . The mesh thickness was measured to be  $2 \mu\text{m}$ . A  $5 \text{ cm} \times 2 \text{ cm}$  section of mesh is cut to fit into the clamps on the mount.

The mesh is ultrasonically cleaned in successive alternating baths of acetone and methanol. This cleaning removes oils and other surface contaminants. A final rinse of the mesh is in ethanol. Meshes are secured to the mount by copper clamps (see Fig. 3-2). After installation of the mesh, the system is pumped to  $\lesssim 10^{-7}$  Torr and brought to operational conditions.

After the atomic beam is started the mesh is exposed to the beam for the first time. The transmission of a newly installed mesh sample not yet heated is much less than the maximum expected transmission of approximately 0.20 discussed in Sec. 5.1. Figure 6-1a shows the transmission through an unheated Au mesh, and Fig. 6-1b shows the transmission through an unheated Ni mesh. These measurements indicate the presence of undesirable adsorbates on the surface.

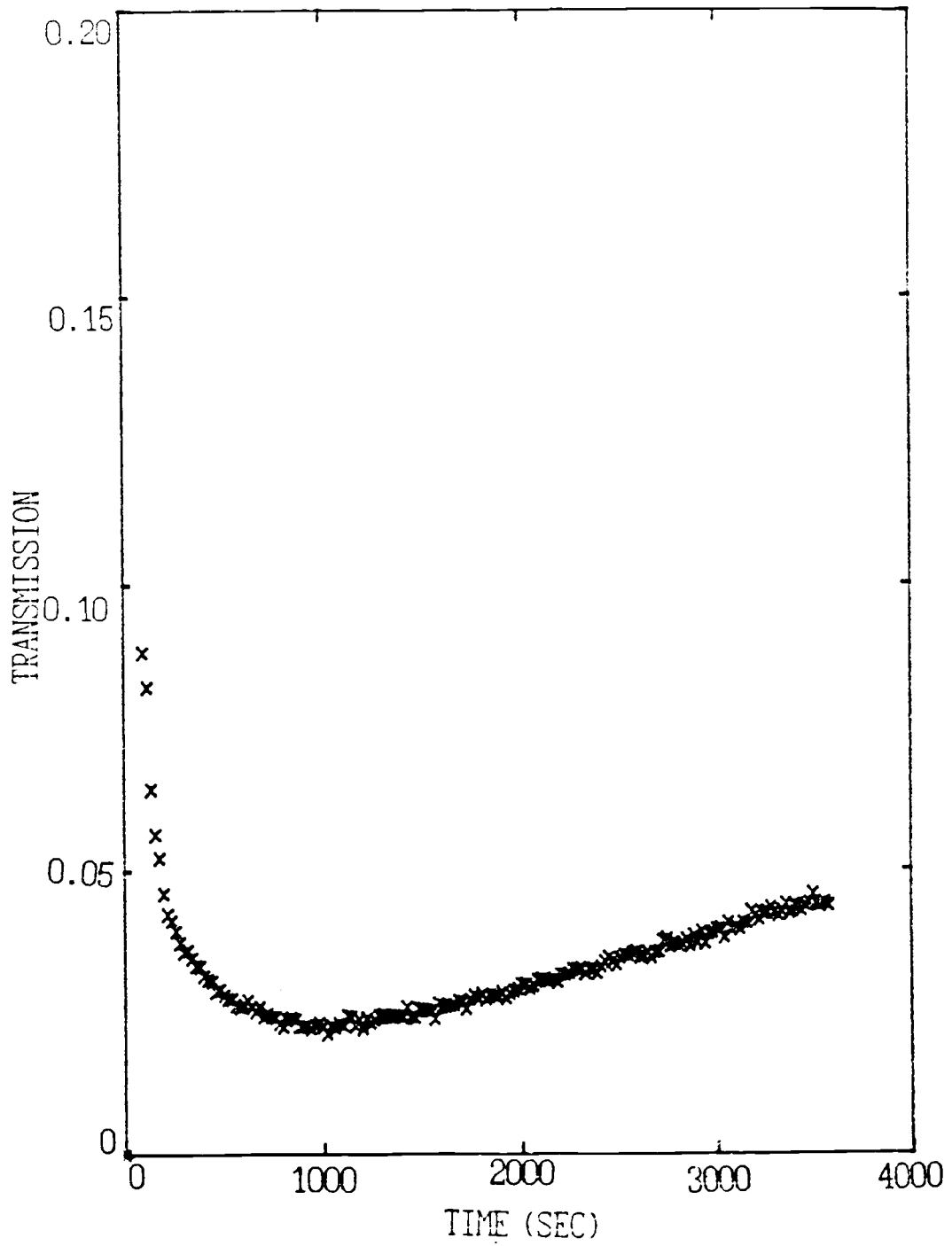


Fig. 6-1a Au Mesh Transmission Prior to Heating

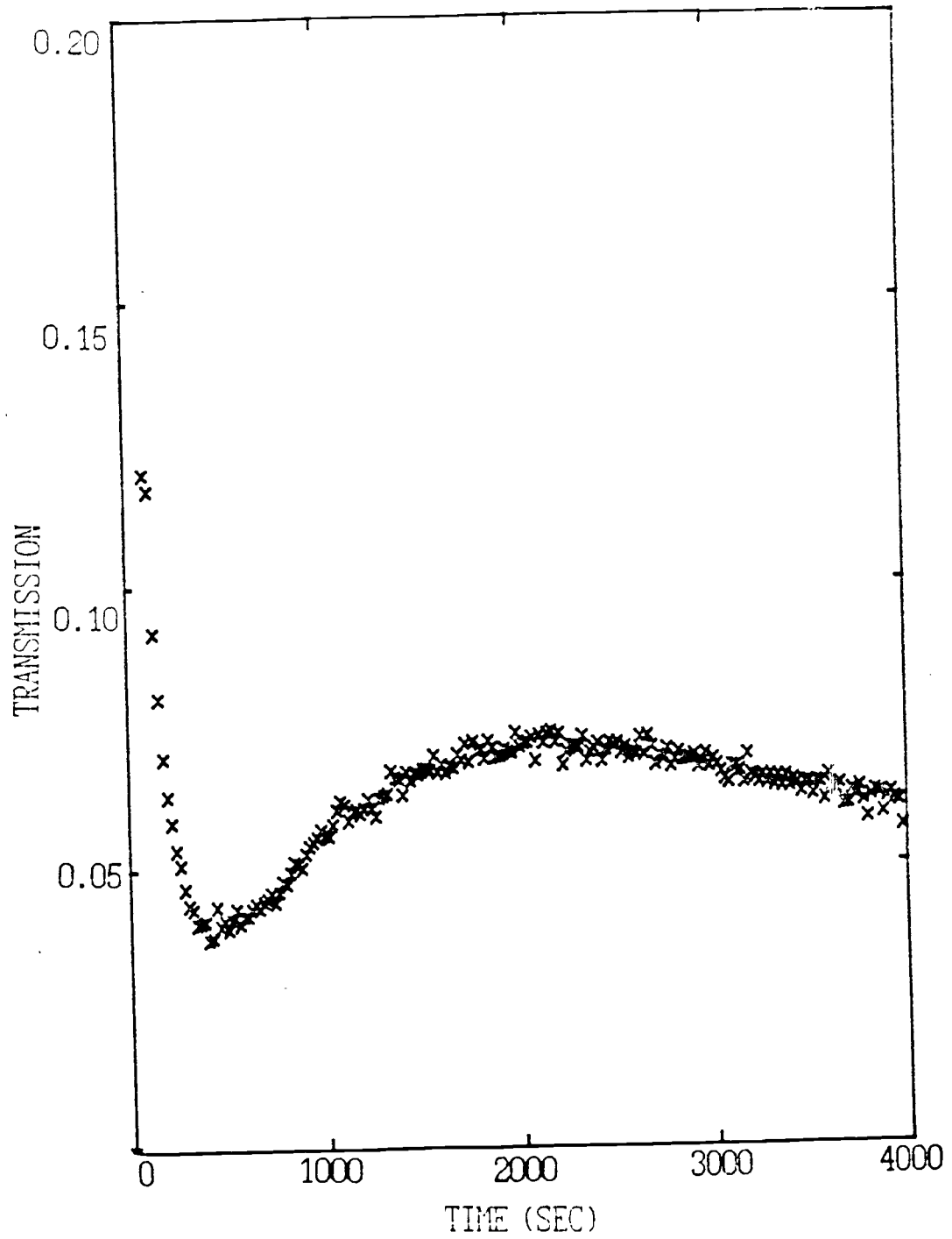


Fig. 6-1b Ni Mesh Transmission Prior to Heating

### 6.1.1 Treatment of the Mesh

The mesh is resistively heated with a current of 3 to 5 amps; the lower values are used for the Ni mesh which has a lower thermal conductivity and therefore, becomes hotter at the center. Heating brings the mesh to a temperature between 700°C and 800°C removing contaminants from the surface, particularly H, O, and H<sub>2</sub>O. Some annealing of the surface may occur: there may be some observable crystal growth seen in Fig. 3-3 as compared to micrographs of new mesh samples taken by Taylor.<sup>2</sup> The heating cleans the surface, yielding a maximum transmission,  $T_{\max} \cong 0.20$ .

Reproducible transmissions are obtained after approximately 4 h of exposure to the Li beam in combination with several heating-cleaning cycles performed during this time. This exposure time assumed to be the time required to form a permanent layer of a Li-complex on the source side of the mesh. When thoroughly degassed, the mesh samples are exposed to the beam and adsorbates during a standard sequence of steps in an experimental run of 200 computer memory channels with a dwell time typically 10 s or 20 s per channel.

A typical experimental run includes the following steps:

- 1) Heating of the surface to approximately 800°C to remove undesired adsorbates, particularly H<sub>2</sub>O. This degassing or cleaning of the mesh for 90 sec to 5 min is more complete than that reported in the preliminary work by C.A. Kocher and C.R. Taylor.<sup>1</sup> Counts are recorded without the mesh in the initial

channels of the bank. The initial data channels are used for normalization and to check beam stability.

2) The mesh sample is inserted into the beam and the mesh heating current is reduced to the desired level to be used for the run: this current was reduced to zero in most runs.

3) The mesh is exposed to an adsorbate, if introduced, in addition to the background gas. Counts are recorded in the computer memory during this time.

4) A number of scenarios are possible after step 3. For example, the introduced adsorbate may be changed or alternately gated off and on. Also variable during the course of a single run or between runs are the mesh surface temperature, introduced adsorbate exposure pressure, gas species and Li exposure. Data may be gathered up to channel 190.

5) Finally the mesh is removed from the beam and counts are recorded in the final channels of the bank, to be compared with the initial channels for normalization.

#### 6.1.2 Mesh Temperature Control and Heating

The temperature of the mesh is controlled and measured by several means. The mesh is heated by passing an electric current through the mesh. Heating current is brought to the mesh by copper wires attached through a vacuum flange; feedthroughs are connected to a power supply outside the vacuum system. Mesh cooling is accomplished by means of a LN<sub>2</sub> coldfinger attached

directly to the mesh by a copper braid. The mesh may also be cooled more slowly by allowing the heat simply to diffuse through the insulating posts to the mount.

Measurement of the mesh temperature is made with chromel-alumel thermocouples attached at one end of each mesh. This type of thermocouple gives a 1 mV potential difference per 25°C change between the reference (room temperature,  $T \cong 293$  K) and the location where the thermocouple is attached.

During the application of the heating current the temperature of the mesh in the region exposed to the beam is greater than at the place where the thermocouple is attached. A calculation to estimate the temperature of the mesh at each point along the mesh, between the mesh clamps, was done by C.R. Taylor.<sup>2</sup> This calculation relates heating current to the mesh surface temperature, taking into account energy input from current, energy conducted away through the mount, and energy radiated away from the mesh. The calculation from Taylor's thesis is the method used to estimate the temperature of the mesh in the region exposed to the beam, while the mesh is being heated. When the mesh is cooled by the coldfinger, the thermocouple measures the mesh temperature directly.

Conduction of current through the mesh causes an increase in the mesh temperature. These changes occur quickly as compared to the sampling time per channel in this experiment, typically 20 s. A simple heat-flow calculation (see Appendix A) shows that the

time constant or characteristic cooling time is 3.3 s for the Ni mesh and is 7.3 s for the Au mesh.

## 6.2 Observations

Adsorption onto the Au and Ni surfaces has been investigated for several experimental conditions and various introduced adsorbates. Observations that have been made are presented in this section. A brief description accompanies each observation. The analysis of the data, with calculation and interpretation, is completed in Chapter 7.

Experimental work of C.R. Taylor<sup>1,2</sup> includes an explanation of the variation of transmission  $T$  through the mesh vs time  $t$ . The time-dependent variation of the transmission was attributed to the change in electric field near the mesh surface due to adsorption of  $H_2O$  onto the front and back of the mesh.  $H_2O$  in the system contributed significantly to the transmission observed in the following data.

### 6.2.1 Au Mesh

A typical experimental run with no introduced adsorbate is presented in Fig. 6-2. Only  $H_2O$  from the background gas and Li from the atomic beam adsorb on the unheated Au mesh in this transmission sequence. The transmission vs time sequence is characterized by a transmission decrease, increase to a cusp, a

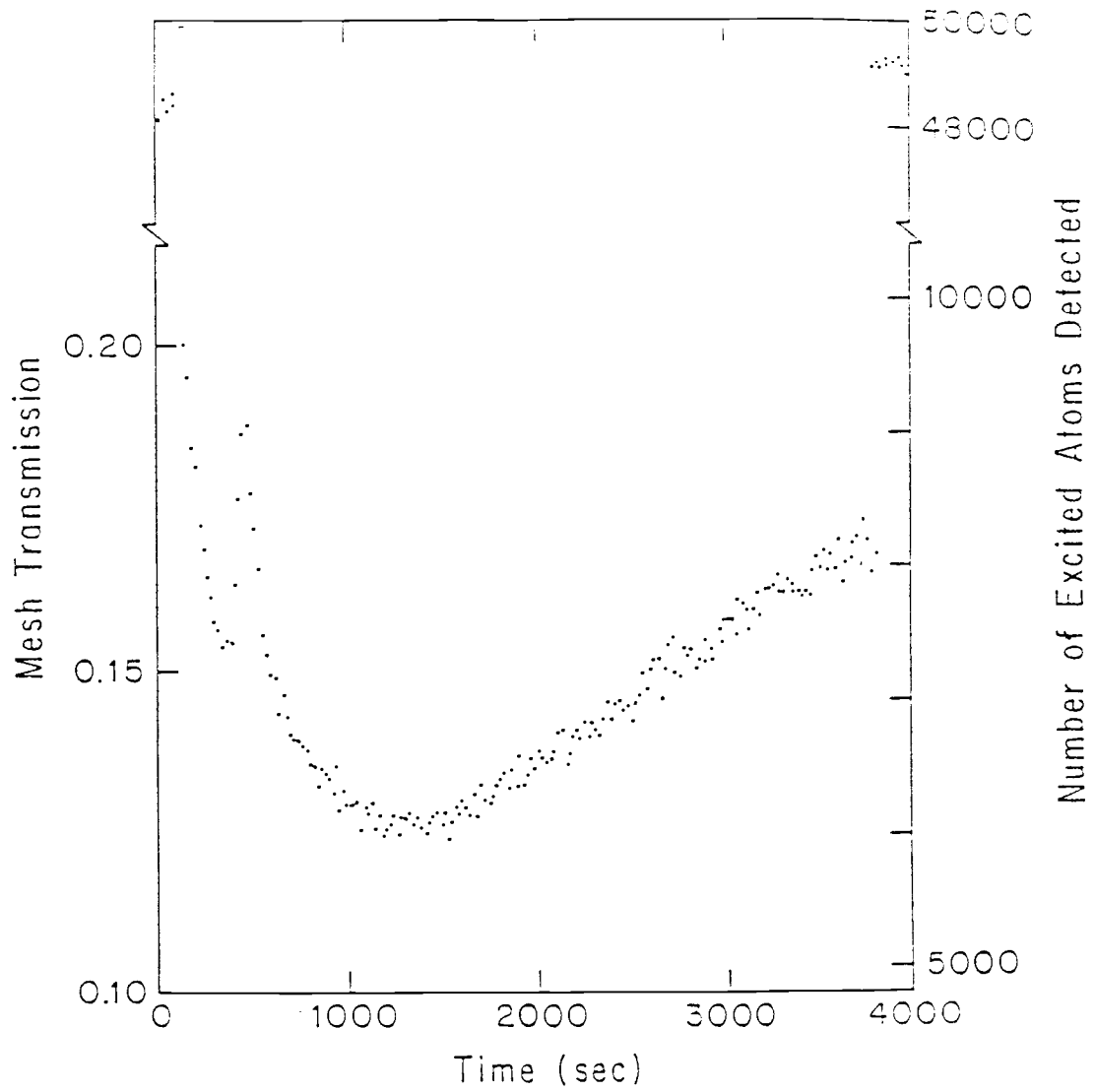


Fig. 6-2 Typical Transmission Sequence for Au Mesh

second decrease, and then a final increase. The transmission sequence is repeatable; the cusp and second dip were not seen by Taylor.<sup>1,2</sup> The vertical axis represents the number of counts recorded per 20-sec channel (right) or transmission through the mesh (left). The horizontal axis shows elapsed time in seconds. The points recorded at the beginning and end of each bank test for stability of the beam. Since the normalization is stable to within 1% - 3%, the normalization channels are omitted in the following figures.

Data in Fig. 6-2 were taken when the incidence time for  $H_2$  on an Au surface site was  $\tau_w \cong 60$  s. The incidence time for Li was  $\tau_L \cong 250$  s. The transmission  $T$  begins at 0.20 immediately after the heating current is reduced to zero.  $T$  then falls to an initial minimum of 0.15 at  $t = 300$  s and then rises to a sharp cusp at  $t = 400$  s.  $T$  falls less rapidly to a second minimum at  $t \cong 1200$  s.  $T$  finally rises a second time and may approach a constant value after  $t \approx 4000$  s. This double-dip sequence is reproducible having been observed in the case of Au in more than 100 experiments.

In previous work published by G. E. McCown et al.<sup>36</sup> it was shown that the transmission event sequence is initiated by the cessation of heating current to the mesh. Initiation of the transmission event is not due to the exposure of the mesh to the Li beam. Adsorption begins after the heating current is reduced to the desired experimental level, adsorption begins to occur in

the following way. As seen in Sec. 3.2 the timing of the primary and secondary dips is dependent upon the incidence times of  $\tau_w$  and  $\tau_L$  for  $H_2O$  and Li, respectively. The first dip is greatly modified when the  $H_2O$  incidence time is varied as seen in Fig. 4-1. The secondary dip is greatly modified when the oven temperature (or Li incidence time) is varied as seen in Fig. 4-3.

An interpretation of the transmission sequence can be proposed, based on the knowledge gained from the experiments presented in Sec. 3.2 and the model presented in Chapter 4. The transmission initially decreases due to the adsorption of  $H_2O$  onto the source side. It is reasonable to presume that the sticking probability for  $H_2O$  on the permanent layer, source side, is greater than that for  $H_2O$  on the detector side. The permanent layer (defined in Sec. 4-1) may result from the chemical bonding on the surface between Li and  $H_2O$ . Accumulation of  $H_2O$  on the source side is probably limited to less than a monolayer because of the accumulation of Li and the permanent layer. Therefore, the adsorption of  $H_2O$  on the detector side begins to reduce the net-dipole-moment produced by the  $H_2O$  on the source side. This adsorption causes an increase in the transmission.

Transmission continues to increase until the net dipole-moment density  $|\langle N\mu \rangle|$  on the detector side equals  $|\langle N\mu \rangle|$  on the source side. When the  $\langle N\mu \rangle$  magnitudes are equal on both sides the electric fields produced from the two mesh surfaces tend to cancel. The cusp in the data is the result of this field

cancellation. The  $\text{H}_2\text{O}$  coverage continues to increase more rapidly on the detector side than on the source side, resulting in a decrease in the transmission  $T$ . Finally, as the  $\text{H}_2\text{O}$  coverage increases toward a monolayer on the detector side, the dipole-moment density decreases as a function of coverage. The decrease in dipole moment  $\mu$  vs coverage  $\theta$  results in the final increase in the transmission. This effect is explained in the following paragraph.

In general, surface dipole moments decrease monotonically with increasing coverage. The model developed in Chapter 4 incorporated a dipole moment with a Lorentzian form to represent this effect: 
$$\mu(\theta) = \frac{\mu_0}{1 + \beta\theta^2},$$
 where  $\beta$  and  $\mu_0$  are adsorbate-species-dependent constants. The form for  $\mu(\theta)$  corresponds to the experimental data obtained by Gerlach and Rhodin<sup>13</sup> and Muscat and Batra.<sup>37</sup> A similar coverage dependence of  $\mu$  results from adsorbate polarizability calculations based on a Topping field determination at each adsorption site.<sup>17,18</sup>

### 6.2.2 Ni Mesh

A typical experimental run is shown in Fig. 6-3 for a Ni mesh with no introduced adsorbate. Figure 6-3 shows a time-dependent behavior similar to that of Fig. 6-2 for the Au mesh, with the exception that a final increase in  $T$  is not observed during the 4000 s scan. Experimental conditions for this scan were  $\tau_w = 100$  sec and  $\tau_L = 300$  sec.

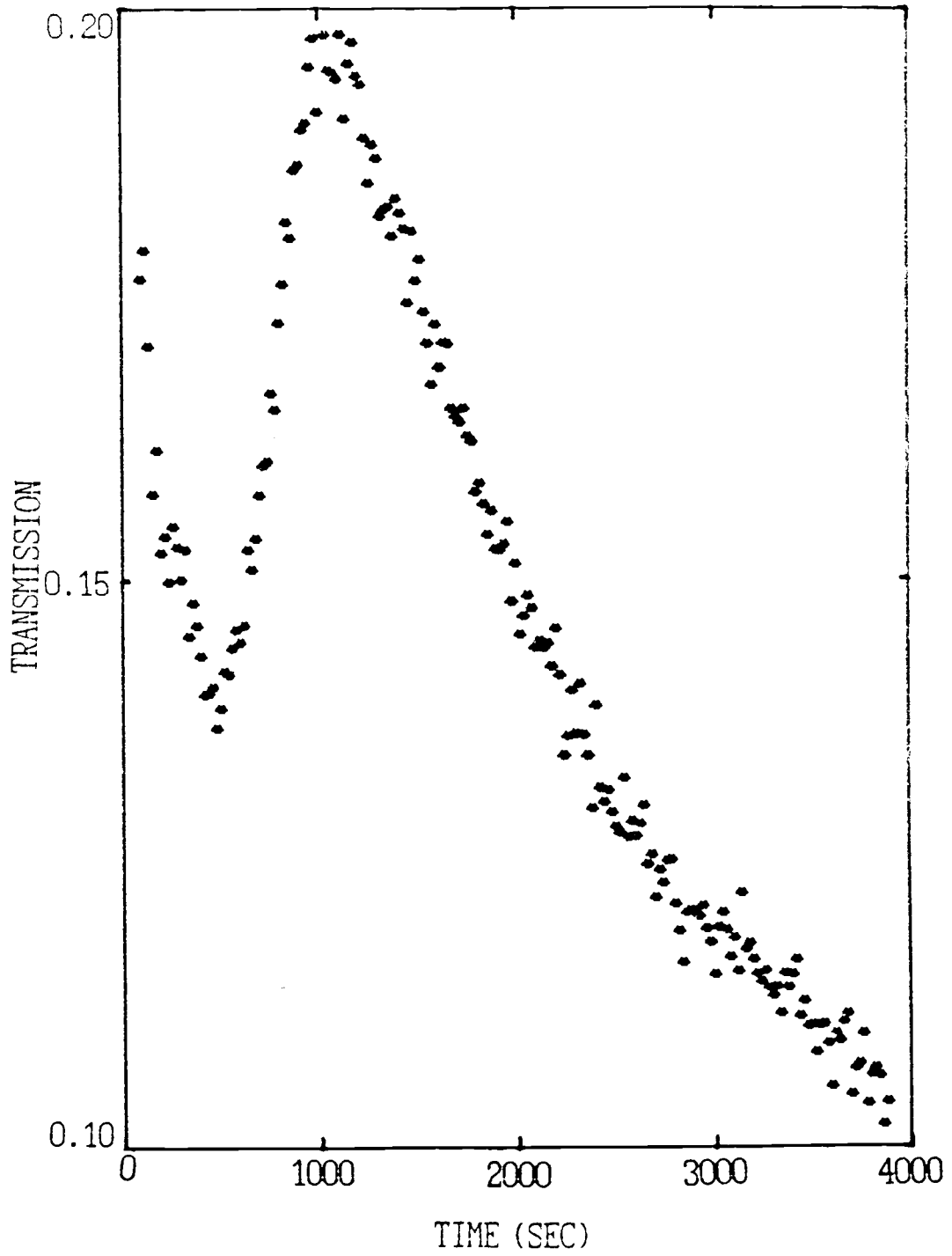


Fig. 6-3 Typical Transmission Sequence for Ni Mesh

Significant variations in the transmission occur when the  $H_2O$  and Li particle currents and Ni surface temperature are varied. The initial dip-rise sequence may vary greatly in duration depending upon these experimental conditions. For example, the  $H_2O$  particle current may be large enough to cause the initial dip-rise to be no longer observable.  $H_2O$  is believed to be the major contribution to the dipole-moment density on the detector side. The transmission sequence then is simply a fall to a minimum and a slow rise for the duration of the scan. If the scan duration were longer, a final increase in T might be observed as in Fig. 6-2.

### 6.3 Externally Introduced Adsorbate Gases

The experiments with the Ni mesh were undertaken for two reasons. First, a large body of literature exists for adsorbates on a Ni surface. The majority of this work is for single crystal faces. Since there is literature available, the results obtained with the experimental technique in this work may be compared to results from other work. Secondly, most molecules adsorb more readily to Ni (  $s$  is larger ) than to Au.

In this section, data with identical figure numbers were taken on the same day with similar experimental conditions. The experimental conditions differ between days in that the Li and background  $H_2O$  particle currents may vary. These variations may lead to variations in the measured transmission. For this reason

data without introduced adsorbates are shown for each set of data with introduced adsorbate.

### 6.3.1 CO Adsorption on Ni

#### 6.3.1.1 CO Gated

Figure 6-4 shows the variation of the transmission with respect to time as the CO particle current is alternately turned on and off. The particle currents are  $c_1 = 0.077$  /s,  $c_2 = 0.143$  /s,  $c_3 = 0.152$  /s and  $c_4 = c_5 = 0.170$  /s . The noticeable change in transmission is seen in the later part of the transmission sequence of Fig. 6-4 when CO is introduced (e.g.,  $c_3$ ,  $c_4$ , and  $c_5$ ). Without CO the transmission is nearly 19%, and when the CO is introduced the transmission falls rapidly to between 16.5% and 17%. When the CO source is turned off, the transmission returns quickly to a higher value.

The CO molecules were introduced twice (e.g.,  $c_1$  and  $c_2$ ) during the initial transmission fall and rise. However, the presence of CO on the surface did not significantly alter the transmission sequence during the initial decline. This behavior may occur because the slope of the dipole-moment density vs transmission curve is greater at lower densities and smaller at higher densities. That is,  $\Delta T / \Delta N\mu$  is 20% transmission per  $ea_0 \times 10^{13}/\text{cm}^2$  near zero coverage and 5% transmission per  $ea_0 \times 10^{13}/\text{cm}^2$  at coverages that result in transmissions of 12%.

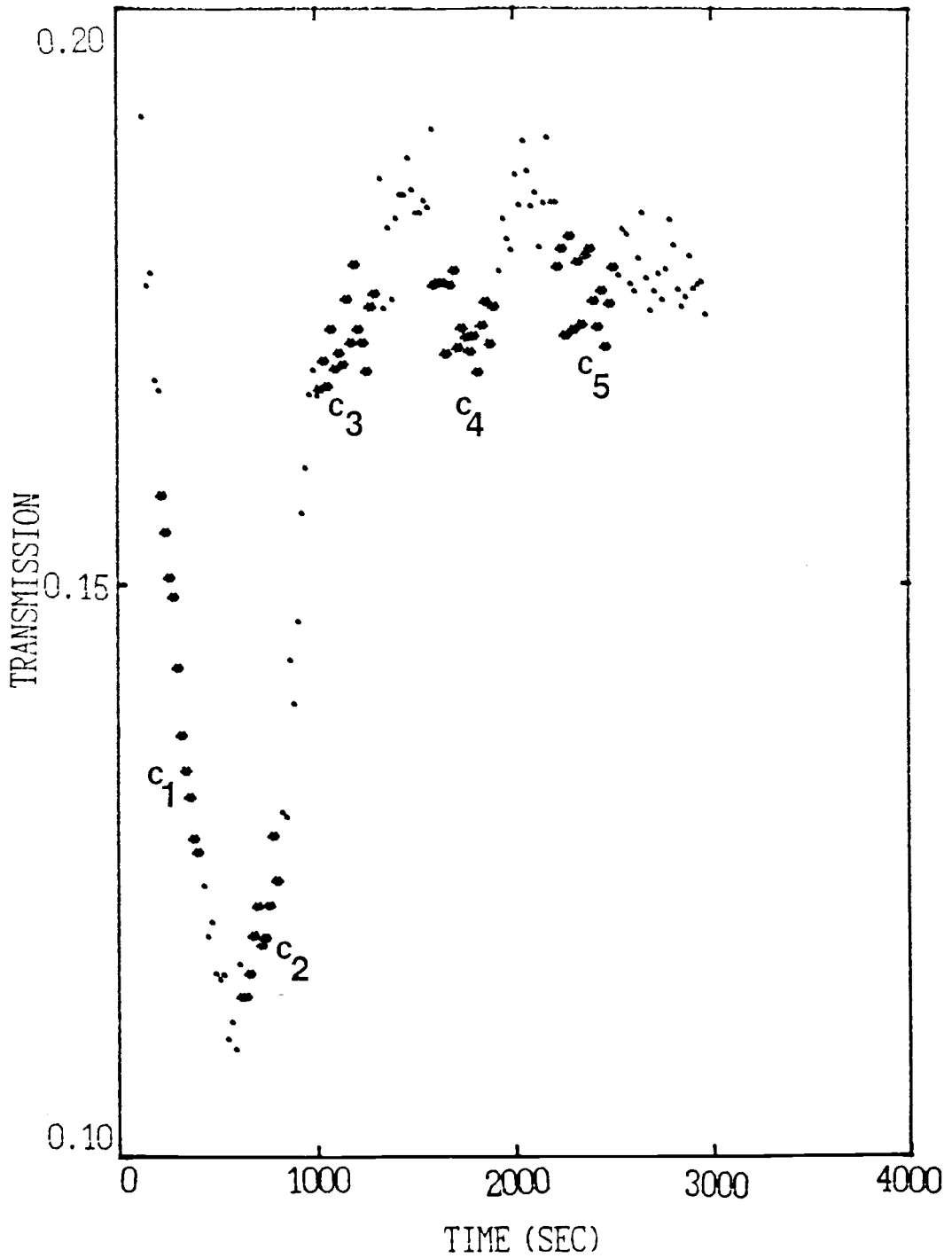


Fig. 6-4 CO on Ni with CO Gated

$$c_1=0.077/s \quad c_2=0.143/s \quad c_3=0.152/s \quad c_4=c_5=0.017/s$$

Therefore, adsorption which occurs at low dipole moment densities will be much more noticeable than adsorption occurring at large densities.

#### 6.3.1.2 CO Introduced Continuously

Figure 6-5 shows the effect on the transmission when CO is introduced continuously onto the detector-side of the mesh. The curve with dots (•) corresponds to no CO incident on the surface, whereas the curve with stars (\*) corresponds to a CO incidence time of  $\tau = 55.9$  s. The surface temperature of the mesh is  $T_s \cong 300$  K.

The important observations are:

a) The transmission with CO has a shallower dip,  $T_{CO} \cong 12.5\%$  vs  $T_{NoGas} \cong 11.0\%$ .

b) The presence of CO on the Ni surface causes a more rapid return to a high transmission: after 640 s with CO as compared to 800 s without CO.

c) The transmission minimum occurs earlier when CO is present -- 340 s after the heating current is removed with CO as compared to 400 s when no CO is introduced.

d) It is seen from the data in Fig. 6-5 that the presence of CO increases the transmission in the initial fall and rise. However, it is seen from Fig. 6-4 that CO reduces the transmission after it has returned to a value near maximum. The data in Fig. 6-4 after the transmission returns to a value near

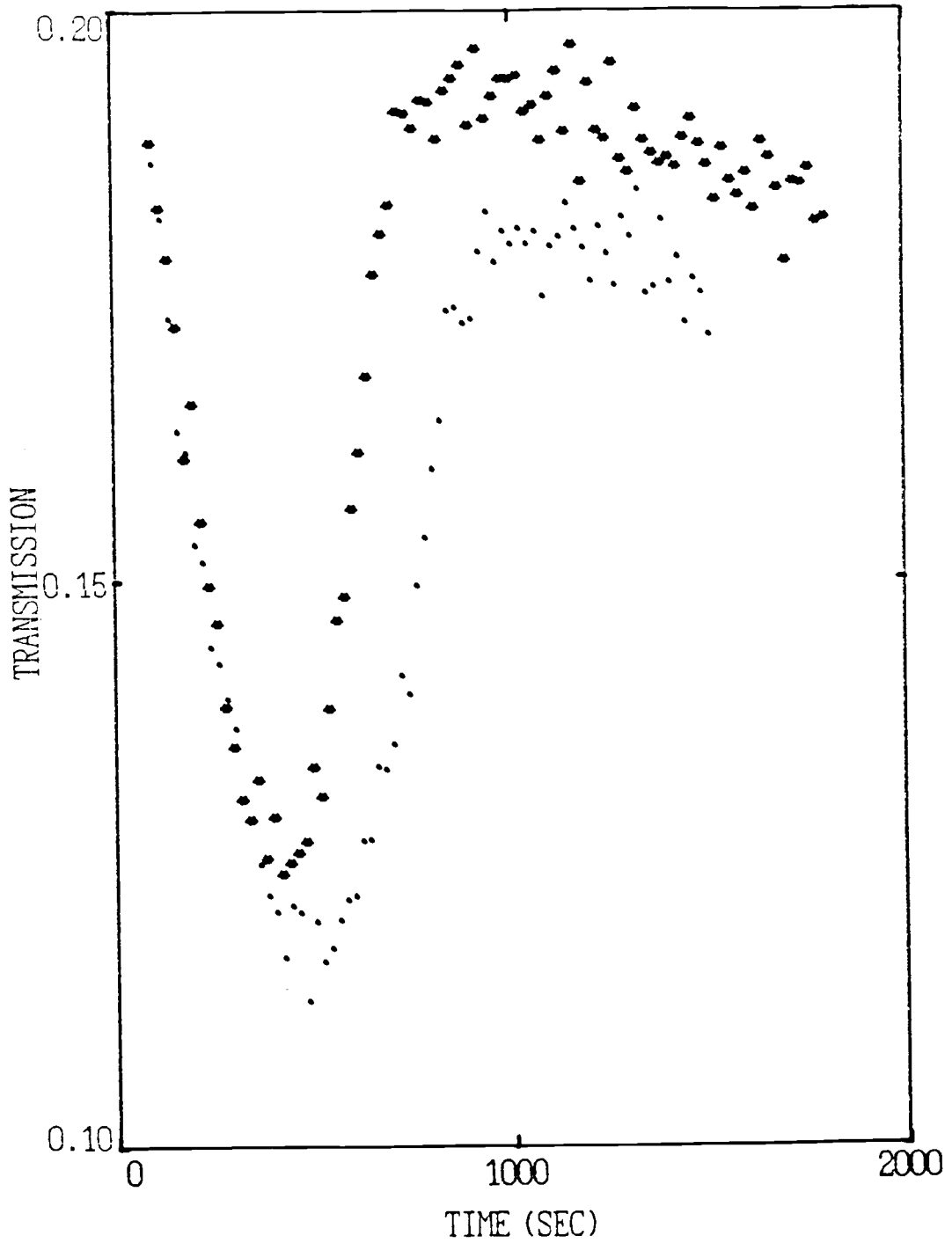


Fig. 6-5 CO on Ni

(\*) Constant CO:  $c=0.018/s$

(•) No Introduced Adsorbate

maximum yields no information about the orientation of the dipole moment. Since the addition of dipoles with either orientation will reduce the transmission when it is near maximum.

The data in Fig. 6-5 can be used to determine the sign of the dipole moment: the orientation of the dipole-moment vector  $\vec{\mu}$ , which is perpendicular to the Ni surface. The initial decrease in transmission is due to more rapid adsorption of  $\text{H}_2\text{O}$  on the detector side. The rise is due to the decrease in the  $\text{H}_2\text{O}$  detector-side dipole moment coincidentally with the adsorption of  $\text{H}_2\text{O}$  on the source side. The shallower dip with CO and the rapid return to maximum T indicate that the CO moment opposes the  $\text{H}_2\text{O}$  moment on the detector side.  $\text{H}_2\text{O}$  on Ni has been reported to be oriented with the negative end into the surface, binding through the oxygen.<sup>38</sup> Similarly,  $\text{H}_2\text{O}$  on Au has been reported to bind to the surface through the oxygen with the dipole moment oriented negative end into the surface. Therefore, a CO molecule is oriented with the positive end, the carbon, into the surface. Agreement is found between this conclusion and the observations presented by Zangwill.<sup>19</sup>

### 6.3.2 $\text{O}_2$ Adsorption on Ni

#### 6.3.2.1 $\text{O}_2$ Gated

Figure 6-6a shows the transmission with only background gases present. Figure 6.6b shows the transmission with  $\text{O}_2$

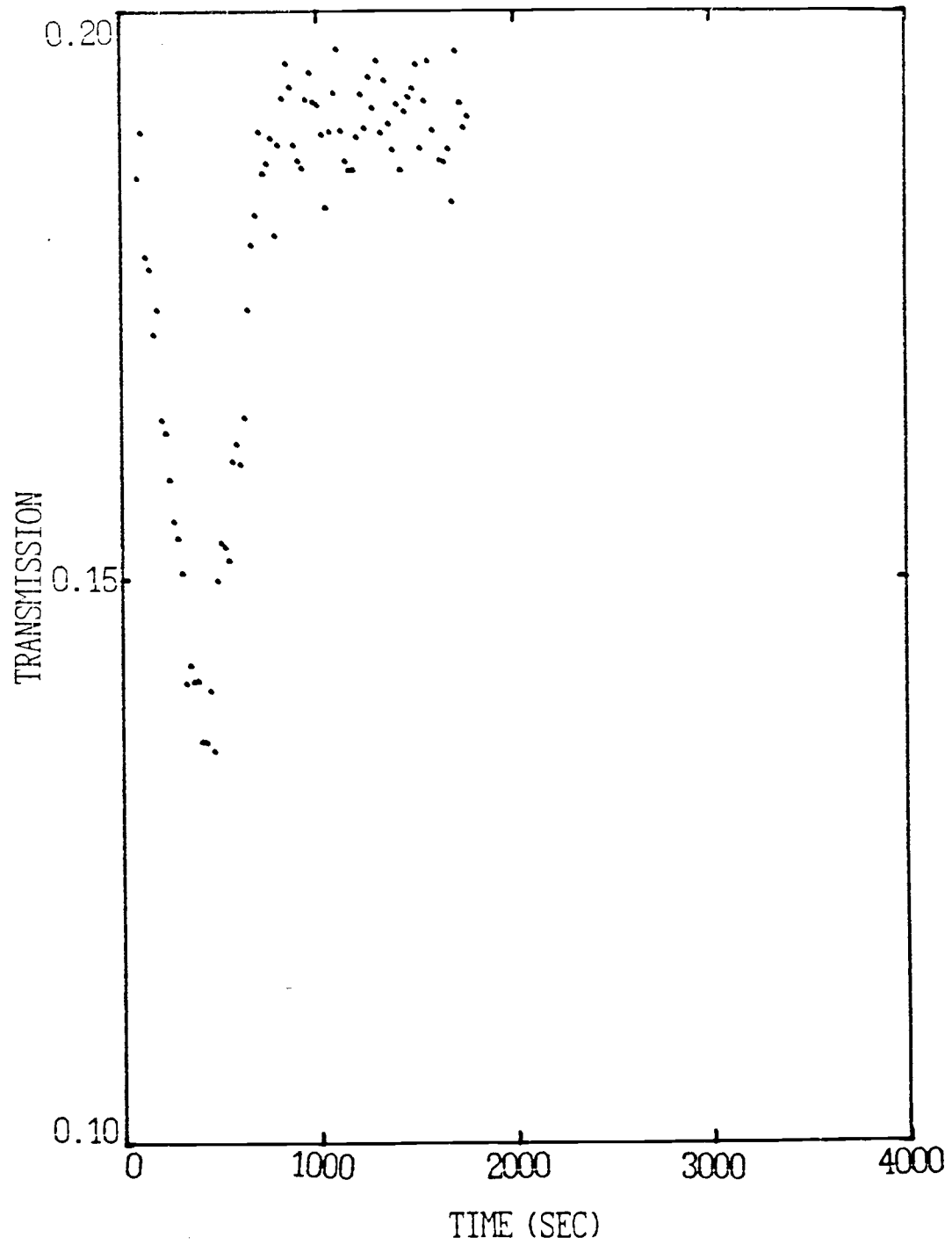


Fig. 6-6a Ni with No Introduced Adsorbate Gas

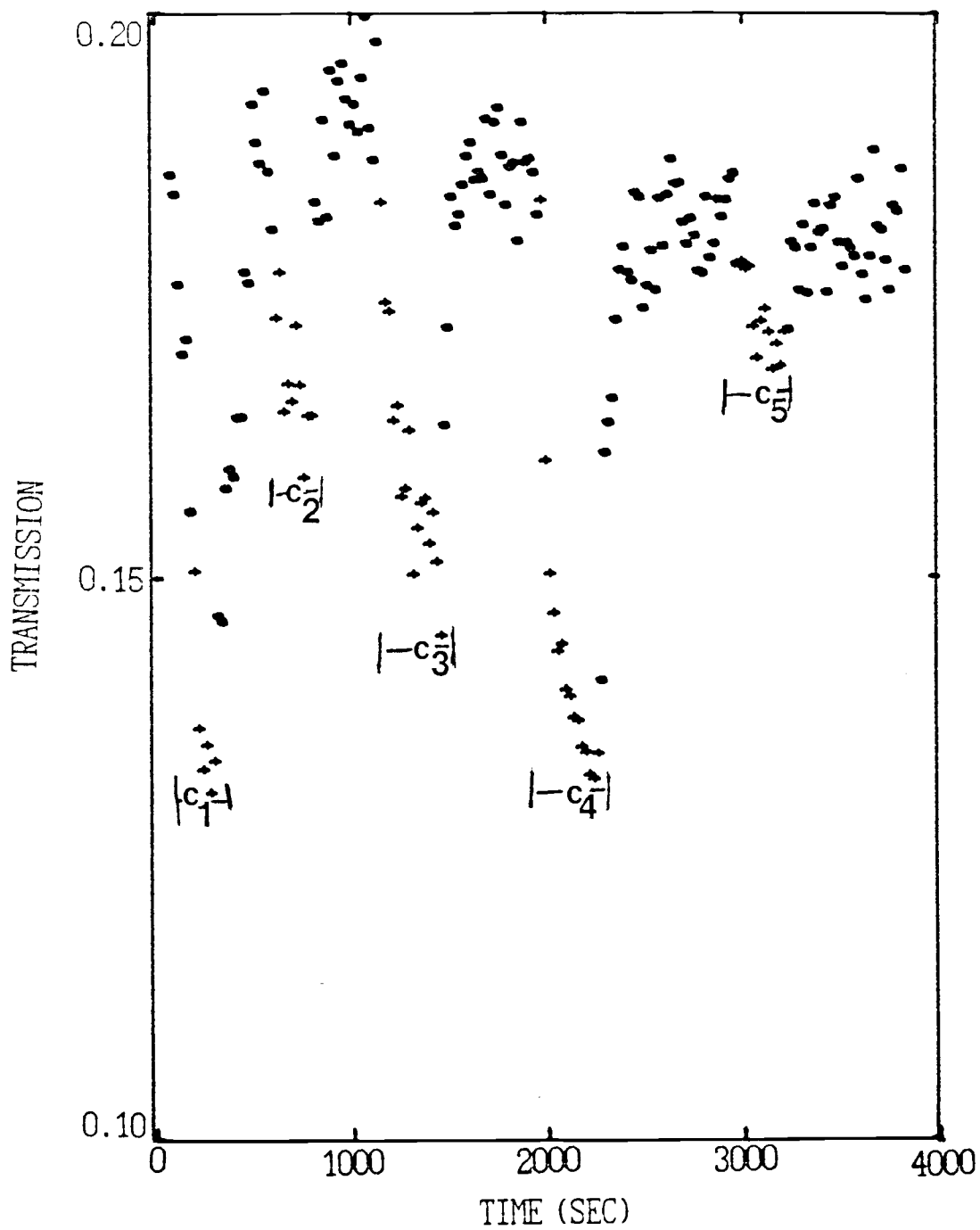


Fig. 6-6b  $O_2$  on Ni with  $O_2$  Gated

$$c_1 = 0.19/s \quad c_2 = 0.25/s \quad c_3 = 0.152/s \quad c_4 = 0.35/s \quad c_5 = 0.12/s$$

introduced in several off-on cycles and at several incident particle currents, which are  $c_1 = 0.19$  /s,  $c_2 = 0.25$  /s,  $c_3 = 0.28$  /s,  $c_4 = 0.35$  /s and  $c_5 = 0.12$  /s. The dots ( $\bullet$ ) in Fig. 6.6b represent data taken when the  $O_2$  source was off, and the crosses (+) represent data taken when the  $O_2$  source was on.

The most important observations are:

a) The  $O_2$  desorbs relatively quickly, in about 100 s. The rapid desorption indicates a short stay time of this order.

b) For the initial decrease in the transmission, the presence of  $O_2$  causes a deeper dip to 12.5%, as compared to 13% without  $O_2$ . This minimum occurs earlier in the transmission sequence, after 220 s when  $O_2$  is present, as compared to 360 s without  $O_2$  present. The more rapid return to a maximum with  $O_2$  seems to indicate that the orientation of the dipole moment for  $O_2$  on Ni is directed outward with the negative end at the surface. On the detector side of the mesh the  $O_2$  dipole moment is then parallel to the  $H_2O$  moment.

c) As in the case of CO on Ni, the most noticeable change in transmission occurs if the  $O_2$  is introduced when the mesh transmission is near its maximum. The change in transmission is dependent upon the  $O_2$  particle current and is seen to change from approximately 20% to approximately 15% for the highest  $O_2$  particle current used.

Figures 6-7a is a reference scan with no introduced adsorbate and Fig. 6-7b show experiments with  $O_2$  introduced in

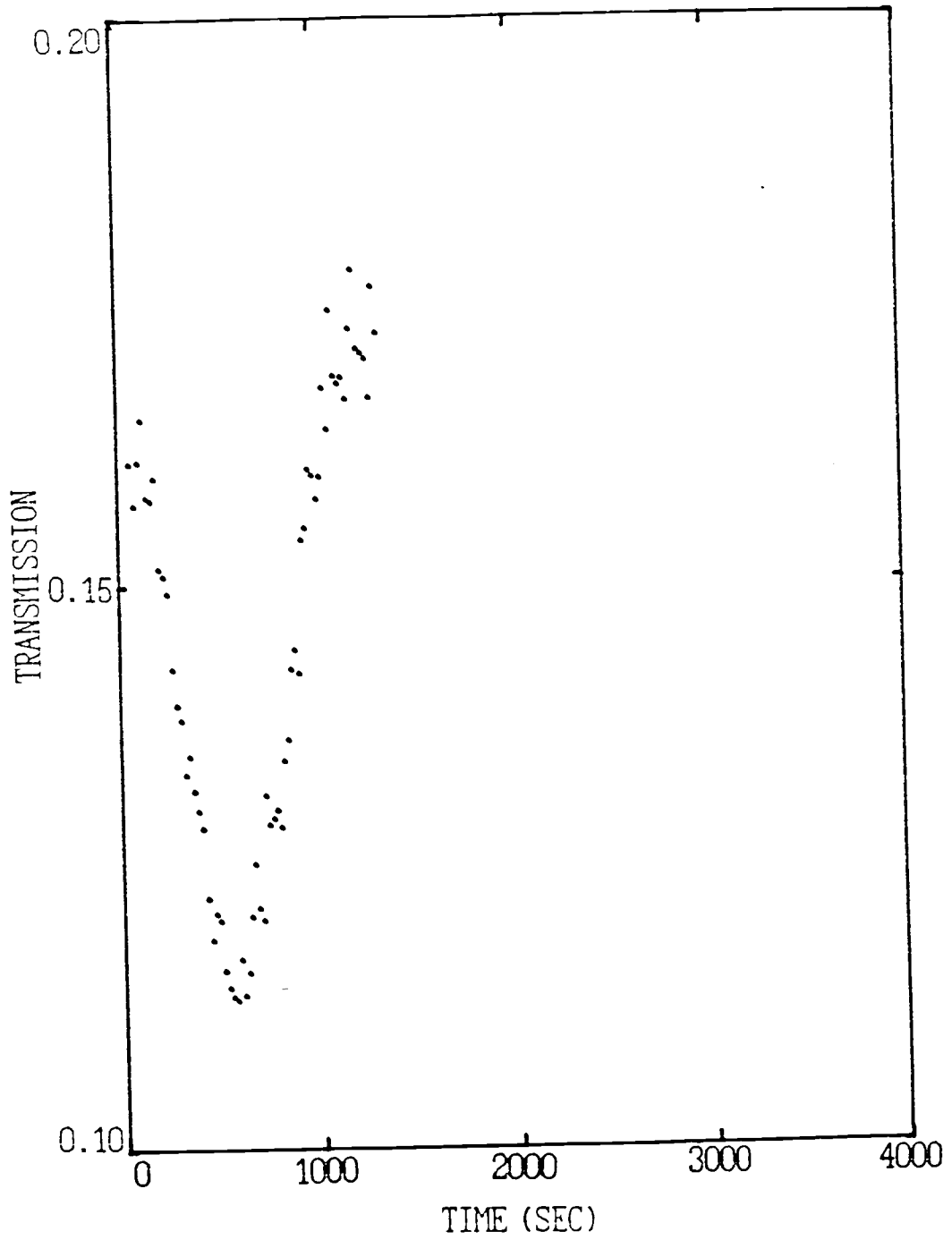


Fig. 6-7a Ni with No Introduced Adsorbate Gas

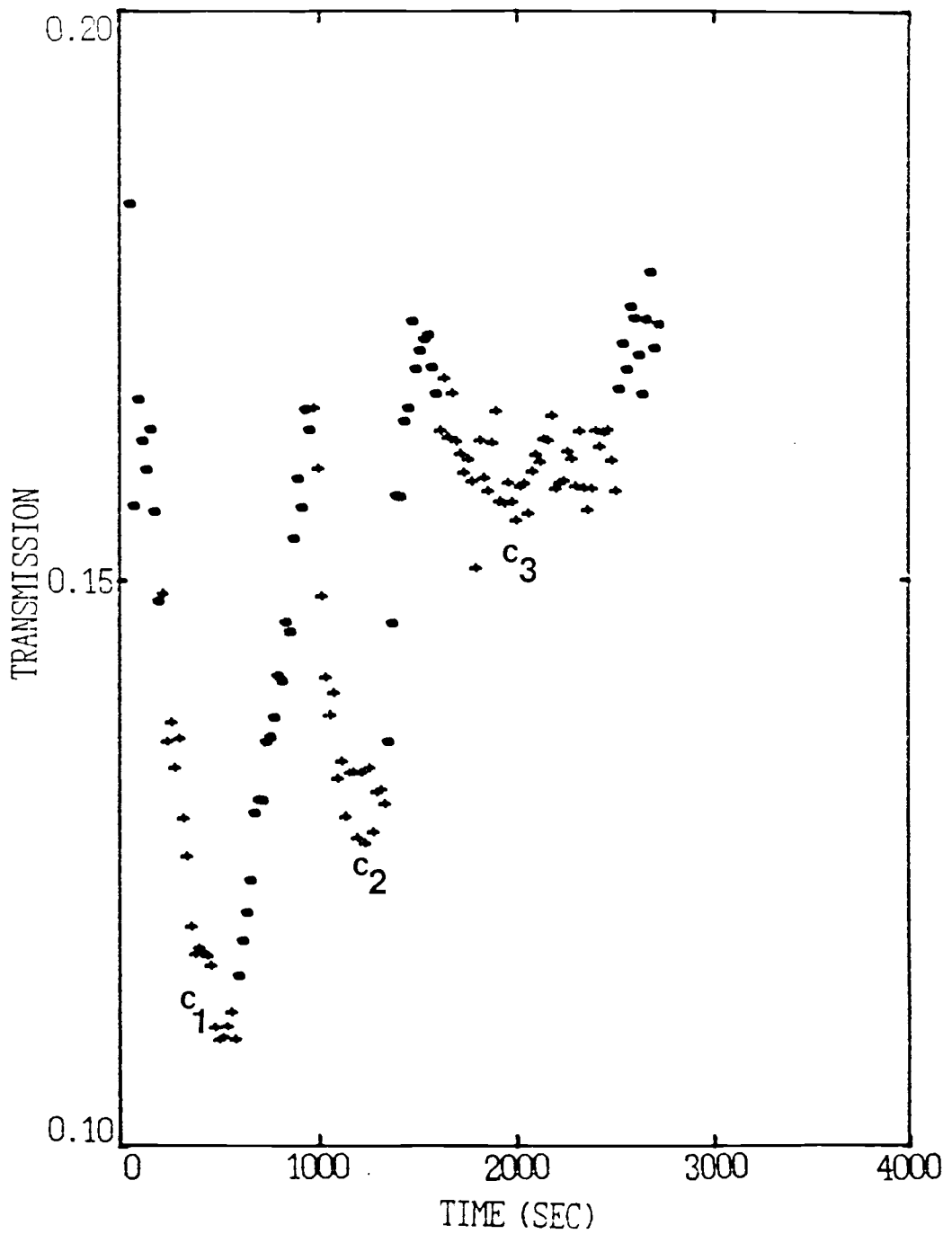


Fig. 6-7b  $O_2$  on Ni with  $O_2$  Gated  
 $c_1=0.15/s$   $c_2=0.33/s$   $c_3=0.15/s$

off-on cycles. The surface temperature of the mesh is reduced to  $T_s \approx 275 \pm K$  from that for the data in Figs. 6.6a and 6.6b ( $T_s \approx 300 \pm K$ ). The particle currents are  $c_1 = 0.15$  /s,  $c_2 = 0.33$  /s, and  $c_3 = 0.15$  /s. For the initial decrease the presence of  $O_2$  causes a deeper dip to 11% as compared to 12% without  $O_2$ .

The initial minimum occurs more rapidly, after 400 s with  $O_2$  present, as compared to 460 s without  $O_2$ . As in Fig. 6-6b,  $O_2$  desorption occurs relatively rapidly, indicating a short stay time no longer than 100 s for  $O_2$  on the Ni surface. Again the change in transmission is dependent upon the  $O_2$  particle current. Accumulation of  $O_2$  on the Ni surface is greater for higher  $O_2$  particle currents. When the particle current is 0.33 /s, the change in transmission is approximately 5%. When the particle current is 0.15/s, the transmission change is approximately 2%.

In Sec. 7.2 the desorption energy  $E_d$  and the product  $\mu s$  for  $O_2$  on Ni will be determined from the data of Figs. 6-6b and 6-7b.

#### 6.3.2.2 $O_2$ Introduced Continuously

Figure 6-8 shows the change in the transmission when  $O_2$  is introduced continuously for an entire bank. The temperature of the surface is elevated for the data in both figures to  $T_s = 340 \pm 5$  K. The data represented by dots ( $\bullet$ ) show the transmission with no  $O_2$  gas incident on the Ni surface. The data represented by stars ( $\ast$ ) show the transmission for  $O_2$  incident on

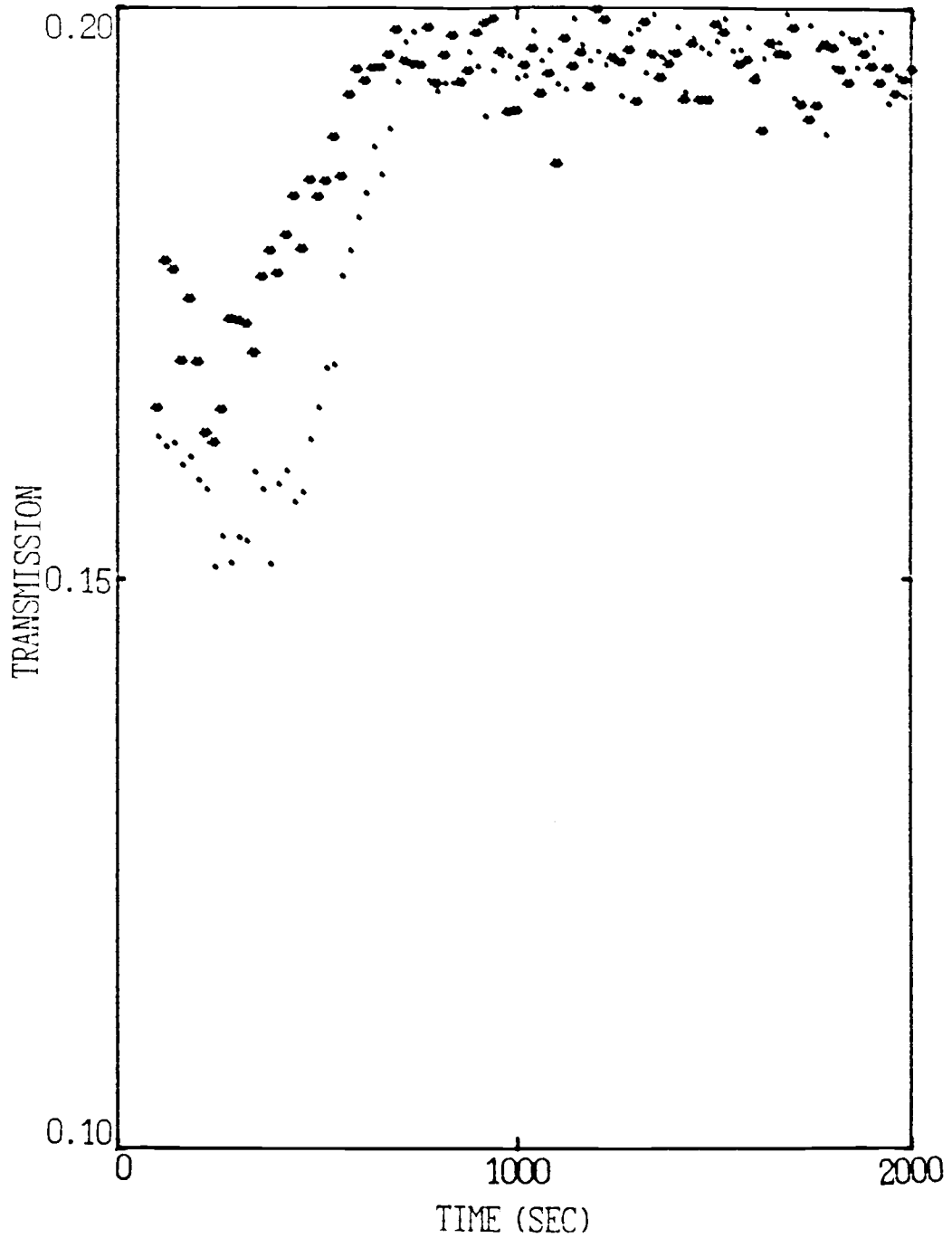


Fig. 6-8  $O_2$  on Ni with  $T \cong 350$  K  
(\*) Constant  $O_2$  :  $c = 0.72/s$   
(•) No Introduced Adsorbate

the Ni surface with a particle current  $c = 0.072$  /s. A third scan, not shown, was taken without introduced  $O_2$  and reproduced the data represented by dots ( $\bullet$ ). The elevated surface temperature can reduce the the sticking probability and therefore reduces the coverage of  $O_2$  or  $H_2O$  that will accumulate on the surface. Masuda et al. report that  $O_2$  on Ni(110) does not dissociate until  $T_s$  reaches 500 K.<sup>39</sup> Therefore, it appears likely that  $O_2$  remains intact on the surface for the conditions of this experiment.

The presence of  $O_2$  on the Ni surface reduces the depth of the minimum from 15% without  $O_2$  present to 16.5% with  $O_2$  present on the surface. These data seem to indicate that at a particle current of 0.072 /s and with an elevated surface temperature the  $O_2$  dipole moment is parallel to that of the  $H_2O$  molecules on the detector side. The particle current for Fig. 6-8 is lower than that for the data in Figs. 6.6b and 6.7b. The accumulation of  $H_2O$  on the source side of the mesh is assumed to account for the initial decrease.

In Sec. 7.2 the product  $\mu s$  for  $O_2$  on Ni will be determined from the data of Fig. 6-8.

### 6.3.3 $H_2O$ Adsorption on Au

$H_2O$  was introduced onto the detector side of the mesh. Figure 6.9 a shows the transmission with background gas only. The experimental conditions for this data differ from those of

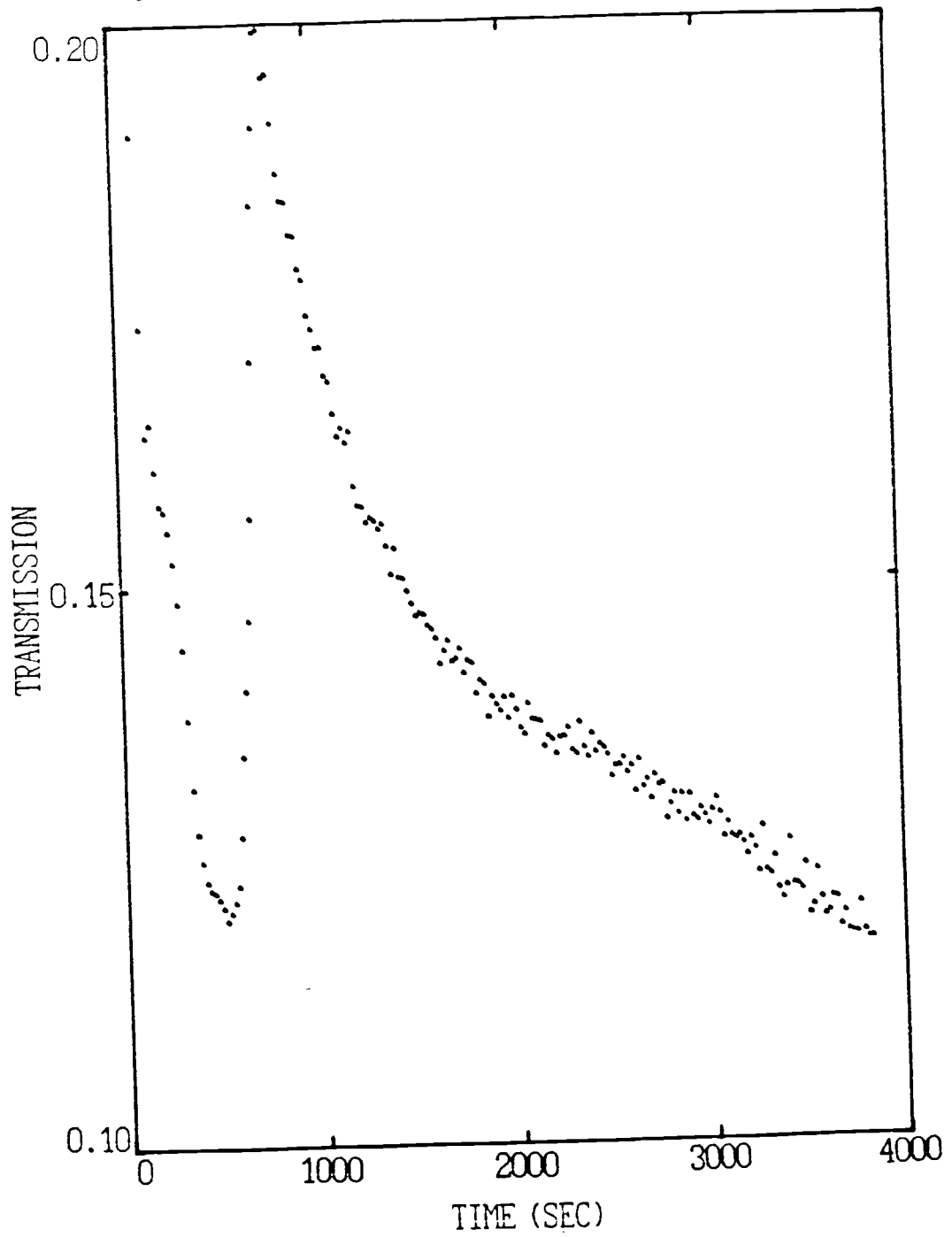


Fig. 6-9a Au with No Introduced Adsorbate Gas

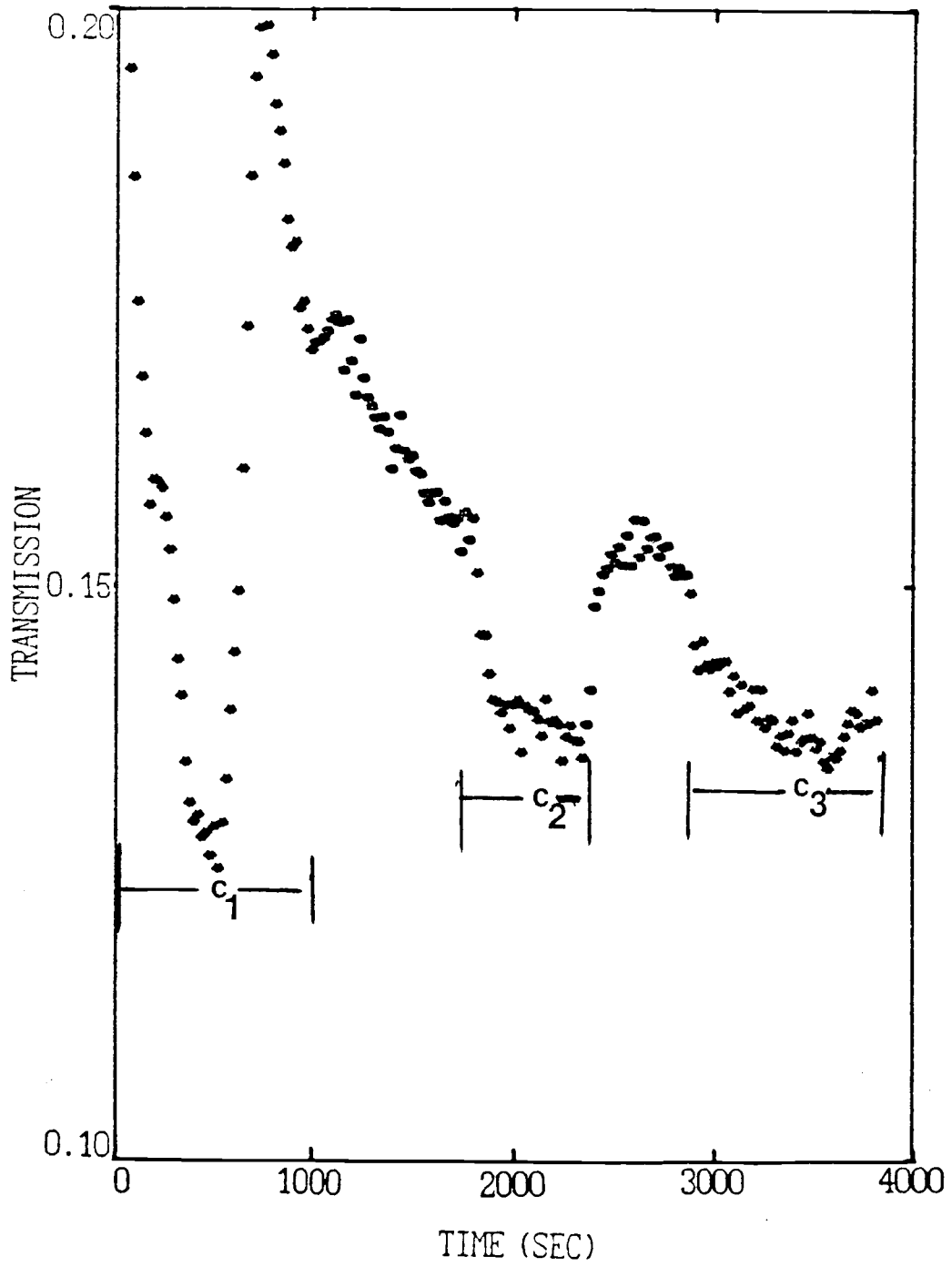


Fig. 6-9b  $H_2O$  on Au with  $H_2O$  Gated  
 $c_1=0.127/s$   $c_2=0.207/s$   $c_3=0.149/s$

Fig. 3-5; a lower oven temperature may account for the difference for  $T$  when  $t$  is of order 2000 s. Figure 6.9b shows the transmission with  $H_2O$  introduced onto the mesh with particle currents of  $c_1 = 0.127$  /s,  $c_2 = 0.207$  /s and  $c_3 = 0.149$  /s. The data in Fig. 6.9 b represented with large dots ( $\bullet$ ) are taken with no adsorbate  $H_2O$  incident on the mesh, and the stars ( $*$ ) represent data with  $H_2O$  incident on the surface. A comparison of the two figures reveals that the initial decrease with the adsorbate  $H_2O$  produces a shallower minimum. This observation agrees with the interpretation that the  $H_2O$  adsorbs onto the permanent layer initially more rapidly on the source side, producing an initial decline in the transmission. However,  $H_2O$  also adsorbs on the detector side and begins to cancel the contribution to the electric field of the  $H_2O$  on the source side, leading to a cusp and a transmission maximum. The  $H_2O$  on the source side reaches a maximum coverage of considerably less than a monolayer as a result of to the coadsorption of Li. Therefore, the contribution due to the  $H_2O$  on the detector side begins to dominate and the transmission again declines. Additional  $H_2O$  on the detector side will decrease the depth of the initial dip and will also lead to a decrease in transmission after the cusp.

When  $H_2O$  is present on the surface, transmission changes rapidly after the cusp. Equilibrium is reached after less than 100 s. After the  $H_2O$  gas source is removed the transmission returns to a higher level rapidly.

In Sec. 7.3 the desorption energy  $E_d$  and the product  $\mu s$  for  $H_2O$  on Au will be determined from the data of Fig. 6-9b.

#### 6.3.4 $H_2O$ Adsorption on Ni

$H_2O$  is introduced onto the mesh with the effect of increasing the depth of the dip. Figure 6-10 shows two transmission sequences. The dots ( $\bullet$ ) represent the data taken when no  $H_2O$  adsorbate was introduced onto the mesh. The crosses ( $+$ ) represent the data taken when  $H_2O$  was introduced onto the Ni surface. The  $H_2O$  was introduced with particle currents of  $c_1 = 0.21$  /s and  $c_2 = 0.14$  /s. The Ni surface temperature for the data in Fig. 6-10 was  $T_s = 300 \pm 5$  K.

Introduced  $H_2O$ , adsorbed onto the detector side of the mesh is observed to produce an additional decrease in the transmission. This result agrees with the interpretation that the  $H_2O$  on the detector side contributes more to the electric field than do the dipole-moments of  $H_2O$  and Li on the source side. It cannot be determined by this experiment alone whether the sticking probability is greater for  $H_2O$  on the detector side or whether the dipole moment per  $H_2O$  molecule is greater on the detector side.

In Sec. 7.4 the desorption energy  $E_d$  and the product  $\mu s$  for  $H_2O$  on Au will be determined from the data in Fig. 6-10.

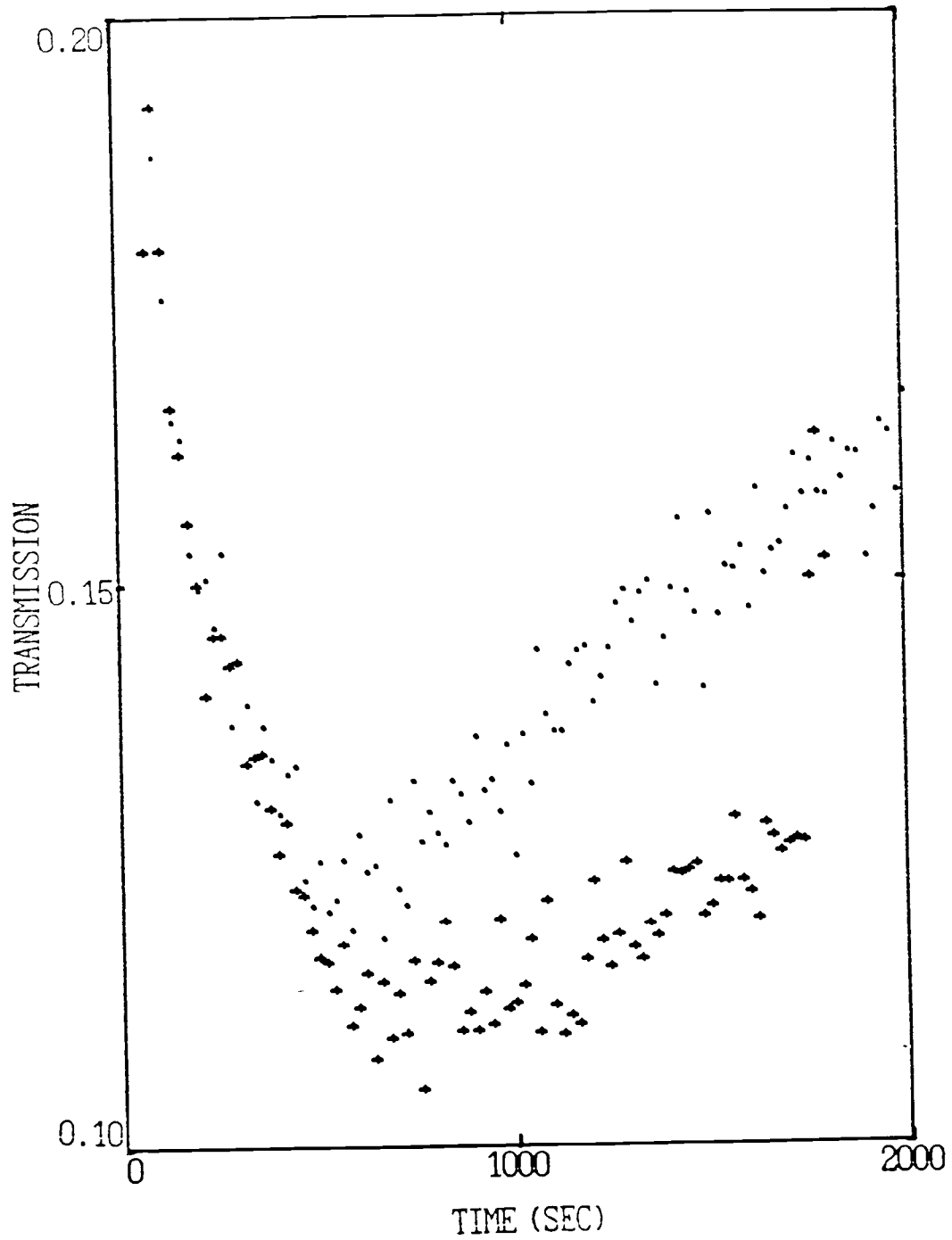


Fig. 6-10  $\text{H}_2\text{O}$  on Ni  
(+) Constant  $\text{H}_2\text{O}$ :  $c = 0.21/\text{s}$   
(•) No Introduced Adsorbate

### 6.3.5 H<sub>2</sub>O Desorption from Ni

Figure 6.11 shows the desorption of H<sub>2</sub>O from the Ni surface. The transmission sequence is initiated by the cessation of the heating current. H<sub>2</sub>O from the background gas and Li from the oven are allowed to accumulate on the Ni substrate for approximately 1400 s causing the transmission to decline to approximately 13.5%. At  $t \cong 1400$  s a heating current is applied across the mesh to increase the surface temperature to  $T_s \cong 350 \pm 5$  K. After the heating current is turned on, the transmission increases, indicating a reduction in the net surface dipole-moment density. The reduction in dipole-moment density is due to the desorption of H<sub>2</sub>O from the surface. After 16 channels, 320 s, the transmission has returned to its initial level of 18%. This value of T corresponds to the situation with no significant coverage of H<sub>2</sub>O adsorbed onto the Ni surface.

In Sec. 7.4 the desorption energy  $E_d$  will be determined for H<sub>2</sub>O on Ni from the data of Fig. 6-11.

### 6.3.6 SO<sub>2</sub> Adsorption on Au

The adsorption and desorption of SO<sub>2</sub> on Au was studied. Figure 6.12 shows the transmission sequences for the case of no introduced adsorbate applied to the surface, represented by dots ( $\cdot$ ), and the case with SO<sub>2</sub> applied to the Ni surface, represented by crosses (+). For the introduction of SO<sub>2</sub> on the surface the particle currents are  $c = 0.23/s$  for region 1 and  $c = 0$  for

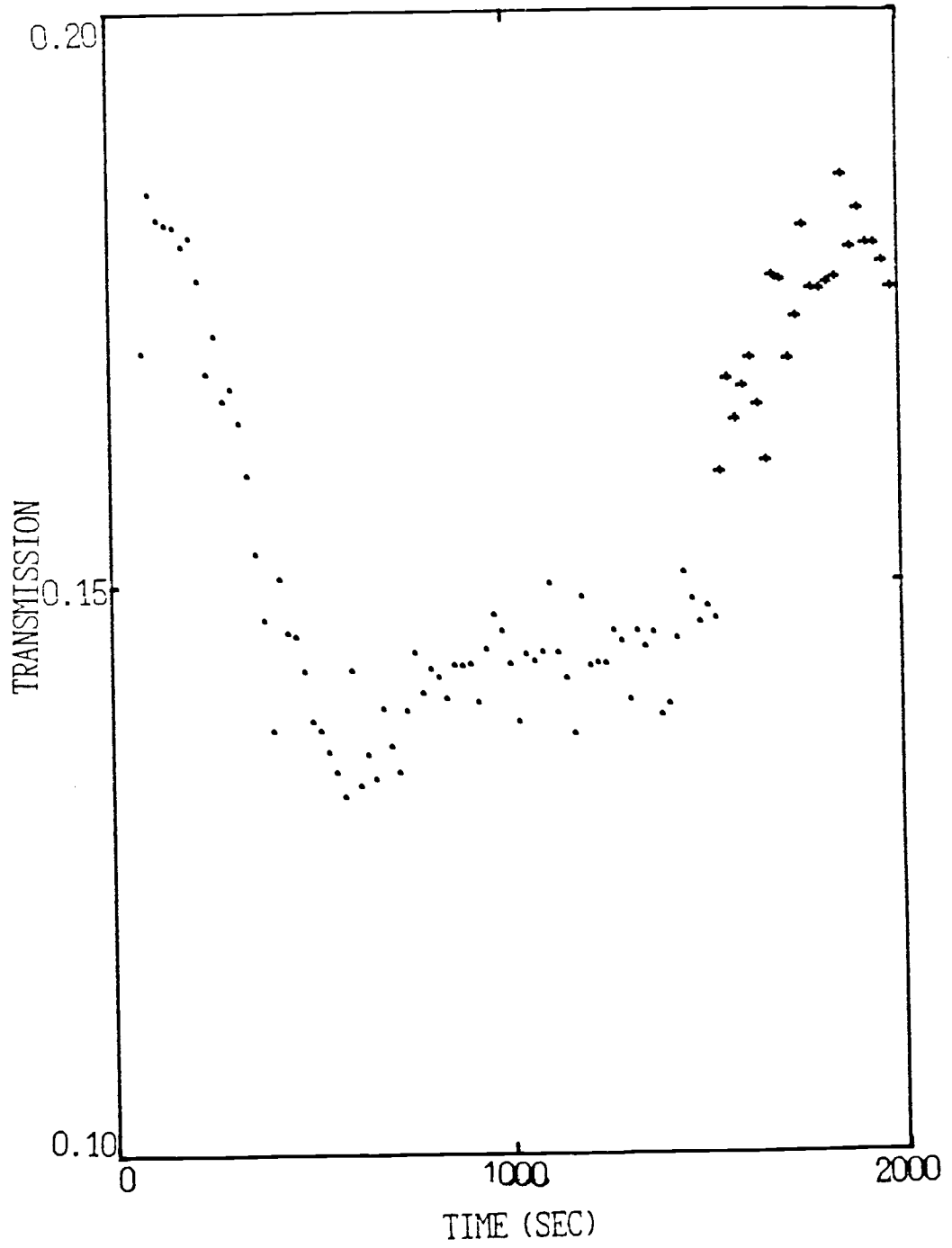


Fig. 6-11 H<sub>2</sub>O Desorption from Ni

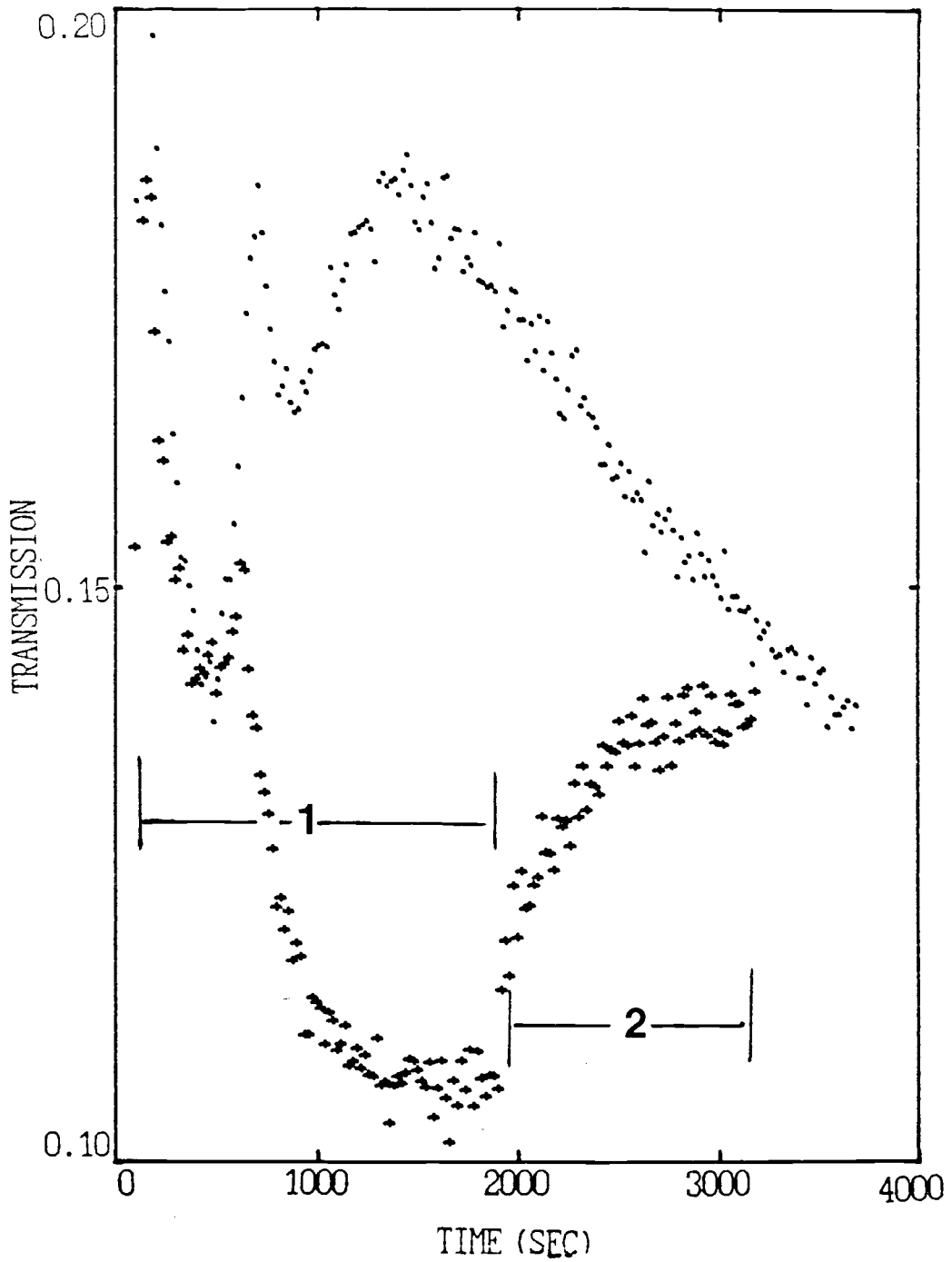


Fig. 6-12  $\text{SO}_2$  on Au with  $\text{SO}_2$  Gated  
 (+)  $\text{SO}_2$ :  $c_1 = 0.23/\text{s}$ ,  $c_2 = 0$   
 (•) No Introduced Adsorbate

region 2. The presence of  $\text{SO}_2$  on the surface may cause the cusp to occur at a lower transmission. If the  $\text{SO}_2$  dipole moment were oriented parallel to that of  $\text{H}_2\text{O}$  on the source side, then the initial dip would be deeper. However, the initial dip is shallower and therefore, the dipole moment of  $\text{SO}_2$  must be oriented antiparallel to the  $\text{H}_2\text{O}$  on the detector side of the mesh.

In Fig. 6-12,  $\text{SO}_2$  introduction ceases after approximately 1800 s. The subsequent increase in transmission is interpreted to be due to by the desorption of  $\text{SO}_2$  from the surface as the dipole-moment density decreases.

In Sec. 7-5 the desorption energy and the product  $\mu\text{s}$  will be determined for  $\text{SO}_2$  on Au from the data in Fig. 6-12.

### 6.3.7 $\text{SO}_2$ Adsorption on Ni

The adsorption of  $\text{SO}_2$  onto Ni does not affect the transmission as greatly as does the adsorption of  $\text{SO}_2$  onto Au. Figure 6.13 shows the transmission sequence for three different situations. The dots ( $\bullet$ ) identify the data for no introduced adsorbate. The crosses (X) identify the data for  $\text{SO}_2$  introduced with a particle current of 0.059 /s. The ovals (O) identify the data for  $\text{SO}_2$  introduced with a particle current of 0.044 /s. The presence of  $\text{SO}_2$  causes the dip and rise to be broader, of longer time duration, and deeper, with a greater decrease in transmission. The final or stable transmission with  $\text{SO}_2$  present

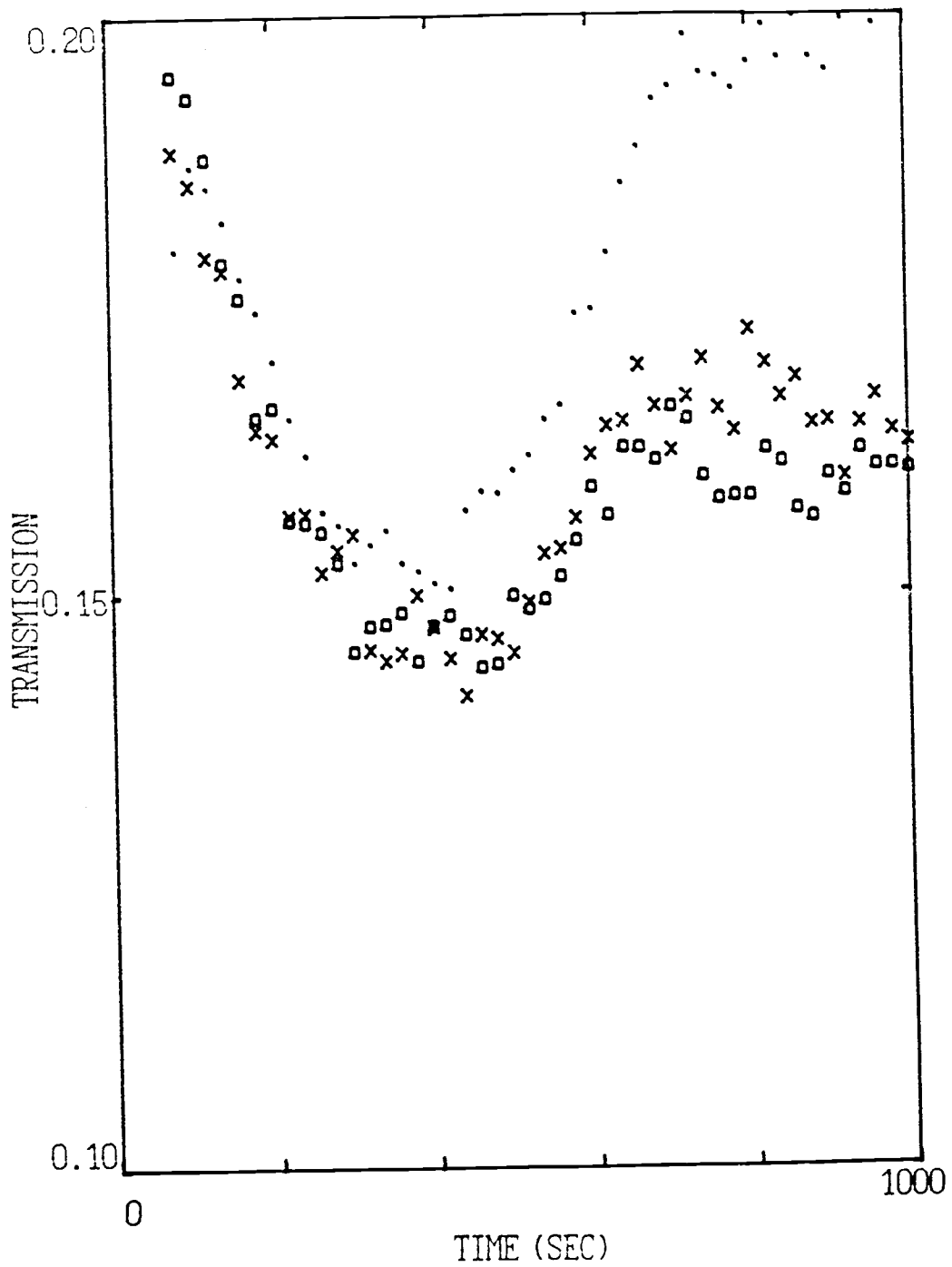


Fig. 6-13 SO<sub>2</sub> on Ni  
 (•) SO<sub>2</sub>: c = 0 (X) SO<sub>2</sub>: c = 0.059/s  
 (O) SO<sub>2</sub>: c = 0.044/s

is not the maximum transmission, as is the case without  $\text{SO}_2$ . The failure of the transmission to return to  $T_{\text{max}}$  in the long term may indicate that  $\text{H}_2\text{O}$  will not adsorb onto or near  $\text{SO}_2$  on the surface. The stable transmission at the end of the run indicates that a layer of  $\text{SO}_2$  has formed on the detector side. The final transmission is smaller for smaller particle currents. A smaller particle current implies a lower coverage, and since the dipole-moment is larger for a smaller coverage, a larger difference is observed in the final transmission for the smaller particle current.

Analysis of the final transmission difference between scans with no introduced adsorbate and  $\text{SO}_2$  yields a value for the dipole moment of  $\text{SO}_2$  on Ni. The dipole moment of  $\text{SO}_2$  on Ni will be calculated in Sec. 7.6 from the data in Fig. 6-13.

#### 6.3.8 NO Adsorption on Ni

The effect of the adsorption of NO is shown in Fig. 6.14. Dots (•) identify data with no NO introduced, and ovals (O) identify data with NO introduced at a particle current of 0.059 /s. Transmission with NO present is altered in the following way. A more pronounced dip is observed when NO is present,  $T \cong 10\%$ , as compared to  $T \cong 12.5\%$  with no NO. The smaller transmission for NO on the Ni substrate may indicate that NO is oriented with the negative end into the surface, parallel to the  $\text{H}_2\text{O}$  on the detector side, possibly being attached through

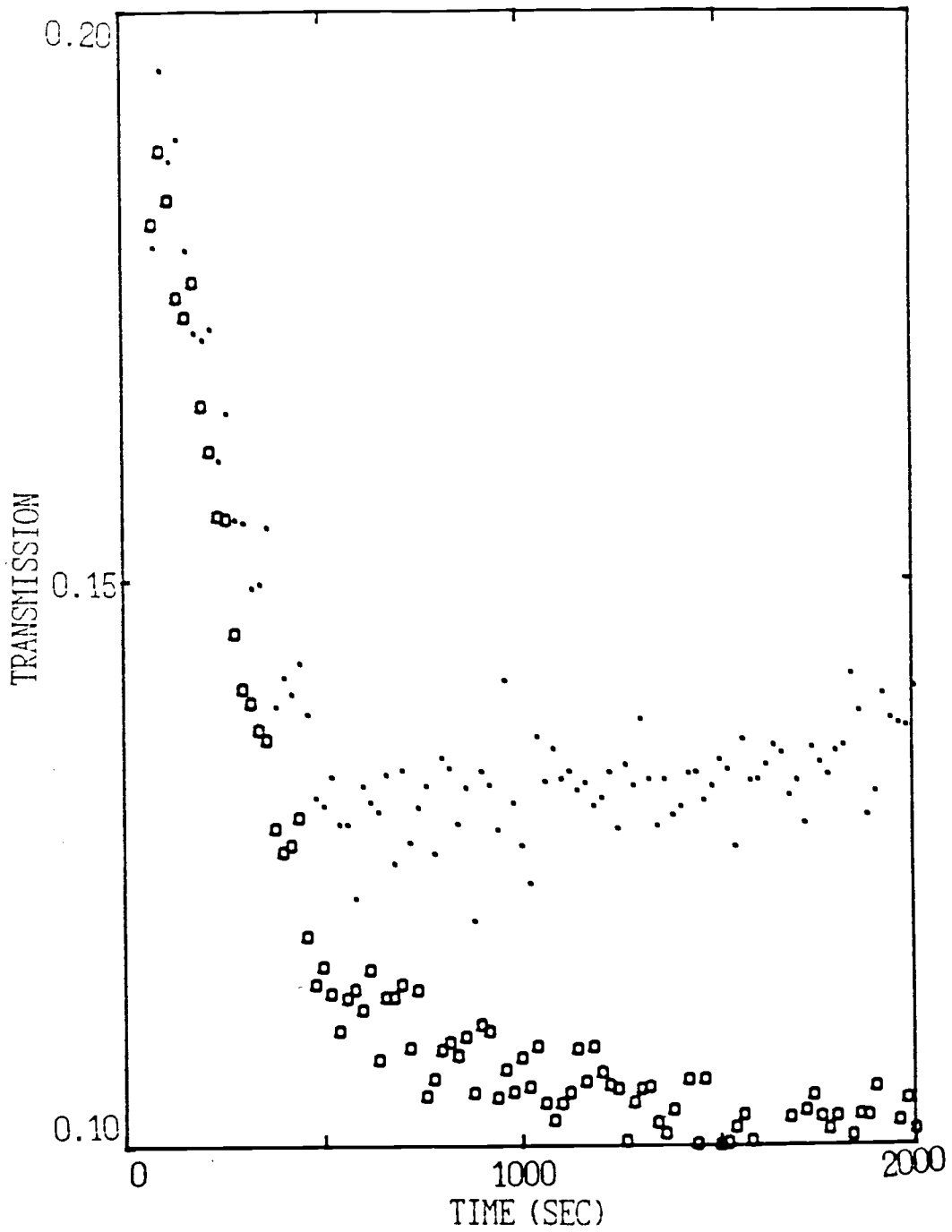


Fig. 6-14 NO on Ni

(•) No Introduced Adsorbate (O) NO:c = 0.06/s

the O, oxygen, to the Ni. The NO continues to adsorb onto the Ni, increasing its coverage for the 2000 s presented in Fig. 6.14.

In Sec. 7.7 the product  $\mu s$  will be determined for NO on Ni from the data in Fig. 6-14.

## CHAPTER 7: ANALYSIS OF EXPERIMENTAL OBSERVATIONS

Qualitative and quantitative conclusions will be made in this chapter concerning the physical properties of adsorbates on metallic surfaces. Information will be obtained about the sticking probability, dipole moment magnitude and orientation, desorption rate, and desorption energy.

The experimental observations reported in Chapter 6 are analyzed with the tools developed in Secs. 5.2.1, 5.2.2, and 5.2.3. The equations from these sections are used in the calculation of the desorption energy and of the product  $\mu s$  from the data in the previous chapter. The constraints required in the use of these equations will be referenced in each section of this chapter.

The physical quantities determined are not all independently measured in this experiment. Therefore, in most cases results from the work of other researchers are used to interpret the data quantitatively. Additional information used from the literature may include, depending on the experiment done, surface diffusion rate, desorption energy, sticking probability, dipole moment magnitude or orientation, and surface lattice structure for the adsorbate. All the data presented in this section have been converted to dipole-moment density  $|\langle N\mu \rangle|$  vs time. The relation connecting transmission  $T$  and dipole-moment density  $|\langle N\mu \rangle|$  was developed in Sec. 5.1.

### 7.1 CO Adsorption on Ni

Figure 6-4 from Sec. 6.3.1.1 shows the effect on transmission when CO is introduced onto the Ni substrate. Changes in the dipole-moment density due to the introduction of CO, occurring after the transmission has returned to a level near maximum, may be understood in the following manner. CO adsorption onto and CO desorption from the Ni substrate reach equilibrium rapidly in comparison to the duration of one data channel, 20 sec. The theoretical development from Sec. 5.2.3 yields the following result for changes in the dipole-moment density when adsorption-desorption equilibrium is reached in less than 200 s. Equation (5-23) gives  $\Delta|\langle N\mu \rangle|$  due to CO as

$$\Delta|\langle N\mu \rangle| = \frac{\mu_a s_a c_a}{A_s \Gamma_s} \quad , \quad (5-23)$$

where  $\Gamma = \Gamma_0 e^{-E_d/kT_s}$  is the desorption rate and  $E_d$  is the desorption energy.<sup>9</sup>  $\Gamma_0 = 10^{13}$  / sec and  $kT_s = (T_s / T_0) 1/40$  eV, in which  $T_0$  is a standard temperature, 300 K, and  $T_s$  is the temperature of the metal surface. Other work is referenced at this point, so that the desorption energy may be calculated with Eq. (5-23).

J.C. Campuzano et al.<sup>34</sup> used work function measurements to determine the dipole moment  $\mu$ , sticking probability  $s$ , and orientation of the CO molecule on the Ni(111) surface. They reported that  $\mu \cong 0.28$  D  $\cong 0.1$   $ea_0$  and  $s \cong 0.91$  at low coverage. Horgan and King<sup>41</sup> reported that the zero-coverage limit of the

sticking probability for CO on Ni was independent of crystal face, i.e.  $s_0 \cong 0.9$  for Ni(100), Ni(110), and Ni(111). Campuzano et al.<sup>34</sup> reported that the CO molecule attaches to the Ni surface through the C atom. Therefore, the dipole-moment vector points inward (the negative end outward). In addition J.C. Campuzano et al. used LEED (Low Energy Electron Diffraction) to determine that at high CO coverage,  $\theta \cong 0.55$ , carbon monoxide forms a  $2 \times \sqrt{3}$  unit cell pattern which implies that  $A_{CO} \cong 2A_{Ni}$ .  $A_{CO}$  is the area occupied by a CO molecule on the Ni surface. They also found that CO can form a surface pattern which has a  $4 \times 2$  unit cell at lower coverages, implying that  $A_{CO} \cong 4A_{Ni}$ .  $A_{Ni}$  is the area of a nickel surface site,  $A_{Ni} = 6.2 \times 10^{-16} \text{ cm}^2$  for the Ni(100).

S. Johnson and R.J. Maddox<sup>42</sup> used thermal desorption to measure the desorption energy  $E_d$  for CO on Ni(100), and reported that  $E_d = 1.1 \text{ eV}$ . They also reported that at saturation coverage CO forms a surface pattern with a unit cell of  $2 \times 2$  which implies that  $A_{CO} \cong 2A_{Ni}$  and the observation was made that the presence of sulfur on a Ni surface reduced the measured  $E_d$  for  $H_2$  desorbed from Ni. This observation may imply that values for  $E_d$  found in this work may be smaller than reported by Johnson and Maddox, since  $H_2O$  is coadsorbed with the CO. These researchers also reported that for the conditions of this work CO does not dissociate on the Ni surface.

Research done by Zhu et al.<sup>20</sup> was used to calculate the time

for a CO molecule to diffuse around a mesh filament in Sec. 2.1.3. The calculation in Chapter 2 shows that for the conditions of this experiment the time to diffuse around a mesh strand is approximately 400 s. In comparison to the time required for the dipole-moment density to change due to CO adsorption, less than 100s, 400 s is a long time. Therefore, the possibility for the surface diffusion of CO from one side of the mesh to the other may be neglected.

Figure 7-1 shows  $|\langle N\mu \rangle|$  vs time obtained from Fig. 6-4. The changes due to the adsorption of CO in the regions of interest are signified by crosses (+). Regions 1 and 2 give the change in  $|\langle N\mu \rangle|$  as 1)  $0.10 \times 10^{13} \text{ ea}_0/\text{cm}^2$  and 2)  $0.12 \times 10^{13} \text{ ea}_0/\text{cm}^2$ . The particle currents  $c$  are experimentally determined and are  $c = 0.152 \text{ /s}$  for region 1 and  $c = 0.170 \text{ /s}$  for region 2. With the relevant additional data and Eq. (5-23), the desorption energy is calculated to be  $E_d = 0.70 \pm 0.03 \text{ eV}$  for CO on a polycrystalline Ni substrate. This value is 0.4 eV lower than the measurement reported by Johnson and Maddox. However, these researchers used a Ni(100) surface Ni surface.<sup>42</sup> For the data in Fig. 7-1, H<sub>2</sub>O is coadsorbed with CO.

Figures 7-2a and 7-2b show the change in  $|\langle N\mu \rangle|$  vs  $t$  due to CO continuously introduced onto the mesh; refer to Figs. 6-5a and 6-5b in Sec. 6.3.1.2. Horgan and King reported that at partial monolayer coverages, CO on Ni had a sticking probability

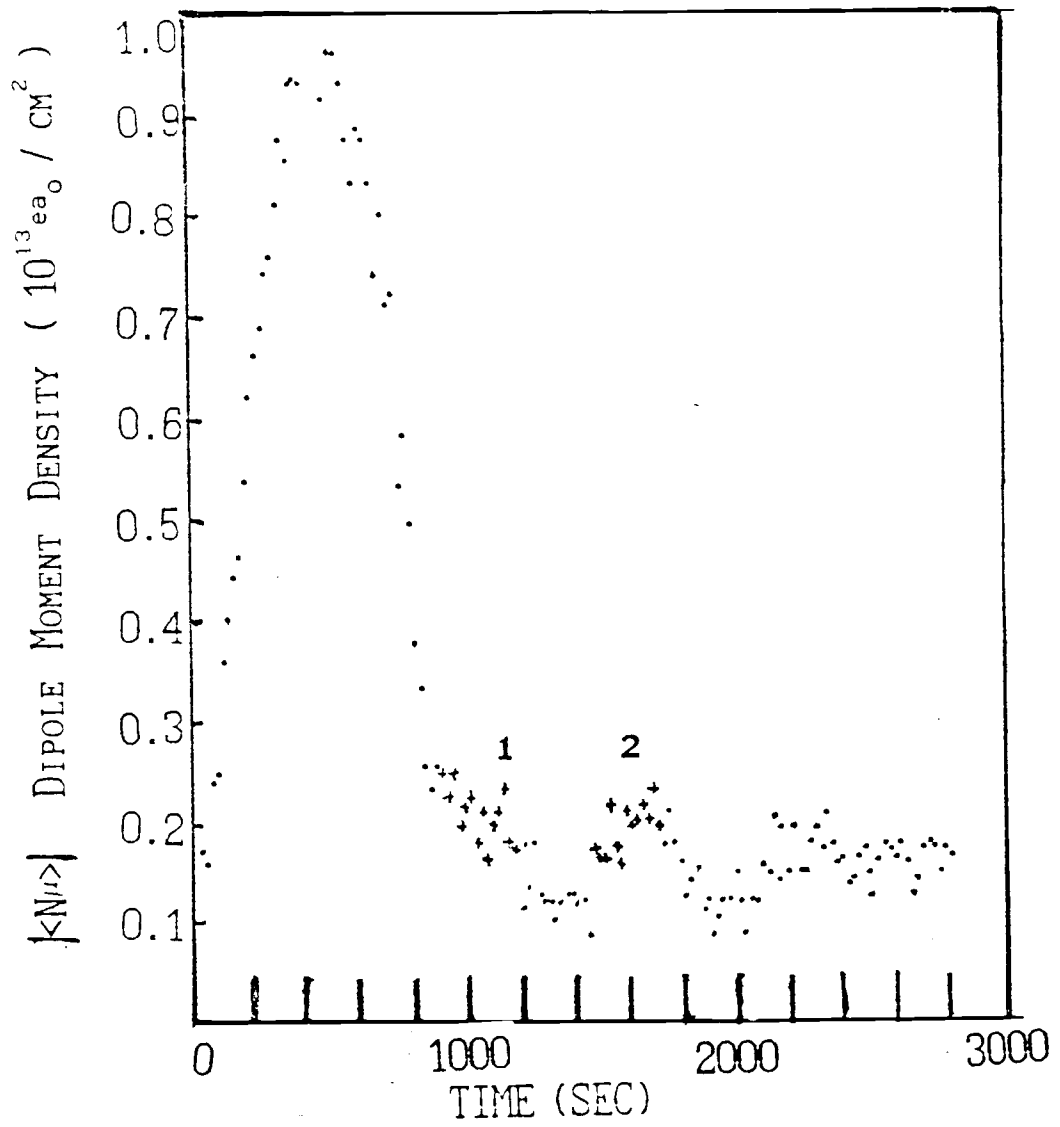


Fig. 7-1 Dipole-Moment Density: Ni Substrate: CO Gated

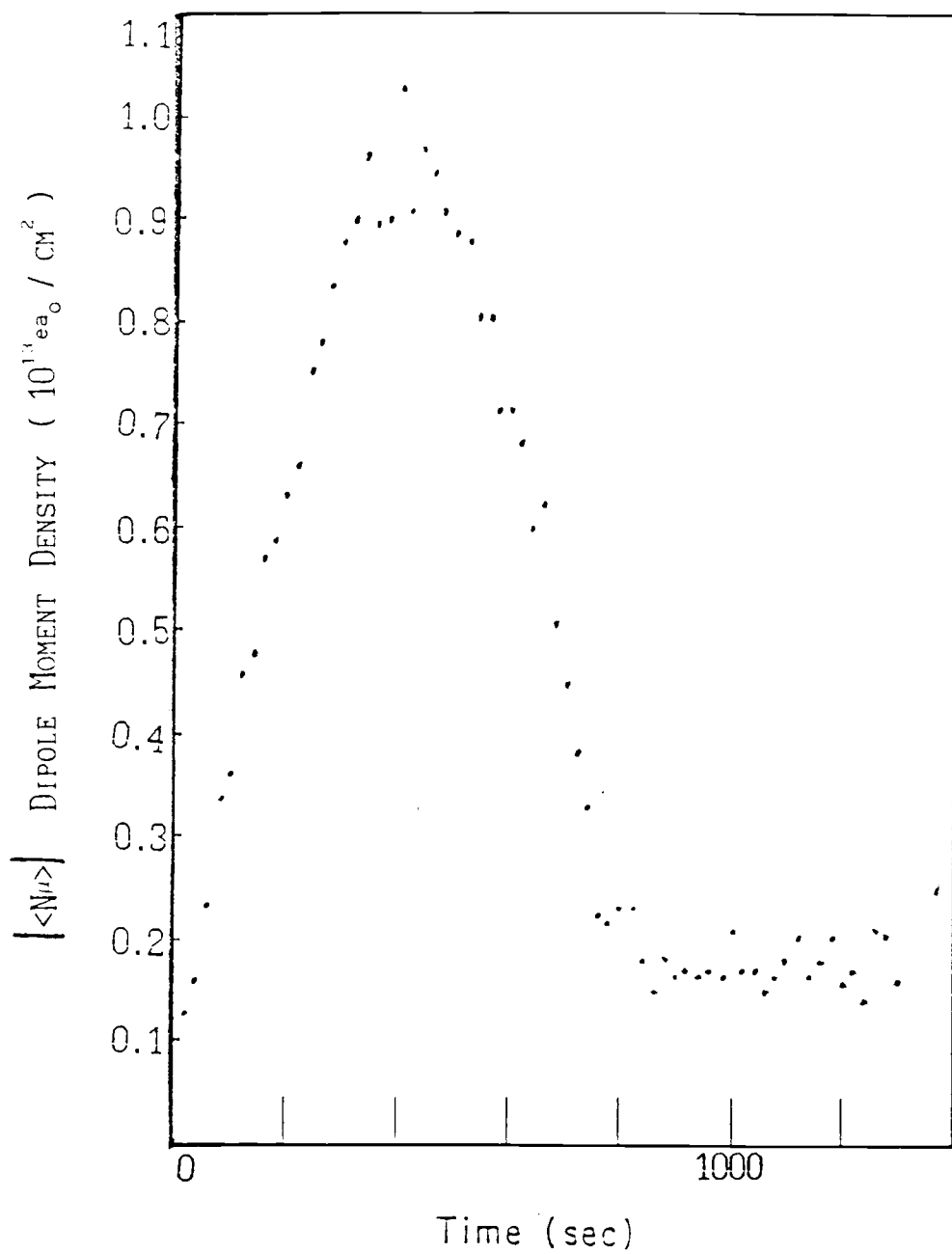


Fig. 7-2a Dipole-Moment Density: Ni Substrate:  
No Adsorbate Introduced

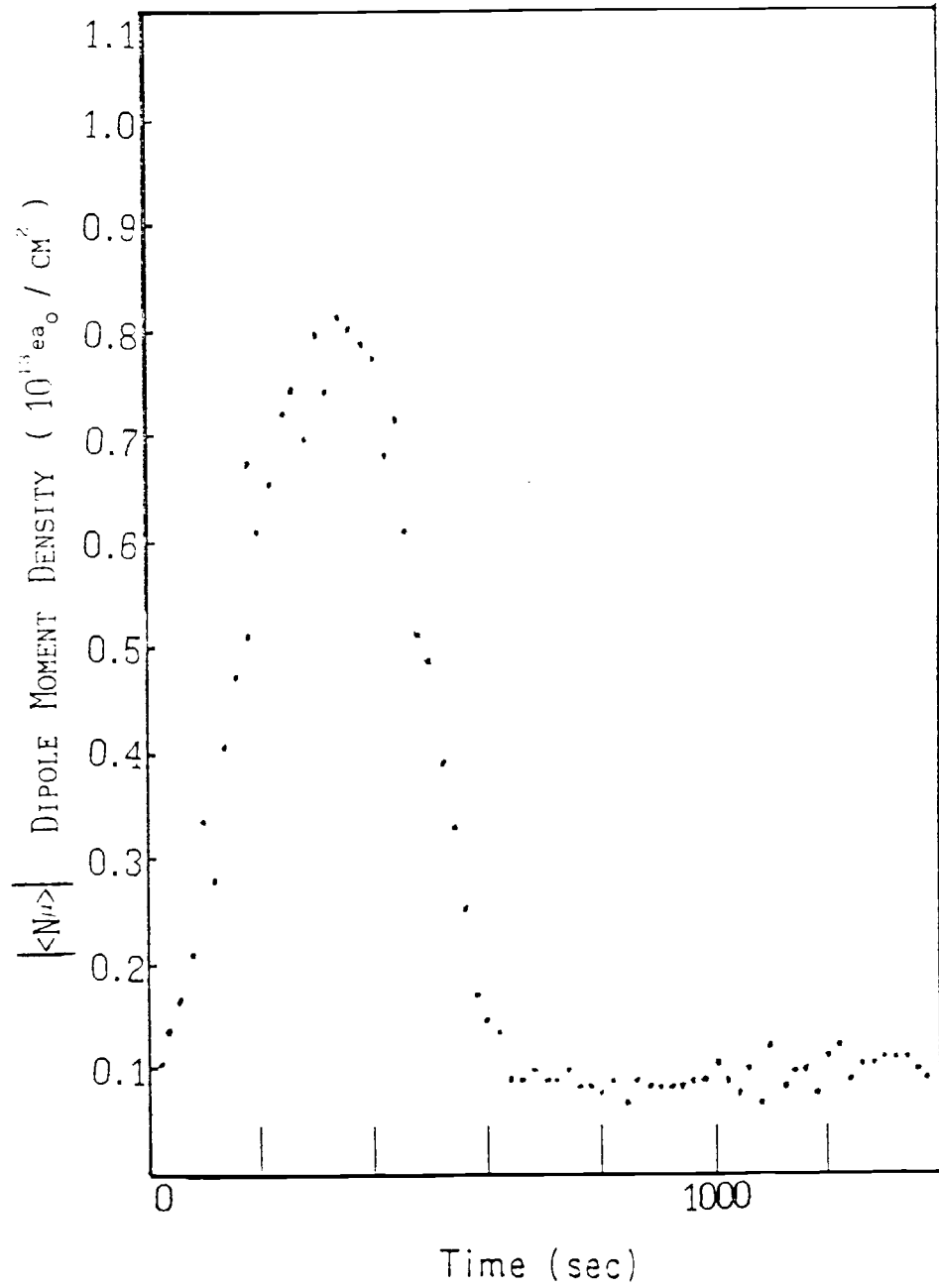


Fig. 7-2b Dipole-Moment Density: Ni Substrate: Constant CO

decreased rapidly from the zero-coverage limit of  $s = 0.9$  to  $s \ll 0.1$  at a coverage of 0.3 monolayers.<sup>41</sup> Therefore, these data are interpreted in the light of their work.

The information from Horgan and King is used to interpret the data in Fig. 7-2b. A significant amount of CO may adsorb in the initial channel or channels, and the sticking probability is assumed to have decreased significantly after 10 channels. However, the CO may continue to adsorb but with a reduced sticking probability.

The CO particle current in this experiment is 0.018/s, which is significantly lower than the particle current for the experiments in Sec. 6.3.1.1. The conditions of this experiment allow the use of Eq. (5-15) from Sec. 5.2.1 for the analysis of the difference in  $|\langle N\mu \rangle|$  between the case with no introduced adsorbate and CO as adsorbate. The duration of the experiment is short compared to  $1/s_w c_w$  and  $1/s_a c_a$ . Figure 7-2c shows the difference  $\Delta|\langle N\mu \rangle|$  vs  $t$  obtained by subtracting the data in Figs. 7-2a and 7-2b. Eq. (5-15) is

$$\frac{\Delta|\langle N\mu \rangle|}{\Delta t} \cong - \frac{\mu_a s_a c_a}{2A_s} . \quad (5-15)$$

The product  $\mu_a s_a$  may be calculated from the slope of the data in Fig. 7-2c directly, without assumptions about the value or coverage dependence of  $\mu_a$  and  $s_a$ . The data are not considered after  $\Delta|\langle N\mu \rangle|$  begins to decrease because the dipole moment density for CO on Ni has reached a stable minimum by this time

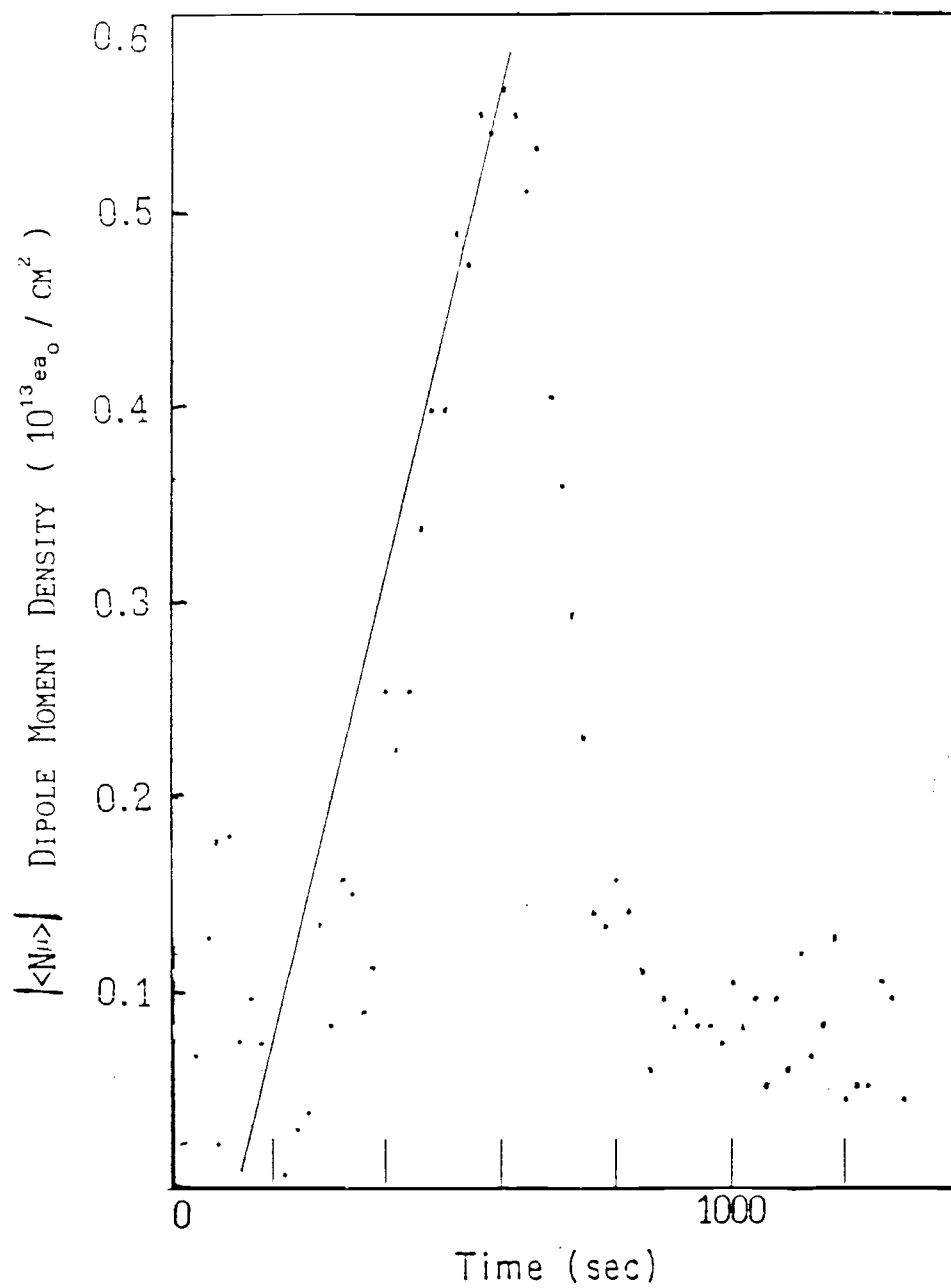


Fig. 7-2c Dipole-Moment Density Difference: CO on Ni Substrate

and the diffusion of CO around a mesh filament may be appreciable; refer to Sec. 2.1.3. The slope of the plot in Fig. 7-2c is  $(0.0010 \pm 0.00015) \times 10^{13} \text{ ea}_0/\text{cm}^2 \cdot \text{s}$ . Therefore,  $\mu_a s_a = (2.8 \pm 0.4) \times 10^{-3} \text{ ea}_0$ . The product  $\mu_a s_a$  implies that if  $\mu_a$  is taken to be  $0.1 \text{ ea}_0$ , as measured by Campuzano,<sup>34</sup> then the sticking probability may be inferred to be  $s_a = (2.8 \pm 0.4) \times 10^{-2}$ . The experiments presented by Horgan and King, in reference 41, report that for this value of the sticking probability the CO coverage is 0.6 monolayer. A coverage of 0.6 ML is near the accepted saturation coverage for CO on Ni, i.e. 0.55 monolayers.<sup>34</sup>

## 7.2 O<sub>2</sub> Adsorption on Ni

The adsorption of O<sub>2</sub> on Ni is analyzed from the data presented in Sec. 6.3.2. Work presented in the literature reported important properties of O<sub>2</sub> on Ni. C. Benndorf et al. reported that O<sub>2</sub> forms a (2 × 1) surface structure on a Ni at saturation coverage, implying that at saturation coverage

$$A_{\text{O}_2} \cong 2A_{\text{Ni}}.^{43}$$

Masuda et al. also found by work function measurements that at zero coverage the dipole moment for O<sub>2</sub> on Ni(111) was  $\mu_{\text{O}_2} = 0.14 \text{ ea}_0$ .<sup>39</sup> Brundle found that at low coverage O<sub>2</sub> on Ni(100) has a (2 × 2) surface structure and also reported that the sticking probability for O<sub>2</sub> on Ni decreases from  $s = 1$  at

zero coverage to  $s \ll 0.1$  at  $\theta = 0.3$ .<sup>35</sup> Horgan and King found that  $O_2$  adsorbs onto clean Ni with unity sticking probability to a coverage of 0.2 monolayer and then the sticking probability declines dramatically for  $\theta > 0.2$ .<sup>41</sup>

Figure 7-3a shows the  $|\langle N\mu \rangle|$  vs  $t$  found from the data in Fig. 6-6b, Sec. 6.3.2.1. Fig. 7-3b shows only channels 20 to 80 from Fig. 7-3a. The crosses (+) indicate introduction of  $O_2$  onto the mesh, and the dots (•) indicate that no  $O_2$  is introduced. The relevant particle currents are  $c_1 = 0.19$  /s,  $c_2 = 0.25$  /s,  $c_3 = 0.28$  /s,  $c_4 = 0.35$  /s and  $c_5 = 0.12$  /s. The surface temperature in this case is  $T_s = 300 \pm 5$  K. Since the duration of this experiment is short compared to  $1/s_a c_a$ , Eq. (5-15) from Sec. 5.2.1 may be used in calculations to determine  $\mu_a s_a$ :

$$\frac{\Delta \langle N\mu \rangle}{\Delta t} = - \frac{\mu_a s_a c_a}{2A_s} \quad (5-15)$$

Equation (5-11) is used to determine the product  $\mu_a s_a$  where the particle current of  $O_2$  on Ni is  $c_3 = 0.28$  /s, the initial slope in Fig. 7-3b is  $(0.0017 \pm 0.0003) \times 10^{13} e a_0 / \text{cm}^2 \cdot \text{s}$ , and the unit area for  $O_2$  on Ni is taken to be  $2A_{Ni}$ . Only the initial slope is taken because after 10 channels the concentration of  $O_2$  on the surface approaches saturation and the sticking probability falls rapidly from unity. The product  $\mu_a s_a = (1.5 \pm 0.3) \times 10^{-4} e a_0$  in the low coverage limit. Repeating the same procedure for region where  $c_4$  is the particle current in Fig. 7-3b yields the product

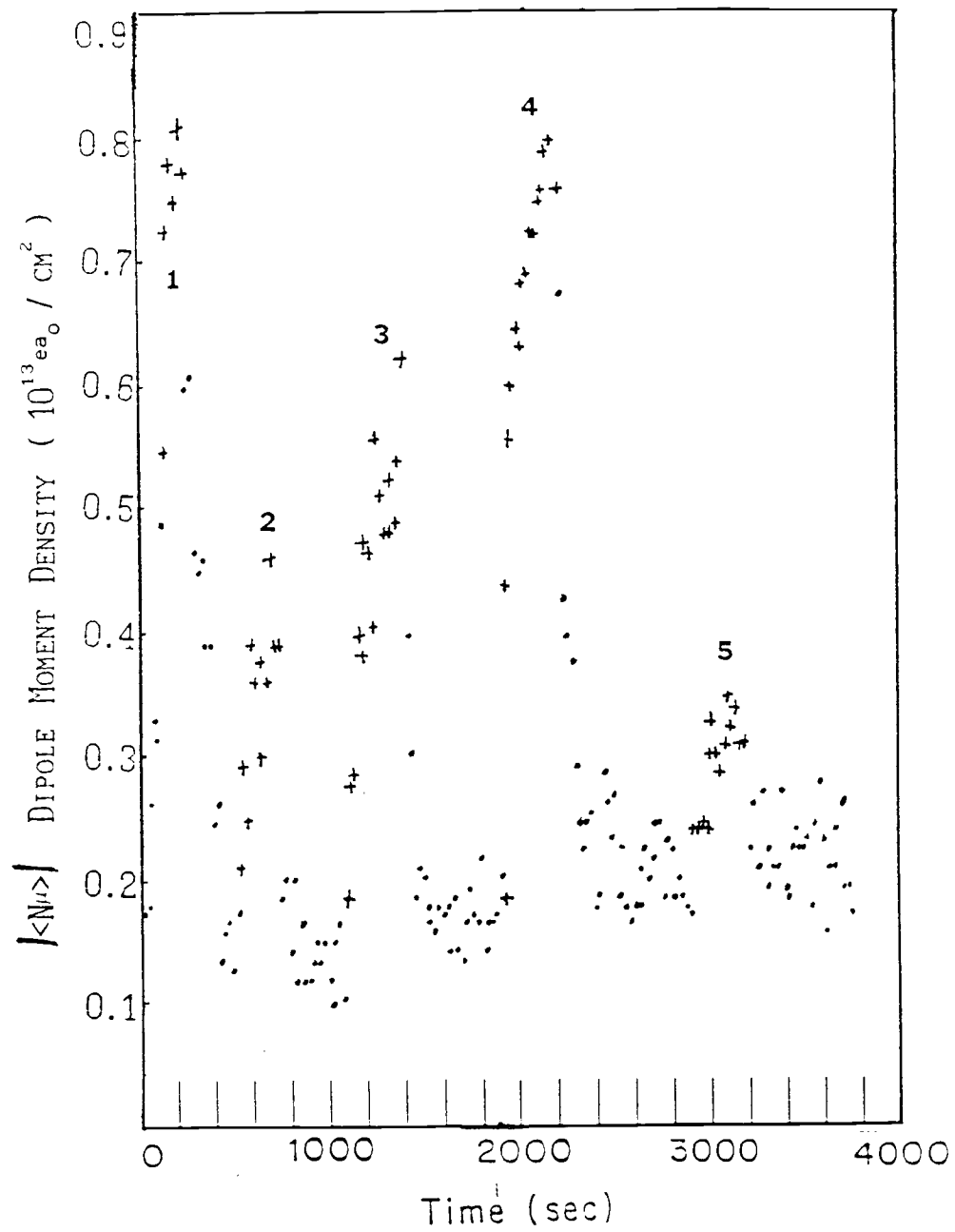


Fig. 7-3a Dipole-Moment Density: Ni Substrate: O<sub>2</sub> Gated

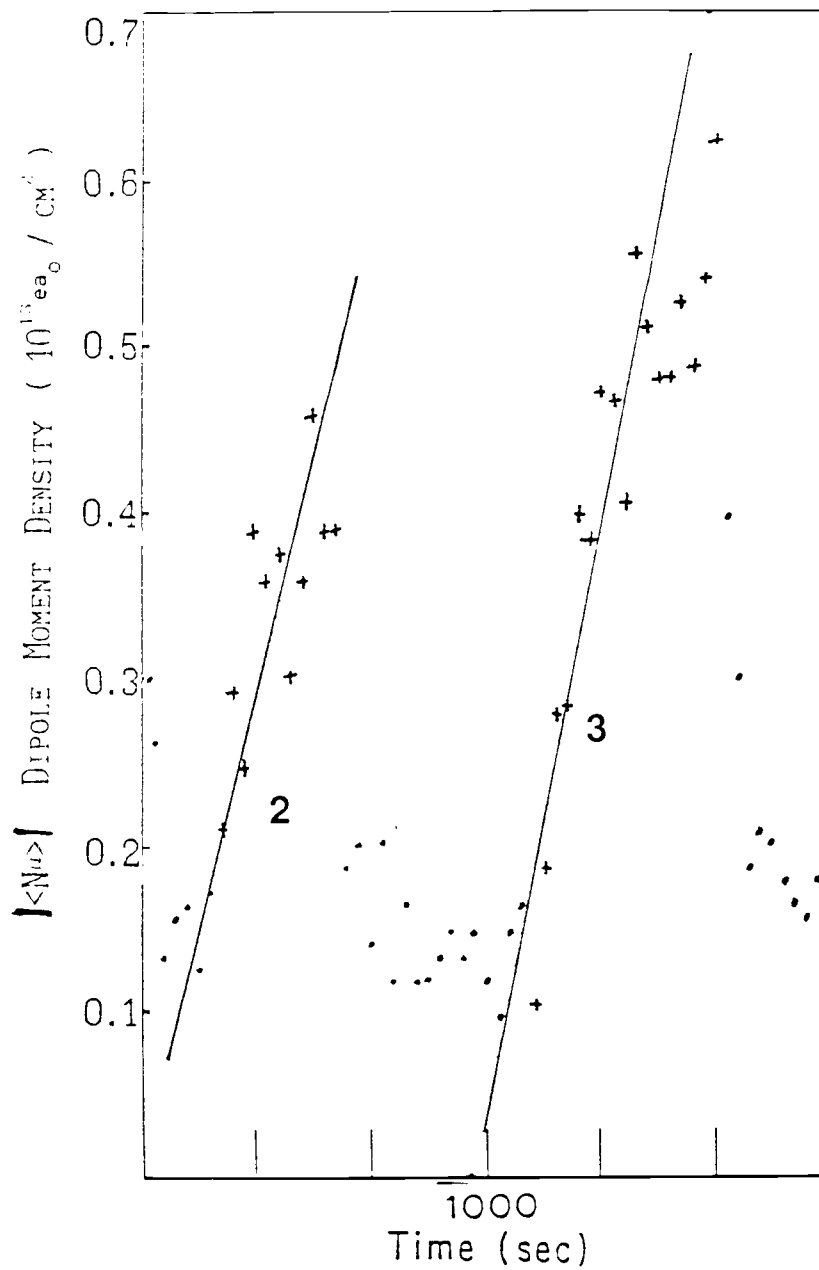


Fig. 7-3b Dipole-Moment Density: Ni Substrate:  $\text{O}_2$  Gated  
(400 s Through 1600 s Shown)

$$\mu_a s_a = (1.7 \pm 0.3) \times 10^{-4} ea_0.$$

The data from Figs. 7-3a and 7-3b can also be used for the calculation of the desorption energy for  $O_2$  on Ni. Eq. (5-23) describes the dependence of  $E_d$  on the change in the dipole-moment density produced by the introduction of  $O_2$ . Equation (5-23) is valid after equilibrium between adsorption and desorption has been reached.

The desorption energy is calculated by taking  $\mu_a s_a$  to be  $(1.7 \pm 0.3) \times 10^{-4} ea_0$  from the previous calculation and  $c_4 = 0.34/s$ . The change in dipole moment density is  $(0.70 \pm 0.05) \times 10^{13} ea_0/cm^2$ . The desorption energy is then calculated to be  $0.89 \pm 0.05$  eV.

Figures 7-4a and 7-4b show  $|\langle N\mu \rangle|$  vs  $t$  corresponding to Figs. 6-7a and 6-7b from Sec. 6.3.2.1. For region 2 in Fig. 7-4b the particle current was  $c_2 = 0.33 /s$  and the surface temperature of the Ni substrate was reduced to  $T_s \cong 275 \pm 5$  K. In this case  $s_a c_a \gg s_w c_w$ ; therefore, Eq. (5-15) is appropriate. The initial slope of the data in region 2 is  $(0.004 \pm 0.0007) \times 10^{13} ea_0/cm^2 \cdot s$  and the product  $\mu_a s_a$  is calculated to be  $(3.0 \pm 0.5) \times 10^{-4} ea_0$ .

Figures 7-5a and 7-5b show  $|\langle N\mu \rangle|$  vs  $t$  corresponding to the data in Figs. 6-8a and 6-8b, respectively, from Sec. 6.3.2.2. The surface temperature of the mesh was elevated in this experiment to  $T_s = 340 \pm 5$  K. The particle current is  $c = 0.072 /s$  in Fig. 7-5b. Figure 7-5c shows the difference in

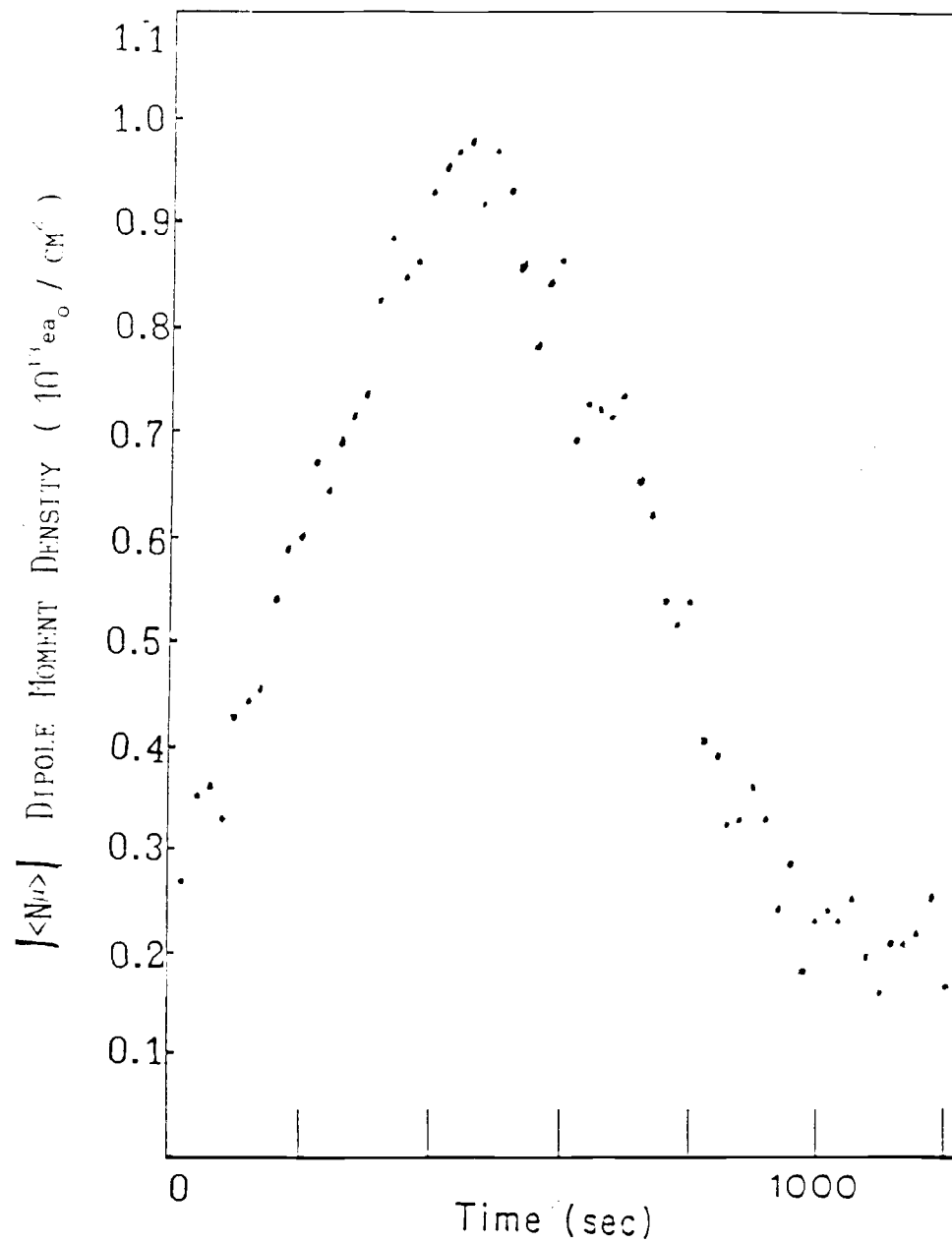


Fig. 7-4a Dipole-Moment Density: Ni Substrate:

No Introduced Adsorbate

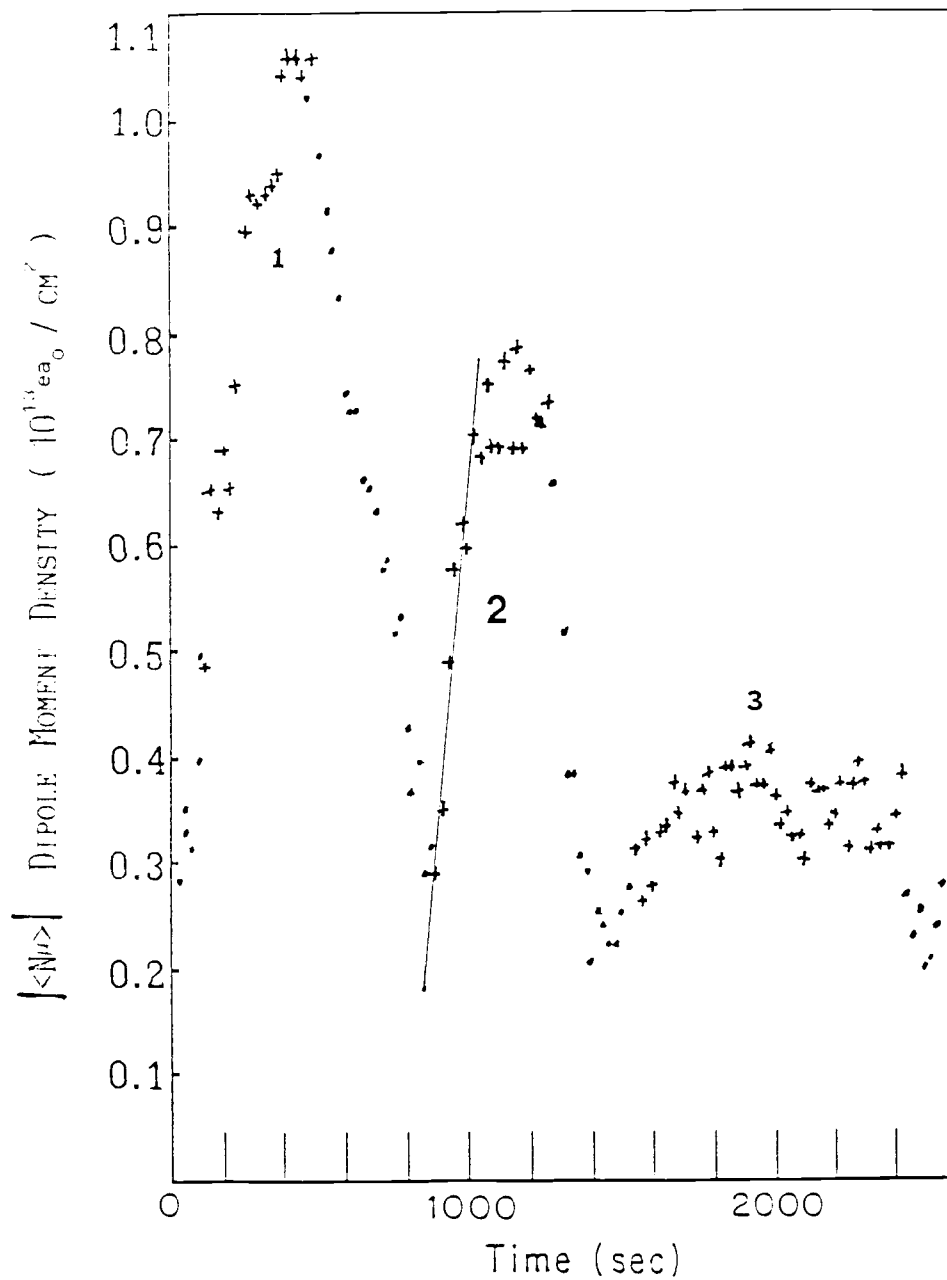


Fig. 7-4b Dipole-Moment Density: Ni Substrate: O<sub>2</sub> Gated

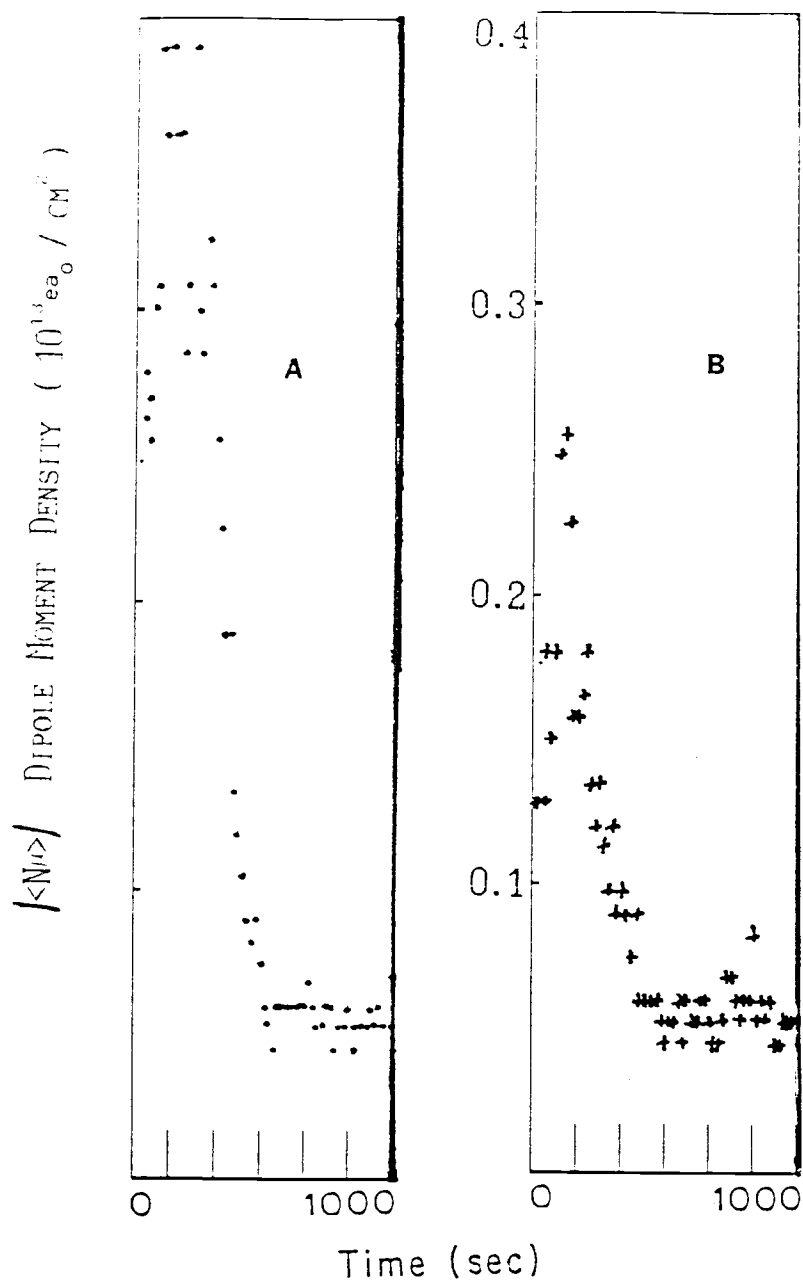


Fig. 7-5 a) Dipole-Moment Density: Ni Substrate  
 No Introduced Adsorbate  
 b) Dipole-Moment Density: Ni Substrate: Constant  $\text{O}_2$

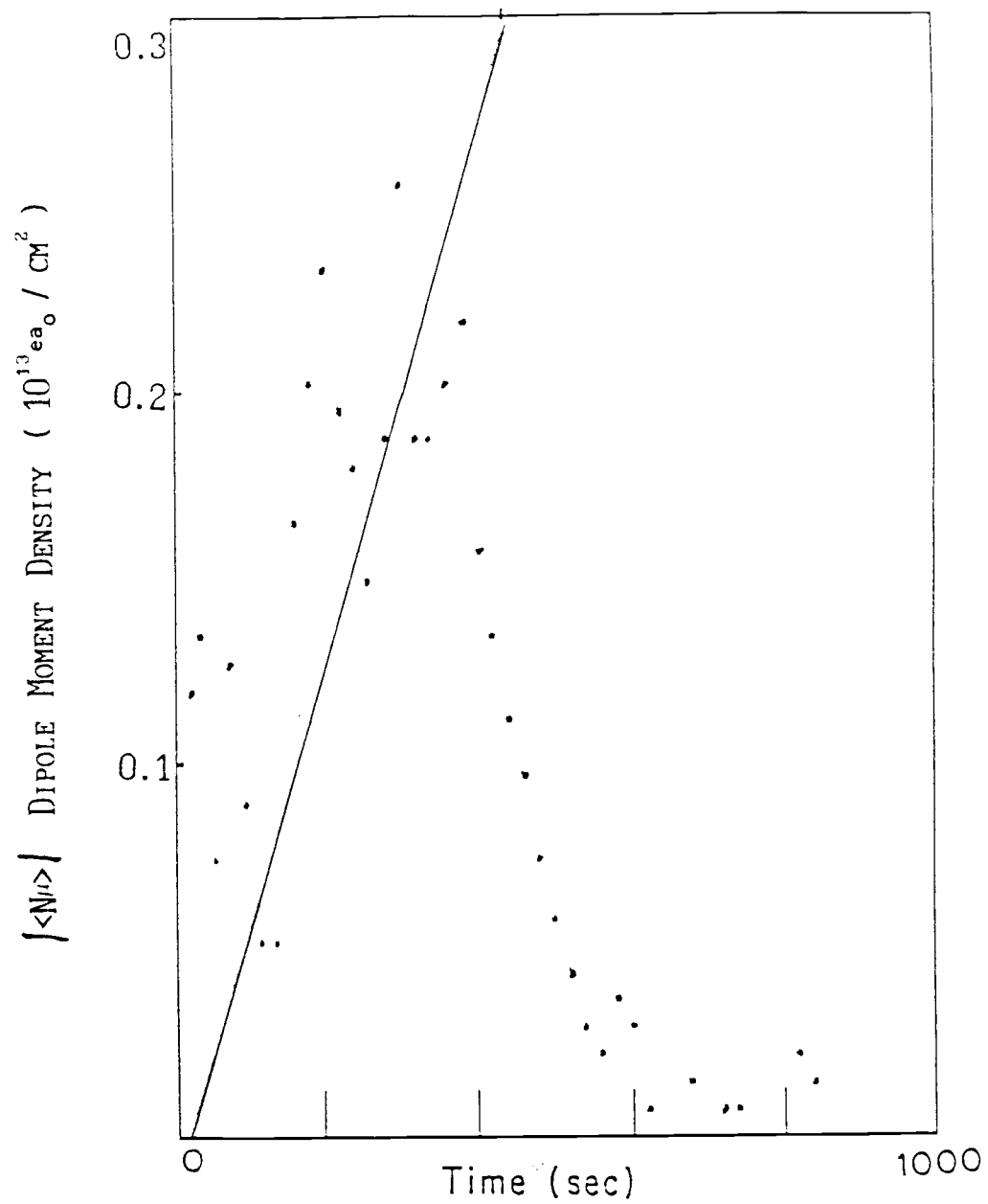


Fig. 7-5c Dipole-Moment Density Difference:  $\text{O}_2$  on Ni Substrate

$|\langle N\mu \rangle|$  due to the adsorption of  $O_2$  on Ni. The experimental conditions are correct for the case described by Eq. (5-11),  $s_{ww} \gg s_{aa}$  and  $s_{wt} \ll 1$ . The slope of the data from Fig. 7-5c is  $(0.00075 \pm 0.0002) \times 10^{13} e a_0 / \text{cm}^2 \cdot \text{s}$ . The product of  $\mu_a s_a$  is then calculated to be  $(2.6 \pm 0.6) \times 10^{-4} e a_0$ . Again only the initial slope is taken because the dipole moment density reaches a stable minimum after 400 s.

### 7.3 $H_2O$ Adsorption on Au

S. Trasatti<sup>40</sup> reports that  $H_2O$  binds through the oxygen onto a Au substrate, thus determining the direction of the electric moment to be outward (negative to positive). R.P. Bajpai et al.<sup>32</sup> reported the results of a work function change experiment. A monolayer of  $H_2O$  on Au produced a change in the work function that implies a dipole moment of  $\mu_{H_2O} = 0.09 e a_0$ . Other properties of  $H_2O$  on Au are not found in the literature.

Figure 7-6 shows  $|\langle N\mu \rangle|$  vs  $t$  found from the data in Fig. 6-9b from Sec. 6.3.3. For region 2 the introduced  $H_2O$  particle current is 0.21 /s. The crosses (+) represent data taken when  $H_2O$  was introduced as an adsorbate, and the dots (•) represent data taken with no introduced adsorbate. In region 2, the  $H_2O$  particle current is initiated and the dipole-moment density increases. The increase occurs over approximately 100 s. After approximately 100 s equilibrium between adsorption and desorption is reached. The equilibrium is seen because  $|\langle N\mu \rangle|$  becomes

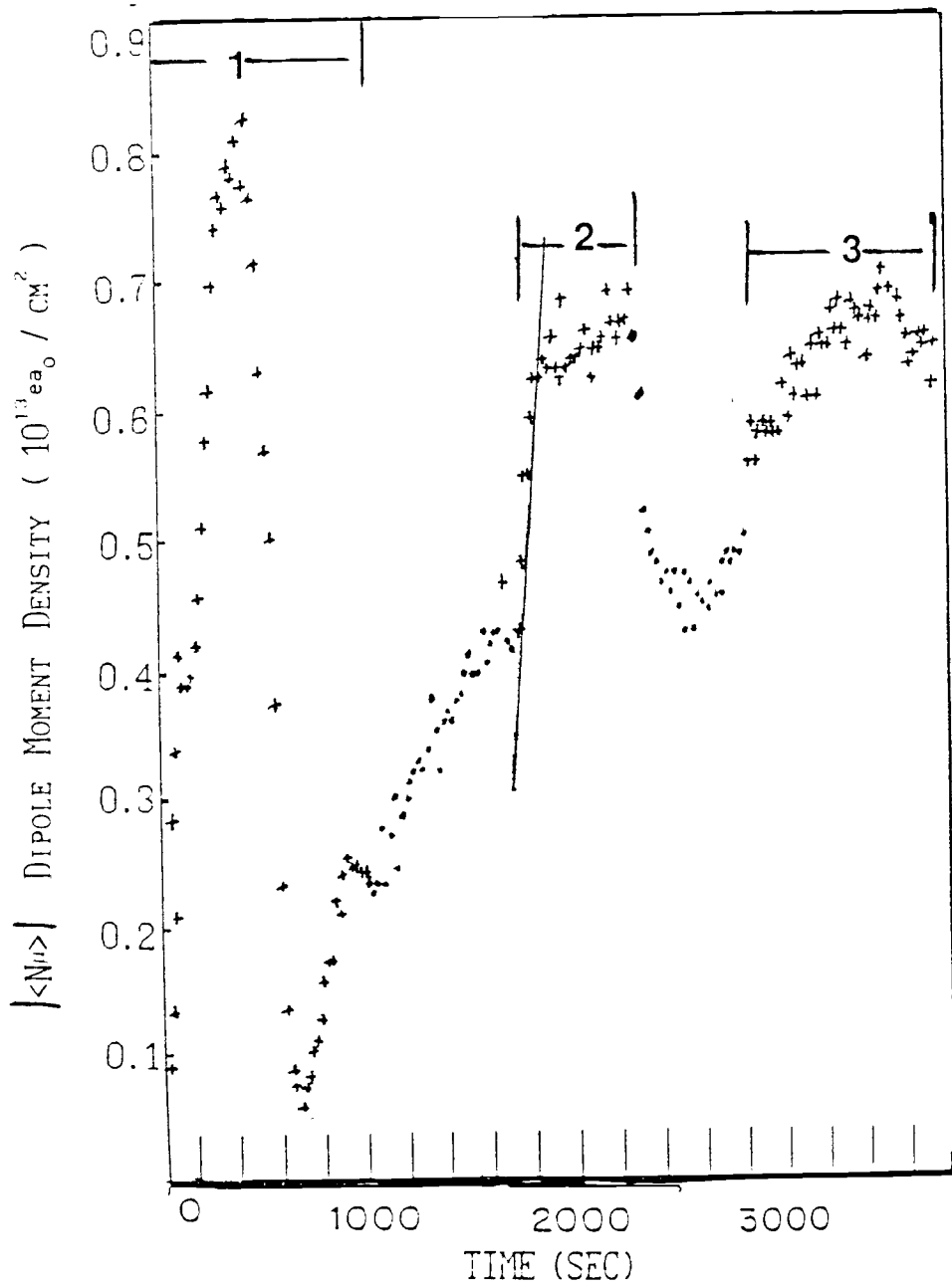


Fig. 7-6 Dipole-Moment Density: Au Substrate:  $H_2O$  Gated

nearly constant after 100 s. For the channels after  $H_2O$  is introduced and before equilibrium has been reached the condition that  $s_w c_w t \gg 1$  and  $s_a c_a t \gg 1$  is met. Therefore, Eq. (5-15) from Sec. 5.2.1 is appropriate in this limit:

$$\frac{\Delta \langle N\mu \rangle}{\Delta t} \cong - \frac{\mu_a s_a c_a}{2A_s}, \quad (5-15)$$

The slope of the data during these channels is  $(0.0023 \pm 0.0002) \times 10^{13} \text{ ea}_0/\text{cm}^2 \cdot \text{s}$ . The product  $\mu_a s_a$  is calculated to be  $(1.1 \pm 0.1) \times 10^{-3} \text{ ea}_0$ .  $A_{H_2O}$  is assumed to equal  $3 A_{Ni}$  as is the case for  $H_2O$  on Ni.

After equilibrium has been achieved between desorption and adsorption, Eq. (5-23) applies. This equation allows the calculation of the desorption energy for  $H_2O$ .

$$\Delta | \langle N\mu \rangle | = \frac{\mu_a s_a c_a}{A_s \Gamma}. \quad (5-23)$$

As seen in Fig. 7-6  $| \langle N\mu \rangle |$  changes by  $2.2 \text{ ea}_0 \times 10^{13}/\text{cm}^2$  and with Eq. (5-23) the desorption energy is calculated to be  $0.90 \pm 0.05 \text{ eV}$ .

#### 7.4 $H_2O$ Adsorption on Ni

Madey and Netzer<sup>44</sup> found that the surface pattern for  $H_2O$  on Ni implied that  $A_{H_2O} \cong 3A_{Ni}$ . The  $H_2O$  was found to attach on top of the Ni, bonding through the O; see also refs. 38 and 43. The desorption energy was reported for  $H_2O$  on Ni(111) to be  $E_d = 1.7 \text{ eV}$  with a surface temperature  $T_s = 80 \text{ K}$ .<sup>44</sup> Holloway *et*

a.<sup>45</sup> found that H<sub>2</sub>O orients on the Ni surface with the oxygen binding to the Ni substrate; this gives a dipole moment pointing outward.

Figures 7-7a and 7-7b show  $|\langle N\mu \rangle|$  corresponding to the data in Figs. 6-10a and 6-10b from Sec. 6.3.4. Figure 7-7c is the difference between the transmissions without and with the introduced adsorbate (Figs. 7-7a and 7-7b, respectively). The particle current is 0.21/s, and the conditions of this experiment,  $t \ll 1/s_w c_w$  and  $t \ll s_a c_a$ , allow the use of Eq. (5-15) in this evaluation. The slope of the data in Figure 7-7c is  $(0.00033 \pm 0.00015) \times 10^{13} \text{ ea}_0/\text{cm}^2 \cdot \text{s}$ . The product  $\mu_a s_a$  is calculated to be  $(1.3 \pm 0.7) \times 10^{-4} \text{ ea}_0$  in the low coverage limit.

The desorption of H<sub>2</sub>O from the Ni surface is presented in Fig. 6-11 from Sec. 6.3.5. Figure 7-8 shows  $|\langle N\mu \rangle|$  corresponding to these data;  $\ln |\langle N\mu \rangle|$  is plotted vs  $t$ . The desorption occurs when the Ni surface is heated to  $T_s = 350 \pm 5 \text{ K}$ . The data are evaluated with the natural log in the following way  $\Delta \ln(|\langle N\mu \rangle|) / \Delta t = -\Gamma$ , where  $\Gamma = \Gamma_0 e^{-E_d/kT_s}$ . The slope of the curve is -0.004 for which  $E_d$  is calculated to be  $1.05 \pm 0.05 \text{ eV}$ . The H<sub>2</sub>O may bind more strongly to the Ni(111) surface than to the Ni(100) surface. Therefore, the desorption energy for a polycrystalline surface would be expected to be less than the measured value of 1.7 eV.<sup>44</sup>

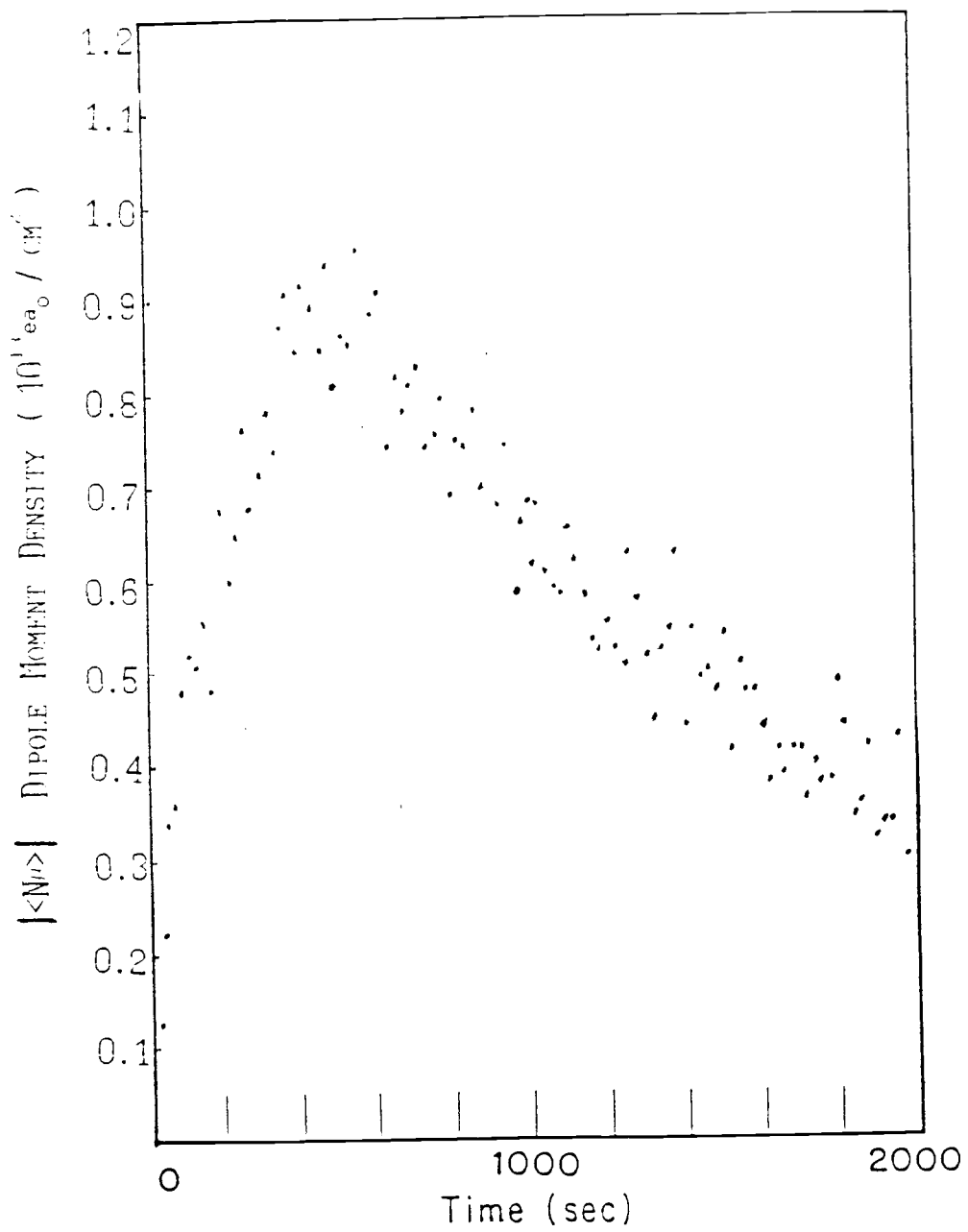


Fig. 7-7a Dipole-Moment Density: Ni Substrate:  
No Introduced Adsorbate

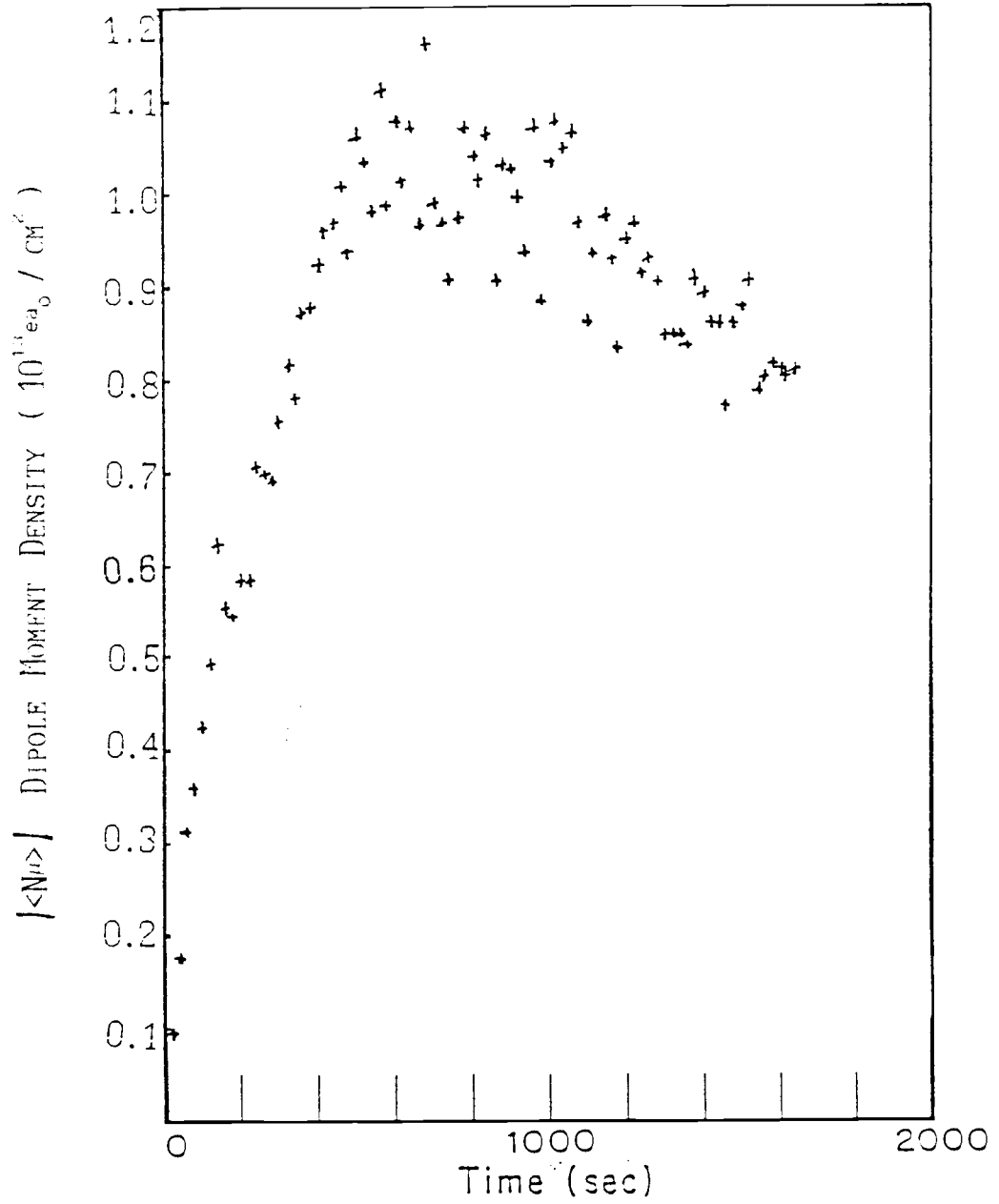


Fig. 7-7b Dipole-Moment Density: Ni Substrate: Constant  $\text{H}_2\text{O}$

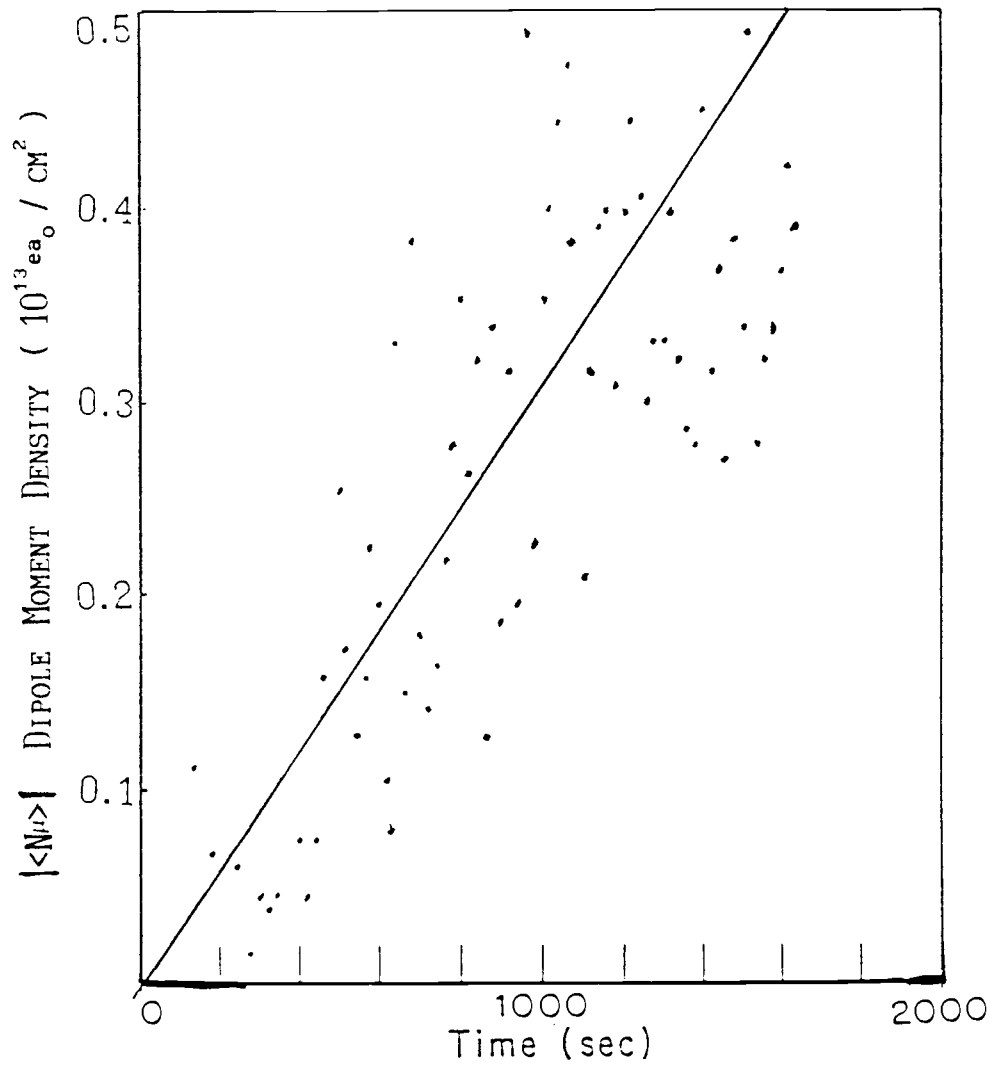


Fig. 7-7c Dipole-Moment Density Difference: H<sub>2</sub>O on Ni Substrate

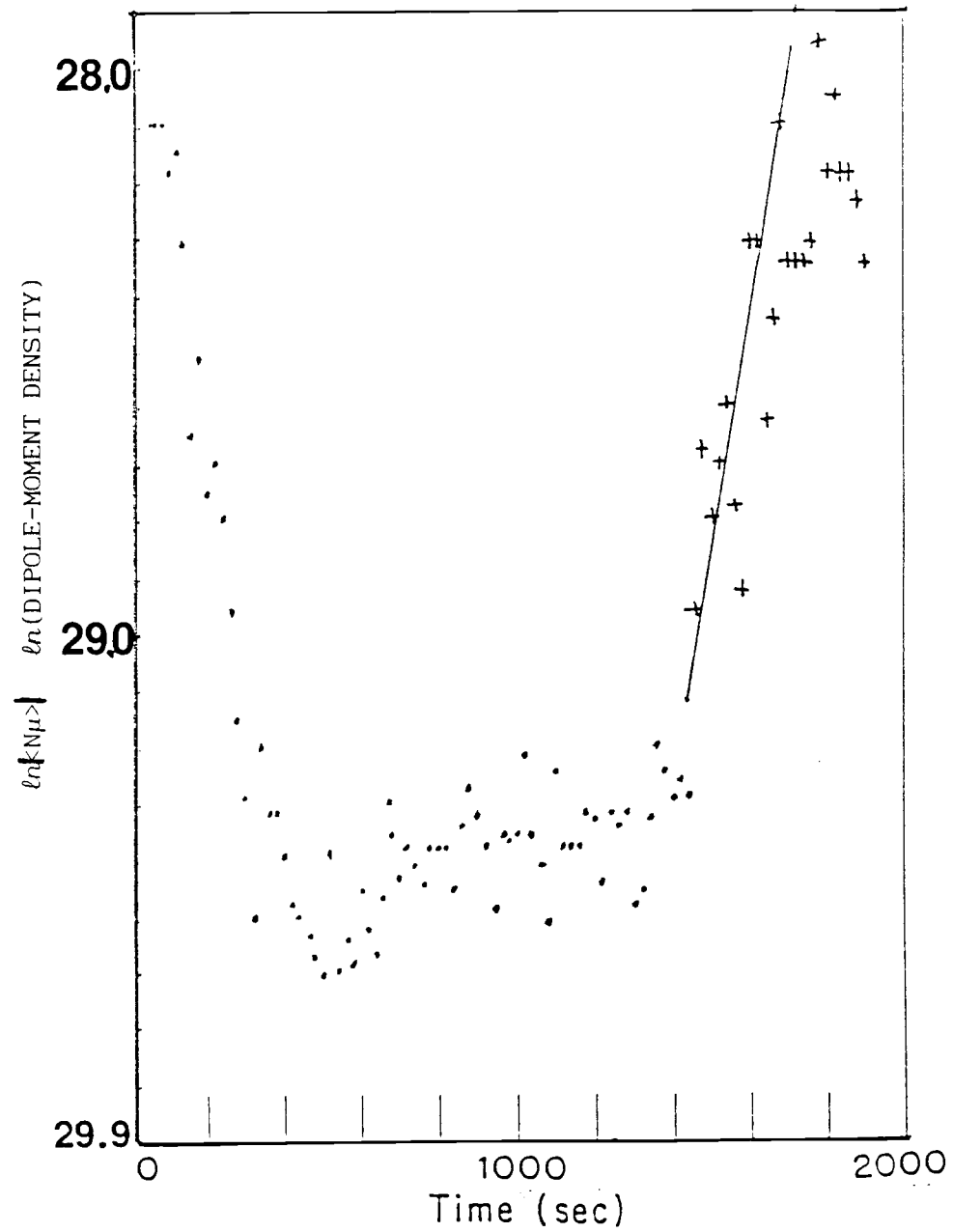


Fig. 7-8 Dipole-Moment Density: Ni Substrate:  $H_2O$  Desorption

### 7.5 SO<sub>2</sub> Adsorption on Au

Figures 7-9a and 7-9b are plots of  $|\langle N\mu \rangle|$  vs  $t$  corresponding to the data in Figs. 6-12a and 6-12b from Sec. 6.3.6. Figure 7-9b shows the accumulation of SO<sub>2</sub> onto Au in less than 200 s (between 1 and 2). SO<sub>2</sub> is introduced with a particle current of 0.23/s and  $\tau_{\text{SO}_2} \gg \tau_{\text{H}_2\text{O}}$ . Therefore, the conditions of the scan allow the use of  $\frac{\Delta \langle N\mu \rangle}{\Delta t} = \frac{\mu_a s_a c_a}{2A_s}$ , Eq. (5-15) from

Sec. 5.2.1. The slope of the plot in Fig. 7-9b is  $(0.0019 \pm 0.0003) \times 10^{13} \text{ea}_0/\text{cm}^2 \cdot \text{s}$ . The product  $\mu_a s_a$  is then calculated to be  $(4.0 \pm 0.6) \times 10^{-4} \text{ea}_0$ .

Figure 7-9c shows the natural log of the difference between the transmission with and without the introduced adsorbate, Figs. 7-9b and 7-9a respectively. The channels at the end of the banks are where the desorption takes place. Therefore,  $\Delta \ln(|\langle N\mu \rangle|)/\Delta t = -\Gamma$ , where  $\Gamma = \Gamma_0 e^{-E_d/kT}$ . The slope of the plot in Fig. 7-9c is 0.0008. This gives a desorption energy  $E_d = 0.93 \pm 0.05 \text{ eV}$ .

### 7.6 SO<sub>2</sub> Adsorption on Ni

Figure 7-10a shows the change in  $|\langle N\mu \rangle|$  corresponding to the difference between  $|\langle N\mu \rangle|$  vs  $t$  in Fig. 6-13a and 6-13c from Sec. 6.3.7. The particle current for SO<sub>2</sub> is 0.044/s. Since  $\tau_{\text{SO}_2} \ll \tau_{\text{H}_2\text{O}}$ , Eq. (5-11) from Sec. 5.2.1 is appropriate. The slope of the plot in Fig. 7-10a is

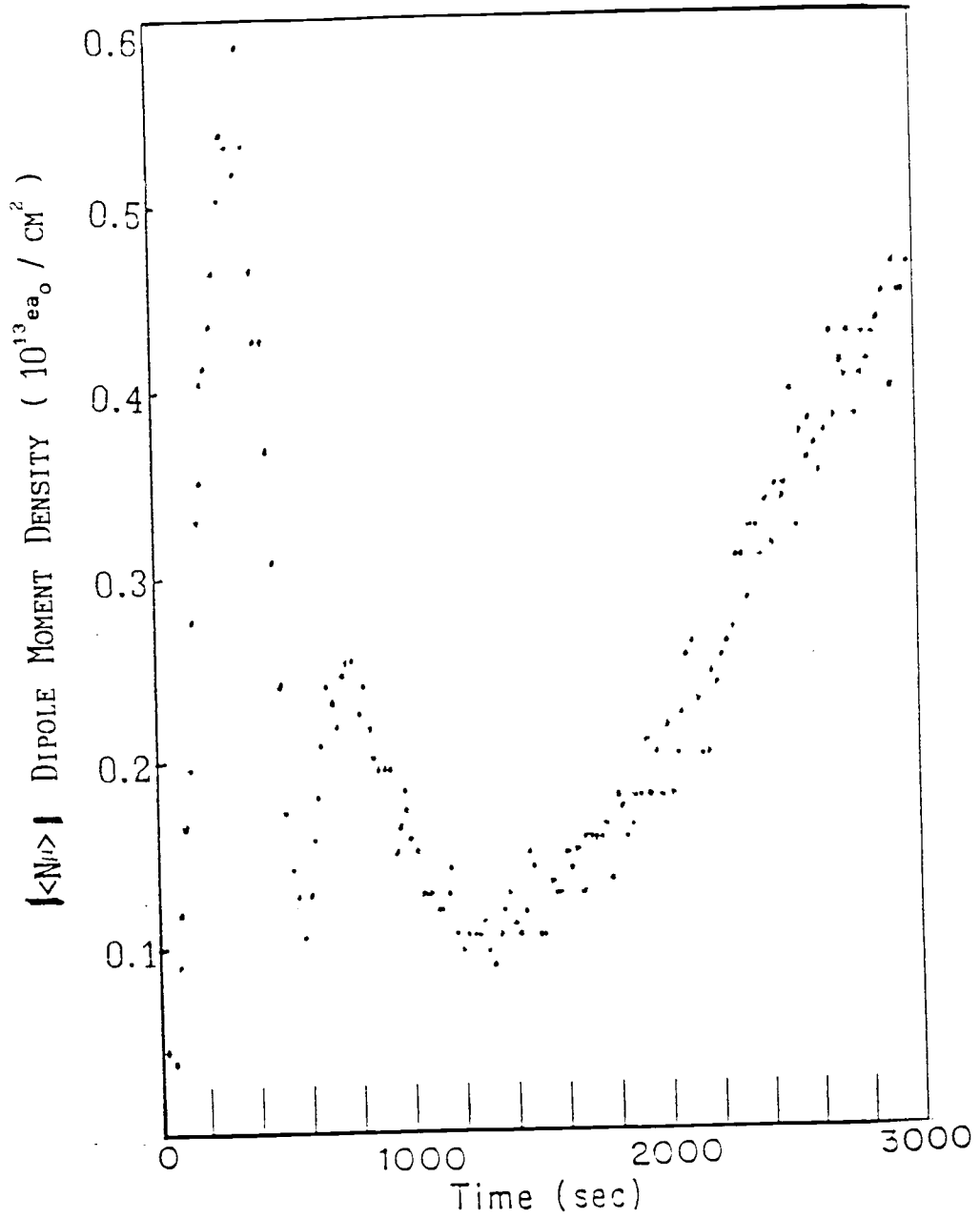


Fig. 7-9a Dipole-Moment Density: Au Substrate:  
No Introduced Adsorbate

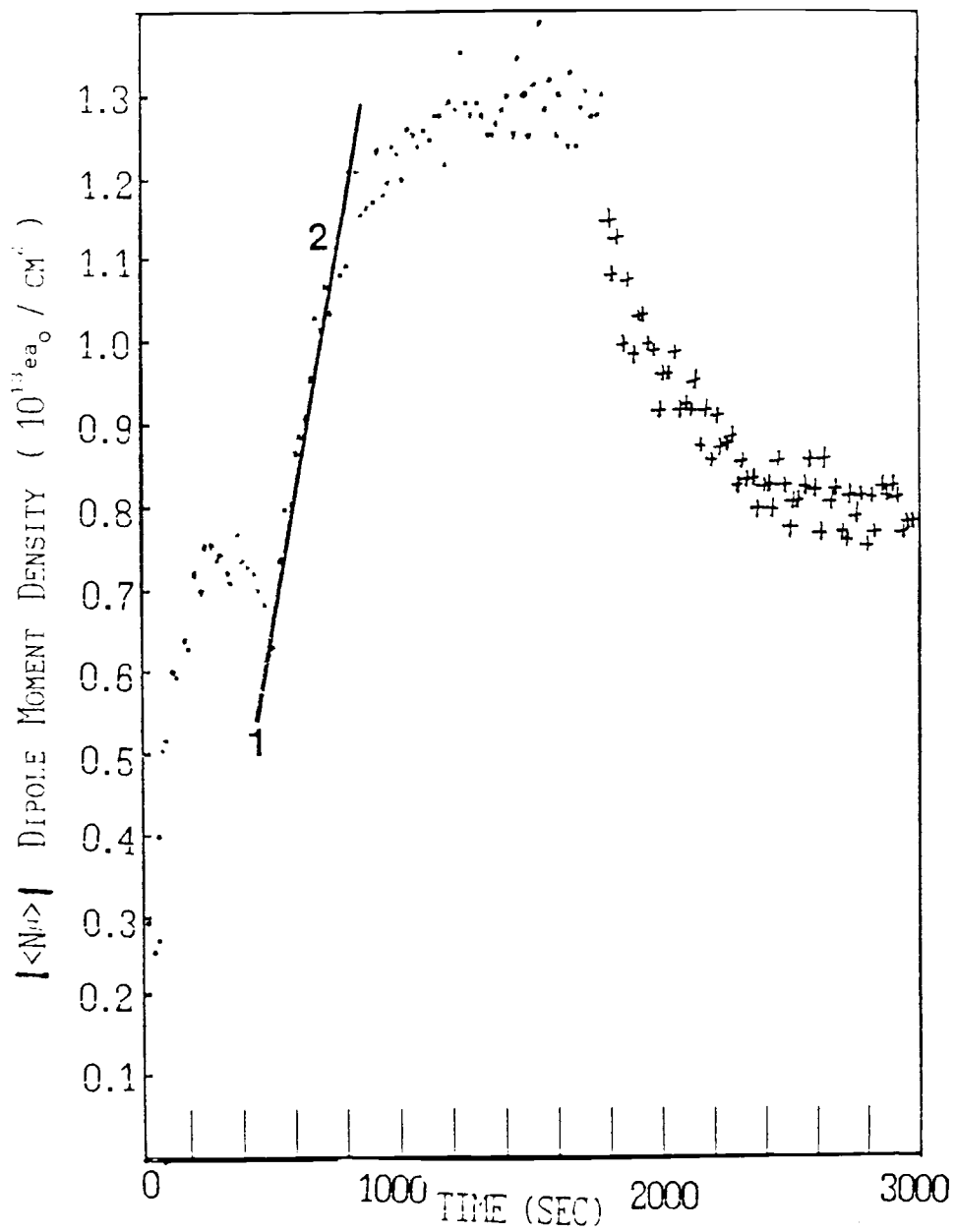


Fig. 7-9b Dipole-Moment Density: Au Substrate:  $\text{SO}_2$  Gated

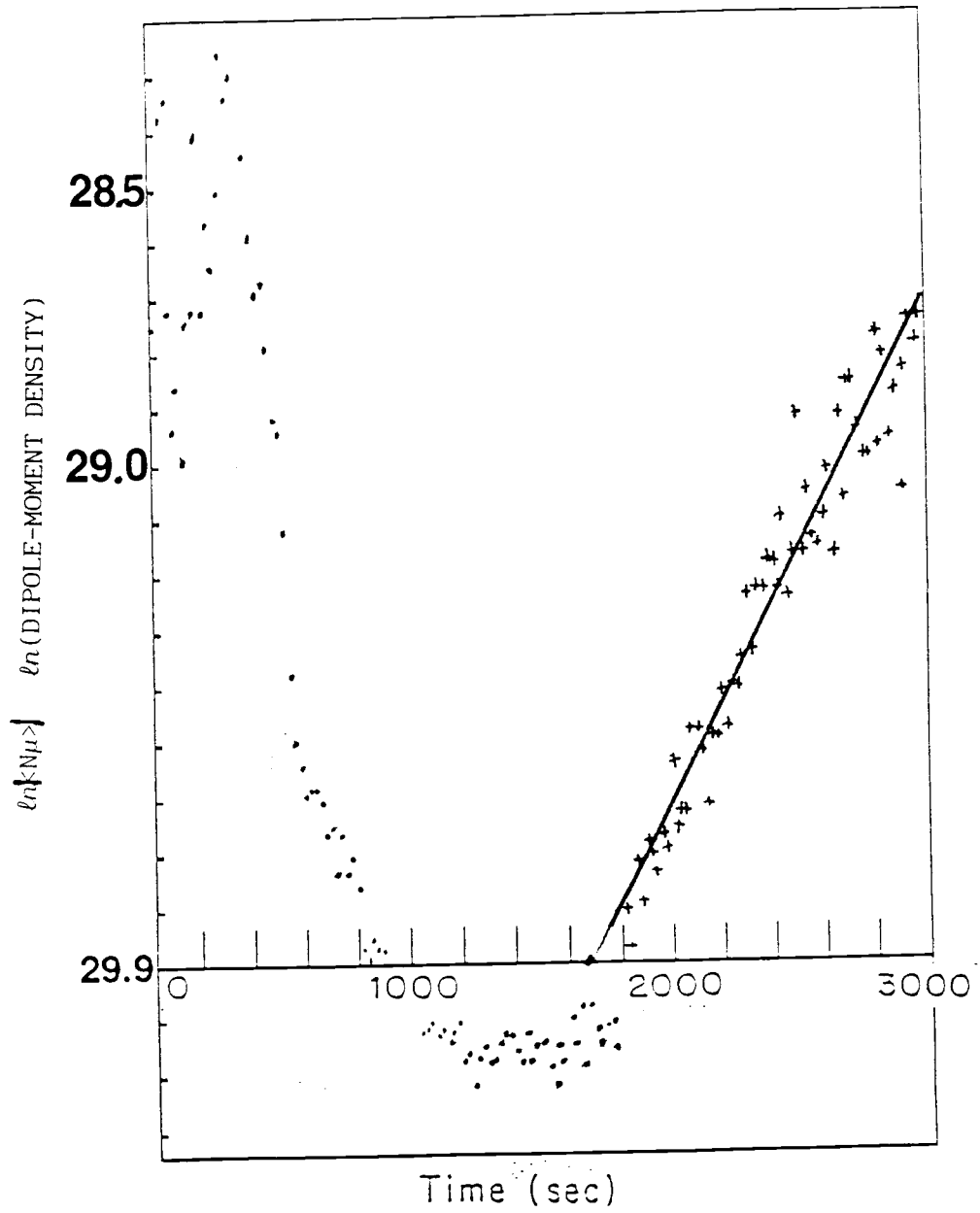


Fig.7-9c Dipole-Moment Density Difference:  $\text{SO}_2$  on Au Substrate

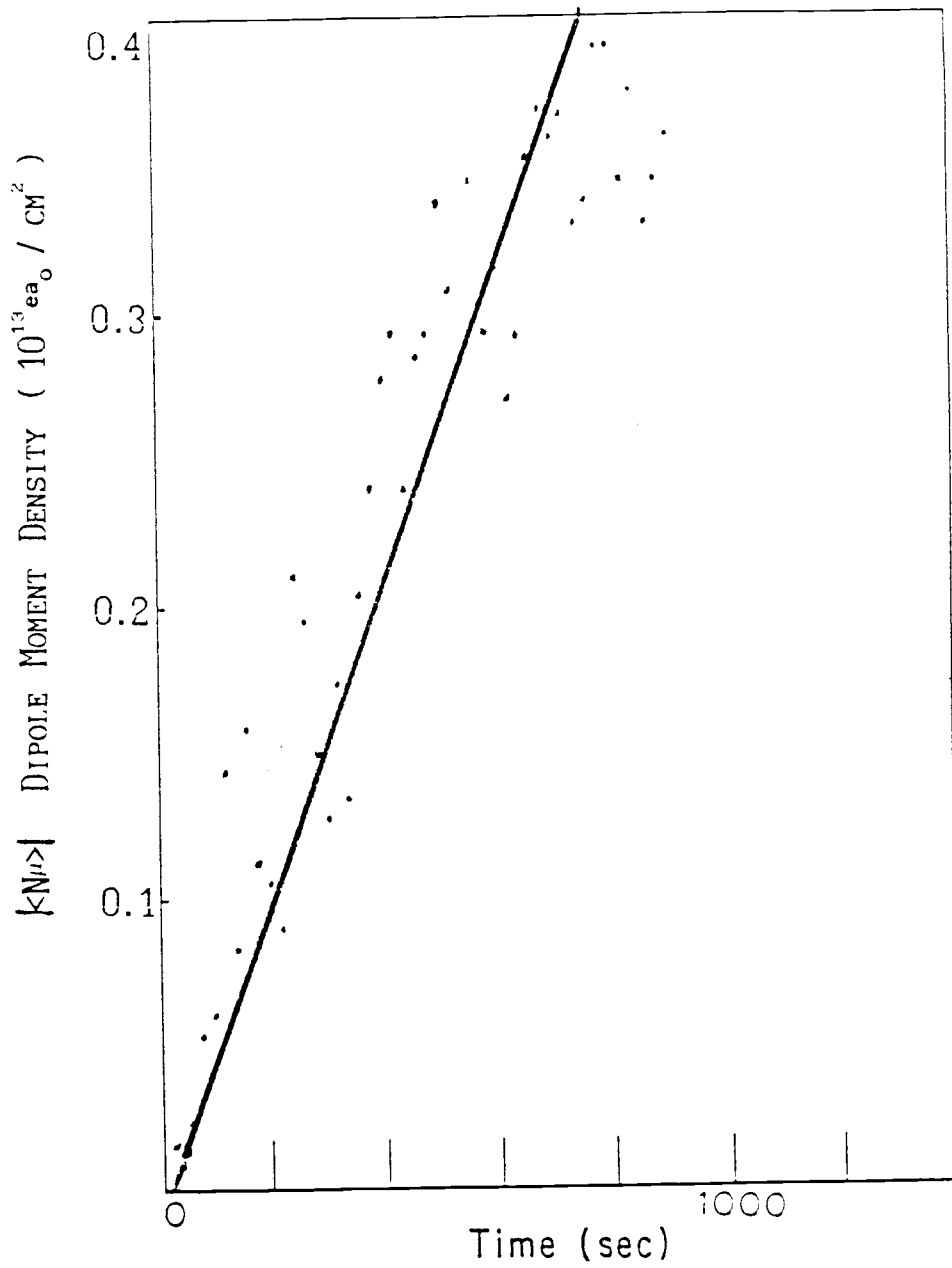


Fig. 7-10a Dipole-Moment Density Difference: SO<sub>2</sub> on Ni Substrate

$(0.00057 \pm 0.00016) \times 10^{13} \text{ ea}_0/\text{cm}^2 \cdot \text{s}$ . The product  $\mu_a s_a$  is found to be  $(5.8 \pm 0.9) \times 10^{-4} \text{ ea}_0$ .

Figure 7-10b shows the change in  $|\langle N\mu \rangle|$  corresponding to the difference between  $|\langle N\mu \rangle|$  vs  $t$  in Fig. 6-13a and in 6-13b. The  $\text{SO}_2$  particle current is 0.059/s. Since  $\tau_{\text{SO}_2} \ll \tau_{\text{H}_2\text{O}}$ , Eq. (5-11) is again appropriate. The slope of the fit in Fig. 7-10b is  $(0.00048 \pm 0.00019) \times 10^{13} \text{ ea}_0/\text{cm}^2 \cdot \text{s}$ . The product  $\mu_a s_a$  is found to be  $(3.0 \pm 0.6) \times 10^{-4} \text{ ea}_0$ . Therefore, for a higher particle current (Fig. 7-10b)  $\mu_a s_a$  is smaller than for a lower particle current. (Fig. 7-10a), indicating a coverage dependence for  $\mu s(\theta)$ . The value of  $\mu_a s_a$  decreases with the  $\text{SO}_2$  coverage.

Long-term exposure of Ni to  $\text{SO}_2$  may be analyzed from Figs. 7-10c, 7-10d, and 7-10e to give values of the  $\text{SO}_2$  dipole moment. Conditions of the experiment for these data allow the use of Eq. (5-14),  $\Delta|\langle N\mu \rangle| = \mu_w - \mu_a/A_s$ . The difference in dipole moment density  $\Delta N\mu$  for long-term exposure is  $(0.42 \pm 0.02) \times 10^{13} \text{ ea}_0/\text{cm}^2 \cdot \text{s}$  (Fig. 7-10d) for the lower particle current and  $(0.37 \pm 0.02) \times 10^{13} \text{ ea}_0/\text{cm}^2 \cdot \text{s}$  (Fig. 7-10e) for the higher particle current. The value of the  $\text{H}_2\text{O}$  dipole moment is found from ref. 32 and Eq. (5-14) is used in the calculation of these values. At the lower particle current (Fig. 7-10e) the moment  $\mu_{\text{SO}_2} = (0.088 \pm 0.004) \text{ ea}_0$  and at the higher particle current (Fig. 7-10d)  $\mu_{\text{SO}_2} = (0.083 \pm 0.0004) \text{ ea}_0$ .

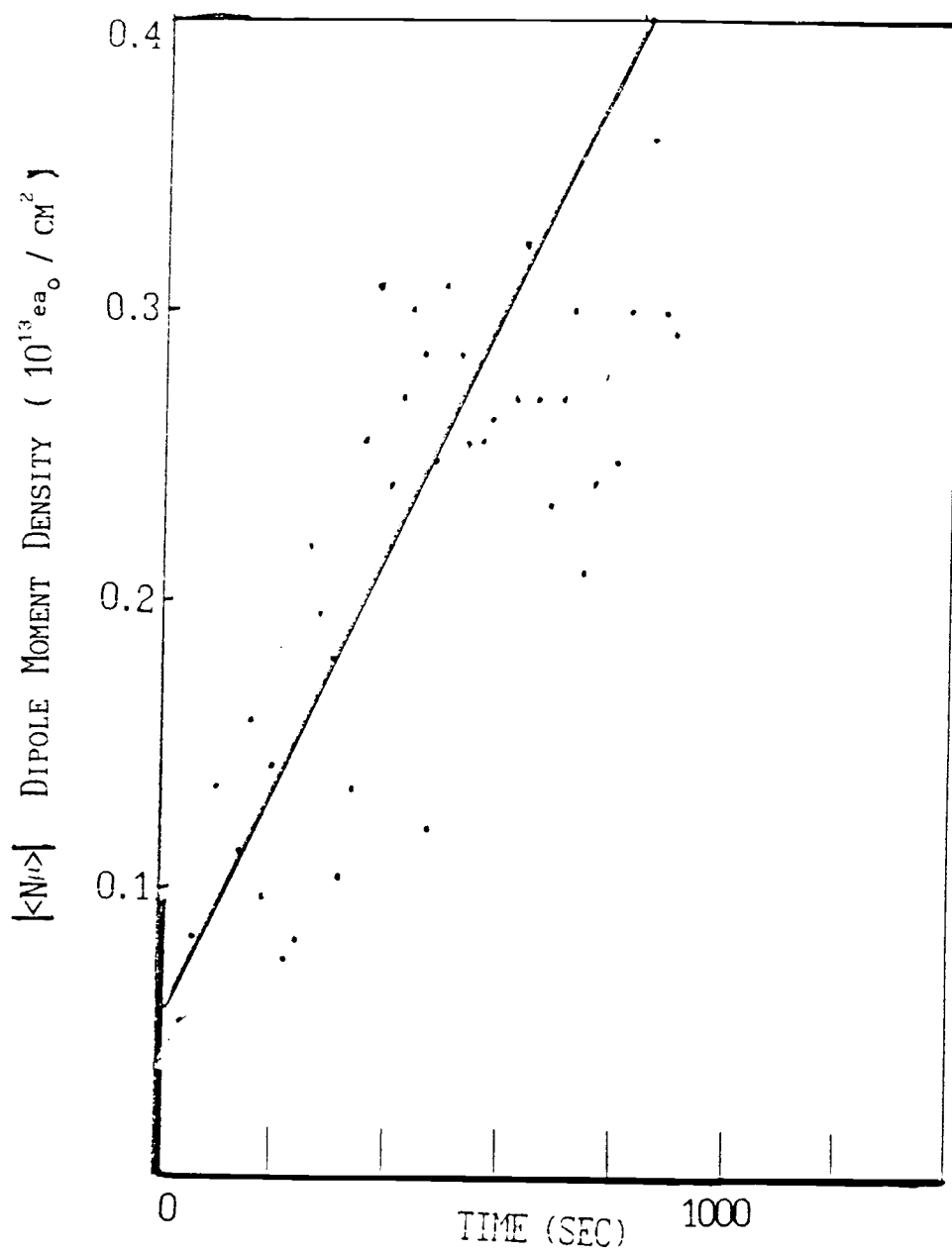


Fig. 7.10b Dipole-Moment Density Difference: SO<sub>2</sub> on Ni Substrate

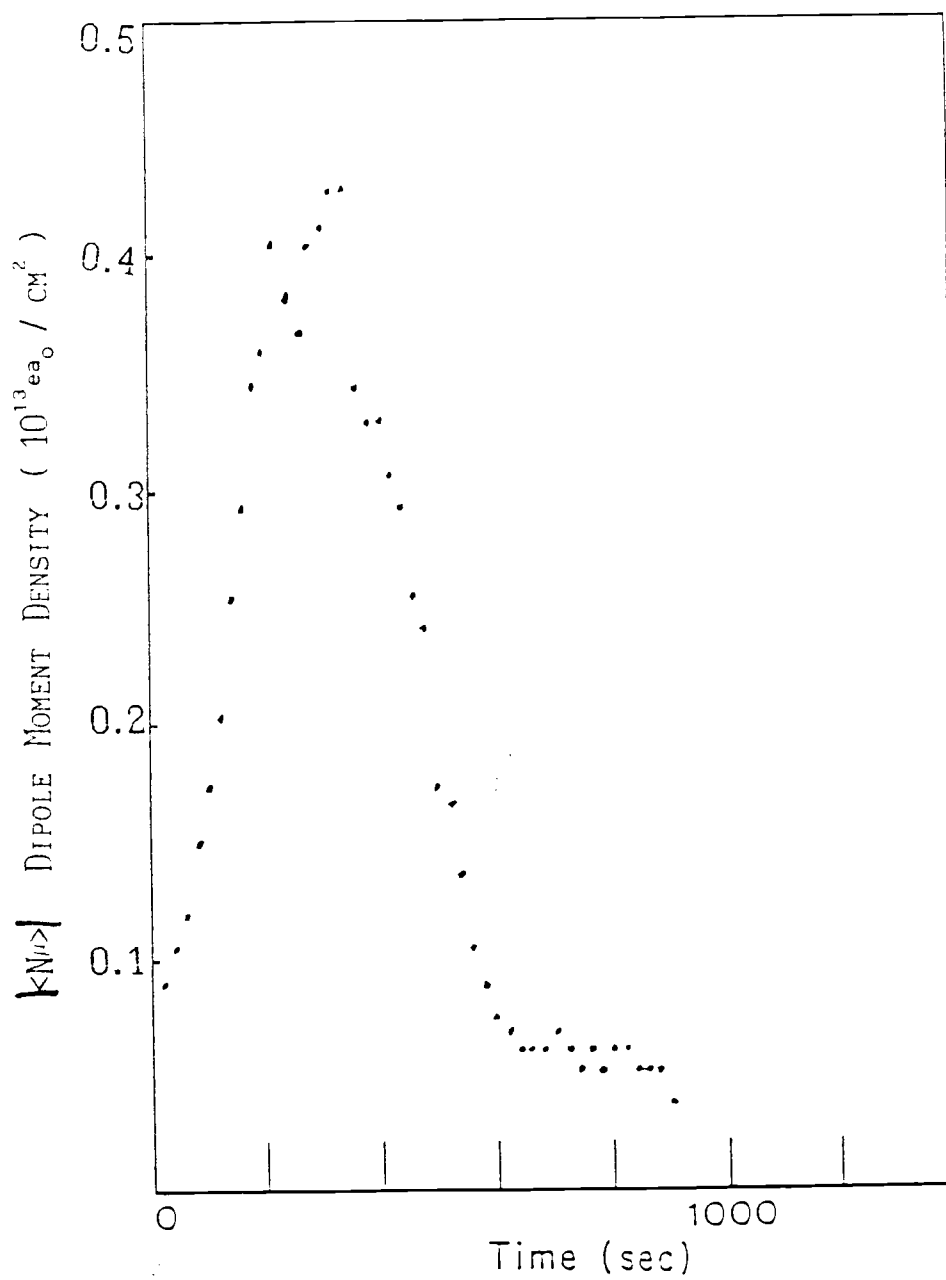


Fig. 7.10c Dipole-Moment Density: Ni Substrate:  
No Introduced Adsorbate

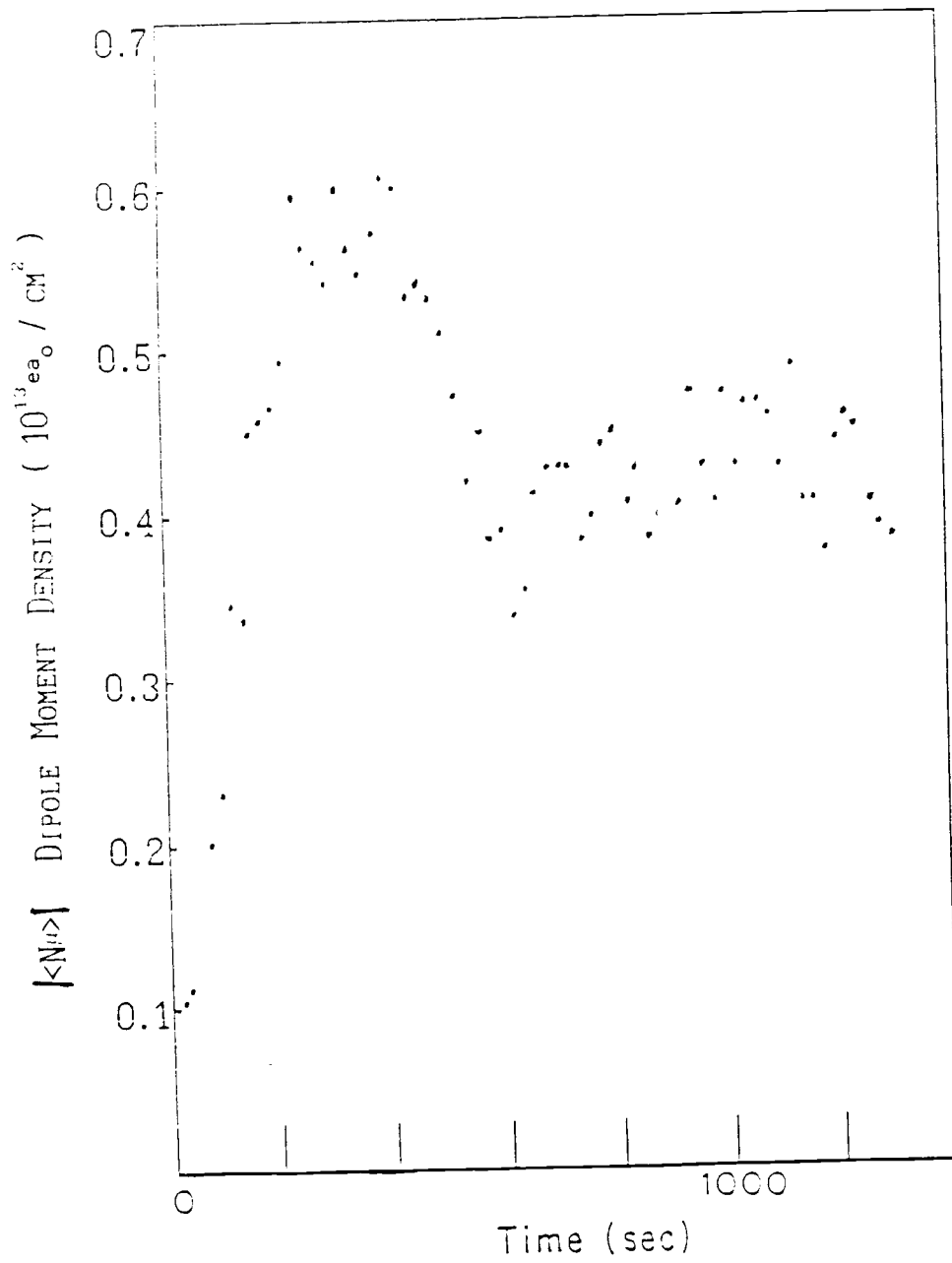


Fig. 7.10d Dipole-Moment Density: Ni Substrate: Constant  $\text{SO}_2$

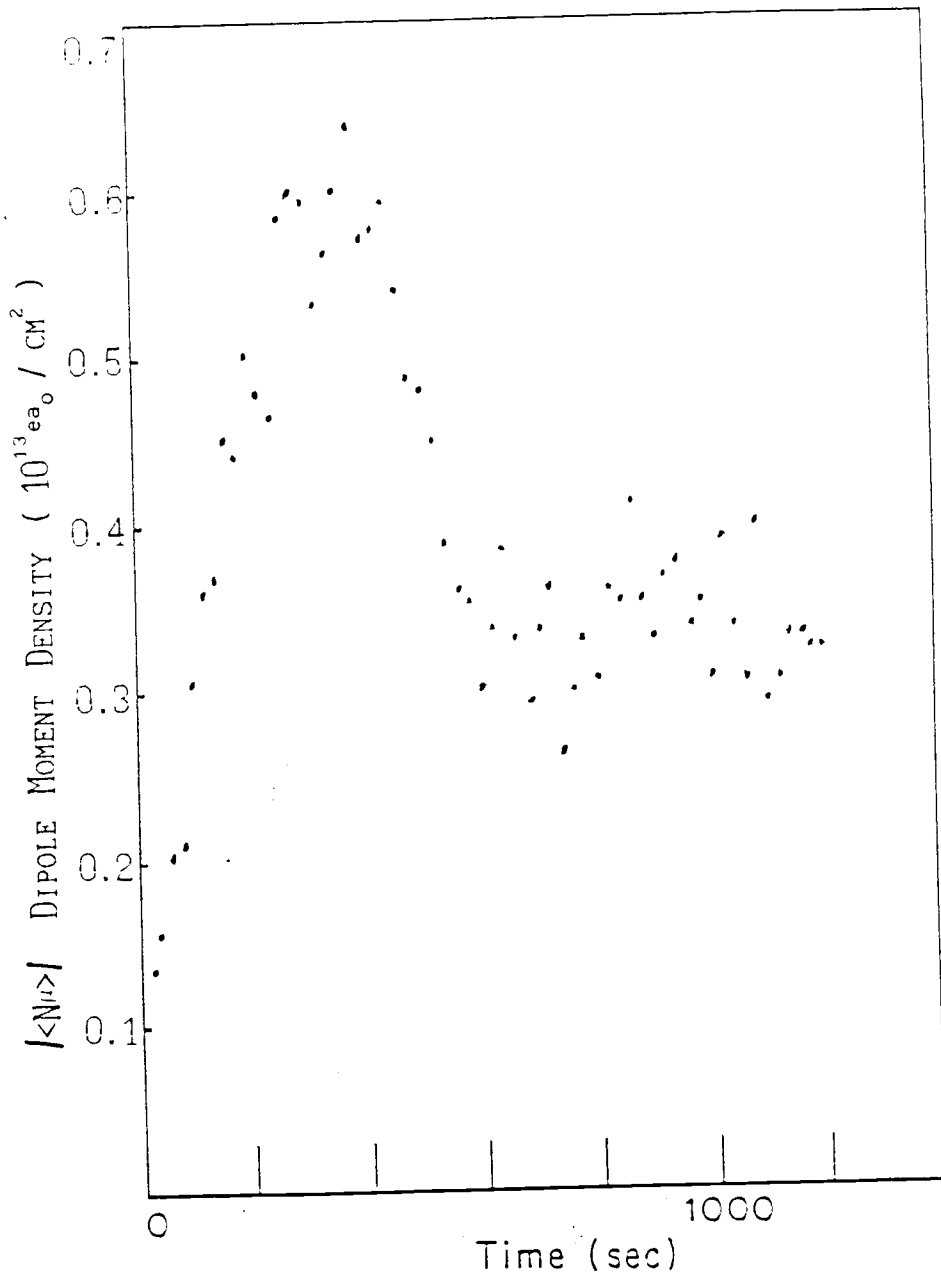


Fig. 7.10e Dipole-Moment Density: Ni Substrate: Constant  $\text{SO}_2$

### 7.7 NO Adsorption on Ni

The surface structure for NO on Ni(111) was found by Steinerück et al.<sup>46</sup> Hamra et al.<sup>47</sup> measured a zero-coverage sticking probability to be  $s_0 = 0.67$  for NO on Ni(100) and that the saturation coverage was 0.55 monolayers. They also found that the desorption energy from the Ni(100) surface was  $E_d = 0.26$  eV.

Figure 7-11 shows the difference in the  $|\langle N\mu \rangle|$  vs  $t$  corresponding to Figs. 6-14a and 6-14b, without and with introduced adsorbate. The NO particle current is 0.07/s. The slope of the fit is  $(0.00033 \pm 0.00010) \times 10^{13} e a_0 / \text{cm}^2 \cdot \text{s}$ . Eq. (5-15) is used to calculate the product  $\mu_a s_a = (2.3 \pm 0.7) \times 10^{-4} e a_0$ .

A summary of results will be presented in Chapter 8 with a discussion of the limitations of the experimental technique. The calculations in this chapter show that this technique may be used to determine significant adsorption properties.

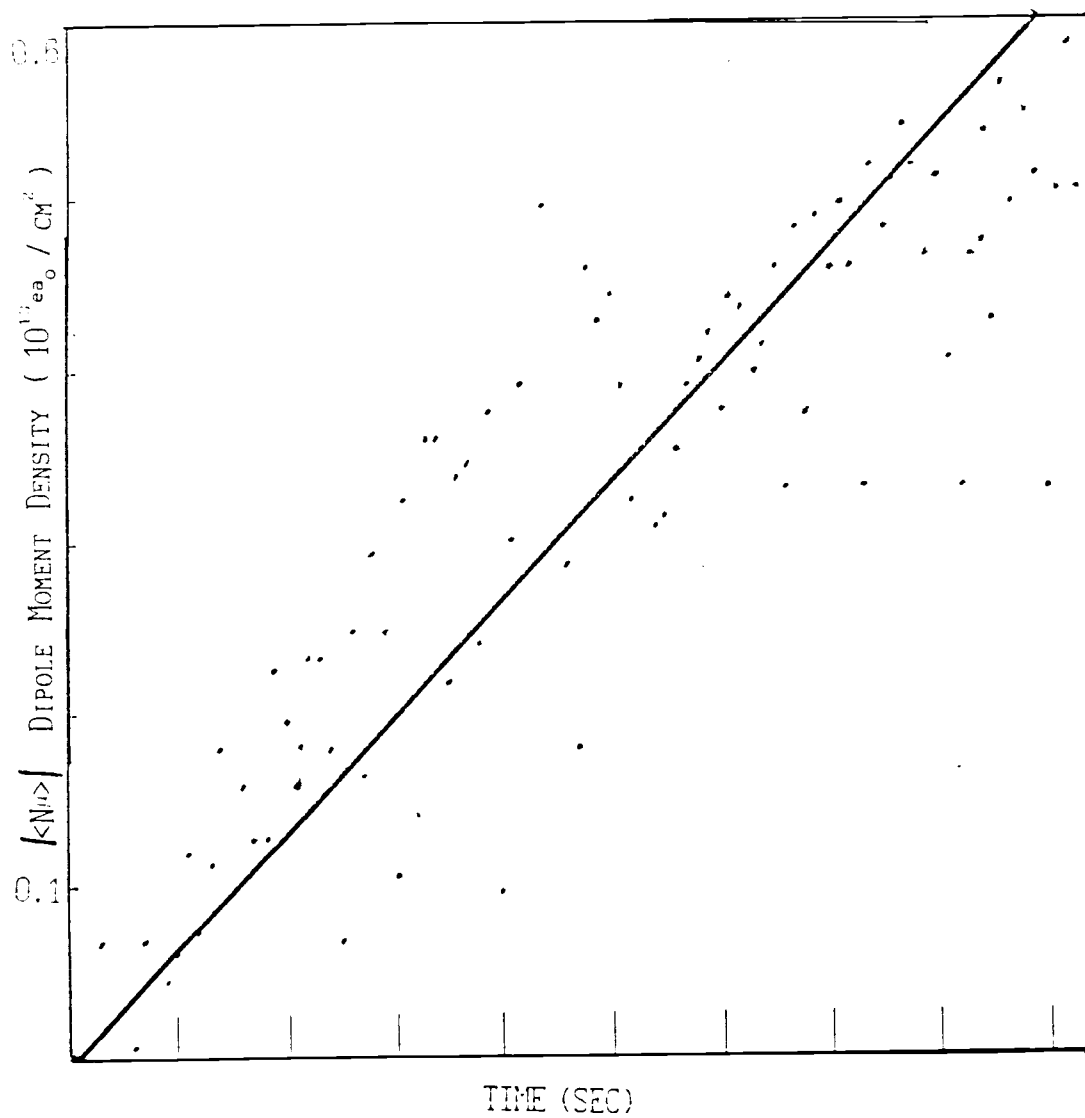


Fig. 7-11 Dipole-Moment Density Difference: NO on Ni Substrate

## CHAPTER 8: SUMMARY

Work has been presented here showing that Rydberg atoms are sensitive to the electric fields produced by adsorbates on the surface of a metal mesh. A relation was constructed between the electric field and the dipole-moment density for adsorbates on a metal surface. Electric fields produced by adsorbates were shown to be capable of ionizing Rydberg atoms that pass within a few microns of the metal surface. A method was developed to convert the measured transmission of Rydberg atoms through the metallic mesh to the dipole-moment density on the surface. The dipole-moment density on the surface, with and without an introduced adsorbate, was shown to reveal several interesting physical properties of adsorbates on a metal surface. These properties included magnitude and orientation of the dipole moment, desorption energy and sticking probability.

### 8.1 Review of the Results

Various experimental conditions have been explored with several introduced adsorbates. This section is devoted to a review and discussion of the results presented in this work, beginning with experimental results that may be compared to results reported in the literature.

Rapid accumulation of CO on Ni was observed (Sec. 7.1) in the limit of adsorption-desorption equilibrium. The desorption

energy of CO (coadsorbed with H<sub>2</sub>O) on a polycrystalline Ni substrate was measured to be  $E_d = 0.70 \pm 0.05$  eV. CO (Sec. 7.1) was also observed to adsorb more slowly when the CO concentration on the surface was near saturation. The product  $\mu_a s_a$  was found to be  $(2.8 \pm 0.4) \times 10^{-3} e a_0$ . A dipole moment of  $0.10 e a_0$ , as measured by Campuzano,<sup>34</sup> implies a sticking probability of approximately 0.03 for CO on Ni at high coverage. A Comparison of this sticking probability to the data presented by Horgan and King<sup>41</sup> indicates from their work a coverage of approximately 0.5 monolayers for CO. This coverage corresponds approximately to the value for saturation coverage of CO on Ni(100) presented by S. Johnson et al.<sup>42</sup> The dipole moment for CO on Ni was inferred with the use of data for H<sub>2</sub>O on Ni. The adsorption of CO caused a shallower dip in transmission, implying a dipole moment antiparallel to that of H<sub>2</sub>O. Therefore, the moment for CO on Ni was found to have the positive end into the surface.

Accumulation of O<sub>2</sub> on Ni was observed (Sec. 7.2) at several Ni substrate temperatures. Adsorbate saturation occurred rapidly, due to the large values for  $s$  and  $c$ . Equilibrium was reached in less than 200 s. The product  $\mu_a s_a$  was measured for several Ni mesh surface temperatures:

$$\text{for } 340 \text{ K } \mu_a s_a = (2.6 \pm 0.6) \times 10^{-4} e a_0,$$

$$\text{for } 300 \text{ K } \mu_a s_a = (1.6 \pm 0.3) \times 10^{-4} e a_0,$$

$$\text{for } 275 \text{ K } \mu_a s_a = (3.0 \pm 0.5) \times 10^{-4} e a_0.$$

Conventional thinking dictates that the sticking probability

decreases with increasing temperature. Values for  $\mu_a s_a$  do not follow this trend if  $\mu_a$  is temperature independent. The desorption energy  $E_d = 0.86 \pm 0.06$  eV could also be determined, since the transmission reached equilibrium quickly. The orientation of the  $O_2$  dipole moment on a Ni substrate was determined in a similar manner as the orientation of CO on Ni.  $O_2$  was found to be oriented with the negative end toward the Ni surface.

The introduction of  $H_2O$  on Au was seen (Sec. 7.3) to reach equilibrium in less 200 s, for the experimental particle currents. Both the desorption energy and the product  $\mu_a s_a$  were determined:

$$E_d = 0.85 \pm 0.05 \text{ eV} \quad \text{and}$$

$$\mu_a s_a = (1.1 \pm 0.1) \times 10^{-3} e a_o.$$

For a dipole moment  $\mu_a = 0.1 e a_o$ , this value of  $\mu_a s_a$  gives a sticking probability  $s \cong 0.01$  at high coverage,  $\theta \cong 1$ .

$H_2O$  on Ni was also observed (Sec. 7.4), and a measurement of both  $\mu_a s_a$  and  $E_d$  were made. The product  $\mu_a s_a$  was found to be  $(1.3 \pm 0.7) \times 10^{-4} e a_o$ , and the desorption energy was found to be  $1.05 \pm 0.05$  eV. A literature search produced a value for  $H_2O$  on the Ni(111) somewhat larger 1.7eV than the value measured in this work. However, the work quoted from the literature was completed with a single crystal face and the surface was at liquid nitrogen temperature.

Adsorbates were studied whose adsorption properties are not well reported in the literature. The following results are for

those adsorbates.

Observations (Sec. 7.5) of the adsorption of  $\text{SO}_2$  on Au allowed the measurement of  $\mu_a s_a$  and  $E_d$ . The product  $\mu_a s_a$  was measured to be  $(4.0 \pm 0.9) \times 10^{-4} e a_0$  and the desorption energy to be  $0.93 \pm 0.06$  eV.  $\text{SO}_2$  was observed (Sec. 7.6) to adsorb onto Ni. The product  $\mu_a s_a$  was measured to be  $(3.0 \pm 0.6) \times 10^{-4} e a_0$ . The long term, equilibrium effect of  $\text{SO}_2$  on Ni was observed, giving a value  $\mu \cong 0.086 \pm 0.004 e a_0$  for the dipole moment of  $\text{SO}_2$  on Ni .

Observing (Sec. 7.7) the adsorption of NO on Ni revealed that  $\mu_a s_a = (2.3 \pm 0.7) \times 10^{-4} e a_0$ .

The molecules that were found to make the most easily observable changes in the transmission when adsorbed onto a surface were those molecules that had the greatest ability to chemically bond and the molecules that had the largest dipole moments.

## 8.2 Difficulties of the Technique

A discussion of some of the questions concerning the experimental technique is presented here. There are at least two facets to these questions, experimental difficulties and theoretical difficulties.

First, the theoretical difficulties occur when an attempt is made to model the electric field produced by adsorbates on a metallic surface. The construction of this model requires an

appropriate way to describe the mesh. In Sec. 2.2.4 the mesh surface is approximated by a square hole in an infinite plane of dipoles. This calculated field is used in the conversion of transmission into dipole moment density. A more exact calculation of the electric field produced by the mesh with a more complete mesh surface is presented in Sec. 2.3. The difference between the two calculations is less than 10% for all transmissions. The difference leads to a maximum change, a decrease, of 10% in the predicted dipole moment density. Figure 8-1 shows the two calculated curves. Curve 1 shows  $T$  vs  $|\langle N\mu \rangle|$  for the model of the mesh as a square hole in an infinite plane of dipoles. Curve 2 shows  $T$  vs  $|\langle N\mu \rangle|$  for the model from Sec. 2-3 that more accurately accounts for more distant holes in the mesh. Curve 3 shows the percentage difference between curves 1 and 2. In reality the mesh is not infinitely thin; A mesh filament is approximately 3 times as wide as the mesh is thick. Therefore, the mesh thickness are considered in Appendix C, where it is shown that the electric field is modified by approximately 10%, an increase, when thickness is included. These two corrections tend to cancel.

An additional theoretical problem is that the behavior of adsorbates on the surface is not completely understood. Therefore, assumptions concerning surface diffusion, adsorbate dissociation, and adsorbate-adsorbate interactions were necessary. Introduced adsorbates were assumed not to diffuse

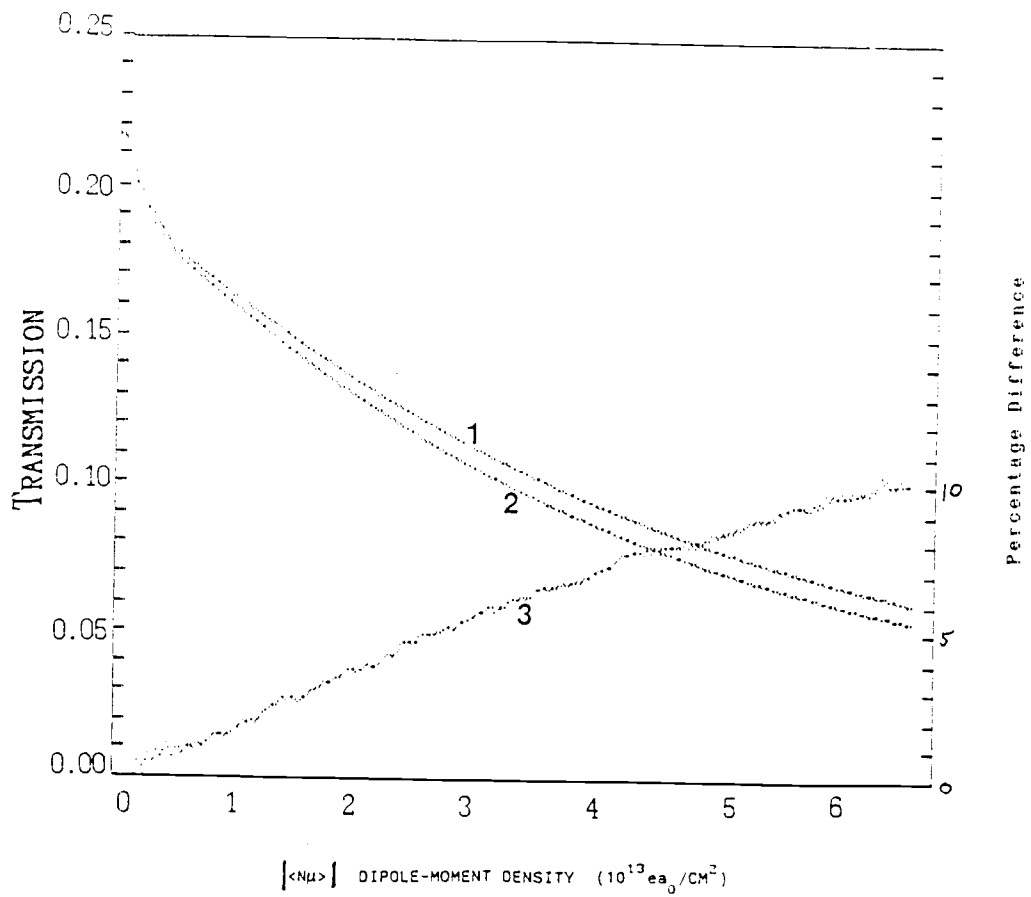


Fig. 8-1 Comparison of T vs  $|\langle N\mu \rangle|$  for Two Calculations of E

around the surface during the experiment. For CO on Ni a calculation was performed to show that diffusion occurred slowly compared to the duration of the experiment (Sec. 2.1.3). Adsorbates were assumed to remain intact on the surface and not to interact with each other explicitly. Implicitly the dipole moment in the model presented in Chapter 4 was assumed to be coverage-dependent, and the interaction between H<sub>2</sub>O and Li on the source side was included in the model.

The sensitivity of this measurement technique is limited and may be viewed in several ways. In ref. 36 two approaches have been taken to this question. Here a different measure of sensitivity will be presented. The sensitivity is limited by the maximum Rydberg state or maximum mean radius of the atom. The electric field plates place a maximum on the value of  $n$  by limiting the critical electric field required for ionization to of 12 V/cm. This electric field implies that the minimum field that may be detected at the center of a mesh opening is 12 V/cm. At the center of the mesh opening, the electric field produced by a dipole moment density  $N\mu$  is given by Eq. (2-19)

$$E_c = 8\sqrt{2}N\mu / b, \text{ where } b = 6.5 \text{ } \mu\text{m}.$$

from which it follows that the absolute sensitivity for this apparatus is limited to  $|\langle N\mu \rangle|_{\min} \cong 6.9 \times 10^{-4} e a_0 / A_s$ .

Another limitation of this technique is revealed when the derived relation between  $|\langle N\mu \rangle|$  and  $T$  is inspected. The rate of

change of the transmission with dipole-moment density is much larger at low adsorbate dipole-moment density, small  $|\langle N\mu \rangle|$ , than at high adsorbate dipole-moment density, large  $|\langle N\mu \rangle|$ . Fig. 5-3 shows that to produce a change of 1% in the transmission requires  $|\langle N\mu \rangle|$  four times larger at a transmission of 12% than at a transmission of 20%. The technique is therefore less sensitive to adsorption at relatively larger adsorbate densities than at zero coverage.

### 8.3 Limits of this Work

The limits to this work are important. The physical nature of the mesh sample is a concern. The mesh is polycrystalline, and not simply a single crystal face. The technique measures the dipole moment that is perpendicular to the mesh surface. Therefore, the component of the moment parallel to the surface is unmeasurable by this technique. Adsorbates behave differently on different crystal faces as a result of the variation of electron densities. For this work, then, the values obtained are an average over several different crystal faces. The polycrystalline surface also has roughness. Surface roughness may cause the dipole moment of a molecule adsorbed on one face to tend to cancel the contribution of a similar molecule on a different crystal face.

Mesh samples were not thermally well isolated therefore surface cooling was difficult. Even with cooled surfaces, the

relatively high surface temperatures,  $T_s \gtrsim 250$  K, lead to a small sticking probability,  $s \ll 0.01$ , for most adsorbates. Many other adsorbates that apparently have a small sticking probability at  $T \cong 300$  K were studied with no measurable change in transmission, e.g.  $N_2$ , He, Ar, Ne, and  $NO_2$ .  $NH_3$  was also studied. However, the presence of  $NH_3$  greatly depleted the Rydberg beam because enough rotational energy is transferred from  $NH_3$  to the excited atom to ionize it. This effect limits the use of any molecule with large rotational moment, e.g.  $H_2$ . Several molecules that readily adsorb at  $T = 300$  K have been used in this work.

#### 8.4 Suggestions for Future Work

The present work has examined the feasibility and usefulness of a beam of Rydberg atoms for the study of adsorption and desorption on a metal surface. Yes, highly excited atoms may be used to study adsorption processes on a metal surface, and yes, specific properties of adsorbates on metal substrates are measurable. However, for more accurate and unambiguous measurements, the vacuum system and atomic beam apparatus described in Chapter 3 must be greatly modified. Because the pressure in the system is greater than or equal to  $10^{-8}$  Torr, a significant layer of background gas adsorbs onto the mesh surface during the course of an experiment. The source of many ambiguities and complex calculations is the presence of the background gas. Therefore, the vacuum system needs to be greatly

upgraded to allow pumping to  $10^{-10}$  Torr. Cryo-pumps, vac-ion pumps, and all-stainless-steel components may allow a pressure of  $10^{-10}$  Torr to be reached.

A redesigned vacuum system should include other surface measurement techniques, such as LEED. These additional methods of surface investigation are necessary in order to corroborate the results from the atomic beam technique and also to analyze the composition and concentration of adsorbates on the surface. Additional surface techniques will allow greater certainty in any measurement and also allow additional parameters to be determined, i.e. both  $\mu$  and  $s$ .

Modification of the excitation system may reduce the complication that a beam with many states causes. The incorporation of newly developed and available diode lasers will allow n-state selection of the atoms that interact with the metal surface. These state selected atoms are off-on sensitive to the electric fields produced by the adsorbates. When the electric field exceeds the ionization limit, the flux of Rydberg atoms can be reduced to nearly zero. The use of diode lasers has been analyzed by C.A. Kocher, unpublished.

The geometry of the metal surface could be changed from that of a mesh to allow for a longer interaction time between surface and atom. One possible alternative geometry would involve a metal plate parallel to the atomic beam within a distance of  $10 \mu\text{m}$ . This geometry would also allow for a clearer

interpretation of the experimental results, since the surface has only one side of interest. Figure 8-2 shows the hypothetical configuration.

The quality of the surface used must be improved in order to make the observation more convincing. The polycrystalline surface provides a source of ambiguity. Any measurement presented in this thesis is an average over all crystal faces present. The mesh could be replaced by a single crystal surface.

In conclusion, the use of Rydberg atoms to investigate adsorbate properties on metal surfaces can be a useful tool in the search for an understanding of the surface. Additionally, through this research it has been learned that Rydberg atoms may be used to probe surface electric fields produced by adsorbates. This technique can augment the present tools used in the analysis of surfaces and provide an area of future investigation for Rydberg-Surface interactions.

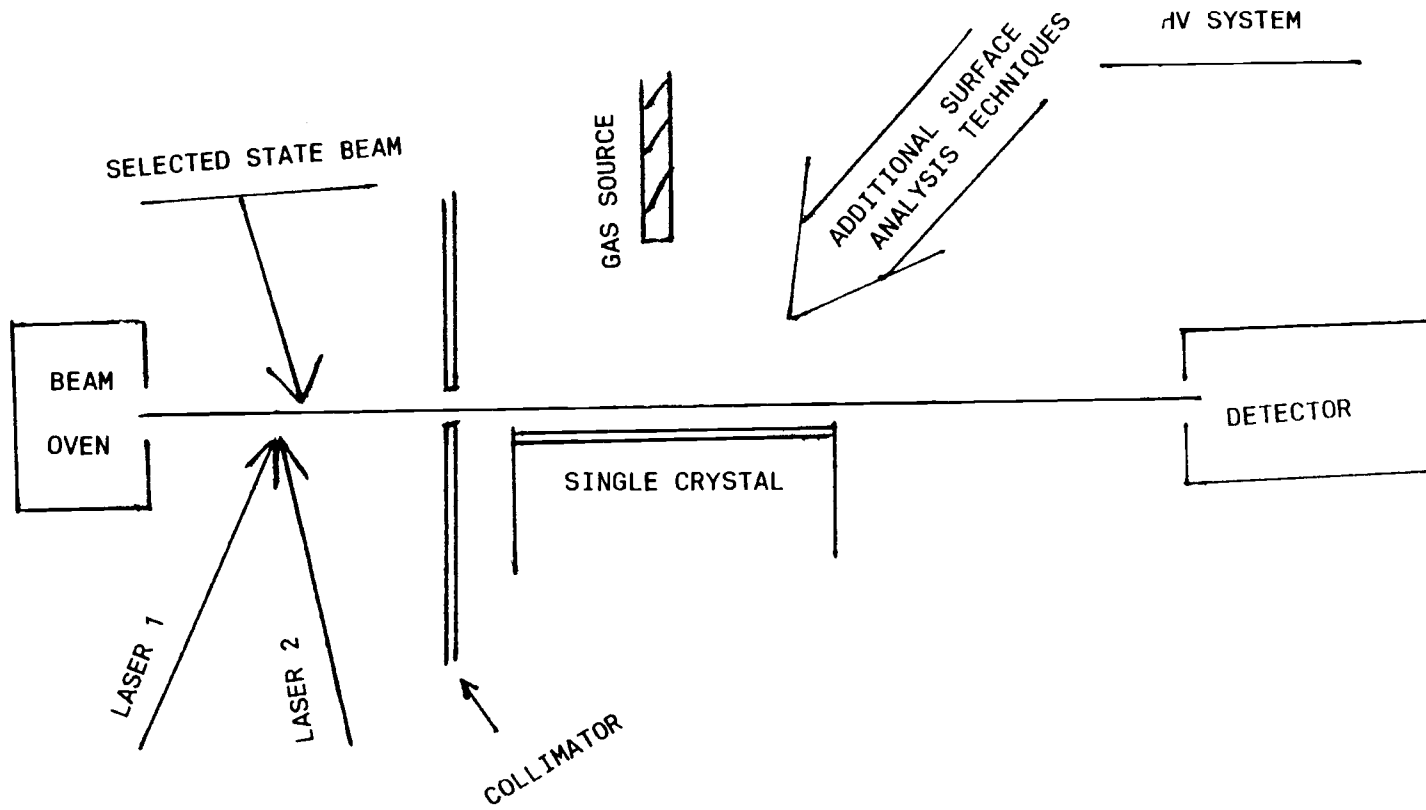


Fig. 8-2 New Apparatus Design

## BIBLIOGRAPHY

- 1) C.A. Kocher and C.R. Taylor, Phys. Lett. A 124, 68 (1987).
- 2) C.R. Taylor, Ph.D. Thesis, Oregon State University, 1987.
- 3) S.A. Edelstein and T.F. Gallagher, Adv. At. Mol. Phys. 14, 365 (1978). see also, T.F. Gallagher, Rep. Prog. Phys. 51, 143 (1988).
- 4) H.A. Bethe and E.E. Salpeter, Quantum Mechanics of One- and Two- Electron Atoms (Springer Verlag, Berlin 1957).
- 5) A.C. Reviere and D.R. Sweetman, Atomic Collision Processes, (North Holland, Amsterdam, 1964), pg.734.
- 6) T.H. Jeys, G.B. McMillian, K.A. Smith, F.B. Dunning, and R.F. Stebbings, Phys. Rev. A 26, 332 (1982).
- 7) See for example:
  - D. Raskin and P. Kusch, Phys. Rev. 179, 712 (1969)
  - A. Shih, D. Raskin and P. Kusch, Phys. Rev. A 9, 652 (1974)
  - A. Shih and V.A. Parsegian, Phys. Rev. A 12, 835 (1975)
- 8) C. Fabre, M. Gross, J.M. Raimond , and S. Haroche, J.Phys B: At. Mol. Phys. 16, L671 (1983).
- 9) M. Prutton, Surface Physics, 2<sup>nd</sup> Ed. (Oxford University Press, Oxford, 1985), Chapt. 6.
- 10) E. Zaremba, and W. Kohn, Phys. Rev. B 15, 1769 (1976).
- 11) S. Andersson, and J. Harris, Phys. Rev. B 27, 9 (1983).
- 12) R.P. Muscat, and D.M. News, Progress in Surf. Sci. 9, 1 (1978).

- 13) R.L. Gerlach and T.N. Rhodin, *Surf. Sci.* 19, 403 (1970).
- 14) N.D. Lang, *Solid State Commun.* 9, 1015 (1971).
- 15) N.D. Lang and A.R. Williams, *Phys. Rev. B* 18, 616 (1978).
- 16) J.E. Muller and J. Harris, *Phys. Rev. Lett.* 53, 2493 (1984).
- 17) J. Topping, *Royal Society Proceedings* 114, 67 (1927).
- 18) M.W. Roberts and C.S. McKee, Chemistry of The Metal Gas Interface, (Clarendon, Oxford 1978), Sec.12.4.
- 19) A. Zangwill, Physics at Surfaces (Cambridge University Press, Cambridge, 1988), Eq. 14.31., pp. 375-384
- 20) X.D. Zhu, Th. Rasing, and Y.R. Shen, *Phys. Rev. Lett.* 25 (1988) 2883.
- 21) A. Zangwill, Physics at Surfaces (Cambridge University Press, Cambridge, 1988), Eq. 14.15.
- 22) J. Frenkel, Kinetic Theory of Liquids (Clarendon Press, Oxford, 1947).
- 23) Adamson, Physical Chemistry at Surfaces (Wiley & Sons, New York, 1982), sec.XVIII-6.
- 24) D. Brennan, and M.J. Graham, *Discuss. Faraday Soc.* 41 (1966), 95.
- 25) J.D. Jackson, Classical Electrodynamics 2<sup>nd</sup> Ed. (Wiley & Sons, New York 1975), sec. 1.6.
- 26) I.S. Gradshteyn and I.M. Ryzhik, Table of Integral, Series, and Products (Academic Press, New York, 1980), Sec. 3.
- 27) N.F. Ramsey, Molecular Beams, (Oxford Press, Clarendon 1963), Sec. II.3

- 28) F. Bozco, G. Ertl, M. Grunze and M. Weiss, *Journal of Catalysis* 49, 18 (1977).
- 29) N.F. Ramsey, *Molecular Beams* (Oxford Press, Clarendon 1963), Chapt. 2.
- 30) P. Browning and P.E. Potter, *Handbook of Thermodynamic Transport Properties of Alkali Metals*, Edited by R.W. Ohse, (Blackwell Scientific Publications, Oxford, 1985), Sec. 6.2.
- 31) T.L. Hill, *Statistical Thermodynamics* (Addison-Wesley Publishing Company Inc., New York, 1976), Chapter 7.
- 32) R.P. Bajpai, H. Kita, and K. Azuma, *Jap. Journ. Appl. Phys.* 15, 2082 (1976).
- 33) D.S. Bailey, S.R. Hiskes, and A.C. Reviere, *Nucl. Fusion* 5, 41 (1964).
- 34) J.C. Campuzano, R. Dus, and R.G. Greenler, *Surf.Sci.* 102, 172 (1982)
- 35) C.R. Brundle, *J. Vac. Sci. Tech.* A3, 1468 (1985).
- 36) G.E. McCown, C.R. Taylor, and C.A. Kocher, *Phys. Rev. A* 38 3918 (1988).
- 37) R.P. Muscat and P. Batra, *Phys Rev. B* 34, 2889 (1986).
- 38) C. Nöbl and C. Benndorf, *Surf. Sci.* 182, 499 (1987).
- 39) S. Masuda, M. Niahyima, Y. Sakisada, and M. Orchi, *Phys Rev. B* 25, 863 (1982).
- 40) S. Trasatti, *Electroanalytical Chemistry and Interfacial Electrochemistry* 33, 351 (1971).

- 41) A.M Horgan and D.A. King, Structure and Chemistry of Solid Surfaces, Ed. G.A. Somarjai, (J.Wiley and Sons, New York, 1968) Sect. 57.
- 42) S. Johnson and R.J. Maddox, Surf.Sci. 108, 77 (1981).
- 43) C. Benndorf and T.E. Madey, Surf. Sci. 194, 63 (1988).
- 44) T.E. Madey and F.P. Netzer, Surf.Sci. 117, 549 (1982).
- 45) S. Holloway and K.H. Bennemann, Surf. Sci. 101, 327 (1980).
- 46) H.P. Steinrück, C. Schneider, P.A. Heiman, T. Poche, E. Umbach, and D. Menzel, Surf. Sci. 208, 136 (1989).
- 47) A.V. Hamra, P.M. Fern, F. Budde, and G. Ertl, Surf.Sci. 199, 13 (1988).
- 48) Morse and Feshbach, Methods of Theoretical Physics (McGraw-Hill, 1953) vol II.

## APPENDICES

## APPENDIX A: CALCULATION OF TEMPERATURE DIFFUSION TIME

A brief, rough calculation of the characteristic time duration required for energy (heat) to diffuse through a mesh sample is made. The heat flow through the mesh, ignoring radiation, is governed by the familiar heat flow equation

$$\frac{\partial T}{\partial t} - \frac{k}{\rho c} \frac{\partial^2 T}{\partial z^2} = \frac{P/A}{\rho c},$$

where  $k$  is the thermal conductivity,  $\rho$  the density,  $c$  the specific heat,  $P$  the power supplied to the mesh,  $A$  the cross-sectional area of the mesh,  $T$  temperature,  $t$  time, and  $z$  is a measure of the length of the mesh. Morse and Feshbach show that the form of the position dependence of the temperature goes as<sup>48</sup>

$$T(z,t) \sim \exp\left(-\frac{k}{z^2 \rho c} t\right). \quad (\text{A-1})$$

The total length of the mesh is defined to be  $\ell$ , therefore to find the characteristic time the following calculation must be made

$$\tau = \frac{\ell^2 \rho c}{k}, \quad (\text{A-2})$$

with the values for Ni taken to be  $\ell = 3$  cm,  $\rho = 8.9$  g/cm<sup>3</sup>,  $c = 0.106$  cal/g deg and  $k = 0.26$  W/m deg and the values for Au taken to be  $\ell = 3$  cm,  $\rho = 19.3$  g/cm<sup>3</sup>,  $c = 0.031$  cal/g deg and  $k = 3.1$  W/cm deg. These values yield  $\tau_{\text{Ni}} = 3.3$  sec for Ni and  $\tau_{\text{Au}} = 7.3$  sec for Au. These values are much shorter than one data channel,  $< 20$  sec, and several time constants are of the same length as one data channel.

## APPENDIX B: SELECTED NOTATIONS

|   | Page of Initial Appearance |
|---|----------------------------|
| $a_o$ - Bohr radius $5.29 \times 10^{-9}$ cm                      | 3                          |
| A - Effective Mesh Open Area                                      | 67                         |
| $A_o$ - Area of oven opening                                      | 35                         |
| $A_s$ - Area of a surface site                                    | 41                         |
| Au(100)- $8.33 \times 10^{-16}$ cm <sup>2</sup>                   |                            |
| Ni(100)- $6.20 \times 10^{-16}$ cm <sup>2</sup>                   |                            |
| $A_T$ - Area of tube opening $2.8 \times 10^{-3}$ cm <sup>2</sup> | 51                         |
| b - Mesh filament width $6.5 \times 10^{-4}$ cm                   | 21                         |
| c - Particle current (number per second)                          | 44                         |
| $E_c$ - Electric field at the center of a mesh opening            | 25                         |
| $E_d$ - Desorption energy   | 10                         |
| $E_{diff}$ - Surface diffusion energy                             | 12                         |
| $E_n$ - Field ionization energy                                   | 3                          |
| k - Boltzmann's constant $1.38 \times 10^{-16}$ erg/ °K           | 4                          |
| $kT_o$ - 1/40 eV for $T_o = 293$ K                                | 121                        |
| $\ell$ - angular momentum   | 3                          |
| $L_{OD}$ - oven-detector separation 60cm                          | 4                          |
| $\ell_s$ - surface site separation                                | 12                         |
| n - quantum number  | 3                          |
| N - Number density (/cm <sup>2</sup> ) of adsorbates              | 11                         |
| $N_s$ - Number density (/cm <sup>2</sup> ) of surface sites       | 11                         |
| $P_a$ - Adsorbate gas pressure                                    | 52                         |

|                              |  |     |
|------------------------------|--|-----|
| $P(E)$                       | - Rydberg Atom survival probability                          | 67  |
| $P_T$                        | - Gas pressure in tube                                       | 42  |
| $r_n$                        | - Orbit radius for quantum state $n$                         | 3   |
| $r_{OM}$                     | - Oven-mesh separation 30cm                                  | 36  |
| $r_{TM}$                     | - Tube-mesh separation 5cm                                   | 42  |
| $s$                          | - Sticking probability                                       | 44  |
| $s_o$                        | - Sticking probability at zero coverage                      | 122 |
| $T$                          | - Mesh transmission  | 8   |
| $T_o$                        | - Oven temperature   | 35  |
| $T_s$                        | - Surface temperature  | 12  |
| $ \langle N\mu \rangle $     | - Absolute value for dipole-moment density                   | 48  |
| $\delta\phi$                 | - Change in work function                                    | 11  |
| $\mu$                        | - Dipole moment  | 11  |
| $\mu_o$                      | - Dipole moment at zero coverage                             | 12  |
| $\tau$                       | - incidence time   | 44  |
| $\tau_o$                     | - Minimum stay time $\sim 10^{-13}$ sec                      | 13  |
| $\theta$                     | - Relative coverage  | 11  |
| $\Gamma$                     | - Desorption rate  | 13  |
| $\Gamma_o$                   | - Desorption rate constant $\sim 10^{13}$ sec                | 13  |
| $\Delta\langle N\mu \rangle$ | - Change in dipole moment density                            | 76  |
| $\Delta T/\Delta N\mu$       | - Percent change in $T$ induced by given<br>change in $N\mu$ | 94  |

## APPENDIX C: ELECTRIC FIELD DUE TO A THICK MESH

The mesh thus far has been assumed to be thin, where the thickness  $d$  is taken to be much less than the strand width  $b$ ,  $d \ll b$ . However, for the mesh in this experiment  $b = 6.5 \times 10^{-4}$  cm and  $d = 2.0 \times 10^{-4}$  cm. A mesh filament may be modeled as an infinitely long rectangular strand. The electric field near a mesh filament due to the dipoles on the three nearest faces of the strand can be estimated with Eqs. (2-13) and (2-15). Figure C-1 shows the geometry of the mesh faces.

The components of the electric field produced by molecules on face 1 is

$$E_x = 2N\mu_1 \left( \frac{d - z}{(x + b)^2 + (z - d)^2} + \frac{z - d}{x^2 + (z - d)^2} \right),$$

$$E_z = 2N\mu_1 \left( \frac{(x + b)}{(x + b)^2 + (z - d)^2} - \frac{x}{x^2 + (z - d)^2} \right).$$

The components of the electric field produced by molecules on face 2 is

$$E_x = 2N\mu_2 \left( \frac{z + d}{(x + d)^2 + z^2} - \frac{z}{x^2 + z^2} \right),$$

$$E_z = 2N\mu_2 \left( \frac{x}{(x + d)^2 + z^2} - \frac{x}{x^2 + z^2} \right).$$

The components of the electric field produced by molecules on face 3 is

$$E_x = 2N\mu_3 z \left( \frac{-1}{(x + b)^2 + z^2} + \frac{1}{x^2 + z^2} \right),$$

$$E_z = 2N\mu_3 \left( \frac{(x + b)}{(x + b)^2 + z^2} - \frac{x}{x^2 + z^2} \right).$$

The components are added together and the field magnitude is found as a function of position for several coverages.

The calculated electric field produced when a density  $|\langle N\mu \rangle|$ ,  $ea_0 \times 10^{13}/\text{cm}^2$ , is placed on faces 1 and 3, only, is appreciable, cancelling only at  $x = d/2$ . However, this does not occur experimentally.

When no adsorbate is introduced. A density of the same order accumulating on faces 1 and 3 also accumulates on face 2. The calculated electric field, when a density  $|\langle N\mu \rangle|$ ,  $ea_0 \times 10^{13}/\text{cm}^2$ , is also placed on face 2, is modified by 10% or less in contrast to the thin mesh case when a density  $|\langle N\mu \rangle|$ ,  $ea_0 \times 10^{13}/\text{cm}^2$ , is placed on it. For the case when adsorbate is introduced the thin mesh analysis is valid. Since the adsorbate is introduced only on one side of the mesh.

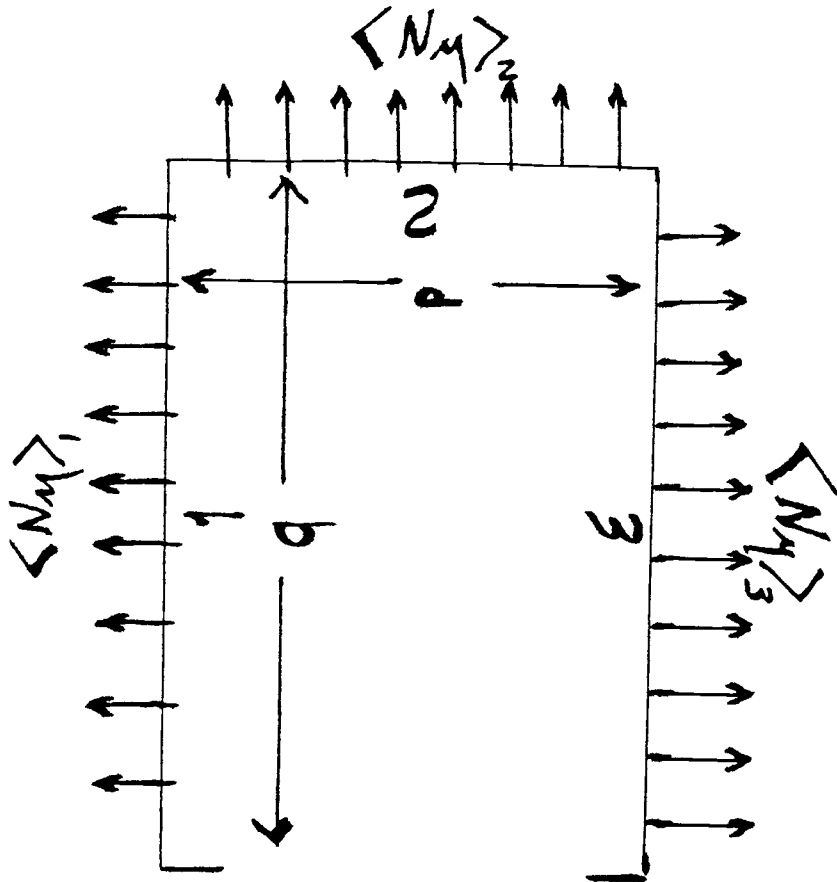


Fig. C-1 Geometry of Thick Mesh